MATERIALS DESIGN FOR LIQUID AND QUASI-SOLID-STATE TELLURIUM-BASED RECHARGEABLE BATTERIES

by

Yue Zhang

MASc., Shanghai Jiao Tong University, 2019

A THESIS SUBMITTED IN PARTIAL FULFILLMENT OF

THE REQUIREMENTS FOR THE DEGREE OF

DOCTOR OF PHILOSOPHY

in

THE COLLEGE OF GRADUATE STUDIES

(Mechanical Engineering)

THE UNIVERSITY OF BRITISH COLUMBIA

(Okanagan)

April 2023

©Yue Zhang, 2023

The following individuals certify that they have read, and recommend to the College of Graduate Studies for acceptance, a dissertation entitled:

Materials Design for Liquid and Quasi-Solid-State Tellurium-Based Rechargeable Batteries

submitted by Yue Zhang in partial fulfillment of the requirements of

the degree of Doctor of Philosophy

Dr. Jian Liu, School of Engineering
Supervisor

Dr. Dimitry Sediako, School of Engineering
Supervisory Committee Member

Dr. Mohammad Arjmand, School of Engineering
Supervisory Committee Member

Dr. Jonathan Holzman, School of Engineering
University Examiner

Dr. Xiangbo Meng, University of Arkansas
University Examiner

Abstract

Rechargeable lithium-ion batteries (LIBs) are regarded as promising battery technology in the applications of large-scale energy storage and electric vehicles due to the merits of high efficiency and long lifespan. Currently, LIBs are mainly challenged by the limited capacity of intercalation-type cathodes and safety issues caused by organic solvents. Recently, conversion-type elements sulfur (S) and selenium (Se) as alternative cathodes have encouraged tremendous studies owing to the remarkable capacity by two-electron electrochemical conversion. However, the further commercialization of Li-S or Li-Se batteries is impeded by the sluggish redox kinetics and indecent capacity caused by their intrinsic low electrical conductivity. Tellurium (Te) with considerably higher electrical conductivity and comparable volumetric capacity, has been focused on solving the problems of volume expansion and cycling instability since 2014.

In this dissertation, durable liquid-based or quasi-solid-state Li-Te batteries are constructed via rational cathode structure design and electrolyte chemistry. The commercially available or as-synthesized activated carbons are employed as Te hosts to buffer the volume change of Te upon lithiation/delithiation. The role of pore structure (pore size, pore volume) on the electrochemical performance of Te/C cathodes is clarified to correlate the interplay between Te and C. The optimized porous carbons are found to ensure highly stable Te cathodes in Li-Te batteries. Moreover, flexible gel polymer electrolytes are prepared to solve the interface incompatibility in quasi-solid-state Li-Te batteries. Composite Te_xS_y cathodes are furtherly synthesized by the integration of low-cost S and high-conductivity Te to achieve excellent specific capacity and cycling stability. Theoretical calculations and comprehensive characterizations demonstrate the fast redox kinetics facilitated by Te and different working mechanisms in Li-Te_xS_y batteries. Meanwhile, the study of electrolyte chemistry in K-Te batteries is involved in broadening the applicability of Te electrodes, including the fabrication of reinforced composite gel polymer electrolytes and the investigations of the K-Te reaction pathways and Te/electrolyte interface engineering design.

The fundamental understanding of the Li/K-Te system is deepened by the systematic *in situ* or *ex situ* characterizations. It is expected that these studies will provide some viable strategies for the

engineering design of Li/K-Te batteries, paving the way for developing high-energy-density battery technology.

Lay Summary

The newly emerging Li/K-Te battery systems are promising candidates for energy storage and clean transportation due to the high electrical conductivity and comparable volumetric capacity of Te. However, their development is challenged by the large volume expansion and cycling/structure instability over cycles.

This dissertation develops highly stable Te/C cathodes by preparing porous carbons with proper pore structure for the accommodation of Te's volume change. Quasi-solid-state Li-Te batteries are constructed with gel polymer electrolytes to ensure good interface contact. Moreover, Te_xS_y composite cathodes are fabricated to enhance the reversible capacity and facilitate the internal reaction kinetics. K-Te electrochemistry is also investigated by revealing the reaction mechanism, identifying electrolyte chemistry, and stabilizing Te/electrolyte interface *via* various characterizations.

These improvements will guide the further development of high-energy-density Te-based rechargeable batteries.

Preface

This dissertation presents the original research work conducted by the author Yue Zhang under the supervision of Dr. Jian Liu at the Advanced Materials for Energy Storage Laboratory on UBC Okanagan campus. I was responsible for the majority of materials preparation and characterization, data collection and analysis, and figure visualization throughout my thesis research. Several research contents were developed in collaboration with individuals from Canadian and International research facilities. The contributions of the main collaborators to each work are described below. My supervisor, Dr. Jian Liu, and the committee members, Dr. Dimitry Sediako and Dr. Mohammad Arjmand, were mentoring and leading me through the thesis direction.A list of any publications arising from work presented in the thesis and the chapters in which the work is located are as follows:

Chapters 1, 2 and 10 of this dissertation include versions of the following:

- **Y. Zhang**, D. Manaig, D.J. Freschi, J. Liu, Materials design and fundamental understanding of tellurium-based electrochemistry for rechargeable batteries, *Energy Storage Mater.*, 2021, 40, 166-188.

I wrote the manuscript draft, organized figures and tables, and edited the manuscript. D. Manaig reviewed and edited the manuscript. D.J. Freschi is our industry partner and provided funding support and revision comments. J. Liu supervised the draft organization and provided guidance in data analysis and manuscript revision.

Chapter 4 of this dissertation includes versions of:

- **Y. Zhang**, W. Lu, P. Zhao, M.H. Aboonasr Shiraz, D. Manaig, D.J. Freschi, Y. Liu, J. Jian, A durable lithium–tellurium battery: Effects of carbon pore structure and tellurium content, *Carbon*, 2021, 173, 11-21. (Front Cover)
- **Y. Zhang**, W. Lu, P. Zhao, L. Tao, Y. Liu, D. Manaig, D.J. Freschi, J. Liu, The role of carbon pore structure in tellurium/carbon cathodes for lithium-tellurium batteries, *Electrochim. Acta*, 2021, 388, 138621.

I conducted the experimental work included in the aforementioned papers and prepared the original draft of the research articles. W. Lu provided help in thermogravimetric measurement and data collection. P. Zhao participated in electrode preparation and battery testing. M.H. Aboonasr Shiraz contributed to the electrode slurry casting procedures. D. Manaig reviewed and edited the manuscript. D.J. Freschi is our industry partner and provided funding support and revision comments. Y. Liu reviewed the manuscript. J. Liu supervised the experiments and provided guidance in data analysis and manuscript revision. L. Tao contributed to the synthesis procedures of the lignin-derived porous carbon.

Chapter 5 of this dissertation includes components from:

- **Y. Zhang**, W. Lu, D. Manaig, D.J. Freschi, Y. Liu, H. Xie, J. Liu, Quasi-solid-state lithium-tellurium batteries based on flexible gel polymer electrolytes, *J. Colloid Interface Sci.*, 2021, 605, 547-555.

I contributed to the experimental work conducted in the research article above, data analysis, and manuscript writing. W. Lu provided guidance in the preparation and characterization of gel polymer electrolytes. D. Manaig reviewed and edited the manuscript. D.J. Freschi is our industry partner and provided funding support and revision comments. Y. Liu and H. Xie reviewed and edited the manuscript. J. Liu supervised the experiments and provided guidance in data analysis and manuscript revision.

Chapter 6 of this dissertation includes components from:

- **Y. Zhang**, O.K. Orhan, L. Tao, W. Lu, M. Ponga, D.J. Freschi, J. Liu, A High-Performance Tellurium-Sulfur Cathode in Carbonate-Based Electrolytes, *Nano Energy*, 2023, 107, 108141.

I conducted the experiment work, data collection, figure visualization, and manuscript writing in the research article above. O.K. Orhan contributed to the theoretical simulation and corresponding results discussion in the manuscript. L. Tao participated in the pouch cell setup and testing. W. Lu provided help in thermogravimetric measurement and data collection. M. Ponga provided support in simulation and manuscript editing. D.J. Freschi is our industry partner and provided funding

support and technical help in tube sealing under vacuum. J. Liu supervised the experiments and provided guidance in data analysis and manuscript revision.

Chapter 7 of this dissertation includes components from:

- **Y. Zhang**, C. Liu, Z. Wu, D. Manaig, D.J. Freschi, Z. Wang, J. Liu, Enhanced Potassium Storage Performance for K-Te Batteries via Electrode Design and Electrolyte Salt Chemistry, *ACS Appl. Mater. Interfaces*, 2021, 13, 16345-16354.

I contributed to the experiments work, data analysis, and manuscript writing in the research article above. C. Liu provided help in the X-ray photoelectron spectroscopy analysis of samples. Z. Wu provided help in K-Te cell assembly. D. Manaig reviewed and edited the manuscript. D.J. Freschi is our industry partner and provided funding support and revision comments. Z. Wang reviewed and edited the manuscript. J. Liu supervised the experiments and provided guidance in data analysis and manuscript revision.

Chapter 8 of this dissertation includes components from:

- **Y. Zhang**, H. Zhu, D.J. Freschi, J. Liu, High-Performance Potassium-Tellurium Batteries Stabilized by Interface Engineering, *Small*, 2022, 18(15), 2200085.

I conducted the majority of the experimental work in the research article above, data analysis, as well as manuscript writing. H. Zhu contributed to the experiment of atomic layer deposition on electrodes. D.J. Freschi is our industry partner and provided funding support and reviewed and edited the manuscript. J. Liu supervised the experiments and provided guidance in data analysis and manuscript revision.

Chapter 9 of this dissertation includes components from:

- **Y. Zhang**, A. Bahi, F. Ko, J. Liu, Polyacrylonitrile-Reinforced Composite Gel Polymer Electrolytes for Stable Potassium Metal Anodes, *Small*, 2022, 18(8), e2107186. (Inside Cover)

I conducted the majority of the experimental work in the research article above, data analysis, as well as manuscript writing. A. Bahi provided electrospinning fibers for further preparation of gel polymer electrolytes in our lab and completed the tensile strength testing of gel polymer

electrolytes. F. Ko reviewed and edited the manuscript. J. Liu supervised the experiments and provided guidance in data analysis and manuscript revision.

During my Ph.D. study, I completed one research article and one review paper about the study of lithium aluminum germanium phosphate solid electrolytes. Meanwhile, I made contributions to the following papers as a co-author. My main contributions include SEM characterization, data analysis, and manuscript editing.

Research paper:

- **Y. Zhang**, H. Liu, Z. Xie, W. Qu, J. Liu, Improving the Stability of Lithium Aluminum Germanium Phosphate with Lithium Metal by Interface Engineering. *Nanomater.*, 2022, 12(11), 1912.

Review paper:

- **Y. Zhang**, H. Liu, Z. Xie, W. Qu, D.J. Freschi, J. Liu, Progress and Perspectives of Lithium Aluminum Germanium Phosphate-Based Solid Electrolytes for Lithium Batteries (Accepted by *Adv. Funct. Mater.* on Apr 3, 2023)

Co-author papers:

- C. Liu[1], **Y. Zhang[1]**, Q.Y. Zhou, Y.K. Dai, Y.L. Zhang, X. Yang, et al., 3D Nano-heterostructure of $ZnMn_2O_4$@Graphene-Carbon Microtubes for High-Performance Li-Ion Capacitors, *ACS Appl. Mater. Interfaces*, 2021, 13(44), 52542-52548. (Co-first author)
- Z. Wu, J. Zou, **Y. Zhang**, X. Lin, D. Fry, L. Wang, et al., Lignin-derived hard carbon anode for potassium-ion batteries: Interplay among lignin molecular weight, material structures, and storage mechanisms, *Chem. Eng. J.*, 2022, 427, 131547.
- X. Lu, L. Tao, K. Qu, **Y. Zhang**, C. Liu, R. Godin, J. Liu, A low-concentration eutectic electrolyte for superior cycling ability of aqueous zinc-ion capacitors. *J. Mater. Chem. A*, 2022, 10(38), 20273-20282.
- H. Zhu, M.H.A. Shiraz, L. Liu, **Y. Zhang**, J. Liu, Atomic layer deposited aluminum oxynitride coating for high-performance Si anode in lithium-ion batteries, *Appl. Surf. Sci.*, 2022, 578, 151982.

- C. Liu, Y. Xia, **Y. Zhang**, Q.Y. Zhou, H.B. He, F.D. Yu, et al., Pseudocapacitive Crystalline $MnCo_2O_{4.5}$ and Amorphous $MnCo_2S_4$ Core/Shell Heterostructure with Graphene for High-Performance K-Ion Hybrid Capacitors, *ACS Appl. Mater. Interfaces*, 2020, 12, 54773-54781.

Table of Contents

Abstract ..... **iii**

Lay Summary ..... **v**

Preface ..... **vi**

Table of Contents ..... **xi**

List of Tables ..... **xvii**

List of Figures ..... **xix**

List of Abbreviations ..... **xxxiii**

List of Chemicals ..... **xxxv**

List of Symbols ..... **xxxvi**

List of Elements ..... **xxxvii**

List of Units ..... **xxxviii**

Acknowledgements ..... **xxxix**

Dedication ..... **xli**

Chapter 1 Introduction **1**

1.1 Research Background 1

1.2 Main Challenges 4

1.3 Scope of Research 7

1.4 Thesis Structure 8

1.5 Novelty and Originality of Research 9

Chapter 2 Literature Review and Research Objectives **11**

2.1 Literature Review 11

2.1.1 Te Cathode Design 11

2.1.1.1 Te/Porous Carbon Cathodes 11

2.1.1.2 Te Nanowires 15

2.1.2 TeS Composite Cathodes 22

2.1.3 Electrolyte Chemistry 28

2.1.3.1 Liquid Electrolytes 28

2.1.3.2 Solid Electrolytes 30

2.1.4 K-Te Electrochemistry 31

2.2 Research Summary 36

2.2.1 Capacity-Voltage-Energy Comparison 36

2.2.2 Challenges 37

2.3 Research Objectives 39

2.3.1 Develop Stable Porous Carbon as Te Host in Liquid Electrolyte Based Li-Te Batteries 39

2.3.2 Develop High-Capacity and Durable Te_xS_y Composite Cathodes 39

2.3.3 Design Highly Conductive and Stable Solid Electrolytes 40

2.3.4 Mechanistic Studies on the Interplay Between Te (or Te_xS_y) Cathodes and Liquid/Solid electrolytes 40

2.3.5 Modify Te Electrode/Electrolyte Interface by the Advanced Surface Coating Technique 40

2.4 Chapter Summary 40

Chapter 3 Research Methodology 42

3.1 Materials Synthesis 42

3.1.1 Synthesis of Porous Carbon 42

3.1.2 Synthesis of Well-Defined Te/C Structure 43

3.1.3 Synthesis of Te_xS_y Compounds and Te_xS_y/KB Composites 43

3.1.4 Preparation of Gel Polymer Electrolytes 43

3.1.5 Preparation of PAN-Based Composite Gel Polymer Electrolytes 44

3.1.5.1 Preparation of PAN Nanofibers 44

3.1.5.2 Preparation of PVDF-HFP-KFSI and PVDF-HFP-KFSI@PAN 44

3.1.6 Te/C or Te_xS_y/KB Cathode Preparation 45

3.1.7 Atomic Layer Deposition of Al_2O_3 on Te/C Electrodes 45

3.2 Cell Assembly 45

3.3 Materials Characterizations 46

3.3.1 Morphology Investigation 46
3.3.1.1 Scanning Electron Microscopy and Energy Dispersive Spectroscopy 47
3.3.1.2 Transmission Electron Microscopy 47
3.3.1.3 Micro X-ray Computed Tomography 47
3.3.2 Structure Analysis 48
3.3.2.1 X-ray Diffraction 48
3.3.2.2 X-ray Photoelectron Spectroscopy 48
3.3.2.3 Pore Structure Characterization 49
3.3.2.4 Tensile Strength 49
3.3.3 Electrochemical Characterization 49
3.3.3.1 Cyclic Voltammetry 49
3.3.3.2 Electrochemical Impedance Spectroscopy 50
3.3.3.3 Battery Performance Evaluation 51
3.3.4 DFT Simulation 52
3.4 Chapter Summary 52
Chapter 4 Te/C Cathode Structure for Li-Te Batteries 53
4.1 Introduction 53
4.2 Effect of Carbon Pore Structure on the Performance of Te/C Cathodes 55
4.2.1 Structural Analysis of Te/C Composites with Micro/Mesoporous Carbons 55
4.2.2 Morphology Investigation of Te/C Composites with Micro/Mesoporous Carbons. 58
4.2.3 Cycling and Rate Performance of Te/C Cathodes with Micro/Mesoporous Carbons 61
4.3 Effect of Te Content on the Performance of ASAC25-Te Cathodes 69
4.3.1 Microstructures of ASAC25-Te Composites with Various Te Content 69
4.3.2 Cycling Stability of ASAC25-Te Cathodes with Various Te Content 70
4.3.3 Working Mechanism Analysis of Te-C Interplay During Charge/Discharge Process 73

4.4 Durable Te/C Cathodes with Biomass-Derived Porous Carbon as Te Host 79
4.4.1 Schematic of Preparation Procedures of Carbon Activation 79
4.4.2 Pore Structure Analysis of Different Porous Carbons 80
4.4.3 Morphology and Structural Characterizations of Te/C Composites 81
4.4.4 Cycling Performance of Te/C Cathodes with Various Porous Carbons 84
4.4.5 Long-Cycling Performance of the Te/AC700 Cathode 88
4.4.6 Kinetics Analysis of Te/C Cathodes with Various Porous Carbons 89
4.4.7 Schematic of Li-Ion Pathways in Te/AC Structure 91
4.4 Chapter Summary 92
Chapter 5 Gel Polymer Electrolytes for Li-Te Batteries 94
5.1 Introduction 94
5.2 Physiochemical Properties of Gel Polymer Electrolytes 95
5.3 Interfacial Compatibility of GPE Against Li Metal 97
5.4 Quasi-Solid-State Li-Te Batteries 99
5.4.1 Battery Performance of Li/GPE/Te Cells 99
5.4.2 Effect of Binder on Li/GPE/Te Cells 101
5.5 Performance Evaluation of Quasi-Solid-State Li-S/Se/Te Batteries 104
5.6 Chapter Summary 107
Chapter 6 Composite TeS Cathodes for High-Energy-Density Batteries 108
6.1 Introduction 108
6.2 Synthesis and Structure Analysis of Te_xS_y Composites 111
6.3 DFT Simulations 114
6.4 Morphology and Structure of TexSy/KB Composites 120
6.5 Cycling Performance of Te_xS_y/KB Cathodes 123
6.6 Galvanostatic Charge/Discharge Profiles, Rate and Long-Cycling Performance of S/KB and Te_1S_7/KB Cathodes in Concentration-Varied Electrolytes 127
6.7 Redox Kinetics Analysis of S/KB and Te_1S_7/KB Cathodes upon Lithiations/Delithiation 131
6.8 Ex-Situ Surface Analysis and Mechanistic Study of Cycled S/KB and Te_1S_7/KB Cathodes 134

6.9 Li-S/KB and Li-Te_1S_7/KB Pouch Cell Performance 141

6.10 GPE-Based Li-S/KB and Li-Te_1S_7/KB Cell Performance 144

6.11 Chapter Summary 145

Chapter 7 Electrolyte Chemistry and Cathode Structure for K-Te Batteries 146

7.1 Introduction 146

7.2 Cycling and Rate Performance of K-Te Batteries with KFSI and KPF_6 Salts 147

7.3 Redox Kinetics Analysis of KFSI and KPF_6 Based K-Te Batteries 153

7.4 Investigation of Solid Electrolyte Interphase Layer on the Te/C Electrode Surface 157

7.5 Chapter Summary 160

Chapter 8 Improving Cathode Structure Stability by Atomic Layer Deposition Technique 162

8.1 Introduction 162

8.2 Te/C Cathode Design 163

8.3 Electrochemical Performance of K-Te/BP2000 Batteries 164

8.4 Reaction Mechanism of K-Te Electrochemistry in Carbonate Electrolytes 168

8.5 Surface Coating on Te/BP2000 Electrode Surface 171

8.6 Effect of Ultrathin Al_2O_3 Film on Electrochemical Performance and Structural Stability of the K-Te/BP2000 Batteries 175

8.7 Working Mechanism Analysis of Surface-Coated Te/BP2000 Electrodes 182

8.8 Chapter Summary 183

Chapter 9 Composite Gel Polymer Electrolytes for K Anode 185

9.1 Introduction 185

9.2 Preparation Process of PVDF-HFP-KFSI@PAN Composite Gel Polymer Electrolytes 186

9.3 Morphology and Structural Stability of PVDF-HFP-KFSI@PAN CGPE 187

9.4 Mechanical Strength, Crystal Structure, and Chemical Composition of PVDF-HFP-KFSI@PAN CGPE 191

9.5 Electrochemical Properties of PVDF-HFP-KFSI@PAN CGPE 192

9.6 Interfacial Stability of PVDF-HFP-KFSI@PAN CGPE Against K Metal Anode 194

9.7 Post-Cycling Observations of GF, PVDF-HFP-KFSI and PVDF-HFP-KFSI@PAN ... 200

9.8 Different Electrochemical Deposition Behaviors of K Metal with GF, PVDF-HFP-KFSI, and PVDF-HFP-KFSI@PAN 203

9.9 Chapter Summary 205

Chapter 10 Conclusions, Contributions, and Perspectives 206

10.1 Conclusions 206

10.2 Contributions 208

10.3 Limitations 209

10.4 Perspectives 209

Bibliography 212

Appendix 229

List of Tables

Table 1.1.1 Voltages, capacities, and specific energies of rechargeable Te batteries in comparison with Li-ion, Li-S and Li-Se batteries. 4

Table 2.1.1 Comparison of Te-based cathodes in Li-Te batteries. 20

Table 2.1.2 Comparison of Li-Te, Na-Te, K-Te, Mg-Te, Zn-Te and Al-Te systems. 32

Table 2.2.1 Typical characteristics of S, Se, and Te. 38

Table 3.1.1. Abbreviation and specification of gel polymer electrolytes and glass fiber separator. 45

Table 3.2.1. Cell configuration of cells tested in this dissertation. 46

Table 4.1.1. Pore structures of ASAC25 and ASAC30. 58

Table 4.1.2. EDS elemental analysis of ASAC25-Te and ASAC30-Te composites. 61

Table 4.1.3. EDS elemental analysis of ASAC25-Te and ASAC30-Te cathodes. 68

Table 4.2.1. Comparison of Te cathodes in Li-Te batteries. 76

Table 4.3.1. Pore structures of AC600, AC700, and AC800. 81

Table 4.3.2. Calculated R_e, R_{SEI}, and R_{ct} from the Nyquist plots in **Figure 4.3.10**. 90

Table 5.2.1. Charge transfer resistance of the Li/GPE/Li cell with varying storage time. 97

Table 5.3.1. Resistances of the Li/GPE/Te cells with PVDF and SA binders. 102

Table 5.4.1. Resistances of the Li/GPE/chalcogen cells. 107

Table 6.2.1. The possible migration pathways in Li_2S, $Li_{16}S_7Te$, and $Li_2Te_xS_y$. The Li atomic site numbering is shown in **Figure 6.2.1**. 116

Table 6.2.2. The formation energies(ΔU) and the lithiation energies (ΔE_{lit}) of the ring structures, and the enthalpy of mixing (ΔH) and the delithiation energies (ΔE_{delit}) of the crystal structures in eV units. 119

Table 6.4.1. Theoretical capacities of Te_xS_y composites. 125

Table 6.7.1. Elemental composition of cycled S/KB and Te_1S_7/KB electrodes from XPS. 140

Table 7.2.1. Calculated R_e, R_{SEI}, and R_{ct} from the Nyquist plots in Figures 5a and 5b. 156

Table 7.3.1. Atomic compositions of the Te/C electrodes discharged to 0.5 V..... 159

Table 8.4.1. Elemental composition of Te/BP2000 and Te/BP2000@$Al_2O_3$10 electrodes before battery tests from XPS. 175

Table 8.5.1. Calculated EIS values of Te/BP2000 and Te/BP2000@$Al_2O_3$10 electrodes. 178

Table 8.5.2. Elemental composition of Te/BP2000 and Te/BP2000@$Al_2O_3$10 electrodes after 100 cycles from XPS. 182

Table 9.4.1. Ionic conductivity and electrochemical stability window of polymer-based electrolytes for K metal batteries in literature and this work. 193

Table 9.5.1. Cycling performance of K/K symmetrical cells in literature and this work. 199

Table 9.5.2. EIS impedance values for K|| PVDF-HFP-KFSI@PAN || K and K|| GF ||K cells. 200

Table 9.6.1. Elemental composition of cycled PVDF-HFP-KFSI@PAN and GF from EDS. .. 202

List of Figures

Figure 1.1.1. Comparison of (a) intercalation-type cathodes, (b) conversion-type cathode, [21] and (c) S, Se, Te. 3

Figure 1.2.1. (a) Li-Te cell configuration, (b) charge-discharge profiles, and (c) phase transformation of Li-Te batteries in carbonate electrolyte [50]. 5

Figure 1.3.1. Comparisons of capacity, redox potential, and abundance of metals for anode materials. [68] 7

Figure 2.1.1. Te/C cathodes prepared by the melt-diffusion method for Li-Te batteries. (a) Synthesis approach, (b) BET, (c) charge/discharge curves, and (d) rate performance of CMK-3/Te cathodes. [69] 13

Figure 2.1.2. (a)TEM image and elemental distribution of Te@ordered microporous carbon (OMC), (b) adsorption-desorption isotherms of OMC and Te@OMC, (c) GITT plot, (d) Nyquist plots, (e) cycling performance and (f) rate capability of S@OMC, Se@OMC, and Te@OMC. [71] 14

Figure 2.1.3. (a) Synthesis process and morphology, (b) CV plots, (c) charge/discharge profiles, (d) cycling, (e) rate performance of Te/C-Co-N cathodes, (f) molecular structure of lithium polytellurides, and (g) DFT simulations of the adsorption energy of lithium polytellurides with C-Co-N derived from ZIF-67. [53] 15

Figure 2.1.4. Nanostructured Te cathodes for Li-Te batteries. (a) Synthesis process and morphology and (b) electrochemical performance of three-dimensional rGO/Te nanowire aerogel (3DGT)**.** [47] 17

Figure 2.1.5. (a) Synthesis and cathode architectures of Te nanowires/elastic carbon nanotube (Te@CNT and Te/CNTs) aerogel, (b) morphology of TeNWs and CNTs, and electrochemical performance of (c-d) Te@CNT and (e-f) Te/CNTs. [77] 18

Figure 2.1.6. Te_xS_y composite cathodes. Charge-discharge profiles of (a) $Te_{0.1}S_{0.9}$/CMK-3 and (b) S/CMK-3, (c) cycling performance of Te_xS_{1-x}/CMK-3 (x=0.05, 0.1, 0.2), (d) capacity stability of

$Te_{0.1}S_{0.9}$/CMK-3 at 1 A g^{-1}, and (e) schematic diagram of the formation of Te-induced SEI layer on Te_xS_{1-x}/CMK-3 cathode surface. [83]. 24

Figure 2.1.7. (a) Electron density differences for S, Li_2S, Te-S, Te-Li_2S, (b) formation energies of lithium insertion and extraction for the initial lithiation and delithiation process, (c) possible Li migration pathways in Te-Li_2S, (d) energy profiles for Li migration pathway 1 in Li_2S aITe-Li_2S, (e) rate performance of Te-3-S/KB and S/KB, (f) discharge capacities and corresponding capacity retention *versus* dopant ratio at the 1st and 50th cycles, and long-term cycling performance of (g) Te-3-S/KB and S/KB, (h) Te-3-S/rGO at 5 A g^{-1}. [85] 25

Figure 2.1.8. (a) Synthetic route of Te_xS_{1-x}@pPAN, cycling performance of $Te_{0.04}S_{0.96}$@pPAN in (b) carbonate electrolyte and (c) ether electrolyte, (d) CV plots, (e) charge-discharge profiles, (f) UV-vis spectra, (g) Li^+ diffusion coefficients, (h, i) reaction resistance during discharge and charge process of S@pPAN and $Te_{0.04}S_{0.96}$@pPAN. [85] 27

Figure 2.1.9. Galvanostatic charge-discharge curves of Te/C cathodes in different electrolytes of (a) 1M $LiPF_6$ in EC:DEC (1:1), (b) 1M LiTFSI in DOL:DME (1:1) [53]**,** (c) 1M $LiClO_4$ in DMSO [71]**,** and (d) solid electrolyte (LiTFSI-PEO) [79]**.** 29

Figure 2.1.10. K-Te batteries. (a) HRTEM image, (b) SAED pattern, (c) HADDF and EDS mapping of Te-G-CNT electrode after discharged to 0.3V, (dI*x situ* XRD and (e) Te 3d XPS spectra of as-prepared, discharged, and charged Te-G-CNT electrodes, (f) formation energy of K_nTe, (g) CV, (h) cycling performance, (i) charge-discharge profiles, (j) rate performance of Te-G-CNT electrode, (1M KFSI in EC:DEC). [104] 34

Figure 2.1.11. (a) synthesis process of TeNWs/CNTs/rGO, (b) K-Te cell structure and reaction pathways, (c) CV plots of TeNWs/CNTs/rGO, (d) chargeIscharge profiles, (e) cathode materials comparison in potassium-ion batteries, and (f) cycling performance of TeNWs/CNTs/rGO using 1M and 5M KTFSI in DEGDME. [105] 35

Figure 2.2.1 A comprehensive comparison of the energy density of various Te-based cathodes for rechargeable (a, b) Li-Te based batteries, and (c) Li/Na/K/Mg/Zn/Al-Te based batteries. The *x*-axis shows (a) and (c) specific capacity normalized to Te (or Te_xS_y) only and (b) specific capacity

normalized to Te/C (or Te_xS_y/C). The *y*–axis shows the average cell voltage. Plotted are the isoenergy lines ranging from 100 Wh kg^{-1} to 1.6 kWh kg^{-1}. 36

Figure 3.1.1. Methodology diagram used in this dissertation. 42

Figure 3.3.1. Digital photo of sample preparation holder for X-ray tomography..... 48

Figure 4.2.1. (a) Nitrogen adsorption-desorption isotherms and (b) pore-size distribution of ASAC25 and ASAC30; (c) XRD patterns of ASAC25, ASAC30, ASAC25-Te and ASAC30-Te, in comparison to standard Te powders (JCPDS PDF # 79-0736), and (d) Te 3d XPS spectra of ASAC25-Te and ASAC30-Te. 57

Figure 4.2.2. (a) XPS full spectra, (b) C 1s spectra and (c) O 1s spectra of ASAC25-Te, (d) XPS full spectra, (e) C 1s spectra and (f) O 1s spectra of ASAC30-Te..... 58

Figure 4.2.3. SEM images of (a) ASAC25, (b) ASAC30, (c) ASAC25-Te, and (d) ASAC30-Te with EDS mapping of Te and C elements..... 59

Figure 4.2.4. (a, d) TEM, (b, e) STEM, and (c, f) HRTEM images for (a-c) ASAC25-Te and (d-f) ASAC30-Te. Inserts on the right top corners of (c) and (f) correspond to fast Fourier transform (FFT) patterns. Insert on the bottom right corner of (f) is an enlarged HRTEM image. 60

Figure 4.2.5. STEM image and EDS mapping of (a) ASAC25-Te and (b) ASAC30-Te..... 61

Figure 4.2.6. TGA curves of Te/C composites measured in (a) N_2, and (b) the air..... 62

Figure 4.2.7. Electrochemical performance of pure Te electrode..... 63

Figure 4.2.8. (a) Cycling performance and (b) Coulombic efficiency (CE) of ASAC25-Te and ASAC30-Te electrodes measured at 0.1 C (1 C=420 mA g^{-1}) in half cells using Li metal as counter electrode and 1M $LiPF_6$, EC:DEC electrolyte; charge-discharge curves of (c) ASAC25-Te and (d) ASAC30-Te in the 1st, 2nd, 51st, and 101st cycles..... 64

Figure 4.2.9. (a) Rate capabilities of ASAC25 and ASAC30, (1C=420 mA g_{Te}^{-1}) (b) cycling stability, and (c) rate performance of ASAC25-Te and ASAC30-Te after removing the capacity contribution of the carbon host. 65

Figure 4.2.10. Charge-discharge profiles of ASAC25-Te and ASAC30-Te in the first cycle. ... 65

Figure 4.2.11. CV curves of (a) ASAC25-Te and (b) ASAC30-Te measured at the scan rate of 0.2 mV s^{-1}..... 66

Figure 4.2.12. (a) Nyquist plots, (b-c) SEM images of pristine and cycled ASAC25-Te, (d) Nyquist plots, (e-f) SEM images of pristine and cycled ASAC30-Te..... 67

Figure 4.2.13. CV results of (a) ASAC25-Te and (b) ASAC30-Te cycled after 100 cycles..... 68

Figure 4.2.14. (a) Rate capability and charge-discharge curves of (b) ASAC25-Te and (c) ASAC30-Te electrodes measured at 0.1, 0.2, 0.5, 1, 2, and 5 C. 69

Figure 4.3.1. (a) XRD patterns and (b) Raman spectra of ASAC25, ASAC25-Te-W49, ASAC25-Te-W60, and ASAC25-Te-W67 in comparison to crystalline Te powders..... 70

Figure 4.3.2. (a) Cycling performance, (b) Coulombic efficiency (CE), and charge-discharge profiles of ASAC25-Te-W49, ASAC25-Te-W60, and ASAC25-Te-W67 in the (c) 2nd and (d) 100th cycles measured at 0.1 C..... 71

Figure 4.3.3. Rate performance of ASAC25-Te composites. (a) Comparison of capacities at 0.1C-5C, charge-discharge profiles of (b) ASAC25-Te-W49, (c) ASAC25-Te-W60, and (d) ASAC25-Te-W67. 72

Figure 4.3.4. (a) Long-term stability and (b) charge-discharge profiles of ASAC25-Te-W49 electrode measured at 0.1 C in the first 5 cycles and 1 C in the subsequent cycles. 73

Figure 4.3.5. Schematic diagram of working mechanisms of ASAC30-Te and ASAC25-Te. ... 74

Figure 4.3.6. Comparisons of (a) discharge capacity in Te/porous carbon [1], Te/CMK-3 [2], Te/rib-like porous carbon [3], Te/hollow carbon@CNT [4], and this work at different current densities and (b) Te content versus pore volume of the carbon host (black circles represent the theoretical maximum value). 74

Figure 4.4.1. Schematic illustration of the preparation process for Te/AC composites. 80

Figure 4.4.2. SEM images of (a) raw lignin, (b) AC600, (c) AC700, (d) AC800, and (e) nitrogen adsorption/desorption isotherm and (f) pore size distribution of AC600, AC700, and AC800. .. 81

Figure 4.4.3. SEM images of (a) Te/AC600, (b) Te/AC700, (c) Te/AC800, (d) XRD patterns of AC600, AC700, AC800, TeI600, Te/AC700, and Te/AC800, and (e) TGA curves of Te/AC600, Te/AC700, Te/AC800 composites obtained under an N_2 environment..... 83

Figure 4.4.4. SEM images and EDS mapping of (a) Te/AC600, (b) Te/AC700, and (c) Te/AC800. 84

Figure 4.4.5. CV plots of (a) Te/AC600, (b) Te/AC700, and (c) Te/AC800 at 0.2 mV s^{-1}..... 85

Figure 4.4.6. (a) Cycling stability, (b) CE, charge-discharge profiles in the (c) 2nd cycle and (d) 100th cycles of Te/AC600, Te/AC700 and Te/AC800 at 0.1 C (1C = 420 mA g^{-1}). 86

Figure 4.4.7. The 1st-cycle charge-discharge profiles of Te/AC600, Te/AC700, and Te/AC800 at 0.1 C..... 86

Figure 4.4.8. Digital photos of Te/C cathode, separator, and Li metal recovered from Li-Te/AC600, Li-Te/AC700, and Li-Te/AC800 cells after cycling..... 88

Figure 4.4.9. (a) Rate performance and (b) voltage-capacity profiles of Te/AC700 at 0.1-5 C, and (c) long-term cycling performance of Te/AC700 at high rates of 1 and 2 C..... 89

Figure 4.4.10. EIS results of (a) Te/AC600, (b) Te/AC700, and (c) Te/AC800 before and after 100 cycles..... 90

Figure 4.4.11. CV plots of (a) Te/AC600, (b) Te/AC700, (c) Te/AC800 at various scan rates of 0.2-0.6 mV s^{-1}, and (d) calculated Li^+ diffusion coefficients in Te/AC600, Te/AC700, and Te/AC800 electrodes. 91

Figure 4.4.12. Schemes of Li-ion pathways in Te/AC600, Te/AC700, and Te/AC800..... 92

Figure 5.2.1. (a) SEM image and a digital photo of GPE, (b) XRD patterns of GPE and PVDF-HFP polymer, (c) ionic conductivities of GPEs versus NMP uptake at 25 °C, (d) Nyquist plot of GPE at 40, 50, 60, 70, and 80 °C, (e) Arrhenius plot of GPE, (f) CV and LSV of the Li/GPE/SS cell..... 96

Figure 5.3.1. Nyquist plots of the Li/GPE/Li cell resting for 0, 0.5, 1, 2, and 3 days at 25 °C. The inset is the corresponding equivalent circuit model..... 97

Figure 5.3.2. Voltage profiles of the Li/GPE/Li symmetrical cell at current densities of 0.05, 0.1, and 0.2 mAh cm^{-2} at 25 °C. 98

Figure 5.4.1. (a) Configuration quasi-solid-state Li-Te batteries, (b) phase transformation between Te and Li_2Te, (c) cycling performance, and (d) 1st-cycle charge-discharge curve of Li/GPE/Te batteries using PVDF and SA binders. 100

Figure 5.4.2. Charge-discharge curves of Li/GPE/Te batteries using PVDF and SA binders in the (a) 2nd and (b) 5th cycle at 0.1 C. 100

Figure 5.4.3. Cycling performance comparison of Te/C cathode with liquid electrolyte and GPE under 0.1C at 25 °C. 101

Figure 5.4.4. (a) Nyquist plots, SEM images of (b) Te/C cathode and (c) GPE recycled from Li/GPE/Te cells with PVDF binder, (d) Nyquist plots, SEM images of (e) Te/C cathode and (f) GPE recovered from Li/GPE/Te cell with SA binder. 102

Figure 5.4.5. (a) Rate performance and (b) charge-discharge profiles at 0.2, 0.5, and 1 C of the Li/GPE/Te battery using PVDF binder. 103

Figure 5.4.6. Digital photos and SEM images of the Te cathode before and after NMP soaking. 104

Figure 5.5.1. TGA curves of carbon and S/C, Se/C, and Te/C composites in a nitrogen environment. 105

Figure 5.5.2. (a) Cycling performance at 0.1 C, (b) capacity retention at 0.2-2 C of the S/C, Se/C, Te/C cathodes in quasi-solid-state batteries, and (c) Nyquist plots of the Li-S/Se/Te batteries before and after cycling. 106

Figure 6.1.1. Digital photos of Te&S mixtures after ball milling. 111

Figure 6.2.2. Preparation schematic of Te_xS_y composites and their structure and morphology. (a) Schematics of Te_xS_y composite synthesis process. (b) Raman spectra. (c) XRD patterns. (d) SIimage and EDS mapping of Te_1S_7 particles. (e) XPS S 2p spectra of S and Te_1S_7 powders. 112

Figure 6.2.3. Te-S phase diagram. [175] 113

Figure 6.2.4. SEM images of (a) Te_1S_7, (b) cross-sIional Te_1S_7 particles, (c) Te_2S_6, (d) Te_3S_5, (e) Te_4S_4, (f) Te_5S_3, (g) Te_6S_2, and (h) Te_7S_1 composites. 114

Figure 6.2.5. (a) XPS survey scans of S and Te_1S_7 powders and (b) Te 3d XPS spectra of Te_1S_7 powder..... 114

Figure 6.3.1. The representative crystIstructures of (a) Li, (b) S_8, (c) Te, (d) Li_2S, (e) $Li_{16}TeS_7$, and (f) $Li_2Te_xS_y$..... 115

Figure 6.3.2. Composition dependence of the energy profile of possible migration pathways of the random-solid solution of $Li_2Te_xS_y$ (x + y = 1) within the conventional Kohn-Sham density-functional theory. 116

Figure 6.3.3. Density functional theory calculations. The molecular structures and electronic charge densities (minus the superposed atomic densities) of (a) S, (b) Te_1S_7, (c) Li_2S_8, (d) $Li_2Te_1S_7$, shown alongside the relative energy differences. The crystal structures,Irmation energies, and the delithiation energies of (e) Li_2S and (f) $Li_{16}Te_1S_7$. The minimum migration paths are shown with black arrows. (g) The energy profiles are calculated using the nudged elastic band. The local density of states (LDOS) of (h) Li_2S and (i) $Li_{16}Te_1S_7$, for which the LDOS of the angular momentum channels of Te are scaled by 100 for a more compact illustration. The electronic charge densities (minus the superposed atomic densities) of (j) the [011] plane of Li_2S and (k) the [012] plane of $Li_{16}Te_1S_7$. The corresponding planes are illustrated in (e) and (f)..... 118

Figure 6.3.4. The energy profiles of possible migration pathways of (a) Li_2S and (b) $Li_{16}TeS_7$ calculated within the nudged elastic band. 119

Figure 6.3.5. The electronic charge densities (minus the superposed atomic densities) of the [001] planes for (a) Li_2S and (b) $Li_{16}TeS_7$..... 119

Figure 6.4.1. SEM images of Ketjenblack (KB, EC600)..... 120

Figure 6.4.2. (a) Nitrogen adsorption/desorption isotherm curve, and (b) pore size distribution of KB. 120

Figure 6.4.3. Morphology and structure information of Te_xS_y/KB composites. (a) SEM, (b) TEM, (c) HRTEM images of Te_1S_7/KB powder. (d) HAADF and corresponding elemental mapping of Te_1S_7/KB powder. (e) XRD patterns and (f) Raman spectra of Te_xS_y/KB composites..... 122

Figure 6.4.4. SEM images of (a) S/KB, (b) Te_1S_7/KB, (c) Te_2S_6/KB, (d) Te_3S_5/KB, (e) Te_4S_4/KB, (f) Te_5S_3/KB, (g) Te_6S_2/KB, and (h) Te_7S_1/KB composites. 123

Figure 6.5.1. Charge/discharge profiles of Te_1S_7 with ASAC25, BP2000 and KB in the (a) first, and (b) second cycle with the electrolyte of 1M $LiPF_6$ in EC:DEC, (c) the Te_1S_7/KB cathode using electrolytes of 1M $LiPF_6$ in EC:DEC, 1M $LiPF_6$ in EC:DEC:15%FEC, and 1M LiTFSI in DEC:FEC. 124

Figure 6.5.2. Cycling performance of S/KB and Te_xS_y/KB cathodes at 0.1 A g^{-1}. (a) Specific discharge capacity over cycles. (b) Coulombic efficiency. (c) Specific capacities in the 1st and 10th cycles, and initial Coulombic effIency. Galvanostatic charge/discharge curves in the (d) 1st and (e) 2nd cycle. (f) Capacity retention over 100 cycles. 125

Figure 6.5.3. CV plots of (a) S/KB, (b) Te_1S_7/KB, (c) Te_2S_6/KB, (d) Te_3S_5/KB, (e) Te_4S_4/KB, (f) Te_5S_3/KB, (g) Te_6S_2/KB, (h) Te_7S_1/KB cathodes at 0.2 mV s^{-1}. 127

Figure 6.5.4. (a) Cycling performance and (b) Charge/discharge profiles of S/KB, Te/KB, and Te_1S_7/KB cathodes at 0.1 A g^{-1}..... 127

Figure 6.6.1. Cycling and rate performance of S/KB and Te_1S_7/KB cathodes. (a-c) Cycling performance and galvanostatic charge/discharge profiles of (d-f) S/KB and (g-i) Te_1S_7/KB cathodes at 0.1 A g^{-1} with 1, 3, and 5 M electrolyte. (j) Rate capabilities at 0.1-10 A g^{-1} and (k) long-term cycling at 1 A g^{-1} of S/KB and Te_1S_7/KB cathodes with 3M electrolyte..... 129

Figure 6.6.2. Rate capabilities of S/KB and Te_1S_7/KB cathodes at 0.1-10 A g^{-1} with (a) 1M and (b) 5M electrolyte, and (c-d) long-term cycling of S/KB and Te_1S_7/KB cathodes at 1 A g^{-1} with 1M and 5M electrolyte. 131

Figure 6.7.1. Reaction kinetics analysis for S/KB and Te_1S_7/KB cathodes. (a) Nyquist plots. (b) charge-discharge curves. (c) CV plots. (d) Li-ion diffusion coefficients of S/KB and Te_1S_7/KB

cathodes. GITT curves of (e) Te_1S_7/KB and (f) S/KB cathodes. Reaction resistance of S/KB and Te_1S_7/KB cathodes during (g) discharge and (h) charge process. 133

Figure 6.8.1. *Ex situ* morphology and surface analysis, working mechanism schematic and pouch cell. (a) SEM, (b) TEM, (c) HRTEM, (d) HAADF and EDS mapping of Te_1S_7/KB electrode after 100 cycles. (e) SEM, (f) TEM, (g) HAADF and EDS mapping of S/KB electrode after 100 cycles. S 2p XPS spectra of cycled (h) Te_1S_7/KB and (i) S/KB electrodes. (j) Mechanism analysis of Te_1S_7/KB and S/KB electrodes. (k) Digital photo of the Li-Te_1S_7/KB pouch cell. (l) Cycling performance of the Li-Te_1S_7/KB and Li-S/KB pouch cells. (m) Voltage-capacity profiles of the Li-Te_1S_7/KB and Li-S/KB pouch cells in the 2nd cycle. 135

Figure 6.8.2. SEM images and EDS mapping of cycled (a) S/KB and (b) Te_1S_7/KB cathodes with the 3M electrolyte. 136

Figure 6.8.3. SEM images of cycled S/KB electrode with 3M electrolyte. 136

Figure 6.8.4. HRTEM images of cycled (a, b) Te_1S_7/KB and (c, d) S/KB cathodes with 3M electrolyte. 137

Figure 6.8.5. SEM images of cycled (a) S/KB and (b) Te_1S_7/KB cathodes with 1M and 5M electrolytes. 138

Figure 6.8.6. Digital photos of disassembled S/KB cathodes immersed in DME solvent for 1 month after being discharged to 1V (sample a), 2V (sample b), or charged to 3V (sample c) and corresponding UV-vis plot of sample c. 138

Figure 6.8.7. XPS survey scans of cycled S/KB and Te_1S_7/KB cathodes. 139

Figure 6.8.8. (a) C 1s, (b) O 1s, (c) F 1s, and (d) Te 3d XPS spectra of cycled S/KB and Te_1S_7/KB cathodes with 3M electrolytes. 140

Figure 6.8.9. SEM images of cycled Li metals from (a, b) Li-S/KB and (c, d) Li-Te_1S_7/KB cells. 141

Figure 6.9.1. Components and configurations of Li-Te_1S_7/KB cells. (a) Coin cell. (b) Pouch cell. 142

Figure 6.9.2. Charge/discharge profiles of (a) Li-S/KB and (b) Li-Te_1S_7/KB pouch cells in the first three cycles. 143

Figure 6.9.3. Nyquist plots of Li-S/KB and Li-Te_1S_7/KB pouch cells before cycling. 143

Figure 6.10.1. Charge/discharge profiles of GPE-based quasi-solid-state (a) Li-Te_1S_7 and (b) Li-S cells. 145

Figure 7.2.1. (a) Cycling stability and (b) CE of the Te/C and bulky Te electrodes in the KPF_6 and KFSIIectrolytes, galvanostatic charge-discharge profiles of (c) bulky Te and Te/C electrodes in the KPF_6 electrolyte, (d) bulky Te and (f) Te/C electrodes in the KFSI electrolyte at 0.1 C (1 C = 420 mA g^{-1}). 149

Figure 7.2.2. Specific discharge capacity of (a) carbon at the same current as Te/C cathodes (0.1C), and (b) Te/C cathodes (subtracting the capacity of carbon) in the KPF_6 and KFSI electrolytes at 0.1 C and 0.2 C. 150

Figure 7.2.3. Cycling performance of Te/C electrodes in KPF_6 and KFSI electrolytes with the Te loading of 1.2 mg cm^{-2} at 0.2 C. 150

Figure 7.2.4. (a) Cycling performance and (b) charge-discharge curves of the Te/C cathode in the 1st, 2nd, and 5th cycle in 1M KFSI in DME. 151

Figure 7.2.5. XRD patterns of the Te/C electrodes after discharge to 0.5 V in the KPF_6 and KFSI electrolytes at 0.1 C. 152

Figure 7.2.6. (a) Rate capabilities of the Te/C and bulky Te electrodes in the KPF_6 and KFSI electrolytes, and charge-discharge profiles of the Te/C electrodes at (b) 0.1 C, (c) 0.2 C, and (d) 0.5 C. 153

Figure 7.3.1. CV curves of the Te/C cathodes in (a) KPF_6 and (b) KFSI electrolytes at scan rates from 0.2 to 1 mV s^{-1}, (c) linear fits of the CV peak current *vs.* square root of scan rate, and (d) calculated K-ion diffusion coefficients in the Te/C cathodes in the KPF_6 and KFSI electrolytes. 155

Figure 7.3.2. (a, b) Nyquist plots of the K-Te cells with KPF_6 and KFSI electrolytes and SEM images of the Te/C electrodes recovered from K-Te cells after (c, d) 7 cycles and (e, f) 105 cycles (inset in (b) is the equivalent circuit used to fit the Nyquist plots after 7 and 105 cycles)..... 156

Figure 7.4.1. (a) XPS full survey, (b) K 2p and C 1s, (c) O 1s, (d) F 1s, (e) P 2p, and (f) Te 3d spectra of the Te/C cathodes discharged to 0.5 V in K-Te cells with KPF_6 and KFSI electrolytes. 158

Figure 7.4.2. (a) Cycling performance and (b-d) charge-discharge curves at 1st, 2nd, and 7th cycle of the Te/C electrode in KPF_6 and KFSI electrolytes in an extended voltage range of 0.1-3 V. 160

Figure 8.2.1. (a) SEM image, (b) pore size distribution, I nitrogen adsorption-desorption isotherm of BP2000 porous carbon; (d) SEM, (e) TEM, (f, g) HRTEM images of Te/BP2000 (the inset in (g) is its corresponding SAED pattern), (h) HAADF and elemental mapping of Te/BP2000, (i) XRD patterns of BP2000 and Te/BP2000. 164

Figure 8.3.1. XRD patterns of S/BP2000 and Se/BP2000..... 165

Figure 8.3.2. TGA curves of S/BP2000, Se/BP2000, and Te/BP2000 composites measured at nitrogen atmosphere..... 165

Figure 8.3.3. Charge-discharge profiles at initial cycles at 0.1 A g^{-1} for (a) S/BP2000, (b) Se/BP2000, and (c) Te/BP2000, (d) rate capabilities, (e) capacity utilization at 0.1-1 A g^{-1}, (f) cycling performance of S/BP2000, Se/BP2000, and Te/BP2000 at 0.1 C (based on their own theoretical capacities)..... 166

Figure 8.3.4. CV curves of (a) S/BP2000, (b) Se/BP2000, and (c) Te/BP2000 cathodes at 0.2 mV s^{-1}..... 167

Figure 8.3.5. (a) Initial charge/discharge curves and (b) cycling performance of a K-BP2000 cell. 167

Figure 8.4.1. (a) Galvanostatic charge-discharge profile of a K-Te battery and XRD patterns of Te/C electrodes at different charge/discharge states, (b-d) SAED and (e-g) HRTEM images for Te/C electrodes at different charge/discharge states, (b, e) for 1.3 V, (c, f) for 0.5 V, (d, g) for 3 V, and (h) phase transformation from Te to K_5Te_3..... 169

Figure 8.4.2. HAADF and EDS mapping of Te/C cathodes at (a) 1.3 V, (b) 0.5 V, and (c) 3 V. 170

Figure 8.5.1. SEM images of (a) Te/BP2000, (b) Te/BP2000@$Al_2O_3$10, (c) XPS survey, (d) Al 2p spectra of Te/BP2000@$Al_2O_3$10, (e, f) O 1s spectra of Te/BP2000 and Te/BP2000@$Al_2O_3$10, (g) the first CV scan, (h) the first charge/discharge profiles of Te/BP2000 and Te/BP2000@$Al_2O_3$10. 173

Figure 8.5.2. EDS spectra of Te/BP2000 and Te/BP2000@$Al_2O_3$10 electrodes. 174

Figure 8.5.3. (a, b) XPS C 1s and (c, d) Te 3d spectra of Te/BP2000 and Te/BP2000@$Al_2O_3$10 electrodes before cycling. 174

Figure 8.6.1. Electrochemical performance of Te/BP2000 and Te/BP2000@$Al_2O_3$10. (a) Discharge capacity, (b) Coulombic efficiency over 100 cycles at 0.1 C, (c) rate performance, (d) long-term cycling performance at 1 C, galvanostatic charge/discharge profiles of Te/BP2000 and Te/BP2000@$Al_2O_3$10 at 2^{nd}, 40^{th}, and 80^{th}, (g) Nyquist plots of Te/BP2000 and Te/BP2000@$Al_2O_3$10 before and after 100 cycles at 0.1 C. 177

Figure 8.6.2. EIS equivalent circuit models of K-Te cells. (a) Before cycling, (b) After cycling. 178

Figure 8.6.3. Top-view and cross-section SEM images of (a) Te/BP2000 and (b) Te/BP2000@$Al_2O_3$10 after 100 cycles, (c) XPS survey spectra, (d) Al 2p of Te/BP2000@$Al_2O_3$10, (e, f) F 1s and (g, h) Te 3d spectra of Te/BP2000 and Te/BP2000@$Al_2O_3$10 after cycling. 180

Figure 8.6.4. Cross-section SEM images of (a) Te/BP2000 and (b) Te/BP2000@$Al_2O_3$10 after 100 cycles..... 181

Figure 8.6.5. (a, b) XPS K 2p, C 1s and (c, d) O 1s spectra of Te/BP2000 and Te/BP2000@$Al_2O_3$10 electrodes after 100 cycles..... 181

Figure 8.7.1. Schematic illustration of the structural change of Te/BP2000 and Te/BP2000@$Al_2O_3$10 after long-term cycles. 183

Figure 8.7.2. Cycling performance of (a) S/BP2000 and S/BP2000@$Al_2O_3$10 and (b) Se/BP2000 and Se/BP2000@$Al_2O_3$10. 183

Figure 9.2.1. Schematics of the preparation process for PVDF-HFP-KFSI and PVDF-HFP-KFSI@PAN. 187

Figure 9.3.1. SEM images of (a, b) PAN nanofibers, (c, d) PVDF-HFP-KFSI, (e, f) PVDF-HFP-KFSI@PAN membranes. Micro X-ray computed tomography (MicroXCT) images of PVDF-HFP-KFSI@PAN from (g) 3D view, and (h) cross-section view. 188

Figure 9.3.2. Micro-XCT images of the PVDF-HFP-KFSI@PAN membrane. (a) 3D view, (b) top view, (c) 3D view in color, and (d) cross-section in color. 189

Figure 9.3.3. SEM images of glass fibers (GF) (Whatman glass fiber (GF/D), thickness 0.67 mm, pore size: 2.7 µm). 190

Figure 9.3.4. Digital photos of PVDF-HFP-KFSI@PAN with (a) 2.5 g and (b) 4 g polymer solution addition. 190

Figure 9.3.5. Size changes of PVDF-HFP-KFSI and PVDF-HFP-KFSI@PAN after heating treatment. 190

Figure 9.4.1. (a) Stress-strain curves of PVDF-HFP-KFSI and PVDF-HFP-KFSI@PAN, (b) XRD patterns of PAN, PVDF-HFP, anIVDF-HFP-KFSI@PAN, (c) XPS full survey and deconvolution of (d) K 2p and C 1s, (e) O 1s, and (f) F 1s spectra of the PVDF-HFP-KFSI@PAN. 192

Figure 9.5.1. Electrochemical properties of the PVDF-HFP-KFSI and PVDF-HFP-KFSI@PAN composite gel polymer electrolyte. (a) CV curve, (b) LSV plot of K|| PVDF-HFP-KFSI@PAN || SS at 0.2 mV s^{-1}, (c) ionic conductivity measured between 20 and 60 °C. 193

Figure 9.6.1. The rate capability of K/K symmetrical cells with PVDF-HFP-KFSI@PAN CGPE comparison with PVDF-HFP-KFSI and GF separators. (a) Cell configuration of K‖PVDF-HFP-KFSI@PAN‖K, and voltage profiles of K/K symmetrical cells at (b) 0.1-1 mA cm^{-2}, (c) 0.1, (d) 0.2, and (e) 1 mA cm^{-2}.. 193

Figure 9.6.2. Electrochemical performance of K/K symmetrical cells with PVDF-HFP-KFSI@PAN compared to PVDF-HFP-KFSI and GF separator. (a) Long-cycling stability at 0.5 mA cm^{-2}, (b)voltage hysteresis of K|| PVDIFP-KFSI@PAN ||K cell, voltage-time profiles during (c) 0-10 h, (d) 180-190 h, and (e) 1190-1200 h, (f) comparison of cumulative K plated capacity in

previous studies and this work, and Nyquist plots of (g) K|| GF ||K and (h) K|| PVDF-HFP-KFSI@PAN ||K cells before and after 50 cycles. 198

Figure 9.7.1. Morphology of PVDF-HFP-KFSI, PVDF-HFP-KFSI@PAN and GF separators recovered from K|K symmetric cells after 100 cycles or failure. (a, b, f, g, k, l) top view, (c, h, m) cross-section view and (d, i, n) EDS mapping of (a-c) PVDF-HFP-KFSI (f-h) PVDF-HFP-KFSI@PAN and (k-m) GF (insets in (a), (f) and (k) are corresponding digital photos of the separators). (j) XPS F 1s spectra of cycled PVDF-HFP-KFSI@PAN surface, (e, o) EDS spectrum of cycled PVDF-HFP-KFSI and GF. 201

Figure 9.7.2. (a) XPS K 2p and C 1s and (b) O 1s of cycled PVDF-HFP-KFSI@PAN. 202

Figure 9.8.1. Schematic illustration of the electrochemical deposition behaviors of K metal using (a) GF separator, (b) PVDF-HFP-KFSI and (c) PVDF-HFP-KFSI@PAN. 204

Figure 9.8.2. Charge-discharge profiles of K-Te cells with PVDF-HFP-KFSI@PAN electrolyte and Te/BP2000 cathode in the 1st, 2nd, and 5th cycles. 205

List of Abbreviations

AC	Activated Carbon
ALD	Atomic Layer Deposition
BET	Brunauer-Emmett-Teller
CE	Coulombic Efficiency
CGPE	Composite Gel Polymer Electrolytes
CV	Cyclic Voltammetry
Eq.	Equation
EIS	Electrochemical Impedance Spectroscopy
EDS	Energy Dispersive Spectroscopy
GF	Glass Fiber
GPE	Gel Polymer Electrolytes
GITT	Galvanostatic Intermittent Titration Technique
HAADF	High-Angle Annular Dark Field
HRTEM	High-Resolution Transmission Electron Microscopy
LIBs	Lithium-Ion Batteries
SAED	Selected Area Electron Diffraction
SE	Solid Electrolytes
SEM	Scanning Electron Microscopy
SEI	Solid Electrolyte Interphase
SS	Stainless Steel
STEM	Scanning Transmission Electron Microscopy
TEM	Transmission Electron Microscopy
TGA	Thermogravimetric Analysis
XCT	X-ray Computed Tomography

XPS	X-ray Photoelectron Spectroscopy
XRD	X-ray Diffraction

List of Chemicals

CMC	Sodium Carboxymethyl Cellulose	Sigma-Aldrich
DEC	Diethyl Carbonate	Gotion Inc.
DME	Dimethoxyethane	Gotion Inc.
DMF	N, N-dimethylformamide	VWR
EC	Ethylene Carbonate	Gotion Inc.
FEC	Fluoroethylene Carbonate	Gotion Inc.
HCl	Hydrochloric Acid	VWR
$LiPF_6$	Lithium Hexafluorophosphate	Gotion Inc.
LiTFSI	Lithium Bis(trifluoromethanesulfonyl)imide	Gotion Inc.
KOH	Potassium Hydroxide	VWR
KPF_6	Potassium Hexafluorophosphate	TCI
KFSI	Potassium Bis(trifluoromethanesulfonyl)imide	TCI
NMP	1-Methyl-2-pyrrolidinone	Alfa Aesar, 99+%
PAN	Polyacrylonitrile	Self-prepared
PVDF	Poly(vinylidene fluoride)	Alfa Aesar
PVDF-HFP	Poly(vinylidenefluoride-co-Hexafluoropropyle	Sigma Aldrich, molecular weight: 400000 g mol^{-1}
SA	Sodium Alginate	Ward's Science

List of Symbols

R_{ct}	Charge Transfer Resistance
R_e	Electrolyte Resistance
R_{SEI}	SEI Resistance
σ	Ionic Conductivity

List of Elements

Li	Lithium
C	Carbon
O	Oxygen
Na	Sodium
Al	Aluminum
K	Potassium
S	Sulfur
Se	Selenium
Te	Tellurium

List of Units

cm	Centimeter
mm	Millimeter
μm	Micrometer
mAh g^{-1}	Milliampere Hour per Gram
°C	Degree Celsius
K	Kelvin
eV	Electron Volt
g	Gram
M	Molar Concentration
MPa	Mega Pascal
ppm	Parts per Million
h	Hour
V	Volt
Wh kg^{-1}	Watt Hour per Kilogram
μL	Microliter

Acknowledgements

This dissertation was completed in advanced materials for energy storage lab at the University of British Columbia (UBC) under Dr. Jian Liu's supervision. I would like to express my appreciation to all individuals and organizations who provided support and guidance in my life and during my Ph.D. process.

I am grateful for financial support from the Natural Science and Engineering Research Council of Canada (NSERC), Fenix Advanced Materials, Canada Foundation for Innovation (CFI), BC Knowledge Development Fund (BCKDF), Mitacs Program, and UBC. I sincerely acknowledge the funding support of the Province of British Columbia through the Ministry of Energy, Mines, and Low Carbon Innovation and the Pacific Institute for Climate Solutions.

In particular, I would like to appreciate our industry collaborator D.J. Freschi and his company Fenix Advanced Materials. His high vision and materials/financial support always encourage me to overcome challenges and accomplish excellent research findings and publications.

From the bottom of my heart, I would like to express my deepest gratitude to my patient and supportive supervisor, Dr. Jian Liu, for his guidance and support over the past four years. He offered me a Ph.D. position in Sep 2019 to study the possibility of tellurium as electrode material in the application of next-generation batteries. His insight and knowledge of materials science steered me through my research journey. His wisdom and strong leadership bring me to move forward, conquer challenges and grow as a professional engineer in the battery field.

Further, I would like to thank my advisory committee members, Dr. Dimitry Sediako and Dr. Mohammad Arjmand, for their thoughtful comments and recommendations on this dissertation. I am also thankful to the School of Engineering and all its member's staff for all the considerate guidance.

I also would like to express my thanks to my research group members, who have been a great source of support. It's my pleasure to work with all of you in this collaborative team. It truly has been a very good time in this lab.

Finally, I would like to appreciate all scientists and technicians who helped me with the characterization of my samples. These individuals include Dr. Carmen Andrei from Canadian Centre for Electron Microscopy (CCEM) at McMaster University for her assistance on HRTEM, Dr. Sudip Shrestha from FIPKE LABORATORY FOR TRACE ELEMENT RESEARCH at UBC Okanagan for his help on SEM/EDS, Tina Olfatbakhsh and Dr. Abbas Milani at UBC for their help on Micro X-ray Computed Tomography characterization, as well as Dr. Michael Wang from 4D LABS at Simon Fraser University for his help on XPS.

Dedication

This thesis work is dedicated to my family and friends for all their unconditional support and encouragement throughout my graduate studies. My Mom Xueling, Dad Taisheng, sister Chaoyue, and friends Fengjing, Xiongya, Shijie, Zhe, Jing, and Siyu, thanks for listening to my problems and providing helpful suggestions. I am truly thankful for having you in my life. I will also give my special thanks to my fiancé Peter Zhao and his love and spiritual support during the challenges of research and life.

Chapter 1 Introduction

1.1 Research Background

Due to the rapid population growth and fundamental need for electricity in industrialization and the public's lives, the demand for electricity supply worldwide is surging. Based on International Energy Agency (IGA) estimation, worldwide energy consumption will increase by 75% from 2008 to 2035 [1]. Currently, 68% of electricity is generated from conventional fossil fuels, including 42% coal, 21% natural gas, and 5% oil [2]. However, greenhouse gas is unexpectedly produced when a great deal of coal is burned for heating, transportation, and industrial need, which poses a threat to our environment and leads to serious climate issues such as global warming [3]. In the long run, carbon dioxide emissions must be reduced to a minimum level for the sustainability of our society. In this case, many countries have made strict CO_2 emission regulations to reduce the carbon footprint of our society [4]. For example, China has set the target to reduce carbon emissions by 60% by 2030 compared to the year 2005 [5]. On the other hand, fossil fuels have been consumed faster over the few years, caused by the excessive exploitation of natural resources [6]. To meet the increasing energy need, scientists worldwide have been exploring new alternative energy systems to guarantee a sufficient power supply. Renewable solar or wind energy is considered an alternative to electricity generation due to its abundant resources and availability [7, 8]. It should be noted that the share of renewable energy in total energy consumption reached up to 19% in 2015, with an acceleration trend in the next few years [9]. In the year 2015, renewable energies even contributed to 60% of electricity generation in the global market [10]. Despite continuously increased electricity contribution by renewable energies in recent years [11], the utilization of solar or wind energy is highly dependent on climate change or geographical location, thus leading to unreliable power output [12]. To smooth out the intermittency of renewable energy, large-scale electrical energy storage (EES) is urgently required to achieve stable power output [13]. EES is expected to absorb excessive electric energy when electricity generation exceeds demand and release electricity into the power grid to guarantee electricity supply during peak time. The construction of an EES system is comprehensively determined by a couple of factors, such as energy storage capacity, capital cost, reliability, long time, and safety [14]. According to different energy storage mechanisms, EES could be categorized as direct electrical storage (supercapacitors)

and energy conversion from electricity to chemical/kinetic/potential energy (batteries, fly wheel, pump hydro). Currently, most EES systems require the integration of multi-forms of energy storage technologies to supply reliable and high-efficiency electricity utilization [15].

Among groups of batteries, lithium-ion battery (LIB) is one of the leading EES technologies due to the advantageous features of high energy density, fast response, long lifetime, and good safety [13, 16, 17]. However, its commercialization is primarily challenged by the limited practical capacity of current intercalation-type cathode materials: layered $LiMO_2$ (M=Mn, Co, Ni) (about 180 A h kg^{-1}), spinel $LiMn_2O_4$ (< 120 A h kg^{-1}) and olivine $LiFePO_4$ (< 180 A h kg^{-1}) as illustrated in **Figure 1.1.1a** [18-21]. These cathodes have been reported in previous studies to experience structure and chemical instability over long-term cycling [17, 22]. The high cost of these cathode materials (about 40% of the total battery cost) also hinders the rapid development of LIB [2]. Therefore, extensive efforts have been dedicated to developing cost-effective and high-capacity cathode materials [23-27]. The conversion-type chalcogen element sulfur (S) has attracted much attention over the decades due to its promising capacity in batteries. Lithium-sulfur (Li-S) batteries can theoretically deliver a super-high capacity of 1675 mAh g^{-1} via the electrochemical conversion of lithium and sulfur into lithium sulfide (**Figure 1.1.1b**) [28]. However, the poor electrical conductivity of sulfur (10^{-28} S m^{-1}) leads to low sulfur utilization and unsatisfying capacity [29]. Another challenge in the sulfur cathode is the dissolution of long-chain polysulfides (Li_2S_n, $4 \leq n \leq 8$) into ether-based electrolytes, which migrate across the separator and then react with Li anode ("shuttle effect") [24, 30, 31]. To mitigate the rapid capacity decay caused by shuttle effect, various strategies have been attempted and reported [26, 32, 33]. In addition, lithium-selenium (Li-Se) batteries have received increasing attention due to their higher electrical conductivity (10^{-3} S m^{-1}) [34]. However, Li-Se also suffers from a serious "shuttle effect" in ether-based electrolytes, which causes poor electrochemical performance [35, 36]. Interestingly, a single-plateau mechanism in Li-Se batteries has been found in carbonate-based electrolytes [37-39]. It means Se can be directly reduced to Li_2Se without the shuttle effect because of the insolubility of Se, Li_2Se and polyselenides in carbonate-based electrolytes. This finding suggests that Li-Se battery using carbonate-based electrolyte is a promising high-energy energy storage device [38, 40, 41]. Despite great achievements, the practical capacity of Li-Se batteries is still far away from its theoretical

value, especially at high current density, which could be ascribed to the slow reaction kinetics caused by the intrinsic electrical conductivity of Se element [23].

Tellurium (Te), discovered by Müller in 1782, is another element in the chalcogen family, which has two allotropes, amorphous and trigonal Te. The trigonal Te has a narrow bandgap of 0.35 eV and excellent photoconductivity, thermoelectricity, piezoelectricity, and nonlinear optical properties [42-44]. Te is widely utilized in steel production for improving machinability and solar panels as semiconductor materials [42, 43, 45]. Moreover, Te has shown great potential as a new electrode material because of its attractive electric conductivity (2×10^{2} S m^{-1}) (**Figure 1.1.1c**). This super high conductivity (30 orders of magnitude higher than S) ensures higher utilization of active species and faster kinetics during lithiation/delithiation process [46]. Due to the high density (6.24 g cm^{-3}), Te could deliver a theoretical volume capacity of 2621 mAh cm^{-3} comparable to S (3467 mAh cm^{-3}) and Se (3254 mAh cm^{-3}) (**Table 1.1.1**), although the specific capacity is not competitive (420 mAh g^{-1}).[47]. This excellent volumetric capacity is preferred for high-energy energy storage batteries due to limited packaging space. Therefore, Li-Te batteries are expected to achieve high energy density for large-scale energy storage applications.

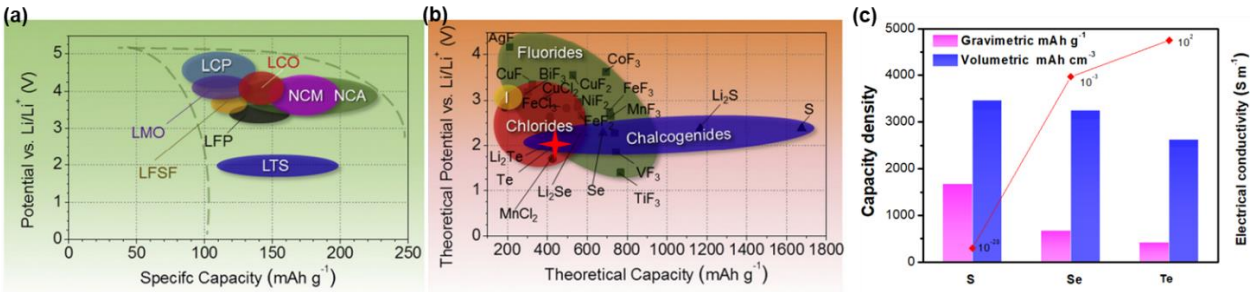

Figure 1.1.1. Comparison of (a) intercalation-type cathodes, (b) conversion-type cathode, [21] and (c) S, Se, Te.

Table 1.1.1 Voltages, capacities, and specific energies of rechargeable Te batteries in comparison with Li-ion, Li-S, and Li-Se batteries.

	Li-ion[a]	Li-S	Li-Se	Li-Te
Cell voltage (V) [b]	3.8	2.2	2	1.7
Specific capacity of cathode (mAh g^{-1})	137	1675	675	420
Capacity density of cathode (mAh cm^{-3})	700	3467	3254	2621
Theoretical specific energy (Wh kg^{-1})[c]	387	2567	1150	644

[a] Data of the $LiCoO_2$/graphite battery (electrochemical reaction: $2Li_{0.5}CoO_2 + LiC_6 \leftrightarrow 2LiCoO_2 + C_6$) as an example of Li ion batteries.

[b] Cell voltage based on discharge plateau voltage.

[c] Theoretical data based on the total mass of active materials on the cathode and the anode.

1.2 Main Challenges

The cell configuration of Li-Te batteries is illustrated in **Figure 1.2.1a,** with Li metal and Te as anode and cathode, respectively. Overall, the electrochemical process in Li-Te batteries is a two-electron reaction: $2Li^+ + 2e^- + Te \leftrightarrow Li_2Te$. The Te crystals possess a hexagonal structure through van der Waals interaction between highly helical chains of covalently bonded Te atoms. This highly anisotropic structure leads to inherent chirality and a strong tendency to grow along [001] direction into a one-dimensional structure [48, 49]. In carbonate electrolyte based Li-Te batteries (*e.g.*, 1M $LiPF_6$ in EC: DEC), the charge and discharge curves possess one single plateau at about 1.8V/1.6V, corresponding to the one-step solid-solid transition from Te to Li_2Te (**Figure 1.2.1b**). In the lithiation process, the hexagonal Te is converted to cubic Li_2Te, which comes back to hexagonal Te during the charge process, as presented in **Figure 1.2.1c** [50].

Discharge process: $Te\ (solid) + 2Li^+ + 2e^- \leftrightarrow Li_2Te\ (solid)$ Eq. 1.1

Charge process: $Li_2Te\ (solid) \leftrightarrow Te\ (solid) + 2Li^+ + 2e^-$ Eq. 1.2

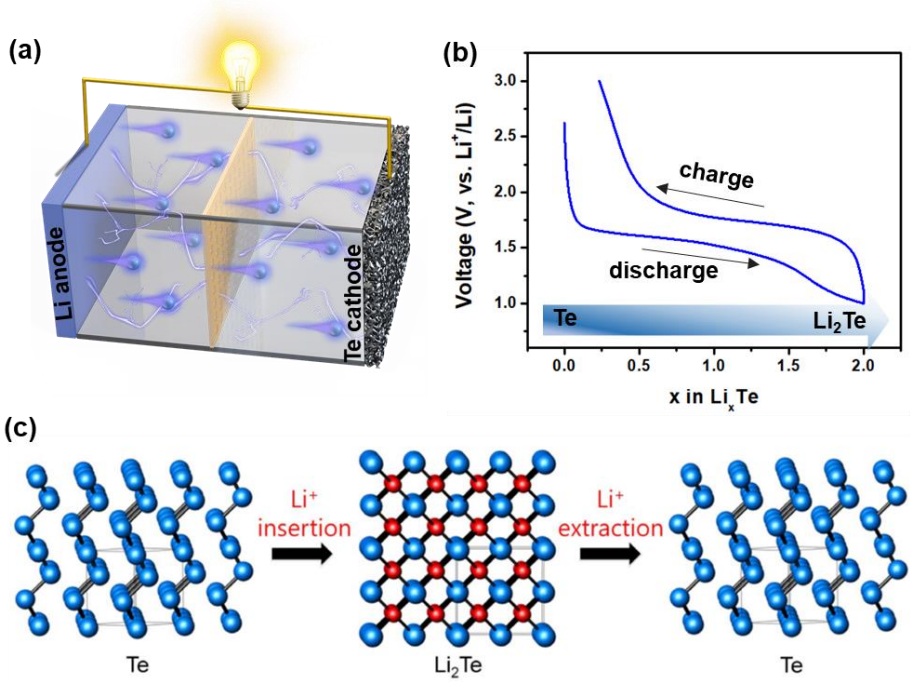

Figure 1.2.1. (a) Li-Te cell configuration, (b) charge-discharge profiles, and (c) phase transformation of Li-Te batteries in carbonate electrolyte [50].

However, the Te cathode seriously suffers from large volume expansion (104%) accompanied by the formation of discharge product Li_2Te, which also occurs in other conversion-type electrode materials (e.g., S, Se) [51]. This acute volume expansion and subtraction would induce structural instability and cause the pulverization of active materials, thus leading to rapid capacity fading [52]. To deal with this problem, one of the commonly used approaches is to tailor cathode architectures for Li-Te batteries. For example, utilizing a porous structure to accommodate the volume change of Te has been reported to be an effective way of improving electrochemical stability [52]. The introduction of conductive carbon also promotes electron transfer and enhances redox kinetics, thus contributing to superior electrochemical performance.

The polytellurides dissolution is another challenge of Li-Te batteries in ether electrolytes (such as 1M LiTFSI in DOL:DME (1:1, volume ratio)), which originates from the formation of long-chain polytellurides Li_2Te_n ($4 \leq n \leq 8$) intermediates in Te cathode. The two-step discharge reaction is described as the following equations:

Step 1: nTe (solid) + $2Li^+ + 2e^- \leftrightarrow Li_2Te_n$ ($4 \leq n \leq 8$, liquid) Eq. 1.3

Step 2: $Li_2Te_n + (2n - 2)\ Li^+ + (2n - 2)\ e- \leftrightarrow nLi_2Te$ Eq. 1.4

These soluble intermediates would migrate across the separator and react with Li metal, leading to the low utilization of active materials and capacity fading [53].

Besides, the safety issue of liquid-based batteries is usually questioned because of the usage of flammable and volatile organic solvents [17, 54]. It is essential to replace liquid electrolytes with solid electrolytes to construct a safer battery system. The usage of solid electrolytes will also simplify battery packing technology and increase energy density [55]. However, the critical challenges in solid-state batteries have not been overcome, including the ionic conductivity and electrochemical stability of solid electrolytes, the compatibility between electrolytes and anodes/cathodes, as well as the electrolyte/electrode interfacial resistance [56, 57]. Extensive efforts should be devoted to designing a well-matched solid electrolyte for high-energy-density Li-Te batteries.

Moreover, the commercialization of LIBs is impeded by the scarcity of lithium (0.0017 wt% in the Earth's crust) and the uneven distribution of lithium resources globally [16, 58]. Recently, significant efforts have been devoted to exploring abundant and low-cost charge carriers, such as sodium and potassium, as an alternative to lithium for rechargeable batteries [59, 60]. In particular, potassium has ample reserve in the Earth's crust (2.09 wt%), resulting in a much lower cost of potassium precursors than their lithium counterparts (1,000 USD per ton for potassium carbonate *vs.* 6,500 USD per ton for lithium carbonate) [61, 62]. Theoretically, the potassium element has a redox potential of -2.93 V (*vs.* standard hydrogen potential, E^o), which is lower than that of sodium (-2.71 V) and close to lithium (-3.04 V), thus promising a higher working voltage and energy density for potassium-ion batteries (PIBs) (**Figure 1.3.1**) [63]. It has also been shown that PIBs possessed fast kinetics and rate performance in organic solvents due to the weak Lewis acidity of K ions and the weak interaction of K ions with organic electrolytes [64, 65]. These aforementioned features have attracted increasing interest in the development of PIBs as a promising candidate for large-scale energy storage in the near future [66, 67]. Te is a potential electrode for high-capacity PIBs due to its excellent electrical conductivity and volumetric capacity. However, the

fundamental basics of K-Te electrochemistry have not been fully revealed. It is critical to investigate the interplay between the Te electrode and electrolyte chemistry.

Based on the above introduction, Li-Te batteries are expected to realize high capacity and cycling stability for energy storage systems. The main challenges are large volume change, electrolyte safety, and limited lithium resources. The feasible strategies include cathode structure design, the usage of solid electrolytes, and interfacial design, which will be discussed in the next chapter. The exploration of K-Te electrochemistry should also be focused on for the scalable application of K-Te batteries.

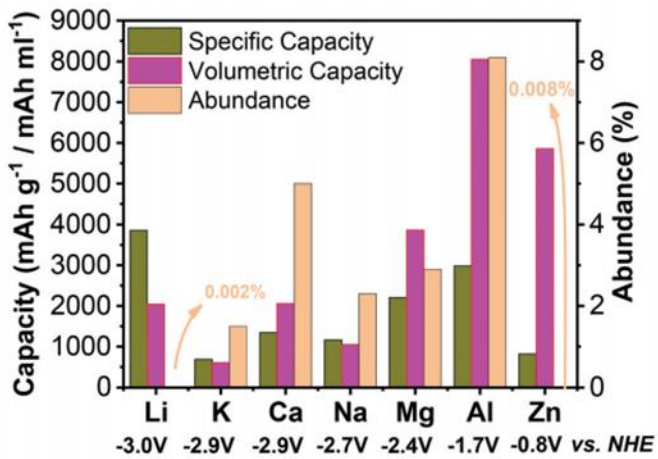

Figure 1.3.1. Comparisons of capacity, redox potential, and abundance of metals for anode materials. [68]

1.3 Scope of Research

This dissertation clarifies the role of Te as a promising electrode material for next-generation high-energy-density batteries and demonstrates its advantages in terms of specific capacity, volumetric capacity, and electrical conductivity compared to current cathode materials. To overcome the main challenges of metal-Te batteries, this research provides a systematic study of Te-based batteries, including cathode structure design, gel polymer electrolytes fabrication, and interface engineering strategies. Furthermore, this dissertation develops a deep understanding of the fundamental electrochemistry and the merits and limitations for the development of Te-based rechargeable batteries with a detailed analysis of materials cost, specific capacity, and energy density. This dissertation also identifies the unanswered scientific and technological questions of the existing

battery evaluation standard and proposes suggestions to improve the establishment of battery testing and assessment criteria for further commercialization. This will contribute to the further development of high-energy-density Te-based rechargeable batteries.

1.4 Thesis Structure

This dissertation has been structured as follows:

Chapter 2 introduces previous studies in the Te-based battery field, including Te/C electrode structure, emerging TeS composite cathode, liquid and solid electrolytes, as well as alternative metal anodes. The main challenges of metal-Te battery systems are also summarized and discussed. The overall and detailed objectives of this dissertation are demonstrated at the end of this chapter.

Chapter 3 primarily presents morphology and structure characterization techniques used in this dissertation. Electrochemical characterizations and battery evaluation methods are also included to help understand the redox conversion and interface chemistry of Te-based batteries.

Chapter 4 clarifies the role of carbon pore structure in Te/C electrodes for Li-Te batteries. The effect of carbon structure on the electrochemical performance of Te/C electrodes is comprehensively discussed using both commercial carbon and lignin-derived porous carbon. Durable Te/C electrodes at various current densities are developed with carbonate electrolytes.

Chapter 5 characterizes flexible gel polymer electrolytes to establish quasi-solid-state Li-Te batteries at room temperature. The advantage of low charge transfer resistance for Li-Te batteries is revealed compared to Li-S and Li-Se counterparts.

Chapter 6 develops a wide range of Te-S solid solutions to integrate both advantages of S and Te electrodes. The Te_xS_y composites are characterized with experiments and simulations to investigate the internal Li-TeS electrochemistry. Coin cells and pouch cells are both fabricated and assessed to validate the effect of Te introduction into S molecules.

Chapter 7 elucidates electrolyte salt chemistry for the newly emerging K-Te battery system. Cycling stability, K-ion diffusion, and kinetics are evaluated to gain insights into electrolyte salts. The solid electrolyte interphase layers induced by electrolytes are characterized to analyze the role of salts for K-Te batteries.

Chapter 8 demonstrates a two-step reaction mechanism for K-Te batteries as concluded from various characterization techniques. To solve the issue of capacity fading, an ultrathin aluminum oxide film is deposited on the surface of Te electrodes by atomic layer deposition (ALD) technique. The electrochemical performance of coated Te electrodes is evaluated, and the corresponding cycling stability mechanism improved by the Al_2O_3 layer is discussed.

Chapter 9 reports composite gel polymer electrolytes (CGPE) reinforced by the electrospun polyacrylonitrile (PAN) nanofibers for K metal anodes. Electron microscopy and X-ray spectroscopy techniques are utilized to identify the morphology and microstructure. Further, tensile strength, ionic conductivity, and electrochemical stability window tests of the CGPE are carried out. The battery lifetime and accumulated K plating/striping of the CGPE are recorded. Finally, the protection mechanism of the CGPE is discussed and illustrated.

Chapter 10 highlights the conclusions drawn from Chapters 4-9, outlines detailed contributions this dissertation made, and proposes suggestions for further development and evaluation of metal-Te batteries.

1.5 Novelty and Originality of Research

The novelty and originality of research from this dissertation are listed as follows:

This research pioneers the materials design and fundamental investigation of Li-Te or K-Te battery systems, addresses the issues of cycling/structural instability of Te electrodes, and develops strategies to achieve durable Te-based rechargeable batteries with liquid and gel polymer electrolytes.

In Chapter 4, I clarified the role of carbon pore structure in Te/C electrodes for Li-Te batteries by investigating its effect on Te/C cathode structure and cycling performance. It is the first study focusing on the discussion about carbon pore properties in Li-Te batteries.

In Chapter 5, I constructed quasi-solid-state Li-Te batteries with flexible gel polymer electrolytes. I demonstrated the advantage of Li-Te batteries over Li-S and Li-Se batteries with the same cell configuration for a fair comparison.

In Chapter 6, I synthesized a wide range of TeS composite cathodes and completed a systematic study of Li-TeS batteries. I revealed the optimal Te/S ratio that could enable a durable and high-capacity TeS cathode in carbonate electrolytes.

In Chapter 7, I disclosed the effect of electrolyte salt on K-ion storage capability, kinetics, and SEI layer formation for K-Te batteries.

In Chapter 8, I addressed the cathode/electrolyte instability issue in K-Te batteries by introducing a precisely controlled nanofilm on the Te cathode surface. To the best of our knowledge, this is the first application of the atomic layer deposition technique in K-Te batteries.

In Chapter 9, I developed a composite gel polymer electrolyte that could regulate K dendrites growth and extend the lifetime of K metal.

Chapter 2 Literature Review and Research Objectives

This chapter begins with an introduction to Te cathode design, TeS composite cathode, and electrolyte chemistry for Li-Te batteries. The following section presents the latest research progress in the promising cost-effective K-Te battery system with ether and carbonate electrolytes. Next, a comparison of capacity and energy density for different metal-Te batteries is provided and discussed. The chapter concludes with the main challenges of metal-Te batteries and detailed research objectives in this dissertation.

2.1 Literature Review

This section provides a comprehensive review of the development of Te-based rechargeable batteries consisting of Te cathode design, TeS composite cathodes, electrolyte chemistry, as well as K-Te electrochemistry.

2.1.1 Te Cathode Design

Generally, the common Te cathode structure can be divided into Te/porous carbon and Te nanowires. The detailed cathode structure and its interplay with electrolytes will be introduced in the following sub-sections.

2.1.1.1 Te/Porous Carbon Cathodes

Wang and co-workers [46] designed a Te/C electrode via a melt-diffusion method in 2014, in which the mixture of Te and C was heated at 600 ^{o}C (above Te's melting point: 450 ^{o}C) to ensure the good impregnation of Te into porous carbon. This pioneering work in carbonate electrolyte based (1M $LiPF_6$ in EC:DEC) Li-Te battery using Te/C as the cathode delivered a volumetric capacity of 1400 mAh cm^{-3} after 1000 cycles at 50 mA g^{-1}, confirming the great potential of Te as high-volumetric-capacity electrode materials.

Since then, various porous carbon materials (CMK-3 [69], microporous carbon [70], ordered macroporous carbon [71], metal-organic framework-derived carbon [53], biomass-derived carbon [72], carbon nanotubes [73]) have been developed and explored as Te hosts for Li-Te batteries. CMK-3 is a well-known mesoporous carbon widely used in Li-S/Se batteries [39, 74]. Strasser

and co-workers [69] extended its application in Li-Te batteries as a robust Te host in 2016 (**Figure 2.1.1a**). The as-synthesized CMK-3 had a large specific area of 1231 m^2 g^{-1} and a pore volume of 1.41 cm^3 g^{-1}, offering sufficient loading sites for Te to accommodate its large volume change during charge/discharge processes. Notably, the Te/CMK-3 cathode delivered ultrahigh rate capabilities of 96% (0.5C), 86% (1C), 78% (2C), 69% (5C) of the theoretical capacity (420 mAh g^{-1}), and showed exceptional durability with a capacity retention of 85% even after 990 cycles at 10C (**Figures 2.1.1b-d**). The biomass-derived carbon also receives much attention due to its unique pore structure and abundant resources on the earth. Li *et al.* [72] utilized discarded lotus to synthesize rib-like hierarchically porous carbon (RHPC) by a facile hydrothermal-pyrolyzation method. Benefiting from the hierarchical pore structure, the Te/RHPC cathode showed exceptional capacity stability with a reversible capacity of around 288 mAh g^{-1} (1797 mAh cm^{-3}) for 3600 cycles at 2C. The nitrogen-doped hierarchical porous carbon (NPCS) is employed by Li *et al.* [75] as a Te host for boosting the electrochemical performance of the Te electrode. The defects along the NPCS matrix induced by the nitrogen heteroatom (pyridine-like, pyrrolic-like, and quaternary nitrogen) are favorable for accelerating electron transfer and capacity contribution [76]. In the long-term cycling test, the Te/NPCS cathode exhibited excellent capacity and remained 310 mAh g^{-1} after 200 cycles at 0.25 C. Moreover, Li *et al.* [73] designed a unique muscle-like Te/C electrode in which Te was incorporated into the carbon nanotube/hollow carbon cell (CNT@HCC) matrix. In this structure, HCC acts as a “tissue cell” to accommodate Te, while CNT behaves like a “blood capillary” to facilitate the transportation of ions and electrons. In the rate performance test, the CNT@HCC/Te cathode delivered 242, 212.7, 176, and 124 mAh g^{-1} at 0.5, 1, 2, and 5C.

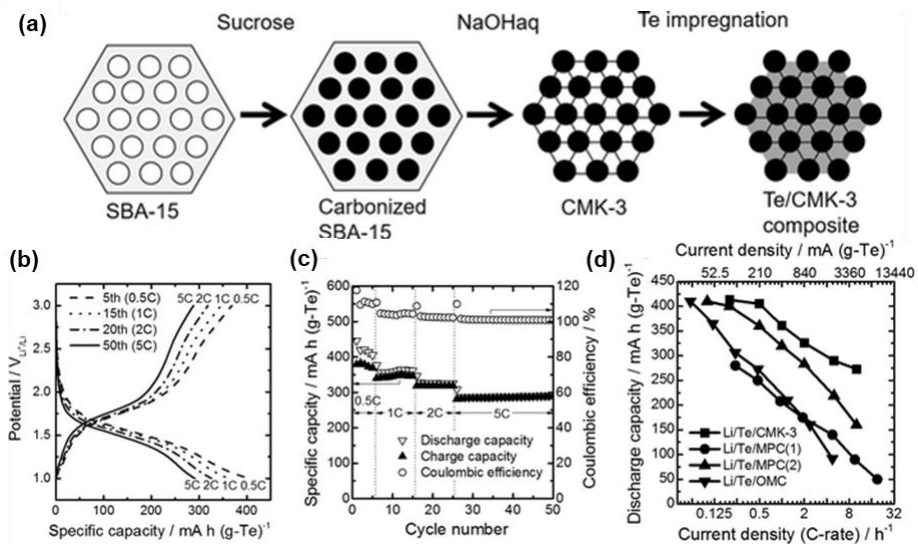

Figure 2.1.1. Te/C cathodes prepared by the melt-diffusion method for Li-Te batteries. (a) Synthesis approach, (b) BET, (c) charge/discharge curves, and (d) rate performance of CMK-3/Te cathodes. [69]

Interestingly, Zong and co-workers [71] compared the cycling performance of S, Se, and Te with ordered microporous carbon (OMC) as hosting material at 1 A g^{-1} with the electrolyte of 1M $LiClO_4$ in DMSO (**Figure 2.1.2**). Despite lower initial capacity, the Te@OMC cathode remained super stable at 130 mAh g^{-1} over 150 cycles, outperforming S@OMC and Se@OMC. The superior stability of Te@OMC could be attributed to the considerably higher electrical conductivity of tellurium and the good solubility of Li_2Te in DMSO. The capacity retention (compared with corresponding theoretical capacity) of the three cathodes versus current density was also tested. Even at a high current density of 2000 mAh g^{-1}, Te@OMC remained up to 21.2% (89 mAh g^{-1}), higher than that of S@OMC (2.6%, 43 mAh g^{-1}) and Se@OMC (7.1%, 48 mAh g^{-1}). Moreover, the workers prepared a carbon-free free-standing Te nanowire mat without any carbon additive or binder. The volumetric capacity and energy density of the Te mat reached about 900 mAh cm^{-3} and 1800 mWh cm^{-3} (50% higher than that of $LiCoO_2$), respectively.

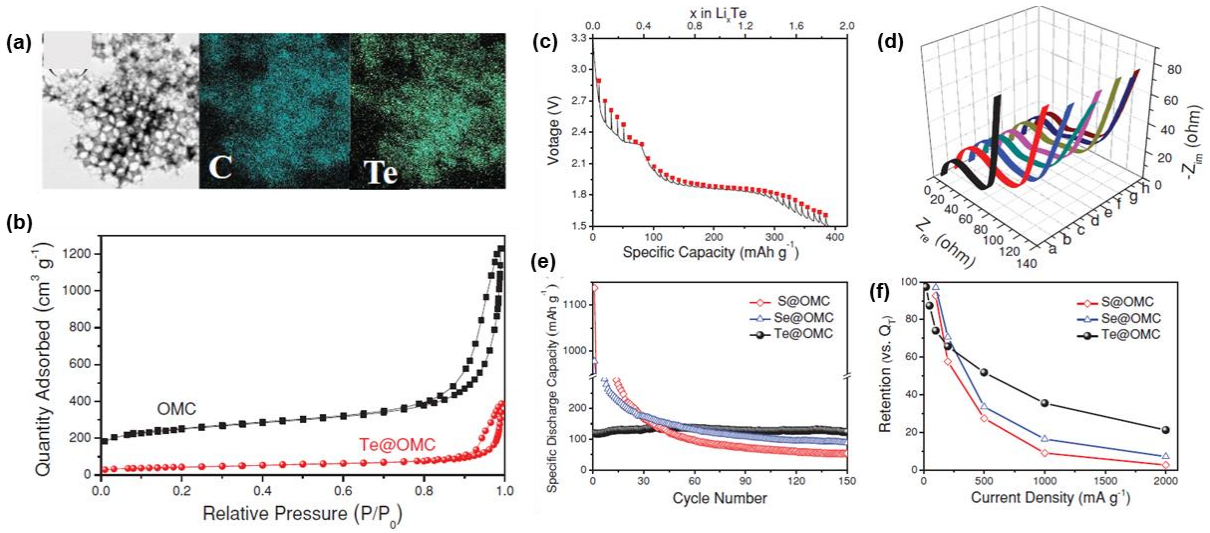

Figure 2.1.2. (a)TEM image and elemental distribution of Te@ordered microporous carbon (OMC), (b) adsorption-desorption isotherms of OMC and Te@OMC, (c) GITT plot, (d) Nyquist plot, (e) cycling performance and (f) rate capability of S@OMC, Se@OMC, and Te@OMC.[71]

It is mentioned that the ether electrolyte induces a two-step electrochemical conversion from Te to soluble intermediates and then to the final product of Li_2Te in Li-Te batteries. Based on the reaction mechanism, He *et al.* [53] prepared a well-confined Te/C-Co-N cathode with a high Te content of 77.2 wt%. The highly conductive porous carbon was synthesized by the synthesis of metal-organic framework ZIF-67, carbonization, and cobalt-nitrogen doping (**Figure 2.1.3a**). With 1M LiTFSI in DOL:DME as the electrolyte, the unique Te/C-Co-N cathode showed ultrahigh capacity retention of 93.6% over 800 cycles and excellent rate capabilities of 2160, 1327.6, 894.8 mAh cm^{-3} at 4, 10, and 20C, respectively (**Figures 2.1.3b-e**). Furtherly, DFT simulations suggest that the adsorption energy between lithium polytellurides and C-Co-N is higher compared to the graphene, indicating stronger immobilization of Li_2Te_n ($n > 2$) on the C-Co-N matrix (**Figures 2.1.3f-g**). In summary, the microporous and highly conductive C-Co-N matrix offers a majority of Te loading sites to suppress the volume change of Te and abundant channels for electron transfer and ions diffusion, thus mitigating the dissolution of polytellurides and improving the durability of Li-Te batteries.

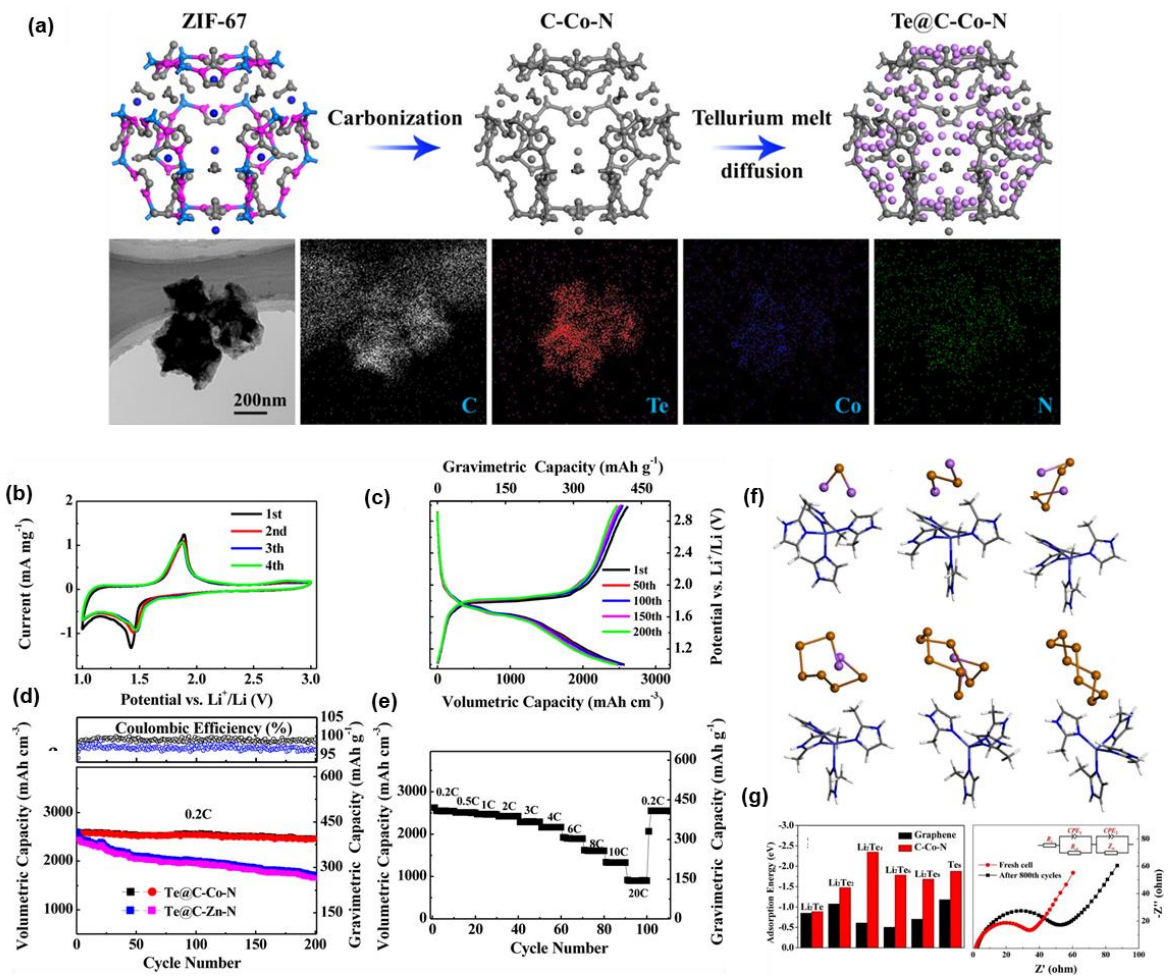

Figure 2.1.3. (a) synthesis process and morphology, (b) CV plots, (c) charge/discharge profiles, (d) cycling, (e) rate performance of Te/C-Co-N cathodes, (f) molecular structure of lithium polytellurides, and (g) DFT simulations of the adsorption energy of lithium polytellurides with C-Co-N derived from ZIF-67. [53]

2.1.1.2 Te Nanowires

Although the introduction of host materials alleviates the volume expansion of Te, the preparation of Te/C electrodes usually involves multiple steps and additional materials costs (carbon additive and binder). This additional materials consumption drags down the energy and power density of the whole Te cathode. In this case, the construction of carbon-free and binder-free Te electrodes typically characterized by Te nanowires has gained increasing attention to develop high-energy Li-Te batteries [47, 77, 78]. One good example is the three-dimensional rGO/Te nanowire aerogel

(3DGT) (**Figure 2.1.4a**) [47]. The Te nanowires were synthesized by a poly (vinyl pyrrolidone) – assisted hydrothermal process and the as-prepared crystalline Te nanowire has an ultrathin diameter of about 40 nm (**Figure 2.1.4b**). The free-standing 3DGT aerogel possessed a hierarchically porous structure with Te nanowires tightly wrapped by thin rGO. When using ether electrolyte, the 3DGT cathode had two sharp cathodic peaks at 1.68 V and 1.56 V, which were assigned to the formation of Li_2Te_n ($4 \leq n \leq 8$) and Li_2Te_2/Li_2Te (**Figures 2.1.4c-d**). The 3DGT cathode exhibited a high initial capacity of 2611 mAh cm^{-3} at 0.2C and capacity retention of 88% after 200 cycles (**Figure 2.1.4e-f**), which are attributed to the fast ions diffusion and electron transfer given by the rich-porosity and conductivity network.

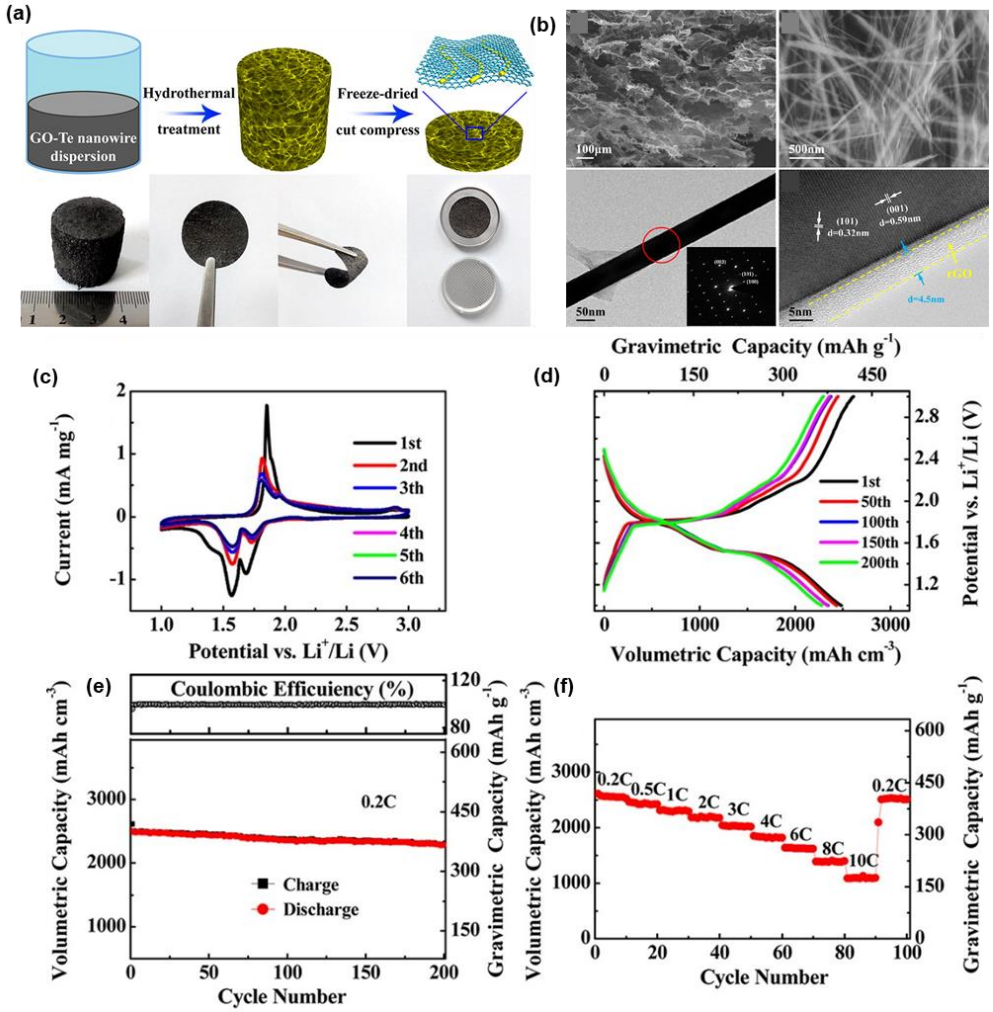

Figure 2.1.4. Nanostructured Te cathodes for Li-Te batteries. (a) Synthesis process and morphology and (b) electrochemical performance of three-dimensional rGO/Te nanowire aerogel (3DGT)**.** [47]

Carbon nanotube (CNT) aerogel was also prepared to combine with Te nanowires for high-capacity Li-Te batteries [77]. The reported CNT aerogel had a large surface area of 1865 m^2 g^{-1} and a pore volume of 0.964 cm^3 g^{-1} and showed excellent compressibility and structural stability in a compressive stress-strain test. The workers designed two battery structures (TeNW/CNT and Te@CNT) with the aerogel CNT as an interlayer between the separator and TeNWs or conductive substrate for Te accommodation in the Li-Te batteries (**Figures 2.1.5a-b**). DMSO-based electrolyte was used in this study to achieve high working voltage and energy density of Li-Te batteries. The TeNW/CNT cathode delivered a discharge capacity of 328 mAh g^{-1} in the first cycle with the voltage plateau at 2.15 V at 0.1 C (**Figures 2.1.5c-d**). It was found that the dissolved Li_2Te molecules in DMSO are trapped by adsorption sites on carbon cloth, leading to the structural transition from TeNW/CNT to Te@CNT over cycling. To ensure closer contact between Te and CNT, the TeNW/CNT was heated above the melting point of Te in an inert atmosphere to form the Te@CNT structure, which showed a long discharge plateau at about 1.7 V, despite a lower working voltage than TeNW/CNT (**Figures 2.1.5e-f**). After 100 cycles at 0.1 C, the Te@CNT cathode still held 330 mAh g^{-1}, revealing good stability of the Te@CNT structure. The capacity stability could be attributed to the effective trap of Te and Li_2Te into nanopores, fast electron transfer by the CNT matrix, and alleviated deformation stress over cycling by the elastic CNT aerogel. Notably, the Te@CNT achieved 400 W h kg^{-1} (1600 W h L^{-1}) after the first cycle, exceeding the theoretical energy density of $LiCoO_2$ (350 W h kg^{-1}).

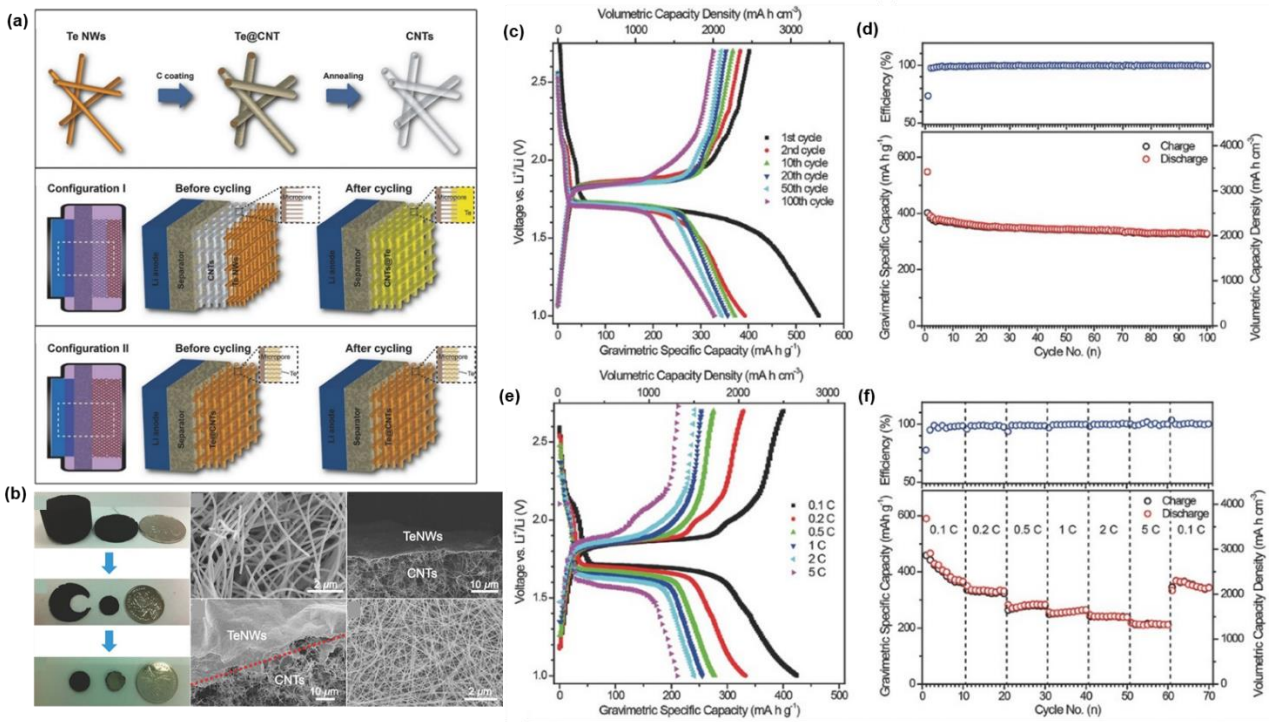

Figure 2.1.5. (a) synthesis and cathode architectures of Te nanowires/elastic carbon nanotube (Te@CNT and Te/CNTs) aerogel, (b) morphology of TeNWs and CNTs, and electrochemical performance of (c-d) Te@CNT and (e-f) Te/CNTs. [77]

Besides, Te nanorods deposited on nickel foam (Te@Ni) were fabricated by Huang *et al.* [78] through a fast galvanic replacement method. The whole process takes only 10 minutes to synthesize a large amount of Te nanorods with a diameter of 97 nm, driven by the large electrochemical potential difference between Te and Ni in an acidic solution. The Te@Ni showed one single plateau in the charge-discharge profiles with both carbonate and ether electrolyte, indicating that Te was directly converted to Li_2Te. However, the capacity experienced a dramatic decline below 80 mAh g^{-1} after only four cycles at the current density of 100 mA g^{-1}, which was caused by large volume expansion (about 200%) due to the formation of Li_2Te. By using the DMSO-based electrolyte, the Te@Ni cathode possessed improved capacity stability, which is due to alleviated volume change by the good solubility of Li_2Te in DMSO solvent. After carbon cloth was introduced between the separator and Te@Ni cathode, the battery showed furtherly enhanced stability due to the strong adsorption capability of nanopores in the carbon cloth. The Li-Te battery

with interlayer delivered a specific capacity of 116.2 mAh g^{-1} compared to that without interlayer (40.4 mAh g^{-1}) after 70 cycles under the current density of 100 mA g^{-1}.

The high-energy mechanical milling (HEMM) technique was a simple method for the preparation of nanosized Te and carbon composite [50]. The nanosized Te with 6.8 nm was obtained. The well-dispersed Te crystallites (5-10 nm) within the amorphous carbon matrix could be observed after Te/C mixture was mechanically milled for 6 h under the high pressure of 6 GPa and temperature above 200 °C. The MR-Te/C composite kept 96% of the initial capacity (597 mAh cm^{-3} or 252 mAh g^{-1}) over 100 cycles with a current density of 100 mA g^{-1}. It is noteworthy that the size of Te nanocrystallites was stable even after 50 cycles, and no agglomerate was observed, suggesting excellent stability of the MR-Te/C cathode. The superior cycling performance was attributed to the nanosized Te confined in a carbon matrix, which shortened the diffusion paths of ions during lithiation/delithiation process.

Table 2.1.1 lists the reported Li-Te batteries with various cathode structures. To sum up, embedding Te molecules into a porous host could significantly improve the specific capacity and cycling stability of the Li-Te batteries by mitigating volume expansion during lithiation/delithiation process. The abundant micro-/mesopores of carbon are also beneficial for ions diffusion and electron transfer, as well as electrolyte infiltration, thus accelerating the reaction kinetics of the Te/C cathode. However, the relatively low Te content and loading indicate low overall energy density, which is far away from the requirements of large-scale energy storage systems. On the other hand, the free-standing Te nanowires are directly used as cathodes without the addition of conductive materials and binders, elevating the energy density of the whole Li-Te battery. At the same time, the electrochemical stability still needs improvement.

Table 2.1.1 Comparison of Te-based cathodes in Li-Te batteries.

Cathode	Te or Te_xS_y content (wt%)	Te loading (mg cm^{-2})	Pore volume (cm^3 g^{-1})	Electrolyte	Discharge capacity: 1st → 2nd cycle*	Cycling performance	Ref.
Te-impregnated porous carbon (Te/C) cathode							
Te/C	50	1	0.44	1M $LiPF_6$ in EC:DEC	324 → 317 mAh g^{-1} at 50 mA g^{-1}	224 mAh g^{-1} after 1000 cycles at 50 mA g^{-1}	[46]
MR-Te/C	65.1	3.16	N/A	1M $LiPF_6$ in EC:DEC	1088 mAh cm^{-3} (740 mAh g^{-1}) →780 mAh cm^{-3} at 10 mA g^{-1}	597 mAh cm^{-3} (252 mAh g^{-1}) after 100 cycles at 100 mA g^{-1}	[50]
Te/CMK-3	55.1	-	1.41	1M $LiPF_6$ in EC:DMC	450 →403 mAh g^{-1} at 0.5C	286 mAh g^{-1} at 10C for 990 cycles (85% retention)	[69]
Te/RHPC	50	2	0.765	1M $LiPF_6$ in EC:DEC	480 → 450 mAh g^{-1} at 0.5C	Keep 288 mAh g^{-1} for 3600 cycles at 2C	[72]
Te/HCC @CNT	50	-	0.882	1M $LiPF_6$ in EC;DEC	700 → 380 mAh g^{-1} at 0.5C	700 → 240 mAh g^{-1} after 500 cycles at 0.5C	[73]
Te/MPC	68	1	0.638	1M LiTFSI in DOL:DME	670 → 481 mAh g^{-1} at 0.1C	274 mAh g^{-1} at 1C after 1000 cycles	[70]
Te/C-Co-N	77.2	2	0.64	1M LiTFSI in DOL:DME	2615.2 → 2600 mAh cm^{-3} at 0.2C	2484.4 → 2324.5 mAh cm^{-3} after 800 cycles at 1C	[53]
Te/NPCS	50	-	0.33	1M LiTFSI in DOL:DME	510 → 420 mAh g^{-1} at 0.25C	510 → 310 mAh g^{-1} after 200 cycles at 0.25C	[75]
Te/OMC	1. 70	-	2.38	1M $LiClO_4$ in DMSO	about 338→290 mAh g^{-1} at 100 mA g^{-1}	130 mAh g^{-1} at 1000 mA g^{-1} for 150 cycles	[71]
Nanostructured Te cathode							

Cathode	Te or Te_xS_y content (wt%)	Te loading (mg cm^{-2})	Pore volume (cm^3 g^{-1})	Electrolyte	Discharge capacity: 1st → 2nd cycle*	Cycling performance	Ref.
TeNWs/ rGO	63.3	1.1	N/A	1M LiTFSI in DOL:DME	2611 →2500 mAh cm^{-3} at 0.2C	2443 mAh cm^{-3} (391.5 mAh g^{-1}) → 1685 mAh cm^{-3} (270 mAh g^{-1}) after 500 cycles at 1C	[47]
TeNW@ CNTs	50	2.55	0.964	1M LiTFSI in DMSO	548 → 400 mAh g^{-1} at 0.1C	488 → 238 mAh g^{-1} after 200 cycles at 1C	[77]
Te nanowires	100	1	N/A	1M $LiClO_4$ in DMSO	About 2100 →900 mAh cm^{-3} at 100 mA g^{-1}	900 mAh cm^{-3} (1800 mWh cm^{-3}) at 100 mA g^{-1} for 80 cycles	[71]
Te nanorods	1.19	0.35	N/A	1M $LiClO_4$ in DMSO	276.6 →230 mAh g^{-1} at 100 mA g^{-1}	70.5 → 47 mAh g^{-1} after 500 cycles at 100 mA g^{-1}	[78]
Te nanotubes	13	0.8	N/A	PEO/LiTFSI	580→405 mAh g^{-1} at 100 mA g^{-1} at 20 °C (cut-off voltage: 0-3V)	580 → 316.7 mAh g^{-1} after 500 cycles at 100 mA g^{-1} at 60 °C	[79]
Tellurized polymer cathode							
Te-3-S/KB	64.45	1-1.2	N/A	1M LiTFSI and 0.1M $LiNO_3$ in DOL:DME	1200→1180 mAh g^{-1} at 0.5 A g^{-1} (1.8-2.8V)	800 → 673 mAh g^{-1} after 400 cycles at 5 A g^{-1}	[80]
Te/Sef-C	70	0.7-1.0	N/A	1M $LiPF_6$ in EC:DEC	6800→4000 mAh cm^{-3} at 0.2C (1C=3454 mAh cm^{-3}) (1.0-2.85V)	4000→ 2275 mAh cm^{-3} after 250 cycles at 0.2C	[81]
CMK-3/S-Te-1	Te: 1wt%	1-1.5	N/A	7M LiTFSI in DOL:DME:10%VC	1650→1200 mAh g^{-1} at 0.1C (1.0-3V)	1800→ 726.9 mAh g^{-1} after 200 cycles at 0.2C	[82]
Te_xS_{1-x}/C	70	2.5-2.9	N/A	1M $LiPF_6$ in EC:DMC	1250→995 at 250 mAh g^{-1} mA g^{-1} (1.0-3V)	1080→ 485 mAh g^{-1} after 500 cycles at 1 A g^{-1}	[83]

Cathode	Te or Te_xS_y content (wt%)	Te loading (mg cm^{-2})	Pore volume (cm^3 g^{-1})	Electrolyte	Discharge capacity: 1st → 2nd cycle*	Cycling performance	Ref.
Te_xS_y@PANI	85.6	1-2	N/A	1M LiTFSI in DOL:DME	1141→1035 mAh g^{-1} at 0.1 A g^{-1} (1.0-2.7V)	223→ 185 mAh g^{-1} after 200 cycles at 5 A g^{-1}	[84]
$Te_{0.04}S_{0.96}$ @pPAN		1-2	N/A	1M LiTFSI (0.1M $LiNO_3$) in DOL:DME	1650→1300 mAh g^{-1} at 0.5 A g^{-1} (1.0-3V)	1350→750 mAh g^{-1} after 600 cycles at 1 A g^{-1}	[85]
$Te_{0.04}S_{0.96}$ @pPAN		1-2	N/A	1M $LiPF_6$ in EC:DMC:DEC	1900→1504 at 0.1 A g^{-1}	1100 after 200 cycles at 0.5 A g^{-1}	[85]

* 1C = 420 mA g^{-1} otherwise noted.

2.1.2 TeS Composite Cathodes

While the well-confined Te/C and nanostructured Te cathodes demonstrated excellent capacity and cyclability, Li-Te batteries intrinsically have relatively low gravimetric energy density due to the limited theoretical capacity of Te (420 mAh g^{-1}). To address this shortcoming, Te is combined with S, a high-capacity conversion-type electrode material, to develop a Te_xS_y composite cathode. The Te_xS_y composites marry the advantages of each component, *i.e.*, superior electronic conductivity of Te and high Li-ion storage capacity of S (1,675 mAh g^{-1}). As extensively studied over past decades, the practical capacity of Li-S battery is far from its theoretical value (1675 mAh g^{-1}), mainly due to the dissolution of polysulfides, shuttle effect, and the intrinsically low electrical conductivity of S [86, 87]. Te_xS_y composites are a promising approach to overcoming the challenges of S-only cathodes. The high electronic conductivity of Te can accelerate the redox kinetics, alleviate polysulfide dissolution, and enhance battery performance [80, 85, 88]. The potential of Te_xS_y composites has been demonstrated in a few recent studies as follows.

Sun *et al.* [83] fabricated heteroatomic Te_xS_{1-x} confined in ordered mesoporous CMK-3 through a melt-diffusion method and applied Te_xS_{1-x}/CMK-3 as the cathode in Li-chalcogen batteries with carbonate electrolytes. The Te-S compound was synthesized by heating the mixture of Te and S at 550 °C for 4 h in a sealed vessel under vacuum. The XPS spectra at 574.7 and 585.1 eV in Te 3D XPS spectra proved the formation of a covalent Te-S bond in the molten mixture at high temperatures [89, 90]. The heteroatomic Te_xS_{1-x} possessed higher electrical conductivity than S due to the introduction of Te with higher *p* orbitals, thus enabling the highly heteropolar Te-S bond to anchor S firmly in CMK-3. The electrochemical evaluation showed that the Te_xS_{1-x}/CMK-3 cathode showed two peaks at 2.3 and 1.6 V in the first cathodic scan, corresponding to the stepwise conversion from Te_xS_{1-x} to polysulfides/polytellurides/polysulfotellurides and then to Li_2S/Li_2Te. In the subsequent scans, only one pair of peaks at 1.8 and 2.0V was observed in Te_xS_{1-x}/CMK-3, indicating a one-step "quasi-solid-state" reaction mechanism in carbonate electrolyte-based Li-Te_xS_{1-x} batteries. Notably, $Te_{0.1}S_{0.9}$/CMK-3 showed extended charge/discharge plateaus and higher capacities, likely due to the enhanced electronic conductivity by Te doping (**Figures 2.1.6a-b**). Moreover, the Te/S molar ratio in the Te_xS_{1-x} composites was optimized, and the $Te_{0.1}S_{0.9}$/CMK-3 cathode with a Te/S molar ratio of 1:9 displayed the best electrochemical performance, with the highest reversible capacity of 845 mAh g^{-1} and CE of 99.6% after 100 cycles at 250 mA g^{-1} (**Figure 2.1.6c**). Furthermore, the $Te_{0.1}S_{0.9}$/CMK-3 cathode exhibited relatively stable cycling performance over 500 cycles at high rates of 1 and 3 A g^{-1} (**Figure 2.1.6d**). The excellent electrochemical performance of the $Te_{0.1}S_{0.9}$/CMK-3 cathode was due to the accelerated reaction activity by Te doping and a Te-induced protective SEI layer (**Figure 2.1.6e**). The *in-situ* generated SEI layer ($Li_2Te_xS_y$, $4 \leq x + y \leq 8$) on the electrode surface prevented the side reactions between polychalcogenides and carbonate electrolytes, therefore promising good reversibility of the Te_xS_{1-x}/CMK-3 cathode. The direct comparison between the $Te_{0.1}S_{0.9}$/CMK-3 and S/CMK-3 cathodes suggests the critical importance of Te doping for accelerating electronic diffusion in the $Te_{0.1}S_{0.9}$/CMK-3 cathode to allow fast "quasi-solid-state" reactions, which is nearly impossible for S/CMK-3 cathodes in the carbonate electrolytes.

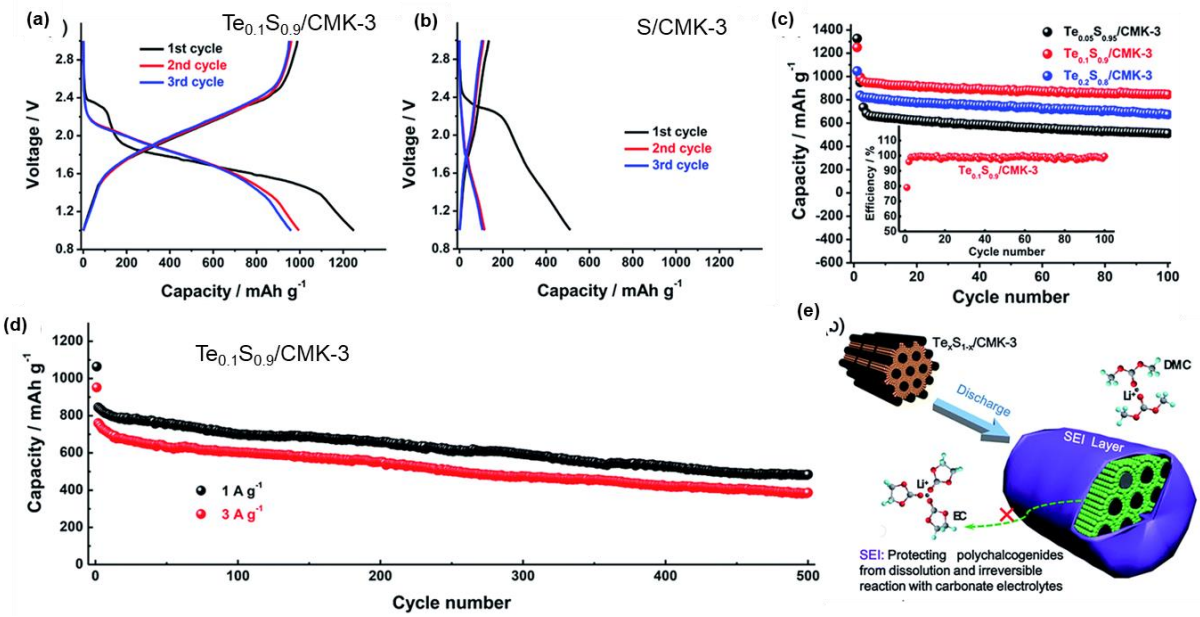

Figure 2.1.6. Te_xS_y composite cathodes. Charge-discharge profiles of (a) $Te_{0.1}S_{0.9}$/CMK-3 and (b) S/CMK-3. (c) Cycling performance of Te_xS_{1-x}/CMK-3 (x=0.05, 0.1, 0.2), (d) capacity stability of $Te_{0.1}S_{0.9}$/CMK-3 at 1 A g^{-1} and 3 A g^{-1}, and (e) schematic diagram of the formation of Te-induced SEI layer on Te_xS_{1-x}/CMK-3 cathode surface. [83].

Qian *et al.* [85] analyzed the effect of Te doping on the electron density distribution of S and found that higher *p* orbitals of Te provided more energy states and reshaped the electrical conductivity of S and Li_2S, as shown in **Figures 2.1.7a**. The improved conductivity of Te_xS_y could be attributed to the narrow bandgap between the valence and conduction bands after the addition of Te. Moreover, Te-S showed lower lithiation energy (-3.31 eV) and de-lithiation energy (4.48 eV) than S (-3.24 eV for lithiation and 5.33 eV for de-lithiation), indicating a lower energy barrier for Li^+ lithiation and de-lithiation in Te_xS_y composites than in solely S (**Figure 2.1.7b**). The theoretical calculations obtained five Li migration pathways near the Te in Te−Li_2S, as shown in **Figure 2.1.7c**. Pathway 1 is through the most favorable potential energy surface with the lowest migration energy barrier for both Li_2S (0.37 eV) and Te−Li_2S (0.08 eV) (**Figure 2.1.7d**). In a CV test, the Te-3-S/KB cathode showed a positive shift for lithiation and a negative shift for de-lithiation, revealing decreased cell polarization and improved electrochemical reversibility. The higher onset potential for lithiation (2.395 V) and lower value for de-lithiation (2.201 V) of Te-3-S/KB also revealed more active electrochemical reactivity in the Te-3-S/KB cathode than in the S/KB cathode.

The increased exchange current density derived from Tafel plots of Te-3-S/KB suggested that electron transfer is facilitated by Te doping. With an electrolyte of 1M LiTFSI and 0.1M $LiNO_3$ in DOL/DME, the Te-3-S/KB cathode exhibited enhanced cycling and rate performance compared to S/KB (**Figures 2.1.7e-h**). As the current density increased to 20 A g^{-1}, the Te-3-S/KB cathode retained 579 mAh g^{-1}, whereas S/KB only delivered 287 mAh g^{-1}. Besides, the specific capacity retention of Te-S/KB increased over the initial cycles, with Te content growing to 5 wt% (**Figure 2.1.7f**). In the long-term cycling test, the Te-3-S/KB cathode maintained 673 mAh g^{-1} after 400 cycles at 5 A g^{-1}, corresponding to a fading rate of 0.026% per cycle, whereas S/KB experienced rapid capacity fading with only 322 mAh g^{-1} remaining after 400 cycles (**Figure 2.1.7g**). The Te-3-S/rGO also displayed an exceptional specific capacity of ~656 mA h g−1 at a current density of 5 A g^{-1} after 1000 cycles (**Figure 2.1.7h**).

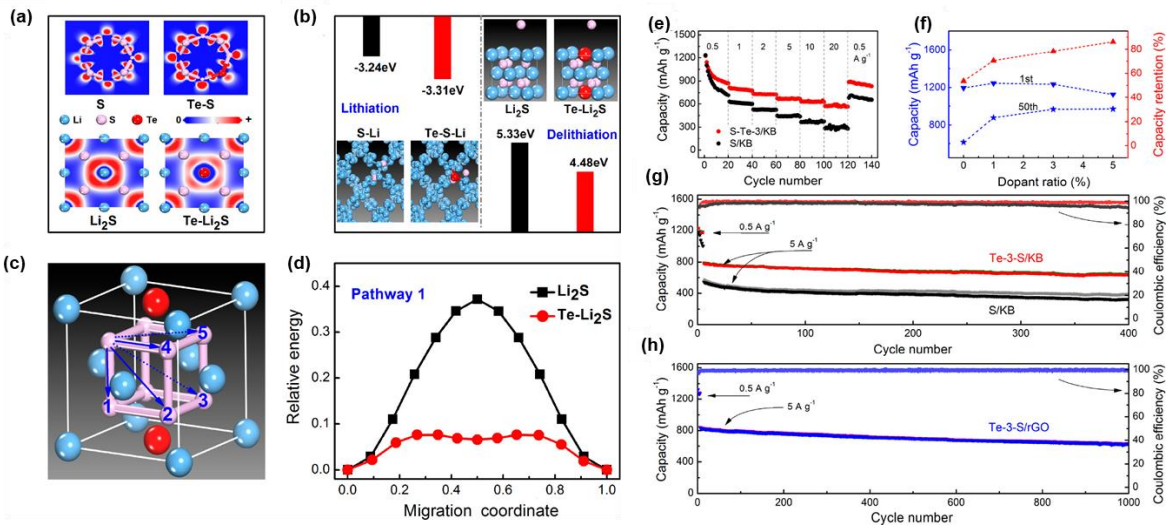

Figure 2.1.7. (a) Electron density differences for S, Li_2S, Te-S, Te-Li_2S, (b) formation energies of lithium insertion and extraction for the initial lithiation and delithiation process, (c) possible Li migration pathways in Te-Li_2S, (d) energy profiles for Li migration pathway 1 in Li_2S and Te-Li_2S, (e) rate performance of Te-3-S/KB and S/KB, (f) discharge capacities and corresponding capacity retention *versus* dopant ratio at the 1st and 50th cycle, and long-term cycling performance of (g) Te-3-S/KB and S/KB, (h) Te-3-S/rGO at 5 A g^{-1}. [85]

From the above research, it becomes apparent that Te doping is an effective way of manipulating the redox kinetics of Li-S chemistry to achieve high energy density and stable cycling in both the

carbonate and ether-based electrolytes. Moreover, the Te_xS_y composite cathodes simultaneously overcome the low gravimetric capacity of Te-only cathodes and the poor reaction kinetics of S-only cathodes. Therefore, Te doping in S cathodes has tremendous promise to address the grand challenges in Li-S batteries hindering practical applications.

Te doping has also been applied to tailor the structure and improve the performance of sulfurized polymer cathodes, another widely investigated approach to mitigate the shuttle effect in Li-S batteries. One typical example is sulfurized polyacrylonitrile (S@pPAN), in which S is chemically bonded to a highly conductive pPAN polymer network [91]. The S@pPAN structure only involved $S_{3-4,}$ and the soluble Li_2S_n ($n \leq 4$) were the main intermediates under the "dissolution-deposition" mechanism [92]. Therefore, the S@pPAN cathode could maintain a high reversible capacity of 1,000 mAh g^{-1} after 1,000 cycles in carbonate electrolytes [93]. The excellent stability could be attributed to protective SEI layers generated by the reaction of carbonate solvents and Li_2S_n ($n \leq 4$) on the cathode surface [94]. However, the S@pPAN cathode performed poorly in ether electrolytes due to the slow redox conversion from polysulfides to Li_2S_2/Li_2S [95]. To boost redox reactions, Li *et al.* [85] adopted Te as a eutectic accelerator in S@pPAN to promote redox kinetics, suppress polysulfide dissolution, and enhance its cycling stability in ether electrolytes. The synthesis process of Te_xS_{1-x}@pPAN included the preparation of Te_xS_y compounds (heating at 445 °C for 24h in a vacuum sealing tube) and subsequent heat-treatment of Te_xS_y and PAN mixture with the ratio of 1:3 (300 °C, 3 h under argon atmosphere) as illustrated in **Figure 2.1.8a**. The as-obtained Te_xS_{1-x}@pPAN particles had an average diameter of 200 nm and uniform distribution of S and Te in the composite. The $Te_{0.04}S_{0.96}$@pPAN cathode maintained a highly stable capacity of about 1250 mAh g^{-1} at 0.5 A g^{-1} in both carbonate and ether electrolytes (**Figures 2.1.8b and 2.1.8c**). It also delivered high-rate capabilities of 1500, 1372, 1292, 1232, 1184, 1122, 1059, 1012, 948, and 861 mAh g^{-1} at various current densities from 0.1 to 10 A g^{-1} in an ether electrolyte. **Figures 2.1.8d-i** demonstrate the thermodynamics and kinetics of S@pPAN and $Te_{0.04}S_{0.96}$@pPAN. The $Te_{0.04}S_{0.96}$@pPAN cathode exhibited a lower overpotential than S@pPAN (0.35 *vs.* 0.52 V), as shown in the CV and charge-discharge profiles (**Figures 2.1.8d-e**). Furthermore, UV-vis spectra detected obvious S_8^{2-}/S_6^{2-} species absorption peaks at 260 nm (**Figure 2.1.8f**), confirming the dissolution and migration of polysulfides intermediates in the S@pPAN electrode. The disappearance of the representative peaks of the S_8^{2-}/S_6^{2-} species for

$Te_{0.04}S_{0.96}$@pPAN indicated the suppressed shuttle effect and fast redox conversion from soluble polysulfides to insoluble Li_2S_2/Li_2S in ether electrolytes. **Figure 2.1.8g** showed that Li^+ diffusion coefficient of $Te_{0.04}S_{0.96}$@pPAN was 3-4 times higher than that of S@pPAN in charge and discharge reactions. The reaction resistance of $Te_{0.04}S_{0.96}$@pPAN was also lower than that of S@pPAN at various states of charge and discharge depths (**Figures 2.1.8h-i**), revealing that Te doping accelerated charge transfer during lithiation and delithiation. The enhanced Li^+ diffusion in $Te_{0.04}S_{0.96}$@pPAN coincided with the lower energy barrier (0.44 eV for $Te_{0.04}S_{0.96}$@pPAN *vs.* 1.33 eV for S@pPAN) calculated by DFT theory. Moreover, the $Te_{0.04}S_{0.96}$@pPAN cathode delivered an outstanding electrochemical performance in Na batteries with carbonate and ether electrolytes [96]. The electrochemical and spectral techniques (CV, UV-vis, XPS, Raman) revealed a two-step reaction pathway of $Te_{0.04}S_{0.96}$@pPAN, with Na_2S_3 and Na_2S the main intermediate and ultimate discharge product, respectively. The Na-$Te_{0.04}S_{0.96}$@pPAN battery delivered a high specific capacity of 629 mAh g^{-1} at the high current density of 6 A g^{-1}, benefiting from the accelerated reaction kinetics resultant of Te doping.

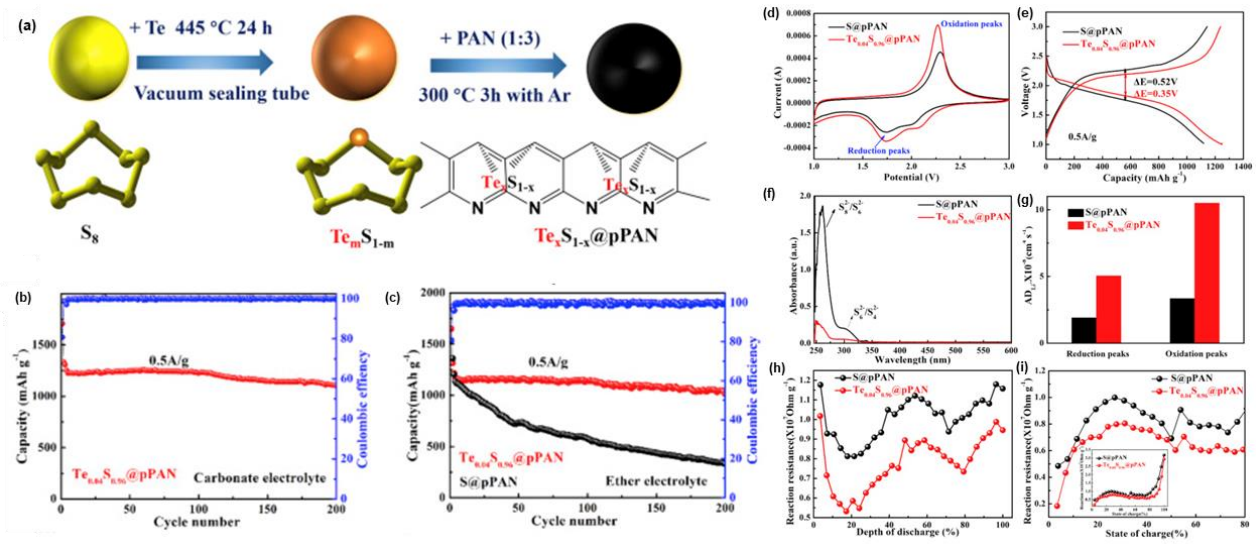

Figure 2.1.8. (a) Synthetic route of Te_xS_{1-x}@pPAN, cycling performance of $Te_{0.04}S_{0.96}$@pPAN in (b) carbonate electrolyte and (c) ether electrolyte, (d) CV plots, (e) charge-discharge profiles, (f) UV-vis spectra, (g) Li^+ diffusion coefficients, (h, i) reaction resistance during discharge and charge process of S@pPAN and $Te_{0.04}S_{0.96}$@pPAN. [85]

Li *et al.* [84] developed a novel one-step nonlinear electrochemical method to synthesize Te_xS_y@polyaniline nanorods from bulky Te flakes. In this approach, Te was first oxidized and then reacted with ammonium sulfide to form Te_xS_y, which was simultaneously encapsulated into polyaniline *via in situ* polymerization. The Te_xS_y@polyaniline nanostructure was controlled in an oscillatory manner. The Te_xS_y@polyaniline cathode delivered a specific capacity of 1035, 785.5, 461.3, and 383.6 mAh g^{-1} at current densities of 0.1, 0.5, 1, and 2 A g^{-1}, respectively. The superior rate performance resulted from the boosted redox kinetics of the nanostructured Te_xS_y@polyaniline during the charge/discharge process. *In situ* TEM characterization revealed the volume change of the Te_xS_y@polyaniline cathode during the lithiation and de-lithiation process. It was found that some small Te_xS_y@polyaniline nanorods remained relatively stable without noticeable volume variation over repetitive cycles due to the effective confinement of Te_xS_y in the polyaniline network.

Above all, the Te_xS_y composite confined in the porous carbon or conductive polymer network showed great potential as a high-capacity cathode in Li-battery applications. By using the Te doping strategy, Te_xS_y compounds, and tellurized/sulfurized polymers exhibited higher polarity, which leads to a lower energy barrier for accelerated Li-ion diffusion and redox kinetics in Li-Te_xS_y batteries. Simultaneously, polysulfide dissolution was effectively alleviated, thus realizing improved cycling and rate performance in carbonate and ether electrolytes compared to Li-S chemistry. More efforts should be devoted to addressing the low loading and content of Te_xS_y active materials for practical applications of Te-based rechargeable batteries.

2.1.3 Electrolyte Chemistry

This section describes the research progress of Li-Te batteries with ether, carbonate, DMSO-based electrolytes, and solid polymer electrolytes.

2.1.3.1 Liquid Electrolytes

The electrolyte is responsible for Li^+ ion conduction between the anode and cathode, which has a determining effect on the overall cell capacity and efficiency. The liquid electrolyte is primarily composed of salt, solvent, and additives. Based on the different types of solvent, the liquid electrolyte for Li-Te batteries is categorized into carbonate, ether and DMSO-based electrolyte.

Here, we summarized the redox conversion of Li-Te batteries under each electrolyte with a similar cathode structure (Te/porous carbon).

When using carbonate electrolyte (*e.g.*, 1M $LiPF_6$ in EC:DEC) in Li-Te batteries, the ASAC25-Te cathode only presents one pair of cathodic/anodic peaks at 1.55/1.85V (**Figure 2.1.9a**), indicating the one-step conversion between Te to Li_2Te. In ether electrolyte (1M LiTFSI in DOL:DME), the Te/C-Co-N cathode shows multiple reduction/oxidation peaks, which are consistent with the discharge/charge plateaus (**Figure 2.1.9b**) [53]. Based on the structure information from *operando* Raman spectroscopy, the sharp redox peaks at 2.7, 2.3, and 1.75 V in CV correspond to the formation of Li_2Te_8 and Li_2Te_6, Li_2Te_4, and short-chain Li_2Te_3 and Li_2Te_2, which are ultimately converted to Li_2Te. In contrast, the more polar solvent DMSO results in a significantly higher voltage of Te@OMC (see **Figure 2.1.9c**) [71], which benefits from the stronger solvation effect of DMSO, thus inducing higher cathodic potential [97]. It is also found that Li_2Te is the sole soluble discharge product confirmed by UV-vis spectroscopy as no peak shift is observed at 254nm with different lithiated Te in DMSO. The absence of polytellurides is beneficial for mitigating the shuttle effect and enhancing battery stability. It should be emphasized that the uplifted average working voltage of 2.03 V is comparable to that of Li-S batteries, which is favorable for the development of higher-energy density Li-Te batteries.

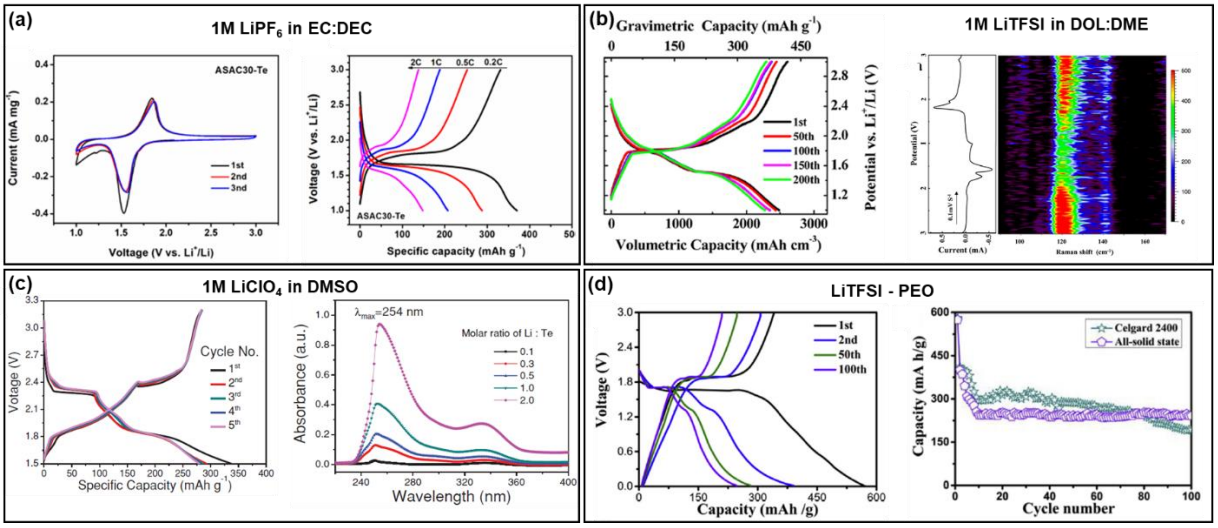

Figure 2.1.9. Galvanostatic charge-discharge curves of Te/C cathodes in different electrolytes of (a) 1M $LiPF_6$ in EC:DEC (1:1), (b) 1M LiTFSI in DOL:DME (1:1) [53], (c) 1M $LiClO_4$ in DMSO [71], and (d) solid electrolyte (LiTFSI-PEO) [79].

2.1.3.2 Solid Electrolytes

However, the traditional liquid electrolytes suffer from the inevitable safety issue due to the flammability and toxicity of organic solvents (*e.g.*, EC, DEC, DME). Herein, solid electrolyte attracts great attention since the introduction of solvent is nearly avoided. In the meantime, the energy density could be increased by replacing liquid electrolytes with solid electrolytes. These advantages of all-solid-state lithium-ion batteries have encouraged attractive research progress [55, 57]. Technically, solid electrolyte acts as both separator and ion conductors, which is expected to possess high ion conductivity, broad electrochemical window, excellent electrochemical, thermal, and structural stability, and low cost. Currently, the development of solid-state batteries is mainly challenged by the relatively low ionic conductivity, electrochemical instability, and poor compatibility with electrodes [54, 56].

Zhu and co-workers [79] firstly reported an all-solid-state Li-Te battery with PEO/LiTFSI as a solid electrolyte in 2018. After the initial 10 cycles, the solid-state Li-Te battery even showed superior stability than the liquid Li-Te battery with commercial Celgard 2400 membrane at 40 °C (**Figure 2.1.9d**). After 100 charge/discharge cycles, the solid-state Li-Te battery maintained 210.4 mAh $g^{-1,}$ whereas the liquid Li-Te battery only retained 190 mAh g^{-1}. When the working temperature increased to 60 °C, the battery showed the highest capacity of 327 mAh g^{-1} after 100 cycles. This work pioneers the exploration of solid electrolytes in Li-Te and demonstrates the comparable electrochemical performance with liquid electrolyte-based Li-Te batteries at a low current density.

In addition to polymer electrolytes, the inorganic and polymer/inorganic composite electrolytes have shown satisfying electrochemical performance in Li-S/Se batteries [98-100]. In view of the faster reaction kinetics in Li-Te electrochemistry, these electrolytes have great potential in the application of Li-Te batteries. Moreover, the engineering design of electrolyte/electrode interface is a significant direction in solid-state Li-Te batteries, although it is rarely reported. The advanced characterizations and theoretical simulations should be well integrated to gain an insightful understanding of solid-state chemistry.

2.1.4 K-Te Electrochemistry

Due to the scarcity and uneven distribution of Li resources, rechargeable batteries with alternative charge carriers, low cost, and high energy density are attracting increasing attention for large-scale energy storage, such as monovalent sodium-ion batteries [101], potassium-ion batteries [61], bivalent magnesium-ion batteries [102], zinc-ion batteries [103], as well as multi-valent aluminum-ion batteries [68]. The exploration of Te in Na/K/Mg/Zn/Al batteries has attracted increasing research interest since Te electrodes have shown excellent electrochemical performance in Li-Te batteries. The advantageous electronic conductivity and high-volumetric capacity of Te make it a promising electrode material for these beyond-Li batteries. **Table 2.1.2** compares the metal-ion radius, crustal abundance, possible intermediates and discharge products, the overall reaction pathways, and energy density of Li-Te, Na-Te, K-Te, Zn-Te, and Al-Te batteries. Each metal anode has a greater abundance than Li and is expected to be suitable for scalable battery applications. It should be noted that the thermodynamically stable metal-Te intermediates are different in rechargeable batteries and may affect their electrochemical behaviors and determine the battery's overall performance. The electrochemical conversion follows $Te + 2M \leftrightarrow M_2Te$ (M = Na, K) or $Te + M \leftrightarrow MTe$ (M = Mg, Zn). The reaction mechanism in the Al-Te system is complicated, having three redox pairs of Te/Te^{2-}, Te/Te^{2+}, and Te^{2+}/Te^{4+}, and involves the chemical dissolution of Te and electrochemical reactions. The larger ionic radius of Na-ions and K-ions compared to Li-ions presents a challenge for Na-ion or K-ion insertion/extraction, leading to the decreased energy density (644, 432, and 417 Wh kg^{-1}, for Li-Te, Na-Te, and K-Te, respectively). The bivalent Mg-Te batteries deliver a lower energy density of 212 Wh kg^{-1} due to the relatively low working voltage. Aqueous Zn-Te batteries possess excellent stability in ambient environments, provide high intrinsic safety, and eliminate the usage of glovebox equipment and device costs. However, these aqueous Zn-Te batteries are limited by the low energy density of 167 Wh kg^{-1}. In comparison, multivalent Al-Te batteries are able to contribute a high energy density of 1328 Wh kg^{-1} and are very safe through the use of a nonflammable ionic liquid electrolyte. Although metal-Te batteries have promising energy densities, they suffer from similar issues to Li-Te batteries, such as large volume changes of the cathode, dendrite growth on the anode, and the shuttle effect. The following sections will discuss the progress in each metal-Te system and highlight the challenges that need to be addressed in the future.

Table 2.1.2 Comparison of Li-Te, Na-Te, K-Te, Mg-Te, Zn-Te, and Al-Te systems.

	Li-Te	Na-Te	K-Te	Mg-Te	Zn-Te	Al-Te
Metal-ion radius (Å)	0.68	0.97	1.33	0.65	0.74	0.5
Redox potential of anode (V, vs. SHE)[113]	-3.0	-2.7	-2.9	-2.4	-0.8	-1.7
Abundance of anode material on earth (ppm)[113]	20	23600	20900	23300	70	82300
Overall reaction pathways	$Te + 2Li \leftrightarrow Li_2Te$	$Te + 2Na \leftrightarrow Na_2Te$	$Te + 2K \leftrightarrow K_2Te$	$Te + Mg \leftrightarrow MgTe$	$Te + Zn \leftrightarrow ZnTe$	$Te + 2e^- \leftrightarrow Te^{2-}$; $5Al_2Cl_7^- + Te^{2-} \leftrightarrow 2Al + 7AlCl_4^- + TeCl_3 \cdot AlCl_4$
Electrolyte	Organic	Organic	Organic	Organic	Aqueous	Ionic liquid
Cell voltage (V)	1.7	1.4	1.6	0.6	0.6	1.5
Gravimetric capacity of Te cathode (mAh g^{-1})[a]	420	420	420	420	420	1260
Theoretical specific energy (Wh kg^{-1}) [b]	644	432	417	212	167	1328

[a] According to an overall electrochemical reaction.

[b] Theoretical data based on the total mass of active materials on the cathode and the anode.

The potassium storage performance of Te electrode also depends on the electrode structure and electrolyte chemistry. Guo and co-workers [104] constructed a novel K-Te battery using Te-G-CNT as the cathode (**Figure 2.1.10a**) and revealed its potassium storage mechanism in carbonate electrolyte (1M KFSI in EC:DEC). After Te-G-CNT is discharged to 0.3 V, the diffraction rings in SAED pattern, XRD pattern, and Te 3d peak shift in XPS spectra (**Figures 2.1.10b-e**) confirm that face-centered cubic (fcc) K_2Te is the ultimate discharge product. This is consistent with DFT calculations (**Figure 2.1.10f**), which suggest that K_2Te has the lowest formation energy of -1.028

eV and is the most thermodynamically stable product. Herein, a two-electron redox reaction process is proposed ($Te + 2K^+ + 2e^- \leftrightarrow K_2Te$) with the carbonate electrolyte, which agrees well with a single plateau in charge-discharge profiles (**Figures 2.1.10g-j**). During potassiation process, the hexagonal Te is converted to cubic K_2Te, which comes back to the hexagonal structure after K^+ extraction. Compared to bulky Te, the Te-G-CNT electrode delivers an ultrahigh reversible volumetric capacity of 2493.13 mAh cm^{-3} at 0.5 C (based on the mass of Te), a high-rate capacity of 783.13 mAh cm^{-3} at 15 C, and superior long-term cycling stability for 1000 cycles at 5 C.

The mechanistic studies in ether electrolyte-based K-Te batteries were recently reported by Sun and co-workers [105]. To buffer the volume change of Te, they synthesized Te nanowires with 25 nm in diameter and mixed them with carbon nanotubes and reduced graphene oxide to obtain a free-standing TeNW/rGO/CNT cathode (**Figure 2.1.11a**). With the electrolyte of 1M KTFSI in DGEDME, the TeNW/rGO/CNT electrode presents two cathodic (1.75/1.00 V) and anodic peaks (2.05/2.42 V), corresponding to a stepwise phase transformation from Te to soluble K_2Te_3 and ultimately to insoluble K_5Te_3 (**Figure 2.1.11b**). Moreover, by increasing the electrolyte concentration to 5 M, the cathode delivers a higher initial capacity of 377 mAh g^{-1} and superior cycling stability with 168 mAh g^{-1} remaining after 100 cycles at 0.2C (**Figures 2.1.10c-f**). The improved electrochemical performance mainly benefits from that, the dissolution of polytellurides intermediates and shuttle effect are effectively suppressed due to the decrease of free solvent in the concentrated electrolyte.

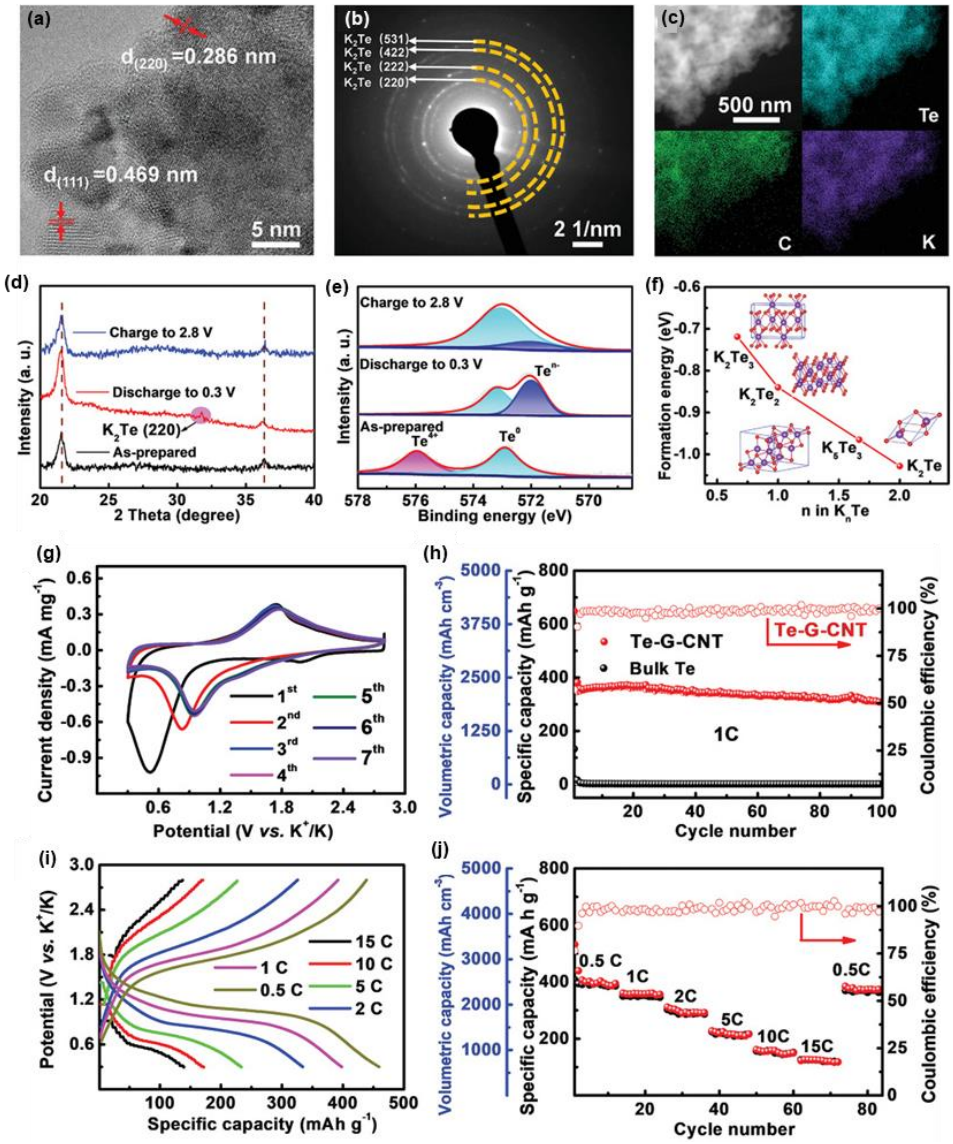

Figure 2.1.10. K-Te batteries. (a) HRTEM image, (b) SAED pattern, (c) HADDF and EDS mapping of Te-G-CNT electrode after discharged to 0.3V, (d) *ex-situ* XRD and (e) Te 3d XPS spectra of as-prepared, discharged, and charged Te-G-CNT electrodes, (f) formation energy of K_nTe, (g) CV, (h) cycling performance, (i) charge-discharge profiles, and (j) rate performance of Te-G-CNT electrode, (1M KFSI in EC:DEC). [104]

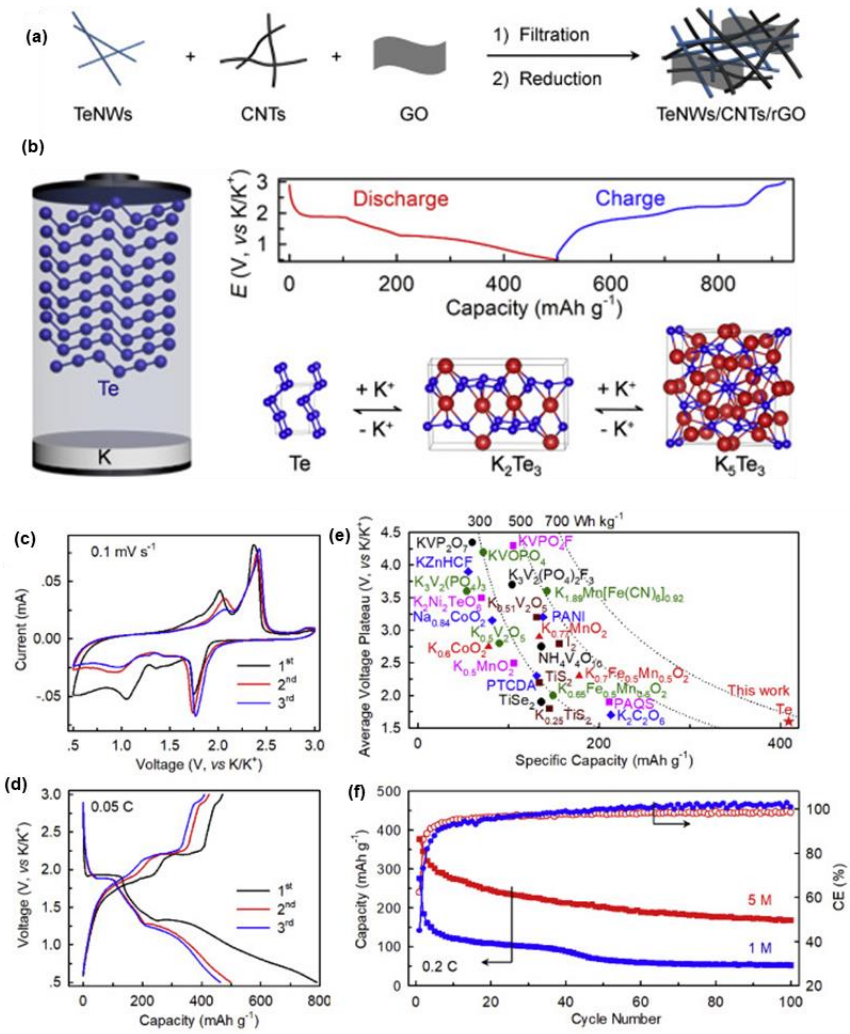

Figure 2.1.11. (a) Synthesis process of TeNWs/CNTs/rGO, (b) K-Te cell structure and reaction pathways, (c) CV plots of TeNWs/CNTs/rGO, (d) charge-discharge profiles, (e) cathode materials comparison in potassium-ion batteries, and (f) cycling performance of TeNWs/CNTs/rGO using 1M and 5M KTFSI in DEGDME. [105]

2.2 Research Summary

2.2.1 Capacity-Voltage-Energy Comparison

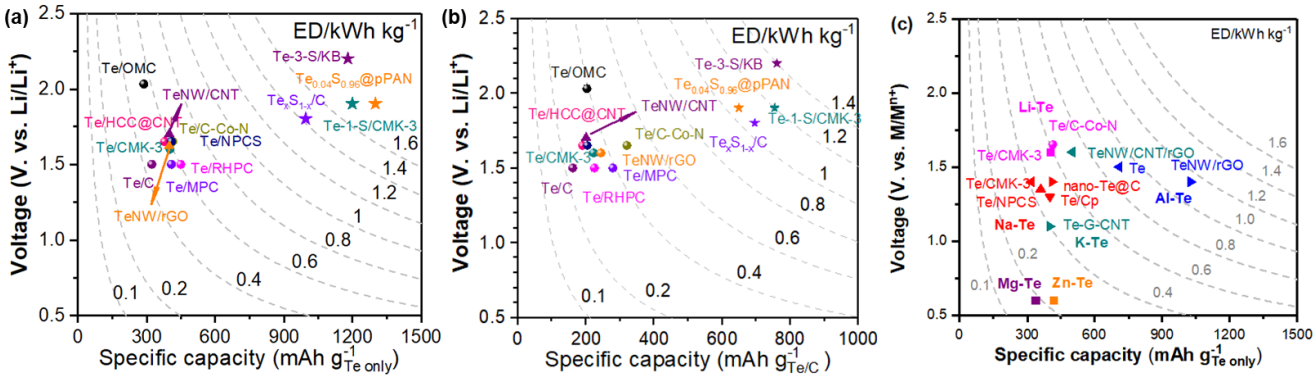

Figure 2.2.1 A comprehensive comparison of the energy density of various Te-based cathodes for rechargeable (a, b) Li-Te based batteries, and (c) Li/Na/K/Mg/Zn/Al-Te based batteries. The *x*-axis shows (a) and (c) specific capacity normalized to Te (or Te_xS_y) only and (b) specific capacity normalized to Te/C (or Te_xS_y/C). The *y*–axis shows the average cell voltage. Plotted are the isoenergy lines ranging from 100 Wh kg^{-1} to 1.6 kWh kg^{-1}.

Figure 2.2.1a graphically summarizes the average voltage, specific capacity, and energy density of what have been reported Te-based cathodes with Li, Na, K, Mg, Zn, and Al metal anodes. **Figure 2.2.1a** shows the specific capacity normalized by solely Te active material, while **Figure 2.2.1b** presents the specific capacity normalized by Te/C, including carbon supports or hosts for Te but excluding conductive additives used to fabricate cathode electrodes. Isoenergy lines are plotted, ranging from 100 Wh kg^{-1} to 1.6 kWh kg^{-1}. It can be seen that the Te normalized capacity of Te/C is in a similar range as those of nanostructured Te (**Figure 2.2.1a**). However, the specific energy becomes scattered if calculated based on the Te/C cathode mass, leading to specific energy values around 500 Wh kg^{-1}. This is due to the varying carbon supports used to prepare Te-based cathode materials and the low levels of Te in some work. Another observation from **Figure 2.2.1** is that Te_xS_y compounds provide substantially higher specific capacity and specific energy than Te cathodes, regardless of the capacity normalized by only active material or cathode mass. The specific energy normalized to the cathode mass changes from 1 to 1.4 kWh kg^{-1}, depending on the weight ratio of Te to S and Te_xS_y to carbon (or polymer) hosts.

It should be noted that the isoenergy lines in **Figure 2.2.1** only employ the theoretical specific capacity of Li metal (3860 mAh g^{-1}) and do not consider the weight of Li metal used for coin-cell evaluations. Many of the published capacity and energy values only take the weight of the active Te or Te_xS_y materials into account, neglecting the weight of carbon hosts, conductive additives, and binders, which might make up at least 40% of the total electrode weight. The amount of Li metal is a significant excess relative to the amount of Te or Te_xS_y active materials. The excessive Li metal might provide an accurate analysis of the cathode's performance due to the "infinite" Li reservoir but make it challenging to evaluate the holistic performance of Li-Te cells, as shown in many recent Li-ion pouch-cell studies [106, 107].

Figure 2.2.1c illustrates the average voltage and capacity of other metal-Te batteries in comparison to the Li-Te system. Overall, Te cathodes in Na/K/Mg/Zn-Te batteries show lower average potentials and specific energy than those in Li-Te batteries due to the higher standard electrode potentials of Na/K/Mg/Zn metals than Li metal. Therefore, the main benefit for these Na/K-Te-based batteries would arguably be the costs associated with Na and K precursors, which, however, are yet to be assessed and validated. Notably, despite a lower average voltage, the Al-Te system presents higher specific energy than the Li-Te system, owing to the multivalence of the Al metal anode.

2.2.2 Challenges

To summarize, we have provided a comprehensive overview of the research advances in Te-based cathode materials and architecture design, a fundamental understanding of Te reaction pathways with various metal anodes (Li/Na/K/Mg/Zn/Al), and metal anode/electrolyte studies associated with Te-based cathode. We also provided an electrochemical performance comparison that includes, to the best of our knowledge, all existing publications on Te-based electrochemistry. Te-based cathodes share common issues of conversion chalcogen cathodes, such as large volume change, shuttle effect, *etc*., but possess significant advantages, such as high electronic conductivity and comparable volumetric energy density. The high electrical conductivity of Te has proven to accelerate electron transfer, enhance rate performance and enable higher utilization of active materials of Te-based battery systems. However, there are still challenges in present Te-based batteries. Due to the short-term study in this field, more mechanistic investigations in metal-Te

electrochemistry should be carried out, and its practical application in large-scale energy storage requires comprehensive evaluation at an industry-relevant scale.

Table 2.2.1 Typical characteristics of S, Se, and Te.

	S	Se	Te
Volume expansion ($X \rightarrow Li_2X$, X=S, Se, Te) [51]	80%	97%	104%
Density (g cm^{-3}) [51]	2.07	4.81	6.24
Electrical conductivity (S m^{-1}) [53]	5×10^{-16}	1×10^{-4}	2×10^{2}
Crustal abundance (mg kg^{-1}) [108]	350	0.05	0.001
Melting point (°C) [108]	114	217-222	450
Price ($ kg^{-1}) (2020)	0.04	40	55

Table 2.2.1 compares some critical parameters of S, Se, and Te and lists several underlying challenges of Te-based electrode materials.

(i) The volume expansion of Te during lithiation is larger than S and Se, raising concern about electrode material stability during long-term cycling. Recent advances have mitigated volume changes by impregnating Te into robust hosts to confine expansion and still deserve enormous investigation to develop advanced Te-based materials in the near future.

(ii) The low crustal abundance of Te is another challenge for the commercialization of Te-based batteries. This might limit Te-based batteries in high-end applications, such as medical implants, wearable devices, *etc*. Nevertheless, the recent U.S. Geological Survey indicates that the current tellurium reserve is sufficient and can satisfy the demand for Te for several decades [109].

(iii) Compared to low-cost S resources, Se and Te are more expensive, causing a major hindrance to the scalable application of Te-based batteries. However, the increasing demand for Te-based batteries could increase production and recycling technologies around Te and eventually reduce the material cost. On the other hand, the price of a metal-Te battery system could be compensated by lowering the cost of electrolytes, negative materials, or other components in the battery system.

(iv) Additionally, the low gravimetric capacity of Te is questioned as a high-capacity cathode, which could be addressed by developing TeS_x composite cathodes as discussed. The addition of low-cost S will significantly reduce the material costs of the battery system.

2.3 Research Objectives

The overall objective of this project is to develop an all-solid-state Li-Te battery with high energy density and good safety. The critical components of the battery system would be tailored, such as the structural design of Te electrode and solid electrolyte, as well as Te/solid electrolyte interfacial engineering to improve the electrochemical stability by addressing the major challenges of large volume expansion, polytellurides dissolution, Li dendrites. In specific, this project includes the following sub-objectives:

2.3.1 Develop Stable Porous Carbon as Te Host in Liquid Electrolyte Based Li-Te Batteries

The top priority in this project is to find suitable hosting materials (e.g., porous carbon) for Te molecules to mitigate the large volume expansion with Te reduced to Li_2Te. The carbon structure, such as pore size distribution, specific area, and pore volume, plays an essential role in the interaction between carbon and Te and the electrochemical performance of Li-Te batteries. In this part, the effect of carbon structure on battery performance (capacity, stability, Coulombic efficiency) will be investigated in terms of morphology, structure, and electrochemical performance of Te/C electrodes. The selected commercial or synthesized carbon from biomass materials with optimal carbon structure will be used to accommodate Te for Li-Te batteries and the Te/C cathodes will be evaluated through comprehensive characterizations.

2.3.2 Develop High-Capacity and Durable Te_xS_y Composite Cathodes

One of the sub-objectives of this project is to develop a durable and high-capacity Te_xS_y composite cathode to integrate the advantages of S (large theoretical capacity) and Te (excellent electron conductivity). The optimal Te/S ratio will be figured out from a wide range of Te_xS_y composites and investigated to enable both electrochemically and thermodynamically stable composite cathodes.

2.3.3 Design Highly Conductive and Stable Solid Electrolytes

The solid-state Li-Te batteries are expected to achieve superior security and energy density, while they face quite a few challenges, especially the slower ion diffusion compared to liquid electrolyte based batteries. In the second stage, the design of solid electrolytes will be the focus, and the goal is to reach the critical requirements such as high ionic conductivity, mechanical strength, and electrochemical stability.

2.3.4 Mechanistic Studies on the Interplay Between Te (or Te_xS_y) Cathodes and Liquid/Solid electrolytes

This section aims to analyze the interplay between Te cathode and electrolyte in both Li-Te and K-Te batteries, *e.g.*, the solid electrolyte interphase layer on the electrode surface. Mechanistic studies are necessary to understand the effect of electrolyte salt chemistry on the electrochemical performance (including reaction kinetics and cyclability) of Te or Te_xS_y cathodes, which will be revealed by *ex-situ* morphology, structure, and electrochemical characterizations.

2.3.5 Modify Te Electrode/Electrolyte Interface by the Advanced Surface Coating Technique

Interface engineering is one of the urgent tasks in the development of solid-state batteries. Excellent compatibility and low interfacial resistance are desirable between electrolyte and electrode. To reach the goal, an advanced atomic layer deposition technique will be applied to make an atomic-level artificial layer between the electrolyte and electrode, which is expected to stabilize the interface and maintain good structural stability.

2.4 Chapter Summary

This chapter introduces the development of metal-Te batteries in the aspects of cathode structure, electrolyte chemistry, and the fundamental of K-Te electrochemistry. The main advantages and challenges in this field are pointed out. Accordingly, the overall and sub-objectives in this dissertation are proposed. The methodology used to fulfill these goals is described in the subsequent chapter. Chapters 4-9 aim to address the following issues in literature:

(1) there is a lack of fundamental understanding of carbon pore structure for Te/C electrodes in Li-Te batteries;

(2) the electrochemistry of the Te_xS_y composites with different Te/S ratios is unknown;

(3) the ion conduction mechanism and interface compatibility of solid-state or quasi-solid-state metal-Te batteries are unraveled;

(4) electrolyte chemistry and kinetics study of the new K-Te system has not been studied sufficiently;

(5) the Te/electrolyte interfacial instability induced by the volume change of Te has not been solved.

Chapter 3 Research Methodology

Systematic experimental and characterization techniques are indispensable to fulfill the above objectives. The methodology used in this dissertation (**Figure 3.1.1**) is introduced following the order of structure design and materials synthesis, cell assembly, morphology/structure characterizations, and electrochemical performance evaluation.

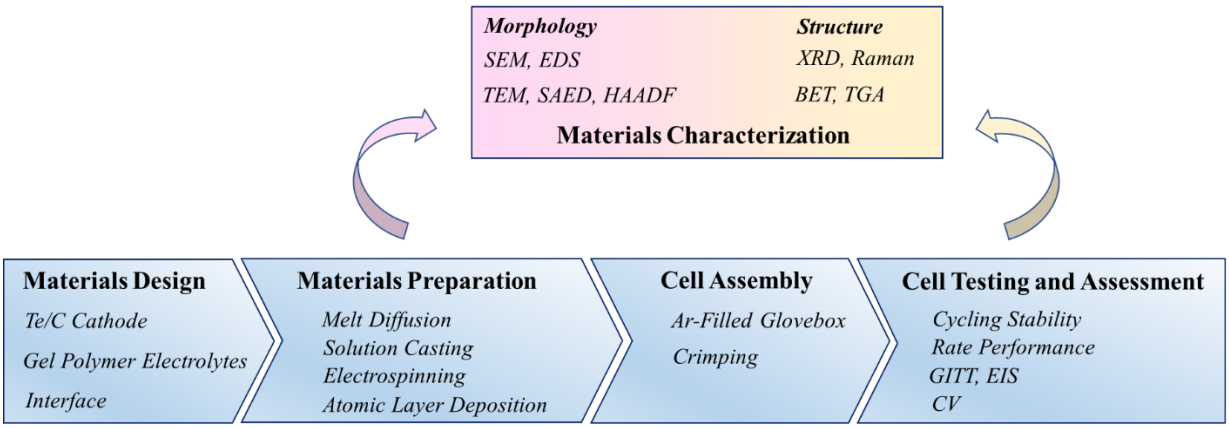

Figure 3.1.1. Methodology diagram used in this dissertation.

3.1 Materials Synthesis

3.1.1 Synthesis of Porous Carbon

Technical-grade lignin (molecule weight: 14060 g mol^{-1}) was provided by Advanced BioCarbon 3D (BC, Canada) and used after complete drying at 80 °C for 12 h to remove residual water. The lignin-derived porous carbon was synthesized through carbonization and activation procedures. The carbon structure depends on the heating temperature, heating time, and ratio of potassium hydroxide (KOH)/carbon. Firstly, the dried lignin was heated at 600 °C for 2 h at a heating rate of 10 °C min^{-1} under a nitrogen atmosphere to obtain a carbonized powder. Subsequently, the carbonized powder was thoroughly mixed with KOH with the mass ratio of 1:2 and then heated at specific temperatures (600, 700, and 800 °C) for another 2 h at a heating rate 10 °C min^{-1} under N_2. Afterward, the obtained carbon was washed with hydrochloric acid (HCl) and filtrated several times until the solution pH reached 7. Finally, the activated porous carbon was successfully

prepared, and was denoted as AC600, AC700, and AC800, with activation temperatures of 600, 700, and 800 °C, respectively. These activated carbons were used as Te hosts in Chapter 4.

3.1.2 Synthesis of Well-Defined Te/C Structure

Porous carbon should be prepared prior to the synthesis of Te/C composite. Commercial porous carbons used as Te host include ASAC25, ASAC30, BP2000, and KB. The Te/C composite is synthesized by a melt-diffusion method. The well-grounded Te/C mixture with a Te/C mass ratio of 2:1 is heated at 550 °C in a tube furnace under nitrogen atmosphere. The heating temperature is above the melting point of Te: 450 °C to ensure the infusion of liquid Te molecules into the porous skeleton.

Similarly, the S/C and Se/C composites were prepared by heating the mixture of S or Se and C at the mass ratio of 1:1 or 6:4 in an autoclave at 160 and 260 °C for 24 h.

3.1.3 Synthesis of Te_xS_y Compounds and Te_xS_y/KB Composites

Te_xS_y compounds used in Chapter 6 were synthesized by ball-milling the mixture of Te and S powders and subsequently sealing the mixture in a quartz tube under vacuum. After being heated at 450 °C for 10 h, the mixture was naturally cooled down to room temperature. The obtained Te-S solid solution was denoted as Te_xS_y compounds. A wide Te/S mole ratio range from 1:7 to 7:1 was designed and prepared, corresponding to compounds from Te_1S_7 to Te_7S_1.

The Te_xS_y/KB composite was prepared by a melt diffusion method. The Te_xS_y and KB powders were mixed at the mass ratio of 6:4 and then ball-milled for 2 h. Afterward, the mixture was sealed in a quartz tube under vacuum and heated at 480 °C for 10 h in a tube furnace. The obtained products were denoted as Te_xS_y/KB. The Te/KB and S/KB composites were also prepared using the same procedures, and the heating temperatures for Te/KB and S/KB were 480 and 160 °C, respectively. The Te_xS_y content in Te_xS_y/KB is about 60 wt%.

3.1.4 Preparation of Gel Polymer Electrolytes

The gel polymer electrolytes (GPE) synthesis in Chapter 5 was by a solution casting method. Firstly, a certain amount of PVDF-HFP was dissolved into N-methyl-2-pyrrolidone (NMP) at a mass ratio of 1:4. The mixture was heated at 50 ^{o}C with continuous stirring for 12 h until a

transparent and homogeneous solution was obtained. Subsequently, LiTFSI salt was added (mass ratio of PVDF-HFP: LiTFSI = 5:4), and the solution was stirred for another 12 h. Then the solution was poured onto glass containers, which were transferred to an oven and heated at 60 ^{o}C under vacuum for different times to control NMP uptake in the GPE membrane. Finally, the GPE membranes were peeled off and cut into 16 mm for further characterization and cell assembly.

3.1.5 Preparation of PAN-Based Composite Gel Polymer Electrolytes

3.1.5.1 Preparation of PAN Nanofibers

To prepare PAN nanofibers, PAN was dried at 95 ^{o}C in a vacuum oven for 48 h prior to dissolving in DMF. Then 10 wt % PAN in the DMF solution was electrospun in a horizontal electrospinning setup with 18-gauge (0.84 mm diameter) stainless steel needle. The electrospinning distance, voltage range, and pump speed were 15 cm, 19 kV, and 0.01 mL min^{-1}, respectively. The thickness of PAN was controlled to be 25 µm by electrospinning technique.

3.1.5.2 Preparation of PVDF-HFP-KFSI and PVDF-HFP-KFSI@PAN

The PVDF-HFP powders (2 g) were dissolved into NMP (10 g) at 50 ^{o}C under continuous stirring for 12 h until a transparent and homogeneous solution was obtained. Subsequently, KFSI salt (1.6 g) was added to the solution, which was stirred for another 12 h. The solution was cast onto a glass container and then dried at 80 ^{o}C under vacuum overnight to obtain a PVDF-HFP-KFSI membrane. To prepare PVDF-HFP-KFSI@PAN, one piece of electrospun PAN nanofibers was immersed in the PVDF-HFP-KFSI/NMP polymer solution for 12 h under vacuum. Afterward, the PAN/polymer solution was transferred to glass plates and heated at 80 ^{o}C under vacuum overnight. Finally, PVDF-HFP-KFSI@PAN CGPE was peeled off and cut into 16 mm for coin-cell assembly. **Table 3.1.1** lists the name, components, and specification of gel polymer electrolytes and glass fiber used in Chapter 9. For each preparation of polymer electrolyte, 4 g solution was poured onto 6 cm × 6 cm PAN fibers in a glass container and dried overnight. Subsequently, the 6 cm × 6 cm area is peeled off and denoted as PVDF-HFP-KFSI@PAN. The residual NMP mass fraction was calculated to be 23 wt% by measuring the weight before/after heating treatment. PVDF-HFP and KFSI were assumed to be left entirely in the composite, and their weights can be obtained by multiplying 4 g and their respective concentration.

Table 3.1.1. Abbreviation and specification of gel polymer electrolytes and glass fiber separator.

Name	Specification
PVDF-HFP-KFSI	PVDF-HFP (2 g), KFSI salt (1.6 g)
PVDF-HFP-KFSI@PAN	PVDF-HFP (2 g), KFSI salt (1.6 g), PAN nanofibers (6 cm × 6 cm)
GF	Glass fibers (Whatman Grade GF/D, pore size: 2.7 μm)

3.1.6 Te/C or Te_xS_y/KB Cathode Preparation

Te/C composite was mixed thoroughly with super P and sodium alginate (2 wt% in aqueous solution) with a mass ratio of 7:2:1 to form a uniform slurry. Afterward, the slurry was cast onto an aluminum foil and dried at 80 ^{o}C in a vacuum oven overnight. Finally, the dried slurry was cut into 12 mm-diameter pellets and used as Te/BP2000 cathodes for coin-cell assembly. The S/C, Se/C, and Te_xS_y/KB cathodes were prepared following the same procedures as Te/C cathodes.

3.1.7 Atomic Layer Deposition of Al_2O_3 on Te/C Electrodes

The Al_2O_3 layer was coated on the Te/BP2000 cathodes via a commercial ALD reactor (GEMStar™ XT Atomic Layer Deposition Systems; Arradiance). The coating process was carried out at 100 °C by following a TMA pulse/TMA purge/H_2O pulse/H_2O purge sequence in each cycle. After 10 cycles, Al_2O_3 films are deposited on Te/BP2000 cathodes noted as Te/BP2000@$Al_2O_3$10.

3.2 Cell Assembly

All coin cell assembly mentioned in this dissertation was carried out in an argon-filled glovebox workstation with water and oxygen content less than 0.1 ppm. Cell configurations, including symmetrical cells and Te-based cells tested in this dissertation, are listed in **Table 3.2.1**.

Table 3.2.1. Cell configuration of cells tested in this dissertation.

Cell type	Anode	Cathode	Separator	Electrolytes	Working voltage (V)	Current density
Li/Li	Li	Li	GPE	GPE	NA	0.05-0.2 mA cm^{-2}
K/K	K	K	GF, GPE or CGPE	1M KFSI in EC:DEC, GPE or CGPE	NA	0.1-1 mA cm^{-2}
Liquid Li-Te	Li	Te/C	Celgard 2500	1M $LiPF_6$ in EC:DEC	1-3	0.1-5C
Quasi-solid-state Li-Te	Li	Te/C	GPE	GPE	1-3	0.1-2C
Liquid Li-Te_xS_y	Li	Te_xS_y/KB	Celgard 2500	3M LiTFSI in DEC:FEC	1-3	0.1-10 A g^{-1}
Liquid K-Te	K	Te/C	GF/D	1M KFSI or 0.8M KPF_6 in EC:DEC	0.5-3	0.1-1C
Quasi-Solid-State K-Te	K	Te/C	CGPE	CGPE	0.5-3	0.1C

1C equals to 420 mA g^{-1}.

3.3 Materials Characterizations

Appropriate analytical techniques are indispensable to gain insights into electrodes, electrolytes, and interfaces inside a battery. This section will introduce morphology, structure characterizations, and battery evaluation methods used in this dissertation.

3.3.1 Morphology Investigation

When electrons hit a sample, there are several possible interactions. Suppose part of the energy is transferred from the incident electrons to the sample (inelastic interaction). In that case, it will cause several signals, such as auger electrons, secondary electrons, backscattered electrons, and characteristic X-rays. These detected signals could be utilized to obtain information about the morphology, composition, and structure of materials.

3.3.1.1 Scanning Electron Microscopy and Energy Dispersive Spectroscopy

Scanning electron microscopy (SEM) produces images through the interaction of an electron beam and constituent atoms on the surface of the sample. As an SEM test starts, secondary electrons or backscattered electrons emitted from the sample are detected to create images of the surface. Energy dispersive spectroscopy (EDS) is usually combined with the SEM technique to identify the elemental composition in the scanned area. Magnification and acceleration voltage are critical parameters in SEM tests. Deposition of platinum or gold coating layer is usually needed for polymer materials in advance.

3.3.1.2 Transmission Electron Microscopy

Transmission electron microscopy (TEM) images are formed by the transmitted electrons through the targeted sample. When the incident electron beam interacts with the sample, scattered electrons are blocked by the objective aperture. Only direct electrons are able to pass through the hole in the center of the objective aperture and contribute to the final image. High-resolution transmission electron microscopy (HRTEM) is a nanoanalytical technique to study the nanoscale properties of materials. In HRTEM, a parallel incident electron beam (wave) hits the sample, and interference occurs. In particular, lattices or fringes could be observed for crystalline materials in HRTEM mode.

3.3.1.3 Micro X-ray Computed Tomography

Micro X-ray computed tomography (MicroXCT, Xradia Inc.) was used to obtain the three-dimensional (3D) structure of the PVDF-HFP-KFSI@PAN membrane that will discuss in Chapter 9. The sample was cut into 0.5 × 0.5 cm and held on the sample stage of MicroXCT (**Figure 3-1**). During imaging, the sample was rotated while being irradiated by an X-ray beam. Radiographs of the X-ray beam passing through the sample were kept being recorded to create 2D projection images, which were then filtered and processed into 3D images using Avizo™Fire software with a voxel size of 1.25 μm^3.

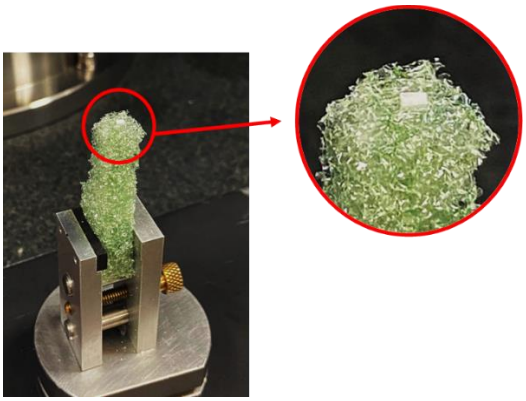

Figure 3.3.1. Digital photo of sample preparation holder for X-ray tomography.

3.3.2 Structure Analysis

3.3.2.1 X-ray Diffraction

X-ray diffraction (XRD) is an essential structural characterization technique for crystalline materials. As the incident X-ray beam hits the sample, elastic scattering of the incident X-ray with the sample occurs in the periodic lattice. Suppose the scattered X-rays are in phase, and incident angle θ, interplanar distance d, and wavelength λ satisfy Bragg's law ($n\lambda = 2d\sin\theta$). In that case, constructive interference will happen, and the diffracted X-rays will be detected and recorded. XRD pattern is an essential technique for identifying an unknown material or analyzing the crystal structure of given materials.

3.3.2.2 X-ray Photoelectron Spectroscopy

X-ray Photoelectron Spectroscopy (XPS) is a widely used surface analysis technique with a depth of less than 10 nm. By exciting the sample surface with mono-energetic Al kα X-rays, photoelectrons would be emitted from the surface and the energy of the emitted photoelectrons would be measured by an electron energy analyzer. The elemental identity, chemical state, and quantity can be determined based on the binding energy and intensity of a photoelectron peak. XPS is a helpful tool for compositional analysis of SEI layer on the electrode surface, which would gain a better understanding of surface chemistry on Te/C electrodes in this dissertation.

Especially, XRD and XPS are preferred to integrate to identify possible reaction products if the reaction mechanism is unclear. Here are the operational procedures to reveal potential reaction

pathways in a K-Te cell. The K-Te batteries at different charge/discharge states (0.5V, 1.3V, 1.9V, 3V) were disassembled in the argon-filled glove box and rinsed with the DEC solvent to remove the electrolyte and salt residuals. After being dried in the glove box overnight, the electrodes were placed in a sealed bag for further SEM, XRD, and XPS characterizations.

3.3.2.3 Pore Structure Characterization

Carbon pore structure is of vital importance to trap Te molecules and accommodate their volume changes. Numerous pores could offer sufficient loading sites for Te, which is also favorable for fast electron transfer and electrolyte infiltration. The pore size should also be paid attention to as large pores are unable to confine Te molecules effectively and might cause capacity fading in long-term tests. Nitrogen adsorption/desorption isotherm is used for collecting pore structure information of carbons (pore volume and pore size distribution). Specific areas can be determined by Brunauer-Emmett-Teller (BET) calculation method.

3.3.2.4 Tensile Strength

Good tensile strength is necessary for polymer electrolytes to resist continuous Li or K dendrites piercing and ensure a long lifetime of solid-state batteries. In Chapter 9, tensile testing was carried out for PVDF-HFP-KFSI and PVDF-HFP-KFSI@PAN with an elongation rate of 0.02 cm s^{-1} at room temperature. The data was collected to plot stress-strain curves.

3.3.3 Electrochemical Characterization

Electrochemical performance can also provide critical information about reaction mechanisms, which are essential for researchers to study the internal electrochemical process deeply. The most commonly used methods include cyclic voltammetry, electrochemical impedance spectroscopy, charge/discharge profiles, cycling stability, and rate capability.

3.3.3.1 Cyclic Voltammetry

Cyclic voltammetry (CV) is an electrochemical technique in which the potential of the working electrode increases linearly versus time to the end potential. Then the potential continues changing in the opposite direction until it returns to the initial potential. The difference between anodic and cathodic peaks represents the reversibility of the electrode. If the electron transfer on the surface

of the electrode is fast enough, then the current will be mainly limited by the diffusion of the active species. In this case, the peak current is proportional to the square root of the scan rate following the Randles-Sevcik equation [110]:

$$I_p = 2.69 \times 10^5\, n^{3/2} A D^{1/2} v^{1/2} C = B \times v^{1/2} \qquad \text{Eq. 3.1}$$

where I_p is the peak current, n is the number of electron transfer, A is the effective reaction area, D is the ion diffusion coefficient, v is the scan rate, C is the K-ion concentration, and B is the slope of the fitted I_p-$v^{1/2}$ curves. The Li-ion or K-ion diffusion coefficients of Te/C electrodes could be calculated from the fitted I_p-$v^{1/2}$ curves. Higher Li^+ diffusivity reflects faster Li^+ migration and better reaction activity of the electrode materials.

3.3.3.2 Electrochemical Impedance Spectroscopy

Electrochemical impedance spectroscopy (EIS) is a valuable tool for measuring the impedance of the electrochemical system when a small alternating current potential wave is applied. The impedance, defined as the ratio of potential to current, is continuously dynamic with the frequency of the wave. The EIS result recorded in the Nyquist plot helps analyze the electrochemical process in Li-Te batteries. Generally, the electrochemical process on the electrode is comprised of three parts: the resistance of the electrolyte and electrode (R_Ω), double-layer capacitance (C_d), and Faraday impedance (Z_f). As the charged ions (non-active ions) from the electrolyte are adsorbed on the surface of the electrode, the charge distribution on the surface changes and the surface possesses the opposite charges. These two layers are separated by space caused by charge interaction. The impedance is defined as double-layer capacitance C_d. Charge and mass transfer are not involved in this process. Faraday impedance resulted from the transfer of active species and charge can be divided into charge transfer impedance (R_{ct}) and mass transfer impedance (Z_w). Each resistance could be simulated by a corresponding equivalent circuit model. By measuring the EIS spectra before and after the cycling/rate test, the interfacial resistance between electrode and electrolyte could be determined, which is a critical parameter for both liquid-based and solid-state batteries.

EIS is also utilized to obtain the ionic conductivity of polymer electrolytes. Here are the procedures. The ionic conductivity (σ) of GPE is tested in an assembled symmetrical cell in which the GPE was sandwiched between two stainless steel (SS) pallets. The conductivity is calculated by Eq. 3.2:

$$\sigma = \frac{L}{RA} \qquad \text{Eq. 3.2}$$

where *L* and *A* are the thickness and effective area of the GPE, and R is tested by electrochemical impedance spectroscopy (EIS) with the frequency range of 0.1-1M Hz under 5 mV AC amplitude. The ionic conductivities of the GPE at various temperatures (from RT to 70 ^{o}C) were tested to calculate the activation energy (E_a), which is expressed in Eq. 3.3:

$$\sigma = Ae^{-\frac{E_a}{RT}} \qquad \text{Eq. 3.3}$$

where *A* and *R* represent the pre-exponential factor and gas constant (J mol^{-1} K^{-1}), respectively.

3.3.3.3 Battery Performance Evaluation

Take the example of Li-Te cells. The Li-Te battery performance is tested at the voltages of 1-3V using NEWARE battery workstation. Each cycle consists of discharge and charge processes with a constant current mode. During discharge process, the hexagonal Te is converted to cubic Li_2Te when the cell is discharged to 1V (versus Li^+/Li). The charge process corresponds to its reverse reaction from Li_2Te to Te. The current density is determined by the mass of Te on the Te/C electrode (1C = 420 mA g^{-1}). The major electrochemical performance involves specific capacity, Coulombic efficiency (CE), cycling, and rate performance. CE is defined as the ratio of charge capacity to discharge capacity in the same cycle, and it represents the fraction of the available capacity for the following discharge process.

A cycling test is necessary to evaluate the electrochemical stability of electrode materials over long-term cycles. Each cycle takes different hours depending on the applied current density. For example, Te/C cathodes tested at 0.1C take 20 hours to complete one full cycle. As for symmetrical Li/Li or K/K cells, a full cycle is composed of 1-hour discharge and 1-hour charge steps. In this dissertation, the cycle numbers of as-prepared Te or TeS cathodes were recorded at different current densities to assess their durability. High CE in the cycling test also suggests the outstanding

stability of the cathode. The rate capability reflects the reaction kinetics of the specific electrode materials at various current densities.

3.3.4 DFT Simulation

First-principles simulations were performed using the plane-wave implementation of the approximate Kohn-Sham density-functional theory (KD-DFT) using semi-local electronic exchange-correlation within the Quantum ESPRESSO (QE) software [111-117]. The preliminary simulations were performed using the virtual-crystal approximation (VCA), which was used to linearly mix to the pseudo-potential of Te and S to obtain the virtual atoms, denoted by Te_xS_y with the atomic fractions of x = 0.125, 0.25, 0.375, 0.5, 0.625, 0.75, 0.875, and x + y = 1. The virtual atoms were used expediently, representing the random solid solution of Te and S. In the interest of relevance and robustness, the configurationally resolved simulations on the S_8 and Te_1S_7 were performed to accurately analyze Li redox kinetics.

3.4 Chapter Summary

This chapter clarifies the main morphology, structure, and electrochemical characterization techniques used in this dissertation. These techniques are usually integrated to reveal the structural properties of materials and elucidate their working mechanisms. With the help of these methods, insightful mechanistic studies are undertaken and discussed in the following chapters.

It is noteworthy that all experimental parameters should be precisely controlled to establish a standard protocol for materials preparation and battery evaluation. For example, during the synthesis of gel polymer electrolytes, the mixing ratio of each component, stirring time, and heating temperature should be the same for each preparation process. Besides, at least three samples should be tested under the same conditions to ensure good data reproducibility and reliability.

Chapter 4 Te/C Cathode Structure for Li-Te Batteries

4.1 Introduction

As summarized in Chapter 2, Te with superior electronic conductivity (2×10^{2} S m^{-1}) is promising electrode material for next-generation lithium batteries compared to less conductive S (5×10^{-16} S m^{-1}) or Se (1×10^{-4} S m^{-1}). This remarkable conductivity promises Te cathode fast kinetics and high utilization of active species during the lithiation/delithiation process [52]. Moreover, the high volumetric capacity (2621 mAh cm^{-3}) of Te, as a result of its high density (6.24 g cm^{-3}), is preferable for devices with limited space, such as wearable sensors, medical implants, etc., and makes Te stand out as promising electrode material [118].

However, pure Te electrodes without support materials only delivered a specific capacity of 280 mAh g^{-1} during the first discharge process and suffered from rapid capacity decay, which resulted from Te pulverization caused by the massive volume change (204%) between Te and Li_2Te transition during the repeated charge-discharge process [50, 69]. One effective approach to address this issue is to confine Te into porous carbon *via* a melting diffusion method. Recently, various carbon materials have been synthesized and applied to provide Te loading sites. Liu *et al.* [46] encapsulated Te into porous carbon, and the Te/C electrode retained 224 mAh g^{-1} at 50 mA g^{-1} after 1,000 cycles. He *et al.* [47] prepared a free-standing cathode comprised of Te nanowires and reduced graphene oxide for Li-Te batteries, which maintained 270 mAh g^{-1} after 500 cycles at 1 C. Nanoporous carbon polyhedra doped with cobalt and nitrogen was developed as a highly conductive and porous matrix for Te, contributing to a prominent rate capacity of 2160, 1327.6, and 894.8 mAh cm^{-3} at 4, 10, and 20 C, respectively [53].

Currently, carbon materials with various pore sizes (micropores, mesopores, and macropores) have been reported to act as Te hosts in Li-Te batteries, and the prepared Te/C cathode exhibited a range of electrochemical performance [46, 69, 73, 119]. It is clear that the performance of Te/C cathode highly depends on the carbon structure, especially pore size. However, the effect of the carbon pore structure on the performance of cathode materials in Li-Te batteries has rarely been studied. Clarification on the correlation between carbon pore structure and Te cathode properties is an urgent task in order to develop high-capacity Li-Te batteries.

Inspired by previous studies, this work investigates the effect of porous carbon on the performance of Te/C electrodes in Li-Te batteries and develops durable Te/C cathodes for liquid electrolyte based Li-Te batteries. Two types of commercialized carbon materials (ASAC25 and ASAC30) and lignin-derived activated carbon with different pore structures were applied to encapsulate Te *via* the melt-diffusion method. This chapter can be broadly divided into the following sections.

(1) Effect of carbon pore structure on the performance of Te/C cathodes

The morphology and structure of the two Te/C electrodes (ASAC25-Te and ASAC30-Te) are investigated by SEM, TEM, EDS, BET, XRD, and XPS techniques. SEM and TEM results suggest uniform Te distribution in the ASAC25 matrix, while bulky Te could be observed in ASAC30-Te. XPS results show that stronger interaction exists between Te and ASAC25, which is due to the complete infiltration of Te in micropores and the larger contact area between Te and ASAC25.

Cycling test results reveal that microporous ASAC25 is able to effectively confine Te into a porous skeleton and maintain superior structural stability, resulting in an ultrahigh discharge capacity of 429.6 mAh g^{-1} after 100 cycles at 0.1 C. In comparison, ASAC30 with both micropores and mesopores only remains 107.2 mAh g^{-1} when used as the Te host. The remarkable cycling stability of ASAC25-Te could be attributed to the effective encapsulation of Te into micropores and strong Te-C interaction, thus buffering large volume expansion and subtraction over long-lasting cycling.

It is also found that the cycled ASAC30-Te cathode has increased charge transfer and evident cracks on the electrode surface, which implies the pulverization and loss of active materials along with repeated lithiation and de-lithiation behaviors. The inferior electrochemical performance of ASAC30-Te is mainly due to the gradual dissolution of bulky Te into electrolytes over cycles, causing the rapid capacity decline in Li-Te batteries.

(2) Effect of Te content on the performance of Te/C cathodes

Moreover, the effect of Te content on the electrochemical performance of Te/C electrodes is also studied. Our results suggest that partial infiltration of Te into the carbon host is required to suppress massive volume expansion and achieve excellent electrochemical stability during the discharge process.

(3) Durable Te/C cathodes with biomass-derived porous carbons as Te host

Additionally, the abundant lignin is used as a precursor to synthesize porous carbons with customized pore structures. These activated carbons are utilized as Te hosts to investigate the electron transfer and Li-ion conduction mechanism in different Te/C structures. The optimized Te/C electrode delivers a reversible capacity of 418 mAh g^{-1}, high capacity retention of 90% after 100 cycles, and exceptional cyclability over 1000 cycles at 2 C.

4.2 Effect of Carbon Pore Structure on the Performance of Te/C Cathodes

4.2.1 Structural Analysis of Te/C Composites with Micro/Mesoporous Carbons

In order to clarify the effect of carbon pore structure on the performance of Te/C cathodes, two types of porous carbon (ASAC25 and ASAC30) are used for preparing Te/C cathodes *via* the melt-diffusion method. **Figures 4.2.1a-b** present the nitrogen adsorption-desorption isotherms and pore size distribution of ASAC25 and ASAC30. ASAC25 exhibits a typical type-I adsorption-desorption isotherm, which is indicative of mainly microporous feature of the carbon material [120]. In contrast, ASAC30 possesses mixed adsorption-desorption isotherms of both type I and type VI, suggesting the co-existence of both micropores and mesopores in the carbon structure [121]. This can be further confirmed by the pore-size distribution curves in **Figure 4.2.1b**. **Figure 4.2.1b** shows that the majority of pores for ASAC25 are below 2 nm (as highlighted by the blue shadow), while ASAC30 has a much larger proportion of mesopores (pore size: 2 - 6 nm, as highlighted by the pink shadow) than ASAC 25. The specific surface area is determined to be 2345.3 and 2403.1 m^2 g^{-1} by Brunauer-Emmett-Teller (BET) analysis, and the pore volume is 1.15 and 1.50 cm^3 g^{-1}, for ASAC25 and ASAC30, respectively (**Table 4.2.1**). Figures 1a and 1b clearly indicate that ASAC25 mainly consists of micropores, while ASAC30 is comprised of both micropores and mesopores.

Figure 4.2.1c illustrates the XRD patterns of as-received ASAC25 and ASAC30, ASAC25-Te, and ASAC30-Te. ASAC25 and ASAC30 show a broad diffraction peak at 21.0°, corresponding to the (101) plane of graphite (JCPDS PDF No. 75-2078). In contrast, the ASAC25-Te composite merely has one broad characteristic peak at 27.6°, corresponding to (011) plane of crystalline Te (JCPDS PDF No. 79-0736). The disappearance of sharp Te diffraction peaks and the broadened

(011) peak in ASAC25-Te suggest the good dispersion of Te into the micropores of ASAC25 [70]. In sharp contrast, the ASAC30-Te composite shows all strong diffraction peaks of hexagonal Te powders, indicating that Te partially diffuses into ASAC30, and there is still some large Te left outside of the pores. This might be due to the difference of micropores and mesopores in the capillary force for Te infiltration into the carbon hosts with different pore sizes.

XPS characterization was carried out to confirm further the existence of Te in the ASAC25 and ASAC30 carbon hosts. The full spectra for ASAC25-Te and ASAC30-Te in **Figure 4.2.2** reveal that the Te element exists in both Te/C composites. **Figure 4.2.1d** compares Te 3d XPS spectra of ASAC25-Te and ASAC30-Te. For ASAC25-Te, the two peaks at 573.9 eV (Te $3d_{5/2}$) and 584.3 eV (Te $3d_{3/2}$) are assigned to Te-Te bond originating from the metallic Te in the composite, while another two peaks at 576.1 eV (Te $3d_{5/2}$) and 586.5 eV (Te $3d_{5/2}$) correspond to the Te-O bond, which is due to a small amount of TeO_2 formed on the surface of the ASAC25-Te composite [16]. For ASAC30-Te, the Te 3d spectra can be well resolved into Te-Te and Te-O bonds as well. One notable difference between ASAC25-Te and ASAC30-Te is the higher binding energy for Te-Te bond in the former than in the latter. The peaks of Te-Te bonds for the ASAC30-Te shift to 573.3 eV (Te $3d_{5/2}$) and 583.6 eV (Te $3d_{3/2}$). The slightly increased binding energy indicates a charge-deficient state of Te during its interaction with a carbon host that possesses higher electronegativity [53, 70]. Since the main structural difference in ASAC25 and ASAC30 is the pore distribution, it is reasonable to believe that Te confined in the microporous carbon (ASAC25) has a stronger Te-C interaction than Te confined in the mixed micropores and mesopores (ASAC30). The stronger Te and C interaction in ASAC25-Te is expected to achieve more effective confinement of active materials (Te and Li_2Te), thus preventing them from dissolution into the carbonate electrolyte in Li-Te batteries.

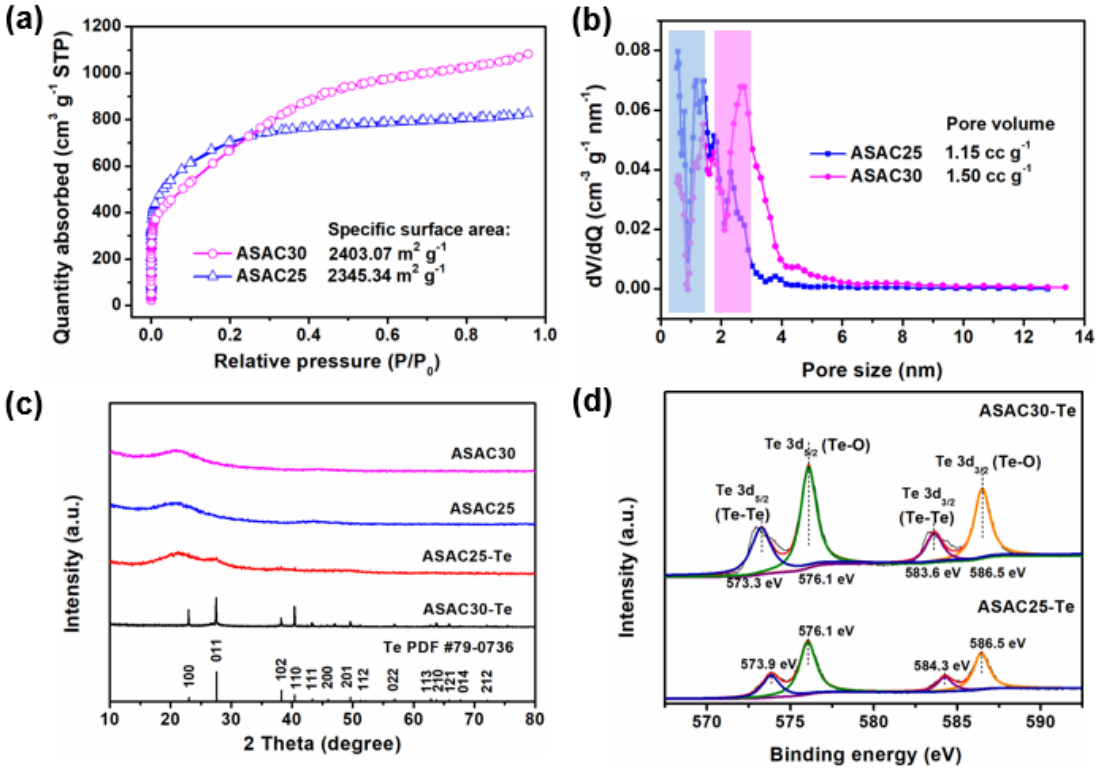

Figure 4.2.1. (a) Nitrogen adsorption-desorption isotherms and (b) pore-size distribution of ASAC25 and ASAC30, (c) XRD patterns of ASAC25, ASAC30, ASAC25-Te and ASAC30-Te, in comparison to standard Te powders (JCPDS PDF # 79-0736), and (d) Te 3d XPS spectra of ASAC25-Te and ASAC30-Te.

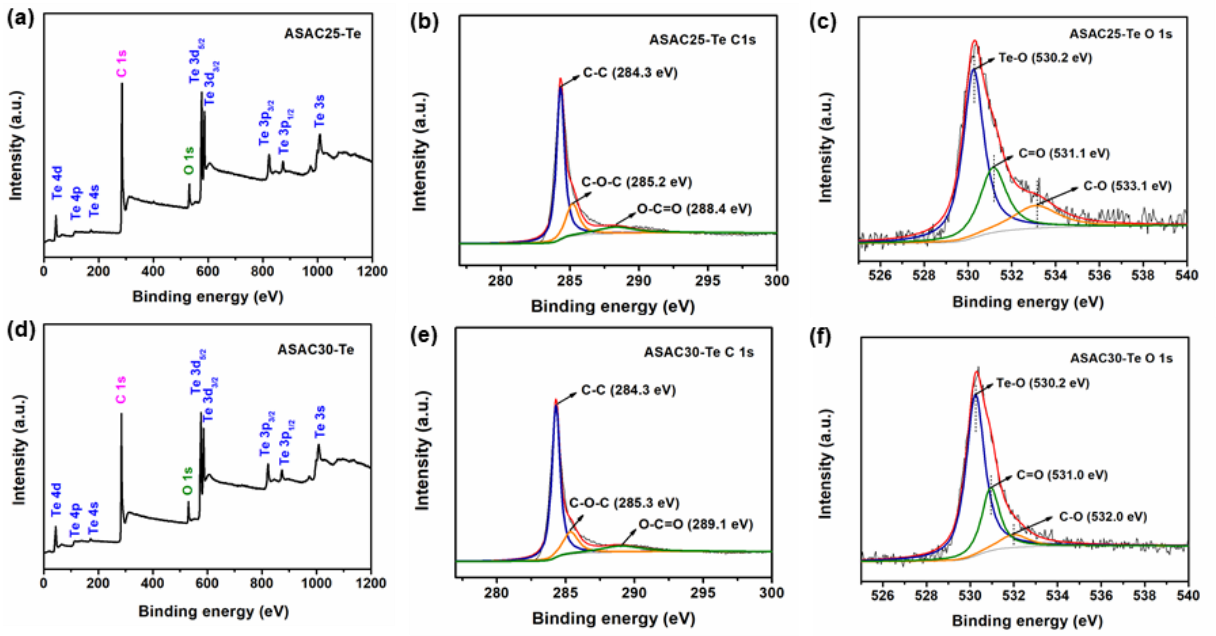

Figure 4.2.2. (a) XPS full spectra, (b) C 1s spectra and (c) O 1s spectra of ASAC25-Te, (d) XPS full spectra, (e) C 1s spectra, and (f) O 1s spectra of ASAC30-Te.

Table 4.2.1. Pore structures of ASAC25 and ASAC30.

	Surface area (m^2 g^{-1})	Pore volume (cm^3 g^{-1})	Average pore size (nm)
ASAC25	2345.3	1.15	0.6
ASAC30	2403.1	1.50	2.6

4.2.2 Morphology Investigation of Te/C Composites with Micro/Mesoporous Carbons

The morphologies of the porous carbon and Te/C composites are shown in **Figure 4.2.3**. It can be seen that ASAC25 and ASAC30 powders have similar porous and interconnected structures (**Figures 4.2.3a-b**), which are beneficial for electrolyte wetting in Li-Te batteries. After Te impregnation, ASAC25-Te and ASAC30-Te show no noticeable morphological change compared to ASAC25 and ASAC30. EDS mapping (**Figure 4.2.3c**) reveals the uniform distribution of Te

and C elements in ASAC25-Te. However, Te agglomerates in some parts of ASAC30-Te show inhomogeneous distribution (**Figure 4.2.3d**).

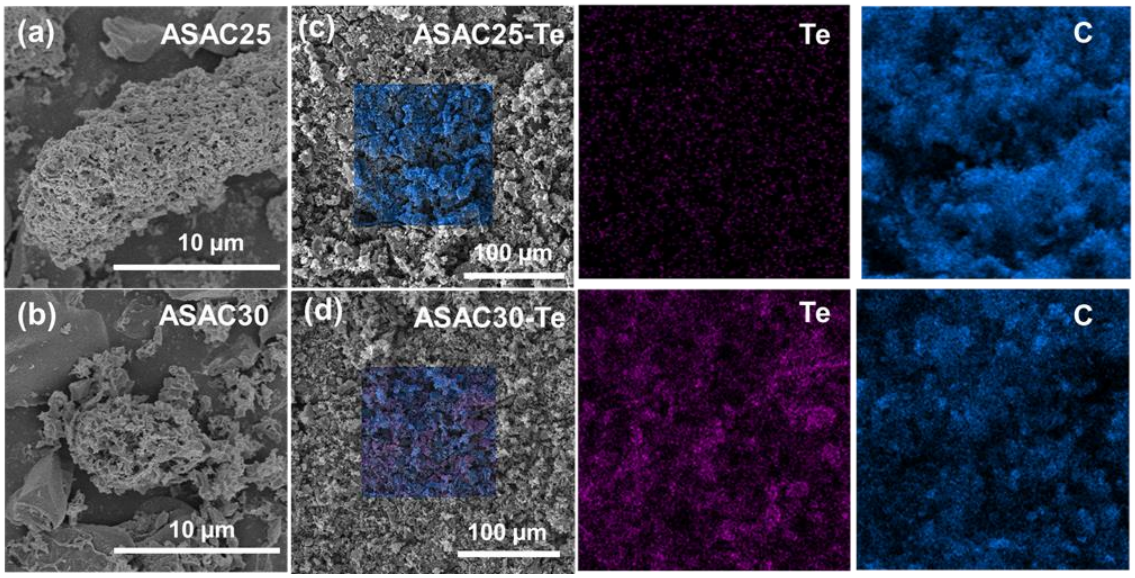

Figure 4.2.3. SEM images of (a) ASAC25, (b) ASAC30, (c) ASAC25-Te, and (d) ASAC30-Te with EDS mapping of Te and C elements.

Figure 4.2.4 shows the morphology and elemental distribution of ASAC25-Te and ASAC30-Te on a smaller length scale. As shown in **Figures 4.2.4 a-c**, ASAC25-Te has an amorphous structure consistent with its XRD pattern (**Figure 4.2.1c**). However, ASAC30-Te showed much more crystalline Te with sizes around 3-10 nm than ASAC25-Te. Lattice fringes could be observed in ASAC30-Te (**Figure 4.2.4f**). The lattice spacing of 0.32 nm corresponds to the (011) plane of the hexagonal tellurium. The strong diffraction peaks in the XRD and STEM-EDS (**Figure 4.2.5**) together suggest the existence of large Te in ASAC30-Te, probably due to incomplete infiltration of Te in ASAC30-Te. The minor O element is detected in ASAC25-Te and ASAC30-Te (**Table 4.2.2**), consistent with XPS spectra. From the above results, Te is confined in both micropores and mesopores in ASAC30-Te with larger sizes and also exists as bulky Te. As a result, the contact surface between ASAC30 carbon and Te is smaller than that in ASAC25-Te. The effect of electronegative carbon host on the state of Te-Te bond is less in ASAC30-Te than in ASAC25-Te. Therefore, the Te and C interaction in ASAC25-Te is more substantial than that in ASAC30-Te. The different pore structure of ASAC25 and ASAC30 results in the difference in Te impregnation

in Te/C composites. Microporous carbon is favorable over mesoporous carbon in promoting Te infiltration into the carbon host by the melting diffusion method. Moreover, carbon pore size also affects the structure of Te in the carbon host, i.e., amorphous Te in ASAC25 and crystalline Te in ASAC30. According to previous studies in Li-S and Li-Se batteries, the existing form of S or Se is mainly influenced by the porous structure of carbon host materials [34, 122]. The smaller pore size might lead to stronger interaction potential between active materials and carbon matrix and trap S or Se in a highly dispersed state [123-127]. Therefore, S or Se molecules confined in such pores exist in the form of an amorphous state. The disappeared crystalline Te peaks in Te/C composite are also reported in the literature [70].

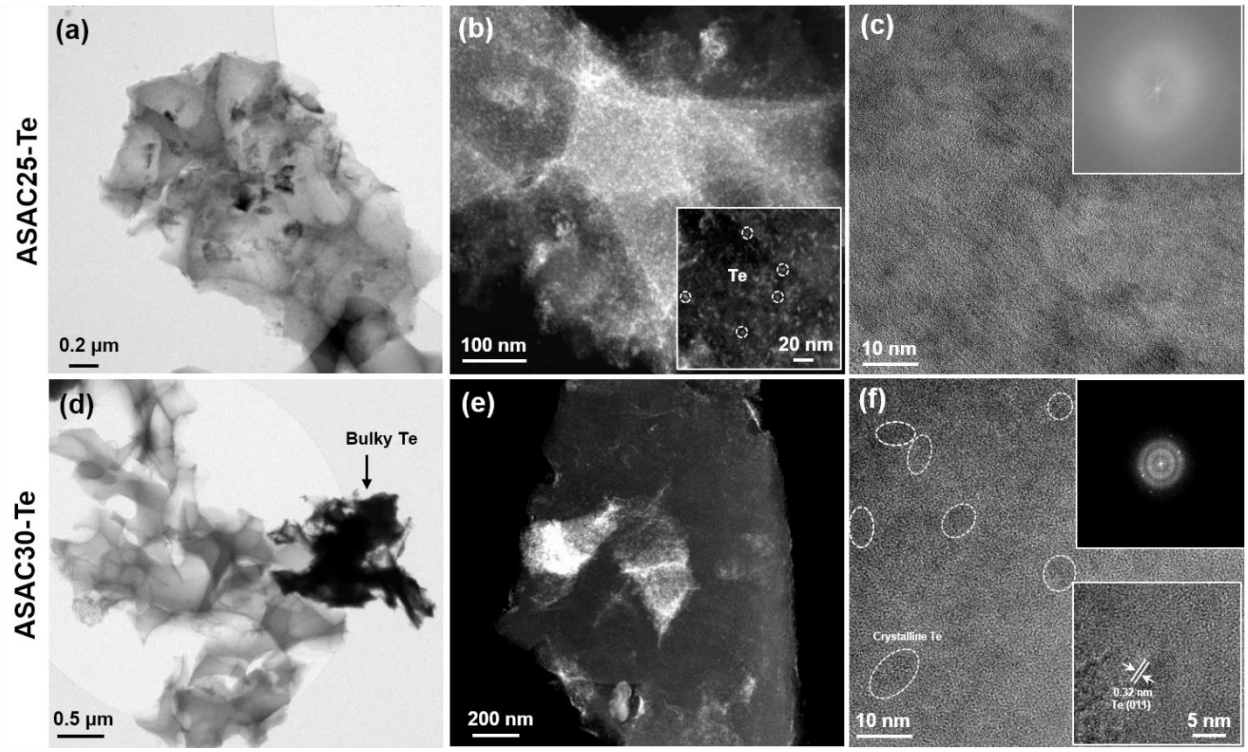

Figure 4.2.4. (a, d) TEM, (b, e) STEM, and (c, f) HRTEM images for (a-c) ASAC25-Te and (d-f) ASAC30-Te. Inserts on the right top corners of (c) and (f) correspond to fast Fourier transform (FFT) patterns. Insert on the bottom right corner of (f) is an enlarged HRTEM image.

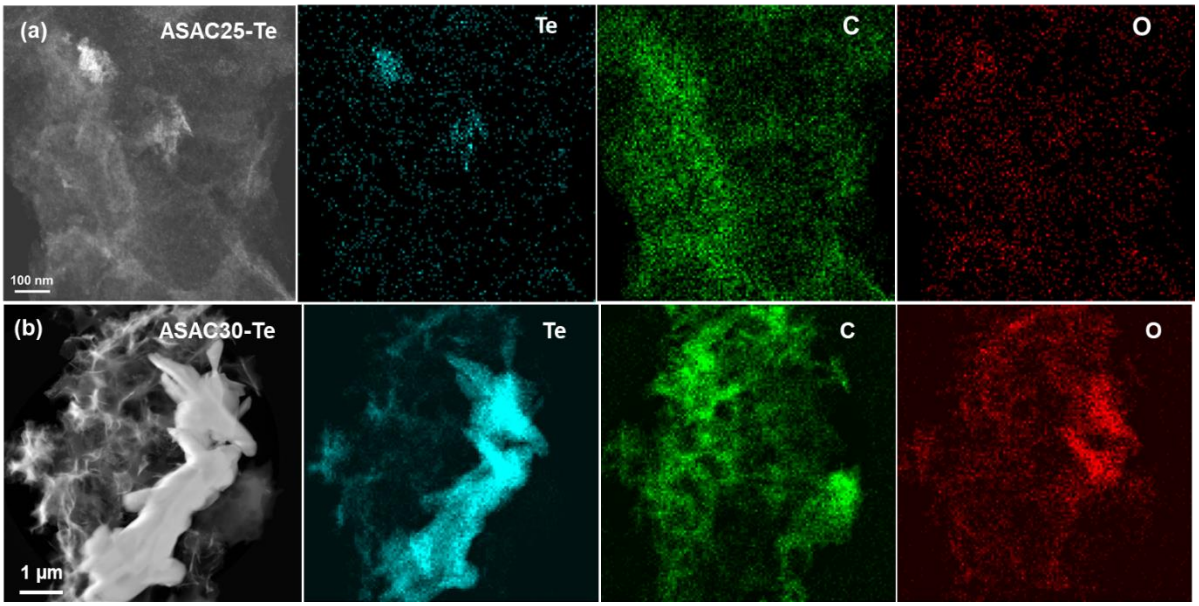

Figure 4.2.5. STEM image and EDS mapping of (a) ASAC25-Te and (b) ASAC30-Te.

Table 4.2.2. EDS elemental analysis of ASAC25-Te and ASAC30-Te composites.

Electrodes	Status	Elemental composition (wt%)		
		Te	C	O
ASAC25	Before cycling	49.3	48.2	2.5
ASAC30	Before cycling	57.1	40.7	2.1

4.2.3 Cycling and Rate Performance of Te/C Cathodes with Micro/Mesoporous Carbons

The electrochemical performance of ASAC25-Te and ASAC30-Te electrodes are evaluated in Li-Te batteries using Li metal as the counter electrode. TGA analysis reveals that Te contents in ASAC25-Te and ASAC30-Te are 49 wt% and 56 wt% (**Figure 4.2.6**), respectively.

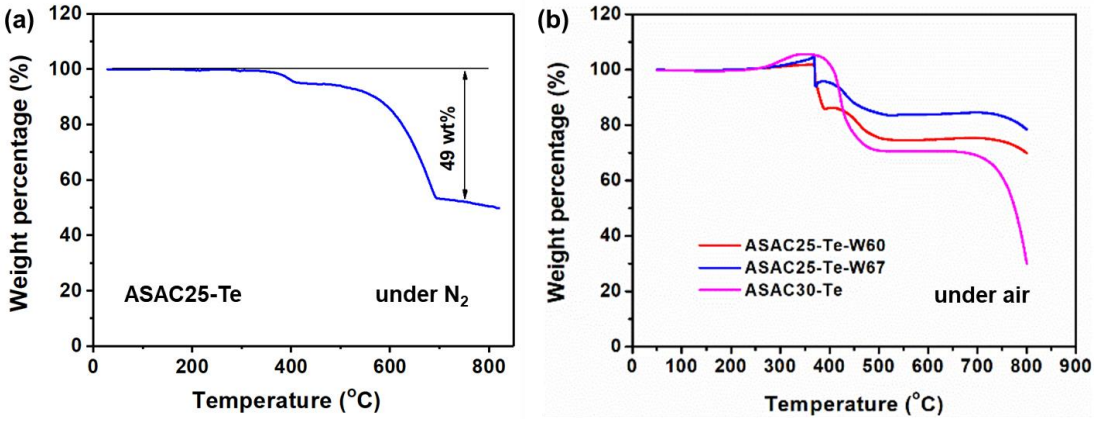

Figure 4.2.6. TGA curves of Te/C composites measured in (a) N_2, and (b) the air.

Te condensation under air in the TGA equipment was observed when the TGA experiments were performed on the Te/C composites under an inert environment (N_2 or Ar). Thus, all the Te/C composites were analyzed by TGA in the air to burn the carbon and leave Te as TeO_2 in the ceramic pan. The TGA data were analyzed following a paper using the same procedure, and the Te content was determined by using the following equation [46]:

Te (wt%) = (molecular weight of Te)/molecular weight of TeO_2 × (final weight of TeO_2/initial weight of Te/C) × 100 Eq. 4.1

The cycling performance of the pure Te electrode is also tested as a comparison (**Figure 4.1.7**). The Te-only electrode shows a low initial specific capacity of 130 mAh g^{-1} at 0.1C, followed by a rapid capacity decline over the subsequent 20 cycles.

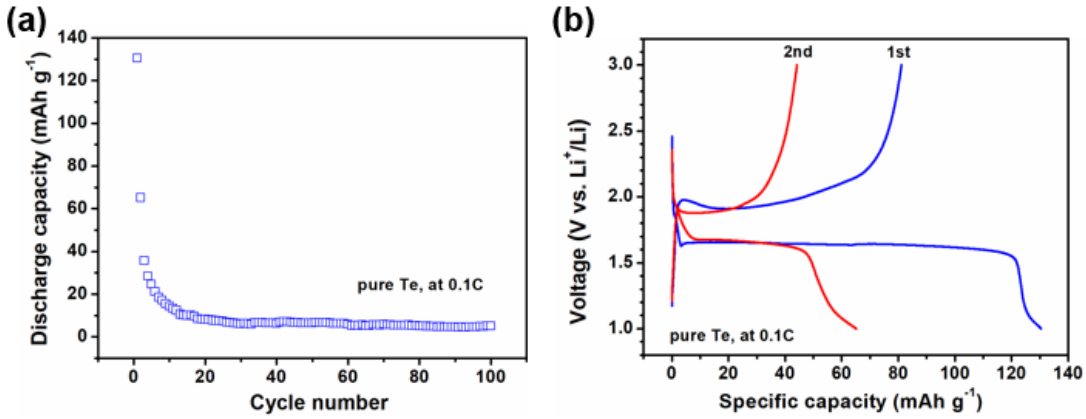

Figure 4.2.7. Electrochemical performance of pure Te electrode.

As shown in **Figure 4.2.8a**, ASAC25-Te cathode exhibits a discharge capacity of 687.9 and 500.6 mAh g^{-1} in the first and second cycles, respectively, exceeding Te's theoretical specific capacity (420 mAh g^{-1}). The possible capacity contribution of ASAC25 and ASAC30 is also tested under the same current as Te-ASAC25 or ASAC30-Te. Considering the weight percentage of carbon, ASAC25 and ASAC30 only delivered about 19 mAh g^{-1} in ASAC25-Te and ASAC30-Te electrodes. Hence, the specific capacity of the Te/C cathodes is primarily provided by Te, which is demonstrated in **Figure 4.2.9**. The extra capacity above 420 mAh g^{-1} is probably due to Li storage adsorption on electrolyte-Te/C interface [72]. The large irreversible capacity in the first two cycles could be due to the decomposition of electrolyte and the formation of solid electrolyte interphase (SEI) on the Te/C cathode [46]. ASAC25-Te exhibits stable cycling performance and maintains a specific discharge capacity of 429.6 mAh g^{-1} with a capacity retention of 85.8% after 100 cycles. In comparison, the specific capacity of ASAC30-Te is only relatively stable at around 420.0 mAh g^{-1} in the first 20 cycles and then undergoes rapid decay afterward. After 100 cycles, ASAC30-Te remains only a discharge capacity of 107.2 mAh g^{-1}. **Figure 4.2.8b** presents the Coulombic efficiency (CE) of ASAC25-Te and ASAC30-Te cathodes. The initial Coulombic efficiency (ICE) is 65.0% and 38.1% for ASAC25-Te and ASAC30-Te, respectively. The CE of ASAC25-Te gradually increases in the initial 5 cycles and stabilizes at around 99.3% until 100 cycles. In contrast, ASAC30-Te cathode experiences a sudden drop in CE from ~ 90% down to 80% between 10 and 50 cycles, which corresponds to the rapid capacity degradation in the cycling (**Figure 4.2.8a**). This low CE is probably due to the side reaction between bulky Te in ASAC30

and the electrolyte [50], which can be further revealed in the galvanostatic discharge-charge profiles (**Figures 4.2.8c-d**). For the first cycle, a voltage slope between 1.7 V and 1.9 V could be observed in ASAC30-Te (**Figure 4.2.10**), which could probably be attributed to the formation of the SEI layer on the Te/C cathode surface or the dissolution of bulky Te into the carbonate electrolyte.

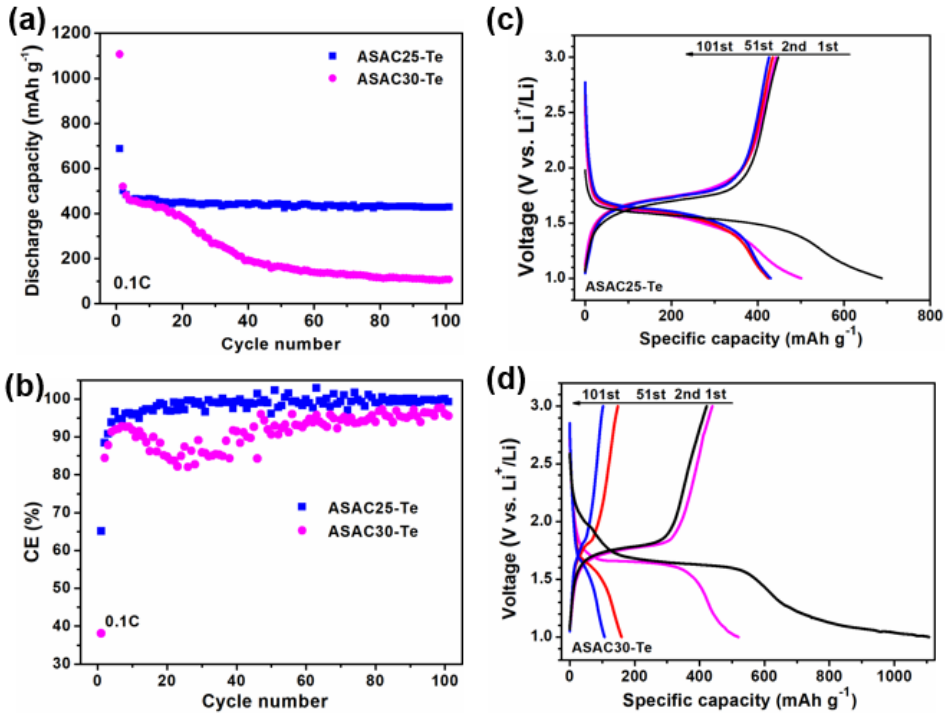

Figure 4.2.8. (a) Cycling performance and (b) Coulombic efficiency (CE) of ASAC25-Te and ASAC30-Te electrodes measured at 0.1 C (1 C=420 mA g^{-1}) in half cells using Li metal as counter electrode and 1M $LiPF_6$, EC:DEC electrolyte; charge-discharge curves of (c) ASAC25-Te and (d) ASAC30-Te in the 1st, 2nd, 51st, and 101st cycles.

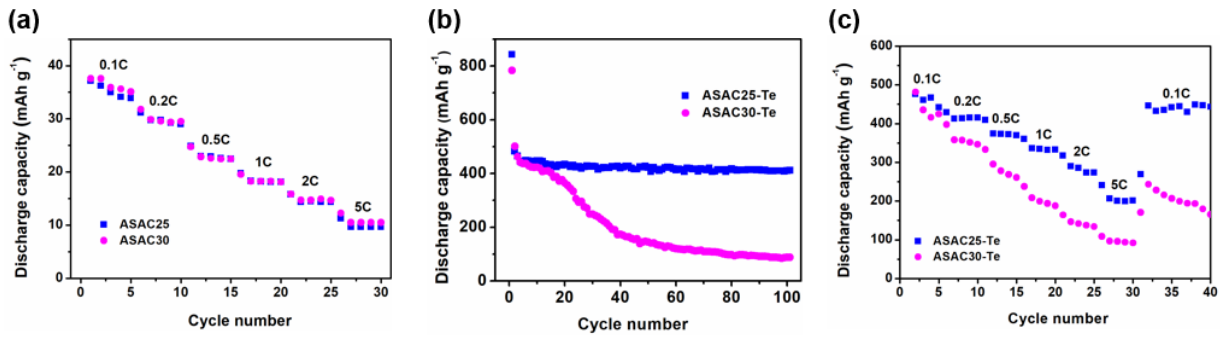

Figure 4.2.9. (a) Rate capabilities of ASAC25 and ASAC30, (1C=420 mA g_{Te}^{-1}) (b) cycling stability, and (c) rate performance of ASAC25-Te and ASAC30-Te after removing the capacity contribution of the carbon host.

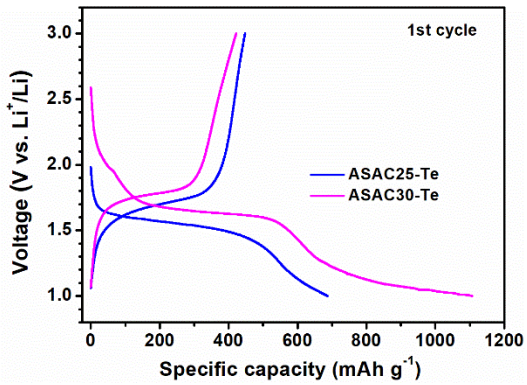

Figure 4.2.10. Charge-discharge profiles of ASAC25-Te and ASAC30-Te in the first cycle.

The CV results for ASAC25-Te in **Figure 4.2.11** show only one charge-discharge plateau at ~1.50-1.75 V, which corresponds to the one-step phase transition between Te and Li_2Te in carbonate-based electrolytes [46]. The cathodic/anodic peak potentials for ASAC30-Te have a slight shift to 1.55/1.85 V, revealing higher overpotential during the charge/discharge process. Notably, the charge-discharge profiles for ASAC25-Te are nearly overlapped from the 2nd to 101st cycle, suggesting the excellent reversibility of ASAC25-Te cathode. Moreover, the voltage difference between charge and discharge plateaus for ASAC30-Te gradually becomes larger from the 1st cycle to the 101st cycle, suggesting the increased polarization over cycling. From **Figures 4.2.8c-d**, it is clear that ASAC25 provides much more effective confinement for Te than ASAC30 does. Since the ASAC25-Te and ASAC30-Te composites have close oxygen contents, we might consider that Te-O on the surface is not the main factor responsible for the difference in the

electrochemical properties. The carbon pore structure is probably the primary cause of the performance difference. Despite the higher surface area and larger pore volume of ASAC30 than ASAC25, it can be found that micropores in the carbon host play the most crucial role in confining Te and preventing it from dissolution into the electrolyte. The dissolved Te in ASAC30-Te could diffuse to and react with Li metal anode, causing a shuttle effect and leading to the low CE (**Figure 4.2.8b**). From the above results, it can be concluded that the critical merits of the carbon hosts for Te are micropores and large pore volume.

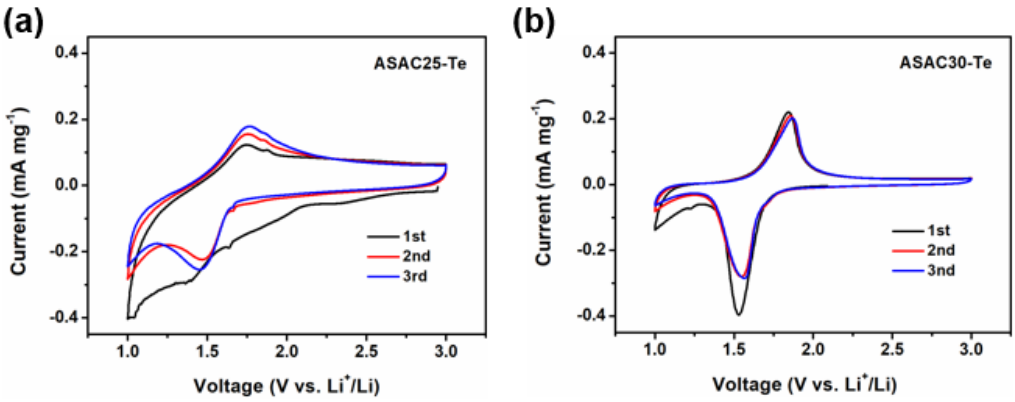

Figure 4.2.11. CV curves of (a) ASAC25-Te and (b) ASAC30-Te measured at the scan rate of 0.2 mV s^{-1}.

To figure out possible structure change of the two Te/C electrodes after 100 cycles, EIS test and *ex-situ* SEM tests of the cycled ASAC25-Te and ASAC30-Te are carried out. As shown in **Figure 4.2.12a**, the charge transfer resistance (R_{ct}) of ASAC25-Te significantly decreased after 100 cycles, which benefits from the effective confinement of active materials (Te and Li_2Te) into micropores. The surface of the cycled ASAC25-Te cathode remained flat as the pristine one (**Figures 4.2.12b-c**). By contrast, a dramatic increase of R_{ct} is found in the cycled ASAC30-Te (**Figure 4.2.12d**), which is probably due to the dissolution of Te bulks from mesopores, thus gradually reducing the utilization of active materials over long-term cycling tests. The apparent cracks on the surface of cycled ASAC30-Te (**Figure 4.2.12f**) compared to the pristine surface (**Figure 4.2.12e**) furtherly confirmed the structural instability of ASAC30-Te, which could be attributed to the ineffective confinement of Te in ASAC30 matrix. The lower Te content (**Table 4.2.3**) and peak current (**Figure 4.2.13**) in the cycled ASAC30-Te cathode also indicate the loss of active materials. The

poor electrochemical and structural stability of ASAC30-Te is probably caused by the weaker interaction between Te and the ASAC30 carbon host. In comparison, the ASAC25-Te possesses stronger Te and C interaction, which ensures effective encapsulation of Te and contributes to exceptional cycling stability [53, 70]. Therefore, micropores are more beneficial for effectively accommodating active materials and providing efficient Li^+ diffusion pathways over long-term cycling.

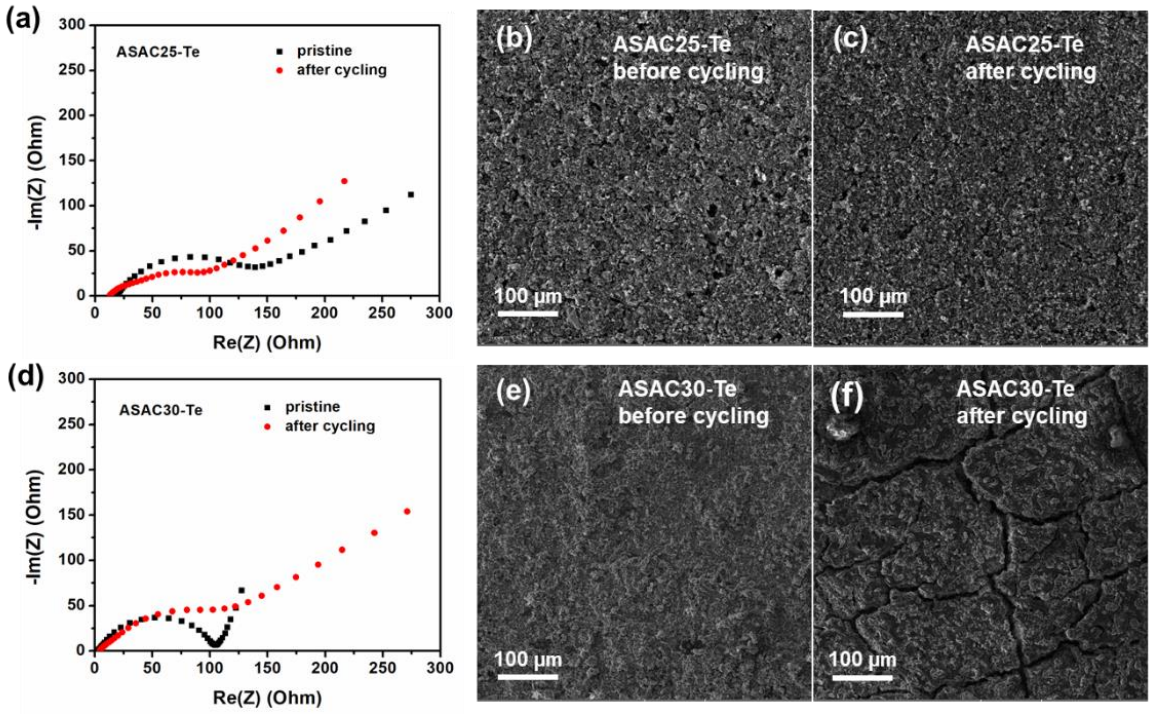

Figure 4.2.12. (a) Nyquist plots, (b-c) SEM images of pristine and cycled ASAC25-Te, (d) Nyquist plots, (e-f) SEM images of pristine and cycled ASAC30-Te.

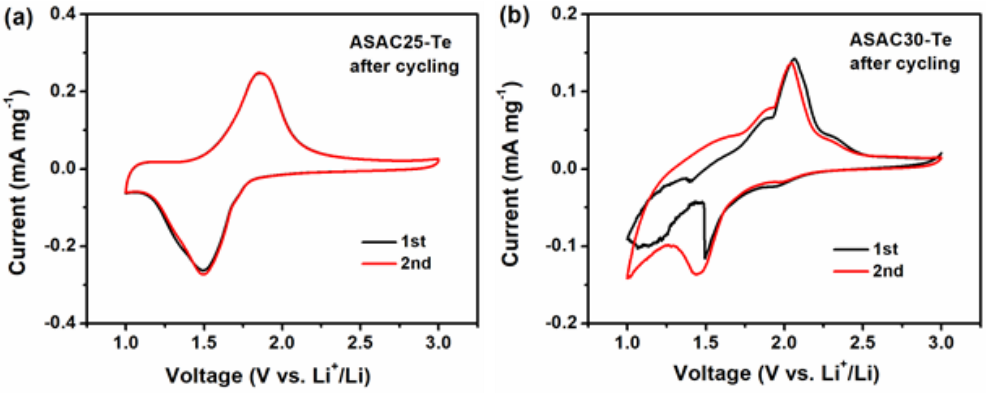

Figure 4.2.13. CV results of (a) ASAC25-Te and (b) ASAC30-Te cycled after 100 cycles.

Table 4.2.3. EDS elemental analysis of ASAC25-Te and ASAC30-Te cathodes.

Electrodes	Status	Elemental composition (wt%)			Te/C weight ratio
		Te	C	O	
ASAC25-Te	Before cycling	32.4	59.2	8.4	0.55
	After cycling	18.1	39.7	42.2	0.43
ASAC30-Te	Before cycling	31.0	62.0	7.0	0.50
	After cycling	10.5	35.2	54.3	0.30

The rate capability of the ASAC25-Te and ASAC30-Te cathodes is evaluated from 0.1 C to 5 C, and the results are illustrated in **Figure 4.2.14**. ASAC25-Te can deliver a reversible capacity of 494.9, 428.5, 384.6, 343.6, 292.8, and 205.4 mAh g^{-1} at 0.1, 0.2, 0.5, 1, 2, and 5 C, respectively. Notably, ASAC25-Te still exhibits a discharge capacity of 461.9 mAh g^{-1} once the current density is reset from 5C to 0.1 C, indicating the good stability of the ASAC25-Te cathode structure. In comparison, ASAC30-Te shows a reversible capacity of 497.8, 370.3, 288.1, 207.2, 148.2, and 100.2 mAh g^{-1} at 0.1, 0.2, 0.5, 1, 2, and 5 C, respectively. When the current density is reversed to 0.1C, ASAC30-Te can only maintain a specific capacity of 258.5 mAh g^{-1} due to the permanent loss of Te active materials during high-rate cycling. The capacity loss could be due to the

destruction of Te structure in ASAC30-Te at high current densities. Charge-discharge profiles of ASAC25-Te and ASAC30-Te at 0.2, 0.5, 1, and 2 C are compared in **Figures 4.2.14b-c**. Overall, the overpotential of ASAC25-Te at each C-rate is much smaller than that of ASAC30-Te, indicating better reaction kinetics in the former than the latter. The superior cycling and rate performance of ASAC25-Te can be ascribed to the effective confinement of active species (Te and Li_2Te) in the microporous carbon structure over repeated cycling. Moreover, the high surface area of ASAC25 can provide sufficient contact surface with the electrolyte, facilitating fast Li-ion diffusion and electron transfer. Thus, ASAC25 is chosen as the model system for further investigation of the Te content.

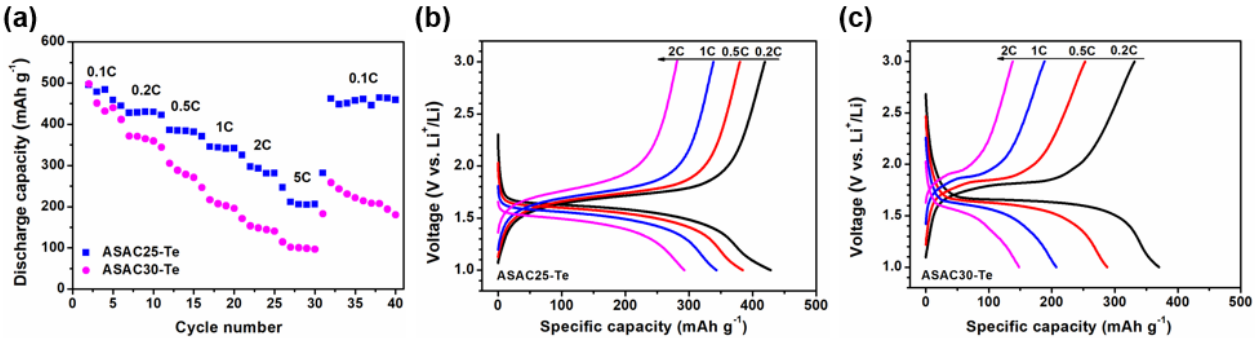

Figure 4.2.14. (a) Rate capability and charge-discharge curves of (b) ASAC25-Te and (c) ASAC30-Te electrodes measured at 0.1, 0.2, 0.5, 1, 2, and 5 C.

4.3 Effect of Te Content on the Performance of ASAC25-Te Cathodes

4.3.1 Microstructures of ASAC25-Te Composites with Various Te Content

The Te content, *i.e.*, the weight percentage of Te in Te/C cathode, is an essential parameter for practical Li-Te batteries because it determines the cells' actual energy density. Increasing Te content is necessary in order to achieve higher-energy-density Li-Te batteries. Te and ASAC25 with different mass ratios were mixed to prepare ASAC25-Te composites with varying Te contents (49 wt%, 60 wt%, and 67 wt%). ASAC25 is selected due to its superior properties in confining Te and delivering stable electrochemical performance in Li-Te batteries. The Te contents in ASAC25-Te composites are obtained by TGA analysis (**Figure 4.2.6**). **Figure 4.3.1** shows the XRD and

Raman results of ASAC25-Te composites with Te contents of 49 wt%, 60 wt%, and 67 wt%, thereafter named as ASAC25-Te-W49, ASAC25-Te-W60, and ASAC25-Te-W67, respectively. As shown in **Figure 4.3.1a**, these three ASAC25-Te composites display only one broad characteristic peak at around 27.6°, belonging to the (011) plane of crystalline Te, suggesting successful impregnation of Te into microporous ASAC25 in all the three samples. For ASAC25-Te-W60 and ASAC25-Te-W67, the (101) peak from graphite is merged into the shoulder of (011) peak of Te, due to the stronger signal from Te. The Raman spectra in **Figure 4.3.1b** show four characteristic peaks located at 160, 270, 400, and 630 cm^{-1} for crystalline Te powders. These peaks are absent in all ASAC25-Te composites due to the complete infusion of Te in ASAC25 [70]. All the ASAC25-Te composites exhibit only two peaks, D band and G band, centered at 1344 and 1592 cm^{-1}, respectively, which originate from the carbon structure of ASAC25. The above result suggests that ASAC25 provides sufficient micropores for the infiltration of Te up to 67 wt%, due to its high pore volume (1.15 cm^3 g^{-1}).

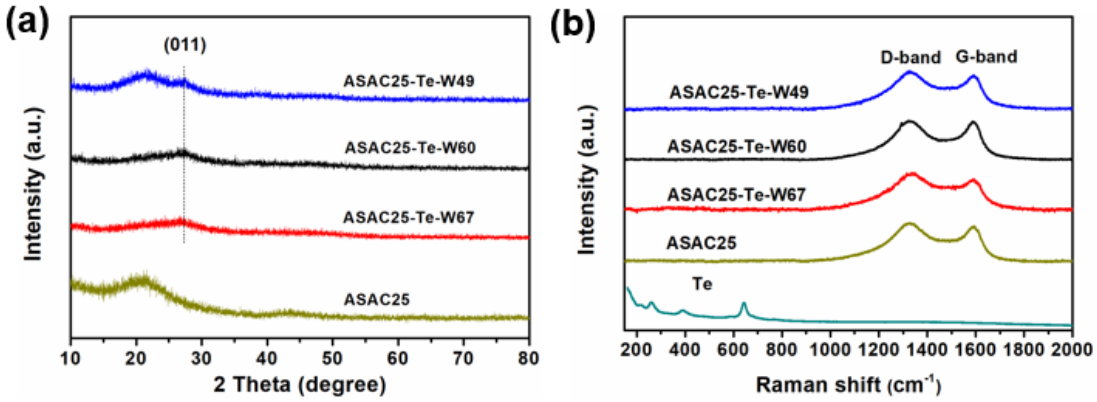

Figure 4.3.1. (a) XRD patterns and (b) Raman spectra of ASAC25, ASAC25-Te-W49, ASAC25-Te-W60, and ASAC25-Te-W67 in comparison to crystalline Te powders.

4.3.2 Cycling Stability of ASAC25-Te Cathodes with Various Te Content

The effect of Te content on the electrochemical performance of ASAC25-Te cathodes is shown in **Figure 4.3.2**. The ASAC25-Te-W49 electrode exhibits a high discharge capacity of 500.6 mAh g^{-1} in the 2nd cycle and possesses the best stability among all the samples. The specific discharge capacity for ASAC25-Te-W60 decreases gradually from 432.8 mAh g^{-1} in 2nd cycle to 237.6 mAh g^{-1} in the 100th cycle. Further increase of the Te content to 67 wt% causes a dramatic decline in the

capacity of ASAC25-Te-W67, which remains only 59.1 mAh g^{-1} after 100 charge-discharge cycles. The CE of ASAC25-Te-W67 also shows an obvious decrease in the first 40 cycles. The charge-discharge profiles of the three cathodes in the 2nd cycle and 100th cycle are shown in **Figures 4.3.2c-d**, respectively. In the 2nd cycle, the three ASAC25-Te cathodes exhibit very close overpotential, and one single charge-discharge plateau, suggesting the one-step transition between Te and Li_2Te. However, ASAC25-Te-W49 has the smallest overpotential after 100 cycles, while the others have increased polarization. The reduced performance for ASAC25-Te-W67 could be due to the acute volume change induced by lithiation and de-lithiation, which might cause damage to the carbon host and exposure of Te to the electrolyte [50, 52]. Therefore, the Te content in the ASAC25-Te cathode should be maintained around 60 wt% or below to obtain optimal cycling performance.

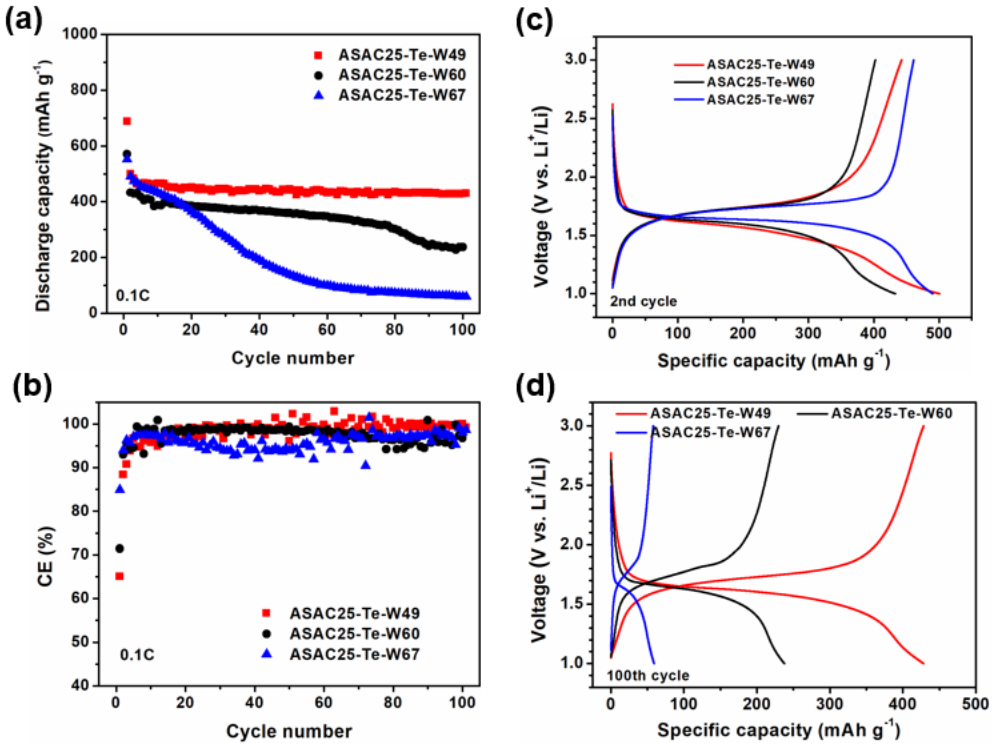

Figure 4.3.2. (a) Cycling performance, (b) Coulombic efficiency (CE), and charge-discharge profiles of ASAC25-Te-W49, ASAC25-Te-W60, and ASAC25-Te-W67 in the (c) 2nd and (d) 100th cycles measured at 0.1 C.

ASAC25-Te-W49 exhibits the highest rate capability from 0.1 to 5 C (**Figure 4.3.3**). The discharge capacities for ASAC25-Te-W60 and ASAC25-Te-W67 are 458.1/466.1, 400.4/393.4, 342.9/340.3, 305.4/307.5, 254.9/256.8 mAh g^{-1} at 0.1, 0.2, 0.5, 1 and 2 C, respectively. As the current density changes back to 0.1 C, ASAC25-Te-W49 and ASAC25-Te-W60 maintain discharge capacities of 461.9 and 412.8 mAh g^{-1}, respectively, while ASAC25-Te-W67 has only 357.2 mAh g^{-1}. The good stability of ASAC25-Te-W49 and ASAC25-Te-W60 cathodes can be attributed to enough pre-reserved empty space inside porous carbon (partial filling), which is essential for accommodating the large volume expansion of active species (Te and Li_2Te) during the lithiation and de-lithiation process. The excessive addition of Te probably causes high stress between Te and the carbon host, which might lead to structural instability during a long-term cycling test.

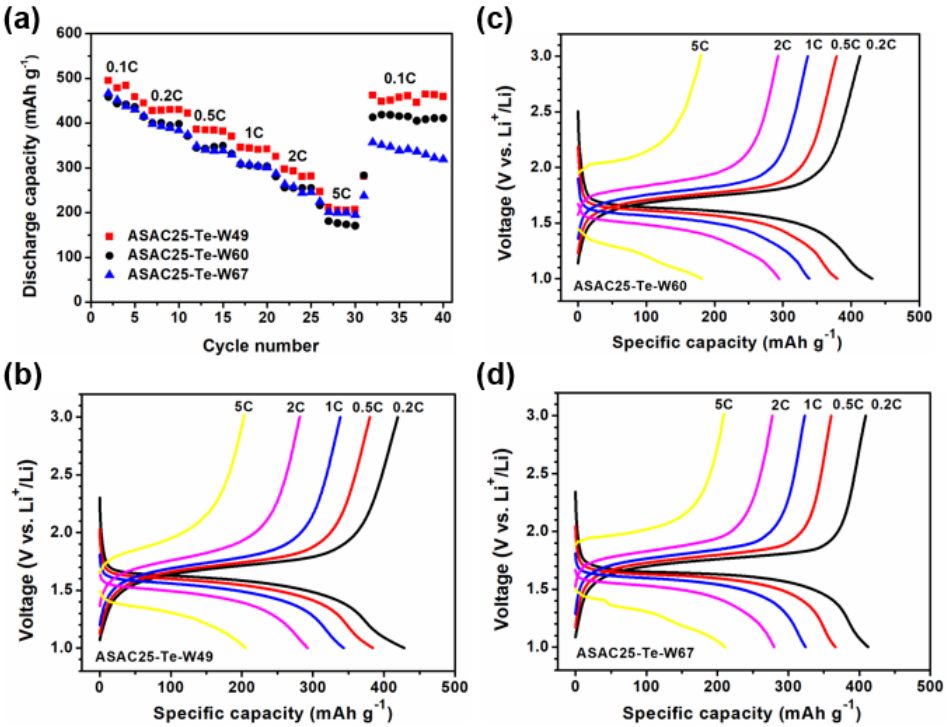

Figure 4.3.3. Rate performance of ASAC25-Te composites. (a) Comparison of capacities at 0.1C-5C, charge-discharge profiles of (b) ASAC25-Te-W49, (c) ASAC25-Te-W60, and (d) ASAC25-Te-W67.

Figure 4.3.4 shows the long cycling stability, CE, and charge-discharge profiles of ASAC25-Te-W49 evaluated at 0.1 C in the initial 5 cycles and at 1 C afterward. It can be observed that this

electrode possesses exceptional cyclability during the first 300 cycles with a high capacity retention of 94.9%. The charge-discharge curves in the 7th, 100th, and 300th cycle are overlapped with each other, suggesting good stability and reversibility of this electrode. Even the capacity experiences a slight decrease in the next 200 cycles, ASAC25-Te-W49 still remains 272.7 mAh g^{-1} after 500 cycles. This remarkable capacity and stability benefit from the effective confinement of Te in the micropores of ASAC25, good accommodation of Te volume change in the partially filled ASAC25, and fast transfer of ions/electrons at the electrode-electrolyte interface facilitated by the high surface area of ASAC25.

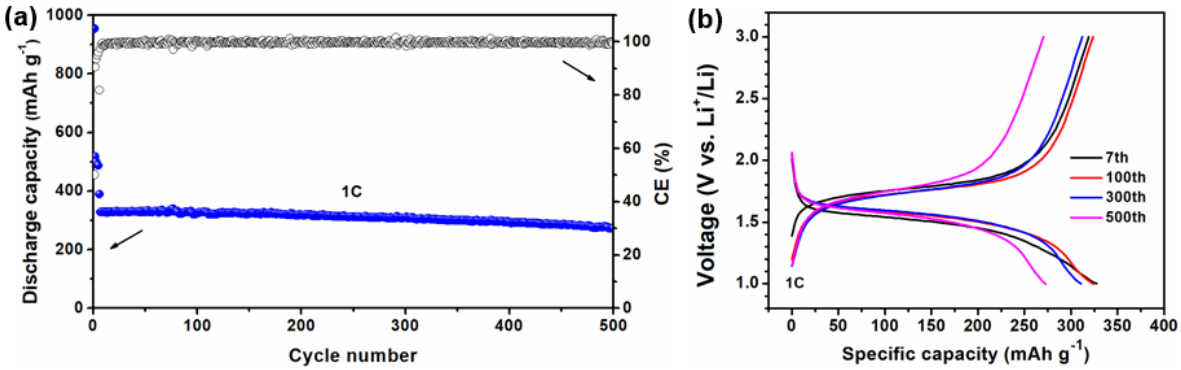

Figure 4.3.4. (a) Long-term stability and (b) charge-discharge profiles of ASAC25-Te-W49 electrode measured at 0.1 C in the first 5 cycles and 1 C in the subsequent cycles.

4.3.3 Working Mechanism Analysis of Te-C Interplay During Charge/Discharge Process

Based on the above analysis, ASAC25, mainly consisting of micropores, possessed superior rate and long-cycling performance compared to ASAC30, which has both micropores and mesopores. A possible mechanism is proposed in **Figure 4.3.5** to explain the role of carbon pore structure on the performance of Te/C cathode in Li-Te batteries. For ASAC30, Te infiltrates into the micropores and mesopores, and the possibility remains on the other surface of the carbon matrix as well. During the lithiation process, the formation of the discharge product (Li_2Te) is accompanied by acute volume expansion. Over repeated cycling, the active species (Te and Li_2Te) inside mesopores and/or on the other surface will dissolve into the electrolyte, causing permanent loss of reversible capacity as reflected by the capacity decay, low CE, and increased charge transfer

resistance. By contrast, microporous ASAC25 results in the impregnation of smaller and more disordered Te (as confirmed by XRD and HRTEM) during the melt-diffusion process. Under the same melt-diffusion condition, the impregnation of Te in microporous carbon is more complete than in mesoporous carbon, probably due to the capillary force difference. Due to the complete impregnation of Te in micropores and the large contact surface between ASAC25 and Te, ASAC25-Te exhibits stronger Te and C interaction than ASAC30-Te (as revealed by XPS). In other words, ASAC25 can better confine Te in the micropores, leading to the better structural stability of Te over cycling. The better confinement and stronger Te-C interaction in ASAC25-Te than in ASAC30-Te are significantly responsible for the reduced loss of active Te from the former than the latter over the repeated cycling and Te/Li_2Te volume expansion/contraction (SEM and EDS after cycling, EIS before and after cycling, and CV for post-cycled electrode). It should be noted that our result suggests that the microporous carbon host should be partially filled with Te (up to ~ 60 wt%) to preserve space to accommodate volume change induced by the Te-Li_2Te phase transition.

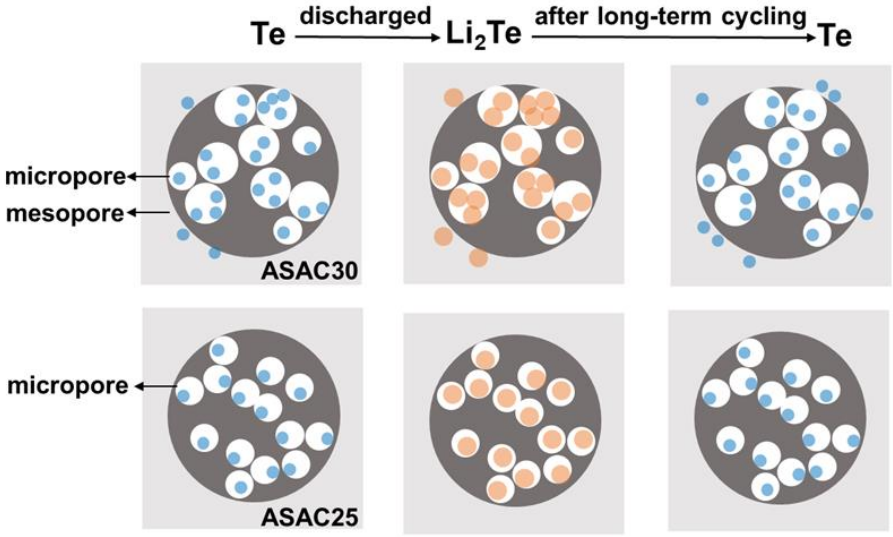

Figure 4.3.5. Schematic diagram of working mechanisms of ASAC30-Te and ASAC25-Te.

Table 4.3.1 summarizes the reported Te electrode in Li-Te batteries using carbonate, ether, DMSO, and solid polymer electrolyte. The rate performance of Te/C electrodes tested in carbonate electrolytes is especially compared in **Figure 4.3.6**, and Te/C electrodes with similar Te contents and loadings are chosen for a fair comparison. It could be seen that the Te encapsulated in ASAC25

showed better performance than Te/hollow carbon @CNT [73] and Te/porous carbon [46] at current densities of 42-840 mA g^{-1}. The performance of ASAC25-Te herein is comparable to those of CMK-3/Te and rib-like porous carbon/Te [69, 72]. Our work shows that excellent performance of Li-Te batteries could be achieved by carefully selecting the carbon hosts from commercial sources. Moreover, the key merits of the carbon hosts include the majority of micropores and high pore volume. **Figure 4.3.6b** shows the relationship between Te content and the pore volume of the carbon host. The black curve represents the theoretical maximum Te contents calculated based on the pore volume of the carbon host. It can be seen that the actual Te contents, without comprising the overall performance, are below the theoretical maximum values because of the empty space required to accommodate structural expansion.

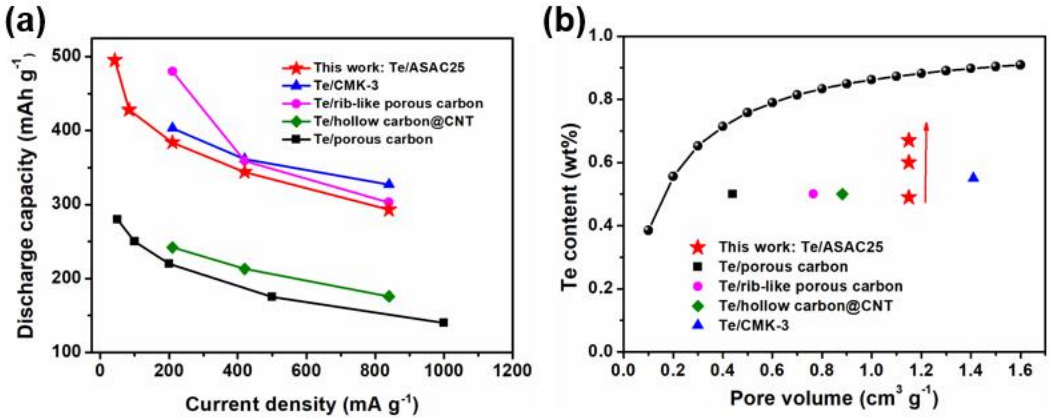

Figure 4.3.6. Comparisons of (a) discharge capacity in Te/porous carbon [1], Te/CMK-3 [2], Te/rib-like porous carbon [3], Te/hollow carbon@CNT [4], and this work at different current densities and (b) Te content versus pore volume of the carbon host (black circles represent the theoretical maximum value).

Table 4.3.1. Comparison of Te cathodes in Li-Te batteries.

Cathode	Te content (wt%)	Te loading (mg cm^{-2})	Pore volume (cm^3 g^{-1})	Electrolyte	Discharge capacity: 1st → 2nd cycle	Cycling performance	Ref.
Te/ porous carbon	50	1	0.44	1M $LiPF_6$ in EC:DEC	324 mAh g^{-1} → 317 mAh g^{-1} at 50 mA g^{-1}	324 → 224 mAh g^{-1} after 1000 cycles at 50 mA g^{-1}	[46]
Te/C	65.1	3.16	N/A	1M $LiPF_6$ in EC:DEC	1088 mAh cm^{-3} (740 mAh g^{-1}) →780 mAh cm^{-3} at 10 mA g^{-1}	597 mAh cm^{-3} (252 mAh g^{-1}) after 100 cycles at 100 mA g^{-1}	[50]
Te/CMK-3	55.1	0.08-0.10 mAh cm^{-2}	1.41	1M $LiPF_6$ in EC:DMC	450 →403 mAh g^{-1} at 0.5C (1C=420 mA g^{-1})	286 mAh g^{-1} at 10 C for 990 cycles (85% retention)	[69]
Te/rib-like porous carbon	50	2	0.765	1M $LiPF_6$ in EC:DEC	480 → 450 mAh g^{-1} at 0.5C (1C=420 mA g^{-1})	Keep 288 mAh g^{-1} for 3600 cycles at 2 C	[72]
Te/hollow carbon@CNT	50	N/A	0.882	1M $LiPF_6$ in EC;DEC	700 → 380 mAh g^{-1} at 0.5C (1C=420 mA g^{-1})	700 → 240 mAh g^{-1} after 500 cycles at 0.5 C	[73]
Te/microporous carbon	68	1	0.638 (0.487 for micropores)	1M LiTFSI in DOL:DME	670 → 481 mAh g^{-1} at 0.1C (1C= 500 mA cm^{-2})	274 mAh g^{-1} at 1 C after 1000 cycles	[70]
Te nanowires/ reduced rGO	63.3	1.1	N/A	1M LiTFSI in DOL:DME	2611 →2500 mAh cm^{-3} at 0.2C (1C=420 mA g^{-1})	2443 mAh cm^{-3} (391.5 mAh g^{-1}) → 1685 mAh cm^{-3} (270	[47]

Cathode	Te content (wt%)	Te loading (mg cm^{-2})	Pore volume (cm^3 g^{-1})	Electrolyte	Discharge capacity: 1st → 2nd cycle	Cycling performance	Ref.
						mAh g^{-1}) after 500 cycles at 1C	
Te/porous cobalt-doped carbon polyhedra	77.2	2	0.64	1M LiTFSI in DOL:DME	2615.2 → 2600 mAh cm^{-3} at 0.2C (1C=420 mA g^{-1})	2484.4 mAh cm^{-3} (398.1 mAh g^{-1}) → 2324.5 mAh cm^{-3} after 800 cycles at 1C	[53]
Te/nitrogen-doped porous carbon	50	N/A	0.33	1M LiTFSI in DOL:DME	510 →420 mAh g^{-1} at 0.25C (1C=420 mA g^{-1})	510 → 310 mAh g^{-1} after 200 cycles at 0.25C	[75]
1. Te/ordered macroporous carbon; 2. Te nanowires	1. 70; 2. 100	1 N/A; 2. 1	1. 2.38; 2. N/A	1M $LiClO_4$ in DMSO	1. About 338→290 mAh g^{-1} at 100 mA g^{-1} 2. About 2100 →900 mAh cm^{-3} at 100 mA g^{-1}	1. 130 mAh g^{-1} at 1000 mA g^{-1} for 150 cycles; 2. 900 mAh cm^{-3} (1800 mWh cm^{-3}) at 100 mA g^{-1} for 80 cycles	[71]
Te nanowires @CNTs	50	2.55	0.964	1M LiTFSI in DMSO	548 → 400 mAh g^{-1} at 0.1C (1C=420 mA g^{-1})	488 → 238 mAh g^{-1} after 200 cycles at 1C	[77]
Te nanorods/Ni/ carbon cloth	1.19	0.35	N/A	1M $LiClO_4$ in DMSO	276.6 →230 mAh g^{-1} at 100 mA g^{-1}	70.5 → 47 mAh g^{-1} after 500 cycles at 100 mA g^{-1}	[78]

Cathode	Te content (wt%)	Te loading (mg cm^{-2})	Pore volume (cm^3 g^{-1})	Electrolyte	Discharge capacity: 1st → 2nd cycle	Cycling performance	Ref.
Te nanotubes/ carbon cloth	13	0.8	N/A	Polymer solid electrolyte	580 →405 mAh g^{-1} at 100 mA g^{-1} at 20 °C (cut-off voltage: 0-3V)	580 → 316.7 mAh g^{-1} after 500 cycles at 100 mA g^{-1} at 60 °C	[79]

4.4 Durable Te/C Cathodes with Biomass-Derived Porous Carbon as Te Host

In addition to commercial carbons, synthesized porous carbons are another choice to customize desired pore structure for Li-Te batteries. Lignin is a naturally abundant polymer with plentiful oxygen-containing functional groups and is easily developed into various pore structures [128-130]. Lignin is a cost-effective precursor for the synthesis of porous carbon to host Te and enable a high-performance Li-Te battery.

In this subsection, lignin-derived porous carbons with different pore structures are synthesized and utilized as Te hosts to mitigate the volume variation of Te. These activated carbons predominantly consist of micropores and have increased surface area and pore volume versus activation temperature. A majority of micropores interconnected with mesopores are found in AC700 carbon, offering sufficient channels for fast electron transfer, Li-ion conduction, as well as electrolyte penetration. Due to the good structure and fast redox kinetics, the Te/AC700 delivers a high reversible capacity of 417.6 mAh g^{-1} and exhibits excellent cycling stability over 1,000 cycles at a high current density of 2C.

4.4.1 Schematic of Preparation Procedures of Carbon Activation

Lignin, with abundant resources from plants, is an attractive and sustainable precursor for the preparation of hierarchical porous carbon. Carbonization and activation treatment are common processes to turn biomass precursors into porous carbon structures [41, 121, 131]. In this work, bulky lignin experienced carbonization and activation with KOH as a pore-forming agent under nitrogen flow to create numerous interconnected pores, as schematically shown in **Figure 4.4.1**. The detailed experimental procedures are described in Section 3.1.1. The majority of cavities are able to confine Te molecules by the melt-diffusion method to accommodate the volume expansion from Te to Li_2Te. It was reported that the porosity of biomass-derived carbon is mainly determined by the KOH/lignin ratio and carbonization/activation temperature [132, 133]. Herein, we select a fixed KOH/lignin ratio of 2:1 and vary the activation temperature from 600 to 800 °C to investigate the difference in the carbon pore structure.

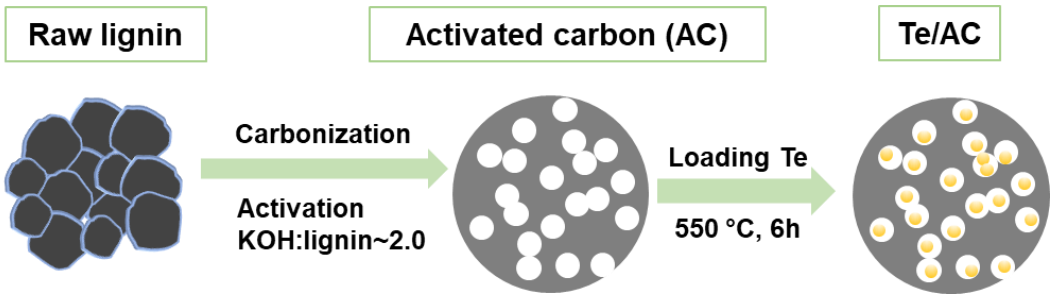

Figure 4.4.1. Schematic illustration of the preparation process for Te/AC composites.

4.4.2 Pore Structure Analysis of Different Porous Carbons

Figures 4.4.2a-d show the microstructure of the raw lignin and as-prepared porous carbon. A number of particles accumulate together in raw lignin, as seen in **Figure 4.4.2a**. After the activation treatment at 600 °C, AC600 carbon possesses quite a few tiny pores with hundred nanometers (the inset image in **Figure 4.4.2b**). With the increase of activation temperature, the carbon matrix displays more pores ranging from hundred nanometers to several micrometers, as presented in **Figures 4.4.2c-d**. These abundant pores provide favorable channels for electrolyte infiltration, fast electron transfer, and Te confinement. **Figure 4.4.2e** presents the nitrogen adsorption/desorption isotherms of AC600, AC700, and AC800. All the carbons show type-I isotherm, indicating the micropores dominant property [120]. **Figure 4.4.2f** reveals the narrow pore size distribution of these carbons with an average diameter of 0.6 nm. The pore volume and Brunauer-Emmett-Teller (BET) surface area are 0.10, 0.33, and 0.38 $cm^3\ g^{-1}$ and 222.43, 769.72, and 1036.99 $m^2\ g^{-1}$ for AC600, AC700, and AC800, respectively (**Table 4.4.1**). One noticeable difference between AC700 and AC800 is that AC700 consists of many micropores and a small portion of mesopores, while AC800 contains only micropores. In specific, the micropore volume is 0.08, 0.28, and 0.38 $cm^3\ g^{-1}$ for AC600, AC700, and AC800, respectively. Elevated activation temperature leads to a growing number of micropores, which might be explained by the following KOH-induced activation reaction [131]:

$$4C + 6KOH \rightarrow 6K + 3H_2 + 2CO + 2CO_2 \qquad \text{Eq. 4.2}$$

This reaction between char and KOH is driven by temperatures to produce porous carbon, and higher temperature facilitates this activation process and therefore results in richer porosity.

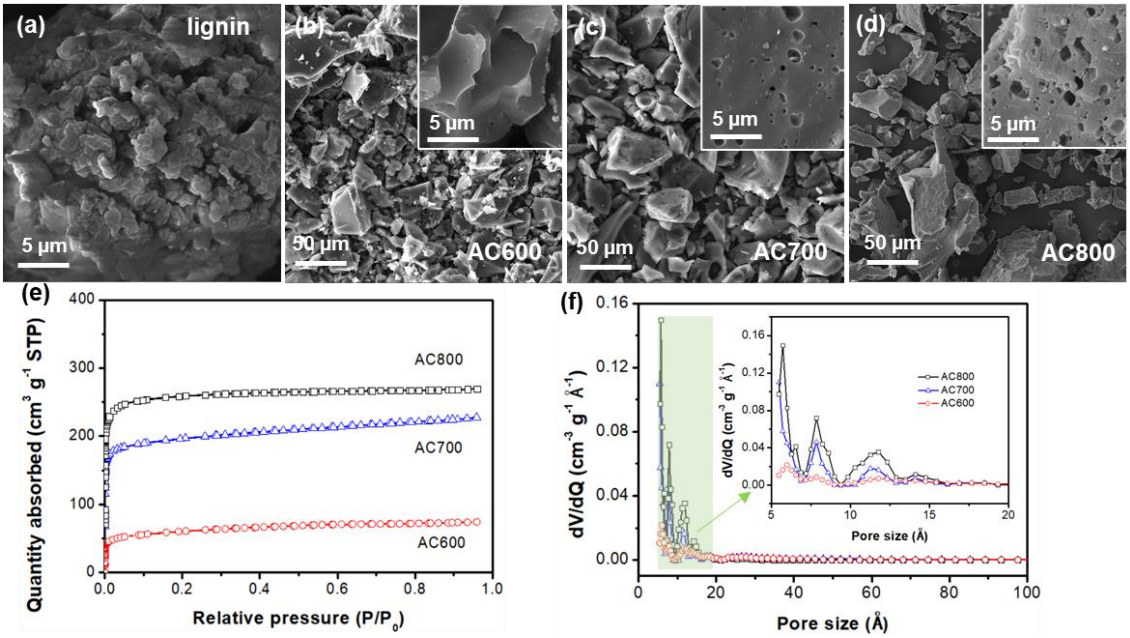

Figure 4.4.2. SEM images of (a) raw lignin, (b) AC600, (c) AC700, (d) AC800, and (e) nitrogen adsorption/desorption isotherm and (f) pore size distribution of AC600, AC700, and AC800.

Table 4.4.1. Pore structures of AC600, AC700, and AC800.

Sample	BET Surface area (m^2 g^{-1})	Total pore volume (cm^3 g^{-1})	Micropore volume of (cm^3 g^{-1})	Mesopore volume (cm^3 g^{-1})	Maximum Te loading (wt %)*
AC600	222.4	0.10	0.08	0.02	38.5
AC700	769.7	0.33	0.28	0.05	67.4
AC800	1037.0	0.38	0.38	0	70.4

* Maximum Te loading is calculated assuming that all carbon pores are occupied by Te.

4.4.3 Morphology and Structural Characterizations of Te/C Composites

The Te/C composites were prepared by a melt-diffusion method to complete the infusion of Te molecules. **Figures 4.4.3a-c** and **Figure 4.4.4** display their morphologies and elemental

distribution of Te and C. XRD patterns in **Figure 4.4.3d** revealing the different forms of Te in the Te/C composites. The three carbons show an identical XRD pattern with two broad diffraction peaks at 23° and 43° corresponding to the (002) and (010) planes (JCPDS No. 50-0927). For the Te/C composites, the Te/AC600 exhibits all the characteristic peaks of hexagonal Te (JCPDS No. 79-0736). The peaks located at 23°, 27°, 38°, and 40° are assigned to the (100), (011), (102), and (110) planes, respectively. The high intensity indicates that a large amount of bulky Te is dispersed in the AC600 carbon matrix instead of being confined inside the micropores, which could be attributed to the low pore volume and specific area of AC600. In contrast, the Te/AC700 composite has a similar XRD pattern but with considerably lower intensity, suggesting that the majority of Te molecules are trapped in the hierarchical pores in AC700. It could be observed that all the crystalline Te peaks disappear in Te/AC800, implying that Te molecules are entirely embedded into microporous AC800 [70]. The TGA curves in **Figure 4.4.3e** determine the Te content in Te/AC600, Te/AC700, and Te/AC800 is 42, 47, and 43 wt%, respectively. The maximum Te loading in AC600, AC700, and AC800 is 38.5, 67.4, and 70.4 wt% (**Table 4.4.1**) based on the pore volume of each porous carbon. It could be found that Te content in AC600 is higher than its theoretical value, indicating that 3.5 wt% Te is not confined into the pore structure. The Te contents in AC700 and AC800 below the maximum values suggest that Te molecules are well encapsulated into the micropores or mesopores. The difference in TGA is probably associated with the pore structure of activated carbon. It is speculated that the plateau starting at 300 °C corresponds to the Te molecules evaporated from mesopores, and the higher temperature at 400 °C is attributed to the evaporated Te from micropores. The previously reported Te/C or Se/C structures prepared by the melt-diffusion method with micropores-dominant carbon hosts also present a similar TGA curve with two plateaus [70, 134].

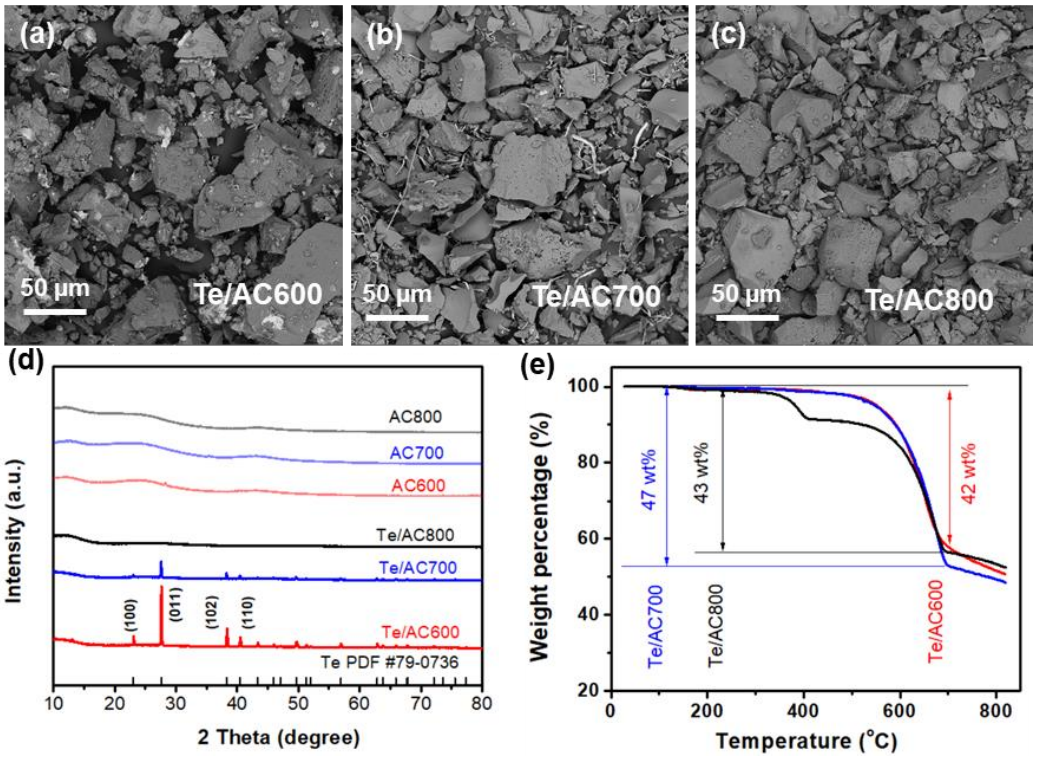

Figure 4.4.3. SEM images of (a) Te/AC600, (b) Te/AC700, (c) Te/AC800, (d) XRD patterns of AC600, AC700, AC800, Te/AC600, Te/AC700, and Te/AC800, and (e) TGA curves of Te/AC600, Te/AC700, Te/AC800 composites obtained under an N_2 environment.

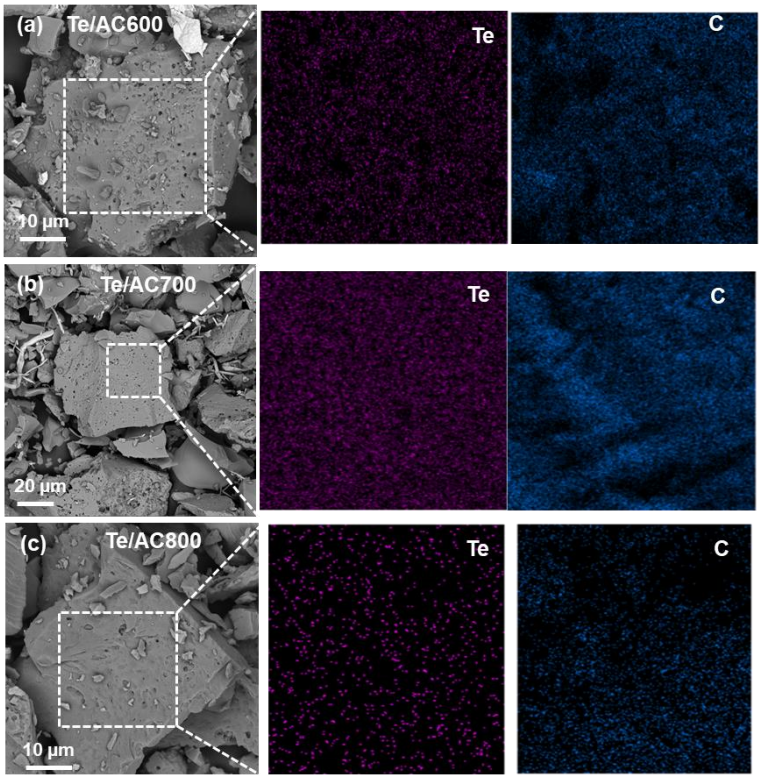

Figure 4.4.4. SEM images and EDS mapping of (a) Te/AC600, (b) Te/AC700, and (c) Te/AC800.

4.4.4 Cycling Performance of Te/C Cathodes with Various Porous Carbons

Figure 4.4.5 illustrates CV curves of the Te/AC600, Te/AC700, and Te/AC800 electrodes at the scan rate of 0.2 mV s^{-1} at 1-3 V. The cathodic/anodic peaks of 1.62/1.94, 1.26/1.67, and 1.15/1.60 V for Te/AC600, Te/AC700, and Te/AC800 could be assigned to the redox conversion between Te and Li_2Te [70]. The inferior peak current of Te/AC800 indicated poor reaction kinetics.

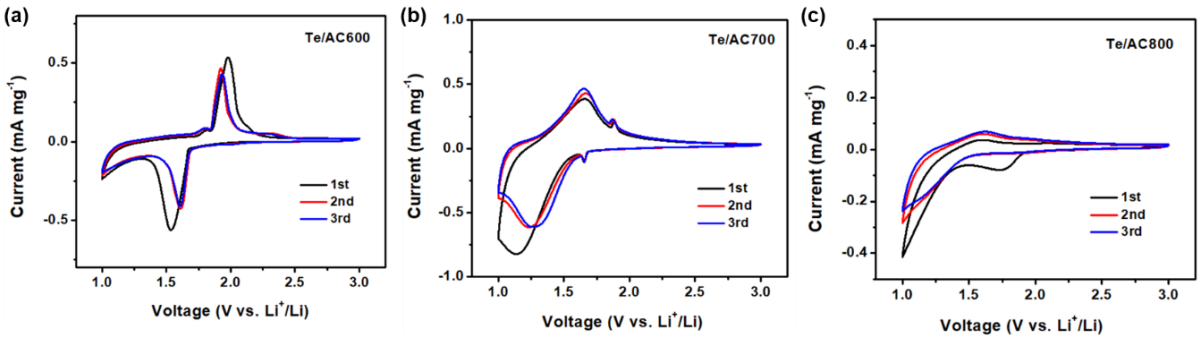

Figure 4.4.5. CV plots of (a) Te/AC600, (b) Te/AC700, and (c) Te/AC800 at 0.2 mV s^{-1}.

The cycling performance of the Te/C electrodes is also tested at 0.1 C (1 C = 420 mA g^{-1}), and the results are compared in **Figure 4.4.6**. The Te/AC600 delivers an initial discharge capacity of 432 mAh g^{-1}, followed by a sharp decline to 124 mAh g^{-1} over 20 cycles. Te/AC700 possesses the highest initial capacity of 734 mAh g^{-1} and then stabilizes at 418 mAh g^{-1} for the next cycles. In comparison, the Te/AC800 delivers discharge capacities of 474 and 175 mAh g^{-1} in the first and second cycles, respectively. Besides, the Coulombic efficiency (CE) of Te/AC700 rapidly increases to 96% after the first discharge process, whereas the CE of Te/AC600 and Te/AC800 gradually grows to 95% after 15 cycles. The higher CE of Te/AC700 suggests a better utilization of Te active material. The initial CE of Te/AC600, Te/AC700, and Te/AC800 is 55, 55, and 27%, respectively.

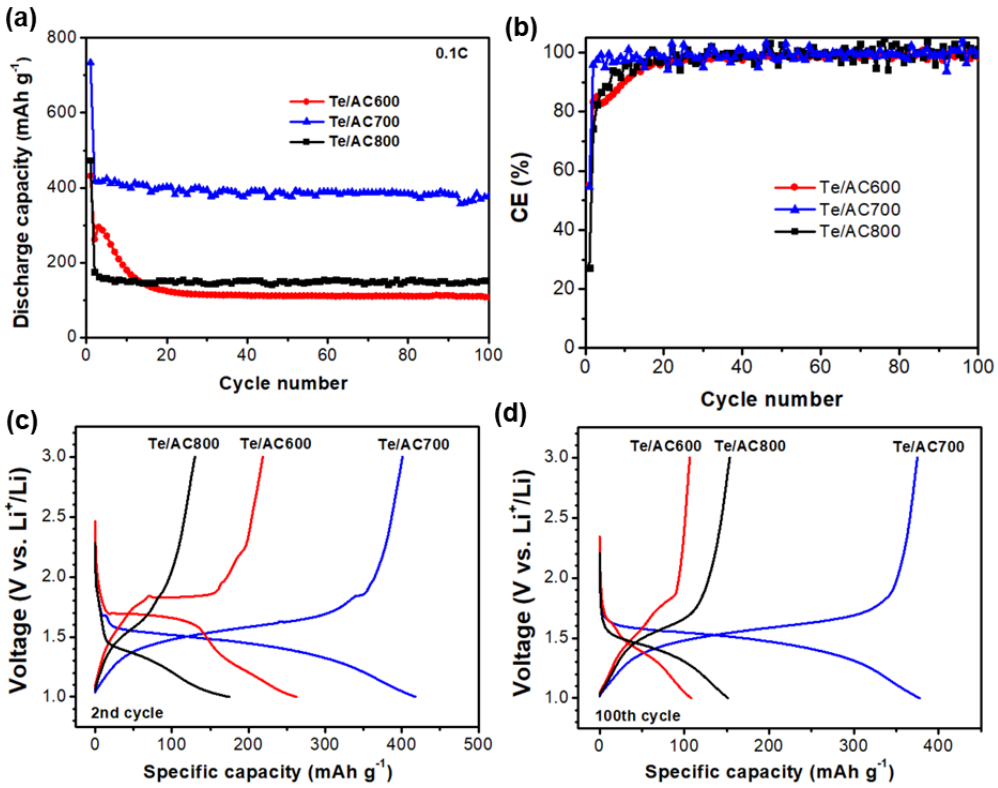

Figure 4.4.6. (a) Cycling stability, (b) CE, and charge-discharge profiles in the (c) 2nd cycle and (d) 100th cycle of Te/AC600, Te/AC700, and Te/AC800 at 0.1 C (1C = 420 mA g^{-1}).

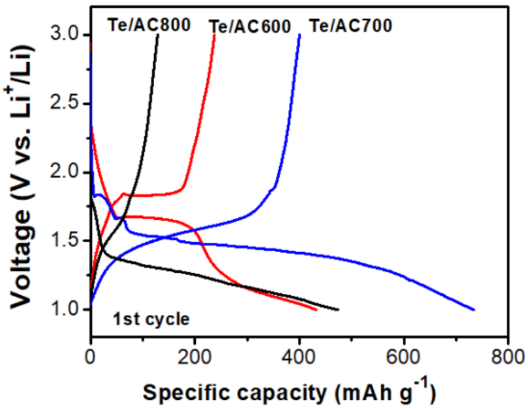

Figure 4.4.7. The 1st-cycle charge-discharge profiles of Te/AC600, Te/AC700, and Te/AC800 at 0.1 C.

Figure 4.4.7 and **Figures 4.4.6c-d** demonstrate galvanostatic charge-discharge profiles of Te/C electrodes in the 1st, 2nd and 100th cycles. In the first lithiation process, Te/AC600 shows a high plateau of about 1.67 V, indicating the electrochemical conversion from Te to Li_2Te. The high discharge plateau is similar to that of bulky Te, proving the existence of Te particles outside the pore walls [50]. The Te/AC700 possesses an extended and lower discharge plateau of about 1.5V, suggesting a complete redox conversion. Therefore, Te/AC600 and Te/AC700 demonstrate similar initial CE despite different specific capacities and discharge voltage. In contrast, the Te/AC800 electrode only displays an inclined slope without an obvious flat plateau, which could be due to the incomplete phase transformation caused by sluggish kinetics after it is discharged to 1 V. Hence, the Te/AC800 electrode shows a lower charge capacity and initial CE compared to Te/AC600 and Te/AC700. By comparing CC-DC curves in the 2nd and 100th cycle, it can be found that the Te/AC700 and Te/AC800 electrodes maintain relatively stable voltage-capacity profiles, whereas the plateau at 1.7 V of Te/AC600 almost disappears after 100 cycles, demonstrating its poor electrochemical irreversibility. It can be speculated that the pore structure of the carbon host plays a critical role in lithium-ion storage performance and redox kinetics of Te/C electrodes. The low pore volume and specific area of AC600 lead to the confinement of only a small portion of Te, while the majority of Te bulks are dispersed in the carbon matrix, as indicated by the strong XRD diffraction peak for Te (**Figure 4.4.3d**). The bulky Te without carbon support experiences acute volume expansion and subtraction and causes the pulverization of active materials, which could be verified from the particles on the separator peeled off from cycled Te/AC600 cathode (**Figure 4.4.8**). In comparison, Te/AC700 and Te/AC800 cathodes possess sufficient micropores as Te hosts and maintain excellent electrochemical and structural stability, benefiting from the effective confinement of Te active material. Although AC800 has the largest surface area and microporous volume, the narrow pore size might slow down the process of ion conduction and electron transfer and therefore results in limited specific capacity, which will be discussed in detail later.

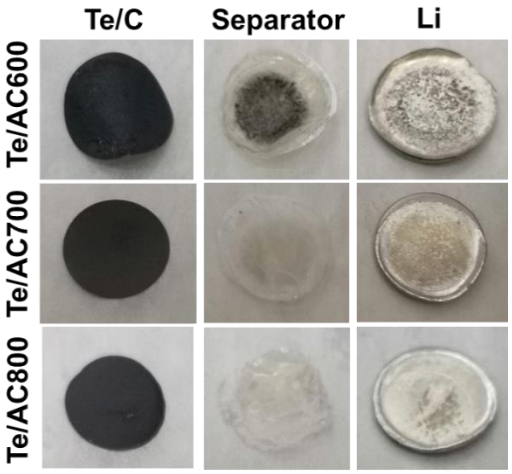

Figure 4.4.8. Digital photos of Te/C cathode, separator, and Li metal recovered from Li-Te/AC600, Li-Te/AC700, and Li-Te/AC800 cells after cycling.

4.4.5 Long-Cycling Performance of the Te/AC700 Cathode

The rate capabilities of Te/AC700 under various current densities (0.1-5 C) are also evaluated and shown in **Figures 4.4.9a-b**. As the current density increases, the Te/AC700 cathode delivers a discharge capacity of 416, 397, 334, 294, 245, and 168 mAh g^{-1} at 0.1, 0.2, 0.5, 1, 2, and 5 C, respectively. When the current density is set back to 0.1C, the capacity is restored to 395 mAh g^{-1}, implying the excellent electrochemical stability of the Te/AC700 cathode. Furtherly, the long-term cycling test is carried out, and the initial few cycles are under 0.1C/0.2 C for activation. The Te/AC700 cathode demonstrates exceptional cycling stability over 1,000 cycles at 1 and 2 C. The discharge capacities are nearly stabilized at 300 and 240 mAh g^{-1} for 1 and 2 C, respectively.

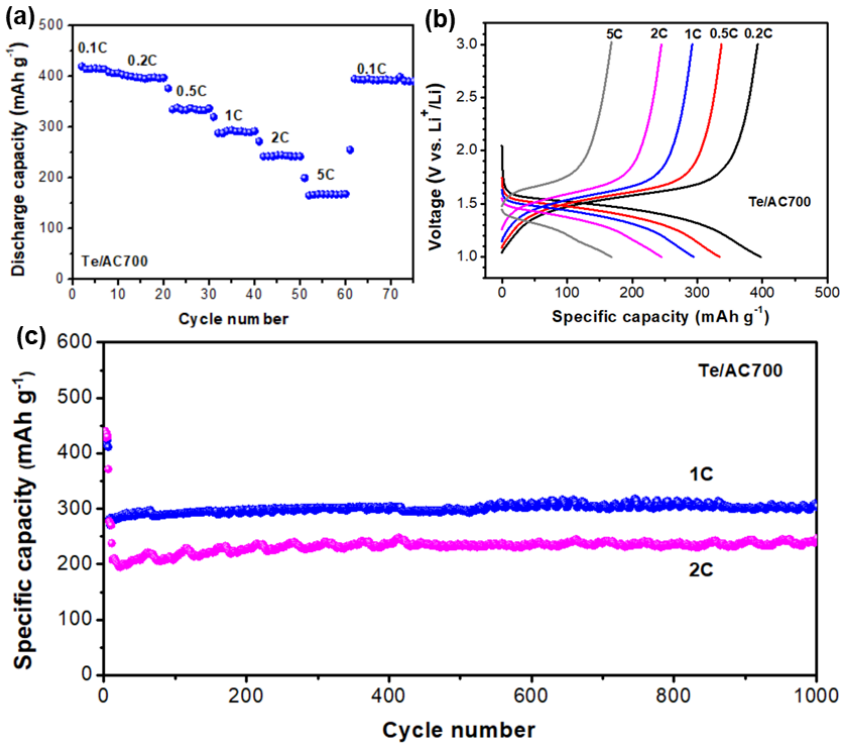

Figure 4.4.9. (a) Rate performance, (b) voltage-capacity profiles of Te/AC700 at 0.1-5 C, and (c) long-term cycling performance of Te/AC700 at high rates of 1 and 2 C.

4.4.6 Kinetics Analysis of Te/C Cathodes with Various Porous Carbons

To gain a better understanding of pore structure on the effect of charge transfer, EIS measurement is performed for Te/C cathodes before and after cyclings. The Nyquist plots are illustrated in **Figure 4.4.10**. Before the cycling test, the charge transfer resistance (R_{ct}) for Te/AC600, Te/AC700, and Te/AC800 is 127.3, 132.7, and 93.7 Ω, respectively (**Table 4.4.2**). After 100 cycles, the semicircle of Te/AC600 expands extensively with a large R_{ct} of 1,968 Ω based on the fitting of the equivalent circuit shown in **Figure 4.4.10a**. The enlarged R_{ct} probably is likely to result from the peeling off active materials from the Al current collector, as observed in **Figure 4.4.8**. The Te/AC700 cathode keeps a relatively similar EIS spectra shape with R_{ct} and solid-electrolyte-interphase resistance (R_{SEI}) of 193.3 and 6.6 Ω, indicating its good structural stability. The Te/AC800 cathode has a larger R_{SEI} of 39.8 Ω, which is indicative of the sluggish redox kinetics.

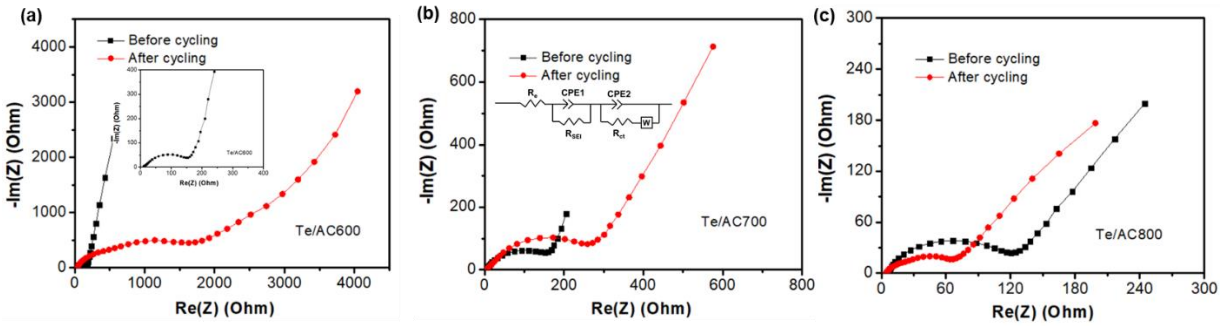

Figure 4.4.10. Nyquist plots of (a) Te/AC600, (b) Te/AC700, and (c) Te/AC800 before and after 100 cycles.

Table 4.4.2. Calculated R_e, R_{SEI}, and R_{ct} from the Nyquist plots in **Figure 4.4.10**.

Electrode	Before cycling		After cycling		
	R_e (Ω)	R_{ct} (Ω)	R_e (Ω)	R_{SEI} (Ω)	R_{ct} (Ω)
Te/AC600	7.7	127.3	41.5	831.6	1968
Te/AC700	4.4	132.7	4.2	6.6	193.3
Te/AC800	5.4	93.7	5.1	39.8	21.7

To furtherly figure out the reaction kinetics in different Te/C electrodes, CV tests are carried out at various scan rates from 0.2 to 0.6 mV s^{-1}. As plotted in **Figures 4.4.11a-c**, with the increase in scan rate, the cathodic peak potentials of all Te/C cathodes become lower, and the anodic peak potentials shift to a higher value. The intensity of peak current follows the order of Te/AC700 > Te/AC600 > Te/AC800, reflecting the stronger electrochemical activity of Te/AC700 than that of the other cathodes. The relationship between peak current and scan rate is described as the following the Randles-Sevcik equation [29]:

$$I_p = 2.69 \times 10^5\, n^{3/2} A D^{1/2} v^{1/2} C = B \times v^{1/2} \qquad \text{Eq. 4.3}$$

where I_p is the peak current, n is the number of electron transfer (n = 2 in this system), A is the effective reaction area (electrode area, 1.13 cm^2), D is the Li-ion diffusion coefficient, v is the scan

rate, C is the Li-ion molar concentration (1 mol L^{-1}), and B is the slope of the fitted I_p-$v^{1/2}$ curves. Based on the fitted I_p-$v^{1/2}$ curves, the Li^+ diffusion coefficients of the Te/C cathodes are 2.95×10^{-10}, 7.97×10^{-10}, and 4.93×10^{-11} cm^2 s^{-1} for Te/AC600, Te/AC700, and Te/AC800 cathode, respectively (**Figure 4.4.11d**). Compared to Te/AC600, Te/AC700 possesses higher Li-ion diffusivity and enables faster lithiation/delithiation of Te molecules due to the sufficient surface area and pore volume to accommodate Te active material. However, the Te/AC800 with the largest surface area and the most micropores shows inferior redox kinetics.

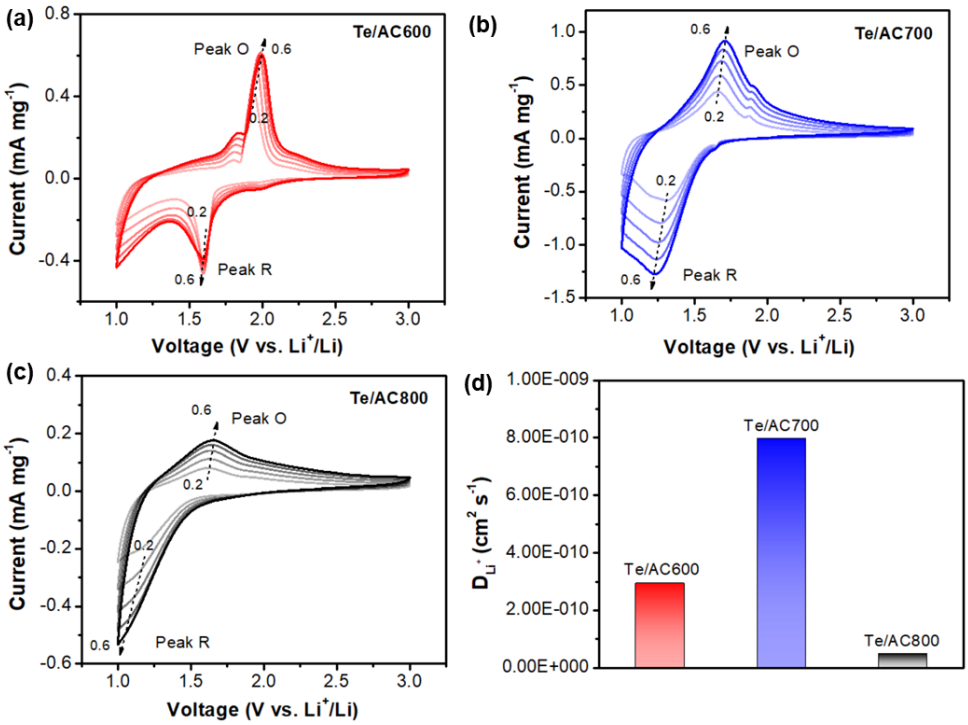

Figure 4.4.11. CV plots of (a) Te/AC600, (b) Te/AC700, (c) Te/AC800 at various scan rates of 0.2-0.6 mV s^{-1}, and (d) calculated Li^+ diffusion coefficients in Te/AC600, Te/AC700, and Te/AC800 electrodes.

4.4.7 Schematic of Li-Ion Pathways in Te/AC Structure

In this study, lignin-derived porous carbons all show typical microporous properties (type-I adsorption/desorption isotherm and narrow pore size distribution below 2 nm), and pore volume and surface area of these carbons increase *versus* activation temperature. **Figure 4.4.12** demonstrates the Li-ion pathways in the Te/AC600, Te/AC700, and Te/AC800 electrodes. The

Te/AC600 displays serious capacity fading mainly because some Te bulks without carbon confinement are irreversibly converted to Li_2Te and lead to the pulverization and loss of active materials. AC800 possesses only isolated micropores as Te host and is insufficient for effective Li-ion transport to satisfy the electrochemical reactions. In contrast, AC700 possesses sufficient micropores to accommodate the volume change of Te, a small portion of mesopores to construct interconnected channels to facilitate electrolyte wetting and fast Li-ion transport, and high pore volume and surface area to confine the majority of Te. Comparison of AC700 with AC800 strongly suggests that a small portion of mesopores is critical for ensuring fast Li-ion diffusion and electron transfer and obtaining desirable electrochemical performance in Te/C cathodes for Li-Te batteries.

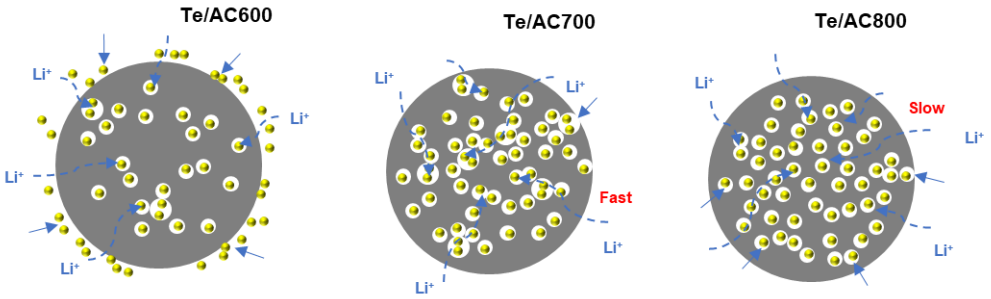

Figure 4.4.12. Schemes of Li-ion pathways in Te/AC600, Te/AC700, and Te/AC800.

4.4 Chapter Summary

Lithium-tellurium batteries have attracted increasing attention as a next-generation energy storage system due to their appealing electrical conductivity and volumetric capacity. Porous carbon hosts are widely used for Te confinement to achieve good electrochemical performance in Li-Te batteries. However, there is a lack of understanding of the effect of carbon pore structure on the performance of Te/C cathodes.

It is found that an ideal porous carbon should possess a majority of micropores to confine Te and accommodate its volume change and a small portion of mesopores to facilitate electrolyte wetting and Li-ion transport.

Detailed investigations in this chapter reveal that micropores, rather than mesopores, are critical for effective Te confinement due to the complete infiltration of Te in micropores and enhanced Te and C interaction, thus enabling superior stability in ASAC25-Te. The dramatic capacity decline

of ASAC30-Te is caused by the dissolution of bulky Te and the loss of active materials in long cycles. ASAC25-Te also achieved exceptional capacity retention of 83.3% after 500 cycles at 1C. Moreover, this work found that the ASAC25 carbon host should be partially filled with Te up to ~ 60 wt% to accommodate volume change. The clarification is expected to provide guidance on the further development of high-energy-density Te-based rechargeable batteries.

Additionally, lignin is a sustainable precursor to tailor carbon pore structure (pore size distribution, surface area, and pore volume) by adjusting activation temperature. The AC700 possessed numerous micropores and a small portion of mesopores, high surface area, and pore volume, providing sufficient channels for Li-ion diffusion and electron transfer and mitigating the volume change of Te. This conductive matrix enabled a high reversible capacity of 418 mAh g^{-1}, close to the theoretical value of Te. Moreover, the Te/AC700 cathode showed ultrahigh capacity retention of 90% after 100 cycles and superior long-term cycling stability over 1000 cycles at 2 C, which could be attributed to the effective confinement of Te and fast redox kinetics. Our finding gives hints to the further development of carbon hosts for Li-Te batteries.

Chapter 5 Gel Polymer Electrolytes for Li-Te Batteries

5.1 Introduction

Previous studies in Li-Te batteries primarily focused on the design of Te/C cathode in liquid electrolyte-based Li-Te batteries and did not address the safety issues associated with the flammable liquid organic electrolytes [52]. To fundamentally avoid safety risk, solid electrolytes have been proposed and extensively studied for constructing reliable and high-performance solid-state batteries [135-137]. To the best of our knowledge, only one literature investigated all-solid-state Li-Te battery with poly(ethylene oxide) (PEO)-based solid polymer electrolyte [79]. The solid-state Li-Te battery showed acceptable cycling performance only at a high working temperature of 60 ^{o}C and underwent capacity decline during initial cycles, probably resulting from interfacial incompatibility between polymer electrolyte and Li or Te electrodes.

In this chapter, high-performance quasi-solid-state Li-Te batteries are demonstrated using a flexible gel polymer electrolyte (GPE), Te/C composite cathode, and Li metal anode. Microporous carbon is utilized as the Te host to buffer volume change and maintain structural stability. The GPE was prepared by using a facile solution casting method using poly(vinylidene fluoride-co-hexafluoropropylene) (PVDF-HFP) as the polymer matrix due to its excellent electrochemical and thermal stability, mechanical strength, and dielectric constant (8.4) [138-140]. The introduction of HFP polymer can decrease the crystallinity of PVDF, increase the amorphous phase in PVDF, and therefore promote Li-ion conduction [138]. 1-Methyl-2-pyrrolidinone (NMP) is employed as a liquid plasticizer to provide better electrochemical properties and interfacial wetting ability [141]. The selection of liquid plasticizers is mainly based on the safety and chemical stability against Li metal. Flammable ethylene carbonate (EC) or diethyl carbonate (DEC) poses a threat to battery safety, whereas NMP is more stable with a high flash point (95 °C) [142]. It is also found that Li metal shows superior stability with NMP compared to other solvents (EC/DMC, ACN, THF, DMF, and Acetone) [143]. Moreover, the strong-electronegativity -CO= groups of NMP are favorable for Li^{+} transportation [141]. By controlling NMP content in GPE, a high ionic conductivity of 8.0 $\times 10^{-4}$ S cm^{-1} is achieved at 25 °C, together with broad electrochemical stability up to 4.82 V and excellent interfacial compatibility with Li metal. The good interfacial contact with Li metal ensures excellent cycling stability in Li/GPE/Li symmetric cells. Moreover, it is found that, compared to

S and Se counterparts, the Li-Te battery exhibits good rate capability due to the high electrical conductivity of Te and excellent interfacial stability among GPE, Li, and Te.

5.2 Physiochemical Properties of Gel Polymer Electrolytes

The synthesis of Gel polymer electrolytes (GPE) is described in Section 3.1.4. A solution consisting of N-methyl-2-pyrrolidone (NMP), poly(vinylidenefluoride-co-hexafluoropropylene) (PVDF-HFP), and bis(trifluoromethanesulfonyl)imide lithium (LiTFSI) is heated at 60 ^{o}C in a vacuum oven. As the NMP solvent gradually evaporates, the solution transforms into GPE with certain NMP remaining. The as-synthesized GPE looks transparent and has a flat and smooth surface (**Figure 5.2.1a**). XRD pattern of GPE shows several broad characteristic peaks at 18.4°, 20.8°, 26.6°, and 38°, corresponding to the (100), (020), (110), (021) planes of crystalline PVDF [144] (**Figure 5.2.1b**). The ionic conductivity of GPE shows a strong dependence on the NMP uptake and reaches up to 8.0×10^{-4} S cm^{-1} at 25 °C with an NMP uptake of 115% (**Figure 5.2.1c**). The amount of NMP in GPE (NMP uptake) is calculated by Eq. 5.1:

$$\text{NMP uptake} = (W_0 - W_1)/W_0 \times 100\% \qquad \text{Eq. 5.1}$$

where W_0 is the weight of PVDF-HFP and NMP in GPE solution, and W_1 is the weight of GPE membrane.

The high ionic conductivity could be attributed to the strong interaction between the electronegative -CO= groups in NMP and Li-ions [145]. It should be noted that Li-ion pathways are different in solid polymer electrolytes and gel polymer electrolytes. The Li^+ hoping and coordinating/de-coordinating is completed with the segmental movement of polymer in solid polymer electrolytes [146, 147]. However, Li^+ transportation in GPE mainly relies on the motion of solvated Li^+ by liquid plasticizer [34], which is also confirmed by the strong dependence between ionic conductivity and NMP uptake in **Figure 5.2.1c**. Swelling behavior is an essential property to assess the dimensional stability of GPE. When liquid plasticizer (NMP) is added to PVDF-HFP polymer matrix, the GPE would have a swelling behavior to absorb a certain amount of plasticizer and promote Li^+ migration [148, 149]. However, serious swelling would cause the risk of NMP leakage and potential safety concern, especially when the Li/GPE/Te cell is assembled

under high pressure in a crimping machine. Therefore, the addition of a suitable amount of liquid plasticizer is important to construct a safe and conductive GPE.

Figures 5.2.1d and 5.2.1e illustrate the Nyquist plots and Arrhenius plot of GPE in a temperature range of 40-80 °C. The impedance of GPE decreases with elevated temperature due to the enhanced ion migration at high temperatures [150]. The activation energy (E_a) of GPE is calculated to be 0.11 eV. Cyclic voltammetry (CV) curve of Li|GPE|SS cells exhibits one pair of peaks at -0.20/0.11 V, assignable to Li-ion plating and stripping on stainless steel (SS), respectively (**Figure 5.2.1f**). Linear sweep voltammetry (LSV) analysis shows that GPE maintains a low current until 4.82 V, indicating excellent electrochemical stability. The wide electrochemical stability window makes this GPE a good candidate for lithium batteries.

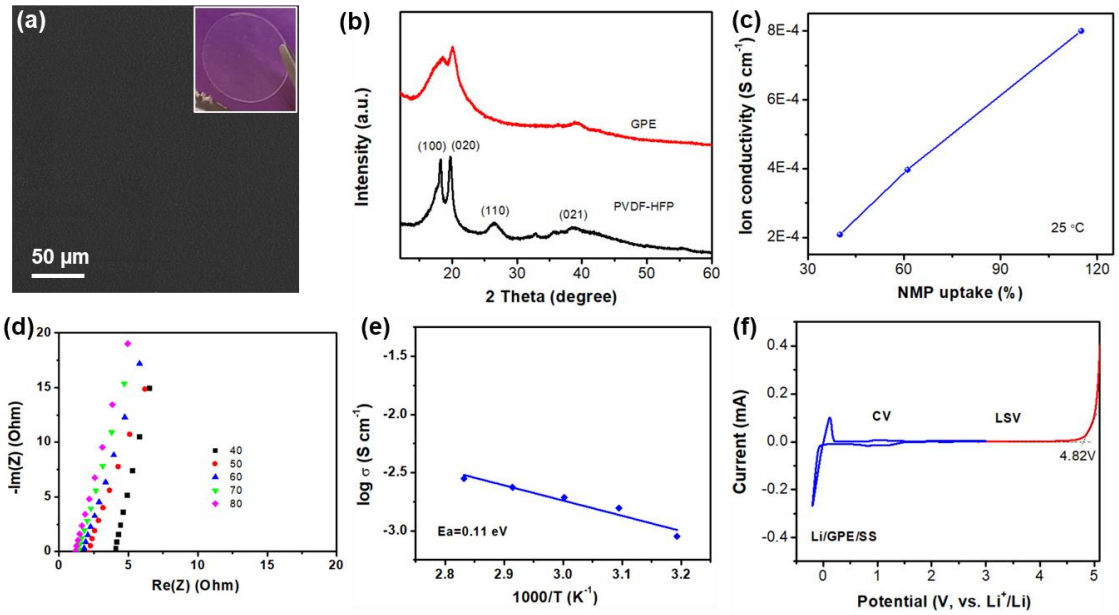

Figure 5.2.1. (a) SEM image and a digital photo of GPE, (b) XRD patterns of GPE and PVDF-HFP polymer, (c) ionic conductivities of GPEs versus NMP uptake at 25 °C, (d) Nyquist plots of GPE at 40, 50, 60, 70, and 80 °C, (e) Arrhenius plot of GPE, (f) CV and LSV of the Li/GPE/SS cell.

5.3 Interfacial Compatibility of GPE Against Li Metal

Moreover, the interfacial compatibility of GPE with Li metal is assessed in Li/GPE/Li symmetrical cells, and the Nyquist plots measured at varying storage times are compared in **Figure 5.3.1.** The electrolyte resistance (R_e) and interfacial resistance (R_{SEI}) of GPE remain stable at 8 and 28 Ω, respectively, even after three-day storage (**Table 5.3.1**), suggesting its excellent interfacial compatibility between GPE and Li metal.

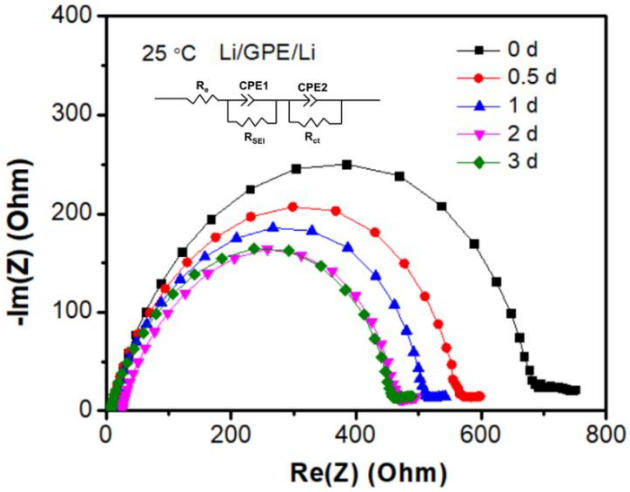

Figure 5.3.1. Nyquist plots of the Li/GPE/Li cell resting for 0, 0.5, 1, 2, and 3 days at 25 °C. The inset is the corresponding equivalent circuit model.

Table 5.3.1. Charge transfer resistance of the Li/GPE/Li cell with varying storage time.

Storage time (d)	R_e (Ω)	R_{SEI} (Ω)	R_{ct} (Ω)
0	9.5	-	684.1
0.5	8.1	30.3	539.6
1	10.0	28.6	485.0
2	26.2	26.8	424.6
3	7.4	28.0	434.6

The Li/GPE/Li symmetrical cell is also tested at various current densities of 0.05, 0.1, and 0.2 mAh cm^{-2} at 25 °C, and the voltage profiles are shown in **Figure 5.3.2**. The Li/GPE/Li cell exhibits flat voltage-time profiles and low overpotentials of 0.05, 0.1, and 0.2 V at varying current densities from 0.05 to 0.1 and 0.2 mAh cm^{-2}, respectively. This good interfacial compatibility probably benefits from the excellent flexibility of PVDF-HFP, efficient Li-ion conduction in GPE and interface, and tight interfacial contact [148, 151]. The above result shows that the flexible GPE possesses fast Li-ion transportation properties, low interfacial resistance, and good electrochemical stability against Li metal.

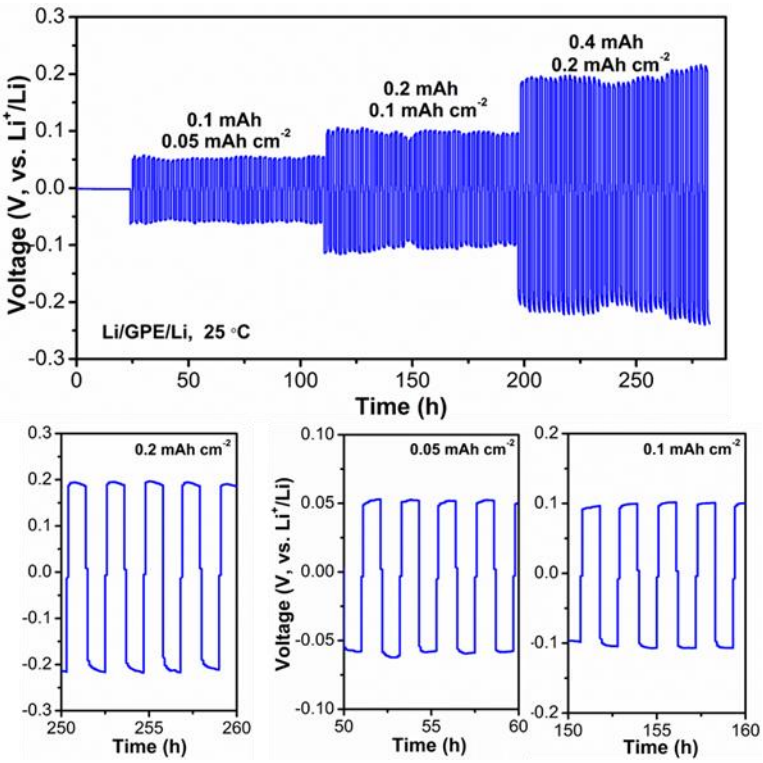

Figure 5.3.2. Voltage profiles of the Li/GPE/Li symmetrical cell at current densities of 0.05, 0.1, and 0.2 mAh cm^{-2} at 25 °C.

5.4 Quasi-Solid-State Li-Te Batteries

5.4.1 Battery Performance of Li/GPE/Te Cells

Quasi-solid-state Li-Te batteries are assembled using the optimized GPE membrane ($\sigma = 8.0 \times 10^{-4}$ S cm^{-1}), Te/C cathode, and Li metal anode (**Figure 5.4.1a**). During the lithiation process, Te reacts with Li-ions to form cubic Li_2Te, which is converted back to Te during the charging process (**Figure 5.4.1b**). This work finds that the binders (SA and PVDF) for preparing Te/C cathodes are critical for obtaining stable performance in Li-Te batteries. **Figure 5.4.1c** presents the cycling stability of quasi-solid-state Li-Te batteries with SA and PVDF binders. As seen, Li/GPE/Te cell with PVDF binder delivers a high initial discharge capacity of 870.3 mAh g^{-1}, and the capacity remains stable at 420 mAh g^{-1} for the subsequent 20 cycles. In contrast, the Li/GPE/Te cell with SA binder experiences a drastic decline from 679.3 mAh g^{-1} in the first cycle to 89.2 mAh g^{-1} in the 50th cycle. The irreversible capacity loss in the initial two cycles is mainly due to the decomposition of LiTFSI salt and the generation of solid electrolyte interphase (SEI) layer on the surface of the Te/C cathode, which is also reported in Li-Te batteries based on liquid electrolytes [46, 50]. It should be noted that after the initial cycles, the Li/GPE/Te cell showed relatively stable discharge capacities close to the theoretical value of Te, implying the formation of a stable SEI layer in the GPE/Te interface. From the galvanostatic charge-discharge curves (**Figure 5.4.1d** and **Figure 5.4.2**), the Li/GPE/Te cell with PVDF shows smaller polarization than that with SA binder in the 1st, 2nd, and 5th cycle. The single charge/discharge plateaus in **Figure 5.4.1d** confirm the one-step redox conversion from Te to Li_2Te in the quasi-solid-state Li-Te batteries. These results indicate that the quasi-solid-state Li-Te batteries with PVDF as the binder possess a higher electrochemical activity and better cycling stability. The unfavorable capacity decay of Li/GPE/Te cell might be associated with the leakage of NMP plasticizer from GPE or interface compatibility between different components [147, 149].

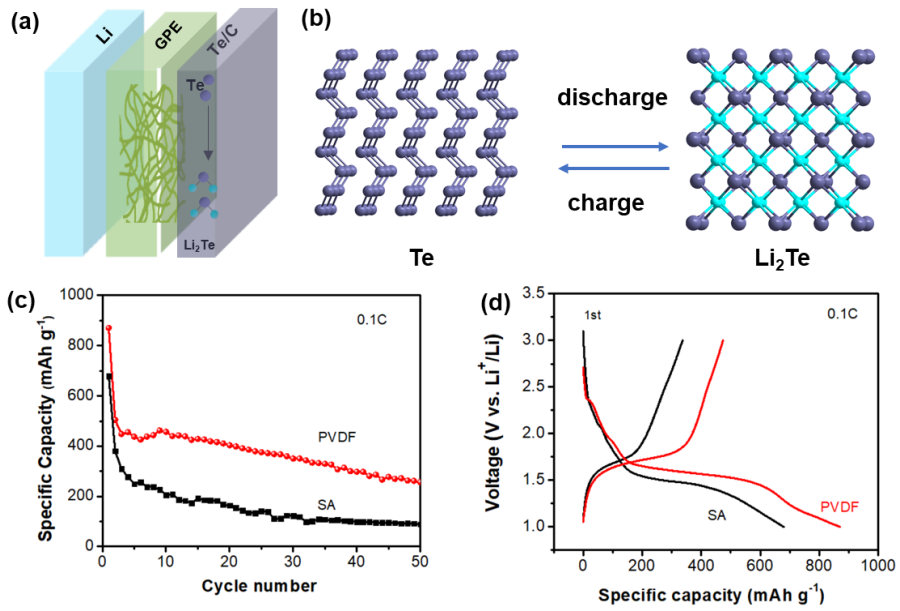

Figure 5.4.1. (a) Configuration quasi-solid-state Li-Te batteries, (b) phase transformation between Te and Li_2Te, (c) cycling performance, and (d) 1st-cycle charge-discharge curve of Li/GPE/Te batteries using PVDF and SA binders.

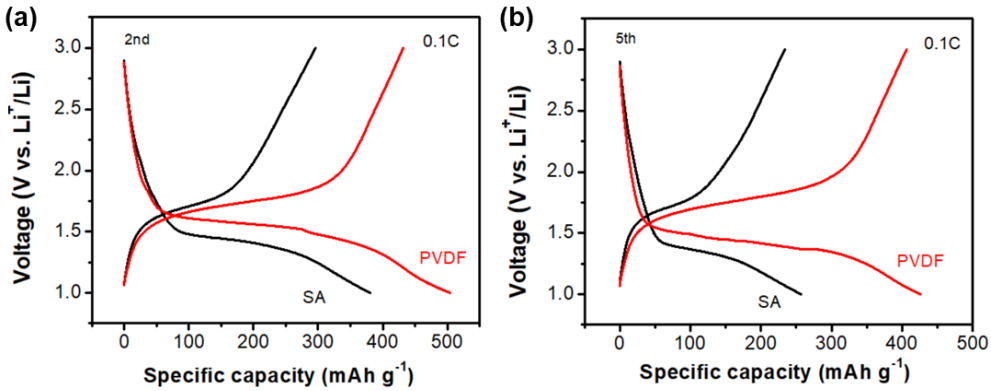

Figure 5.4.2. Charge-discharge curves of Li/GPE/Te batteries using PVDF and SA binders in the (a) 2nd and (b) 5th cycle at 0.1 C.

The Li-Te cell with liquid electrolyte (1M $LiPF_6$ in EC:DEC) and Celgard separator was tested for comparison with the Li/GPE/Te cell. It can be observed that GPE delivers almost the same discharge capacity in the first 25 cycles (**Figure 5.4.3**). The continuously decreased capacity afterward could be attributed to the leakage of NMP from GPE after long cycles or interfacial compatibility issues [146, 151]. It is noteworthy that our Li/GPE/Te cell was tested at 25 °C, and

it remained 256 mAh g^{-1}. However, the previously reported Li/SPE/Te cell with PEO matrix showed a significant capacity decline in the initial 10 cycles, and less than 200 mAh g^{-1} was retained at the working temperature of 20 °C [79]. Therefore, our GPE possesses the advantage of faster Li-ion transfer at low temperature, enabling higher energy output, a simpler testing system, and less cost input. Preventing NMP leakage from GPE or enhancing GPE/Te interfacial stability would be an urgent task in fabricating a stable and high-capacity solid-state Li-Te battery.

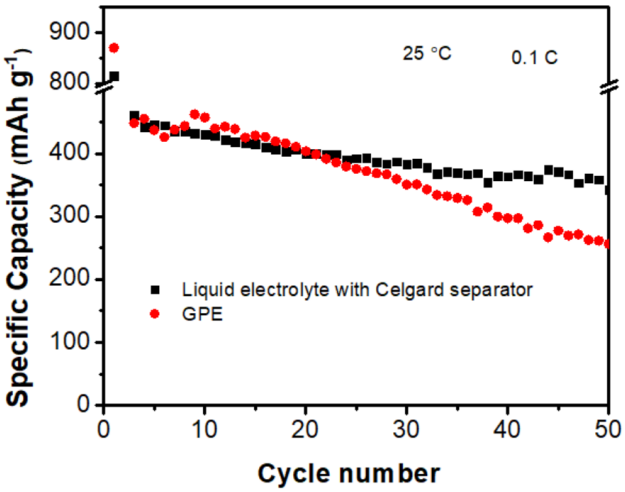

Figure 5.4.3. Cycling performance comparison of Te/C cathode with liquid electrolyte and GPE under 0.1C at 25 °C.

5.4.2 Effect of Binder on Li/GPE/Te Cells

EIS measurement of Li-Te batteries before and after cycling is carried out to understand binders' effect on the interfacial resistance. The initial R_{ct} of Li-Te batteries with PVDF binder is 131.7 Ω, lower than SA binder (284.6 Ω) (**Figures 5.4.4a** and **5.4.4d**, **Table 5.4.1**). After cycling, the PVDF binder-based Li-Te battery shows decreased R_{ct} of 91.8 Ω, still lower than that of SA binder-based one (158.3 Ω). Moreover, post-cycling observation shows that Te/C cathode with PVDF has a relatively flat and compact surface after repeated charge/discharge cycles (**Figure 5.4.4b**). The GPE surface is dense and smooth (**Figure 5.4.4c**), implying the good structural stability of battery components with PVDF binder. However, for the SA-based cells, many Te/C electrode materials are stuck onto GPE and peeled off from the current collector, leading to severe pulverization and delamination (**Figure 5.4.4e**). The active materials are also found on the GPE surface (**Figure**

5.4.4f), and the yellowish GPE membrane indicates partial dehydrofluorination of PVDF-HFP chains [143].

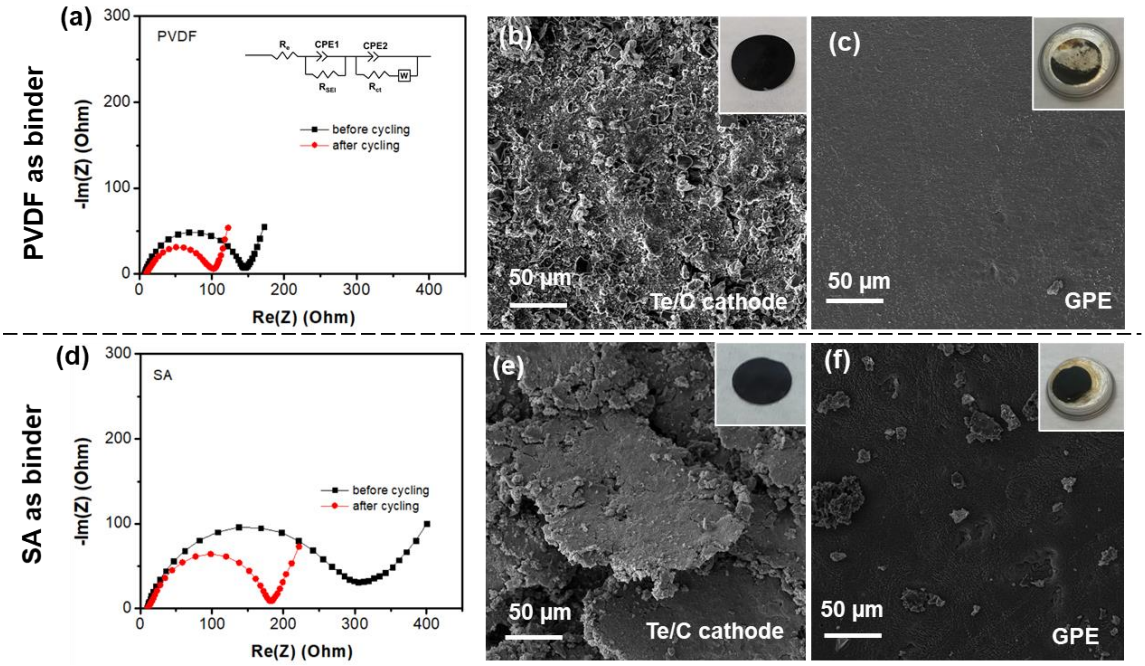

Figure 5.4.4. (a) Nyquist plots, SEM images of (b) Te/C cathode and (c) GPE recycled from Li/GPE/Te cells with PVDF binder, (d) Nyquist plots, SEM images of (e) Te/C cathode and (f) GPE recovered from Li/GPE/Te cell with SA binder.

Table 5.4.1. Resistances of the Li/GPE/Te cells with PVDF and SA binders.

Binder	PVDF			SA		
	R_e (Ω)	R_{SEI} (Ω)	R_{ct} (Ω)	R_e (Ω)	R_{SEI} (Ω)	R_{ct} (Ω)
Before cycling	7.0	-	131.7	9.4	-	284.6
After cycling	2.0	8.1	91.8	10.9	4.5	158.3

The difference in electrochemical performance and structural stability of PVDF and SA-based cells could be due to the following reasons. i) PVDF has better compatibility with GPE components (PVDF-HFP polymer and NMP solvent) and higher electronic conductivity than SA

[152], contributing to the lower interfacial resistance. ii) PVDF has higher adhesive strength with the current collector than SA to prevent active materials from delamination [153, 154], thus maintaining superior structural stability after long cycling. Herein, the PVDF binder is more suitable for the quasi-solid-state Li-Te battery to achieve excellent capacity and stability. The PVDF binder-based Li-Te battery also demonstrates good rate capacities at 0.2-2 C (**Figure 5.4.5**).

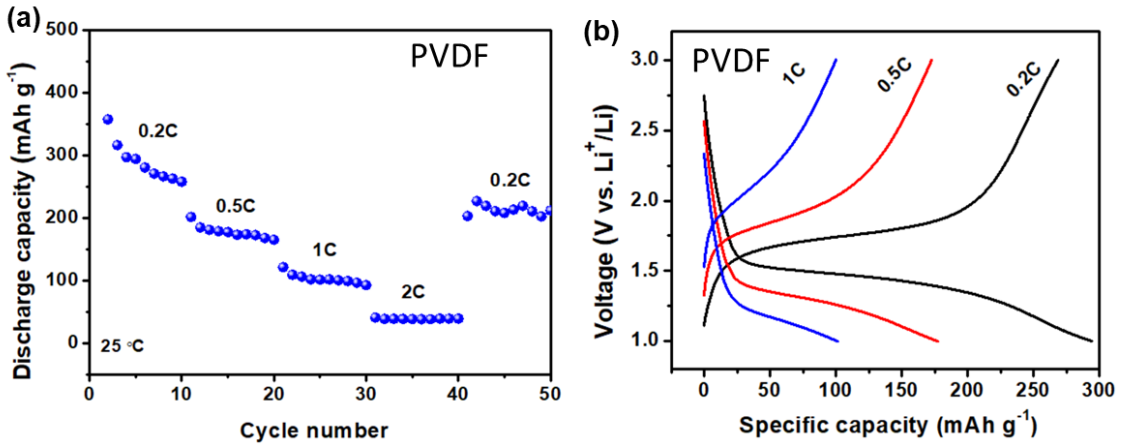

Figure 5.4.5. (a) Rate performance and (b) charge-discharge profiles at 0.2, 0.5, and 1 C of the Li/GPE/Te battery using PVDF binder.

It should be noteworthy that SA was reported to enable better cycling stability than PVDF does in liquid Li-S or Li-Se batteries [39, 155]. The opposite observation in our work is probably due to different lithium-ion migration pathways in the liquid and solid electrolytes. The rich carboxyl and hydroxyl groups in SA are beneficial for absorbing sufficient solvent molecules from liquid electrolytes to enhance lithium-ion diffusion [156, 157]. However, lithium-ion transportation in the GPE primarily requires solvation by liquid plasticizer NMP [147]. Therefore, PVDF with better compatibility with NMP contributes to superior capacity and electrochemical/structural stability in quasi-solid-state Li-Te batteries. On the other hand, the good solubility of PVDF in NMP might cause the dissolution of PVDF binder in Te cathode and result in structural change or failure. To figure out the potential issue, we put one piece of Te/C electrode (with PVDF binder) in a bottle of NMP and observed the change of electrode. The morphology of Te cathode in **Figure 5.4.6** didn't show a noticeable change after even a month, implying good reliability of the NMP plasticizer in GPE for our Li/GPE/Te battery system.

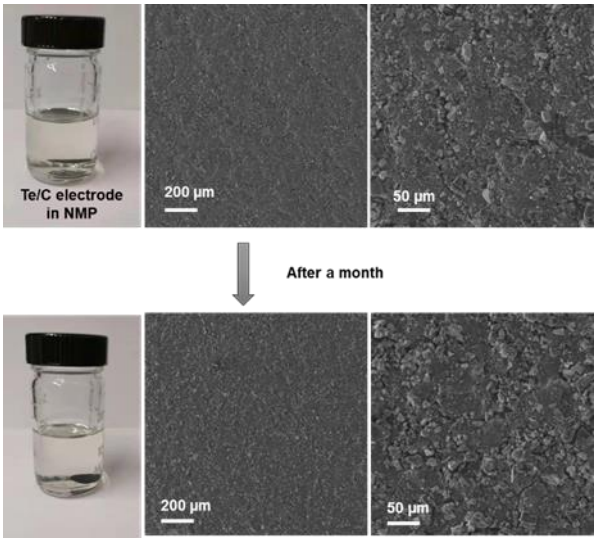

Figure 5.4.6. Digital photos and SEM images of the Te cathode before and after NMP soaking.

5.5 Performance Evaluation of Quasi-Solid-State Li-S/Se/Te Batteries

It is speculated that the good electrochemical performance of the quasi-solid-state Li-Te batteries is also benefited from the considerably high electrical conductivity of Te. S/C and Se/C cathodes are prepared using the same porous carbon and assembled into quasi-solid-state Li-S and Li-Se batteries. The S and Se contents in S/C and Se/C are determined to be 48 wt% and 45 wt% (**Figure 5.5.1**).

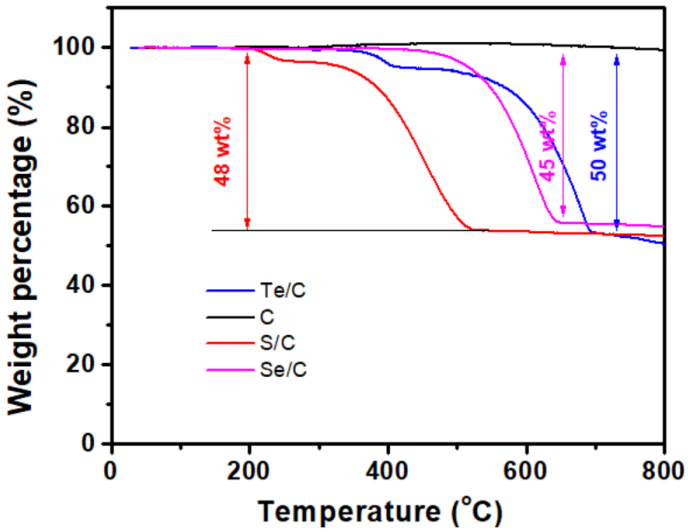

Figure 5.5.1. TGA curves of carbon and S/C, Se/C, and Te/C composites in a nitrogen environment.

Figure 5.5.2a illustrates the cycling performance of the three quasi-solid-state Li-chalcogen cells at 0.1 C (based on the mass of active materials, *i.e.*, 167.5 mA g^{-1} for S, 67.5 mA g^{-1} for Se 42 mA g^{-1} for Te). Although S/C and Se/C cathodes deliver high initial capacities of 1882.6 and 1105.7 mAh g^{-1}, their capacities rapidly drop to 188.6 and 117.3 mAh g^{-1} after 50 cycles. In comparison, Te/C sustains a relatively stable capacity and remains 256.3 mAh g^{-1} in the 50th cycle. **Figure 5.5.3** depicts the galvanostatic charge-discharge profiles of all the Li-S/Se/Te batteries. It could be found that the lithiation/de-lithiation plateaus of the Li-S/Se batteries become narrower versus cycle number, implying poor reversibility of S/C and Se/C cathodes in GPE-based batteries. In contrast, Te/C cathode exhibits well-overlapped voltage profiles. **Figure 5.5.2b** shows capacity retention (vs. corresponding theoretical capacity) of Li-S/Se/Te batteries at 0.2-2 C. The Te/C cathode retains 85.1%, 44.0%, and 26.0%, outperforming S/C (41.0%, 9.5%, and 6.7%) and Se/C (50.8 %, 9.6 %, and 7.3) cathodes, at 0.2, 0.5, and 1 C, respectively. From the Nyquist plot in **Figure 5.5.2c**, the Te/C cathode has the smallest R_{ct} (131.7 Ω) compared to S/C (518.8 Ω) and Se/C (136.0 Ω) cathode before cycling (**Table 5.5.1**), verifying the fastest electron transfer in the Te/C cathode. After repeated redox reactions, S/C and Se/C cathodes have enlarged R_{ct} of 562.8 and 131.2 Ω and R_{SEI} of 98.8 and 49.0 Ω, whereas Te/C cathode presents the smallest R_{ct} of 91.8 Ω and R_{SEI} of 8.1 Ω. The decreased R_{ct} in Li/GPE/Te cell implies faster electron transfer after repeated lithiation/delithiation behaviors, which could be resulted by the absence of polytellurides [71]. GPE-based Li-S and Li-Se cells show significant capacity decay after only 5 cycles. The multi-step discharge curves in **Figure 5.5.3** indicate the presence of polysulfides and polyselenides. These less electrically conductive compounds might impede electron transfer, thus leading to increased R_{ct}, shuttle effect and inferior cycling performance [40, 158], as shown in **Figure 5.5.2**. Therefore, fast electron transfer and low interfacial resistance in the Te/C cathode result in enhanced reaction kinetics, making Te stand out as a promising cathode material in the GPE-based quasi-solid-state batteries. It should be noted that this comparison aims to verify the applicability of the GPE in lithium-chalcogen batteries using the same cathode structure and preparation procedures, and the electrochemical performance of S/Se cathodes could be improved through the optimization of cathode structure.

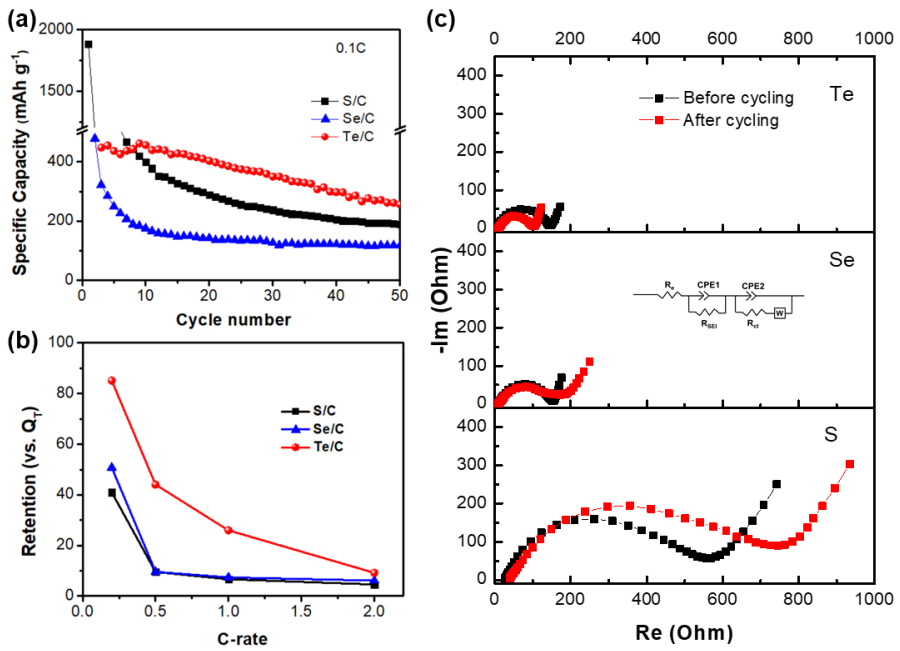

Figure 5.5.2. (a) Cycling performance at 0.1 C, (b) capacity retention at 0.2-2 C of the S/C, Se/C, Te/C cathodes in quasi-solid-state batteries, and (c) Nyquist plots of the Li-S/Se/Te batteries before and after cycling.

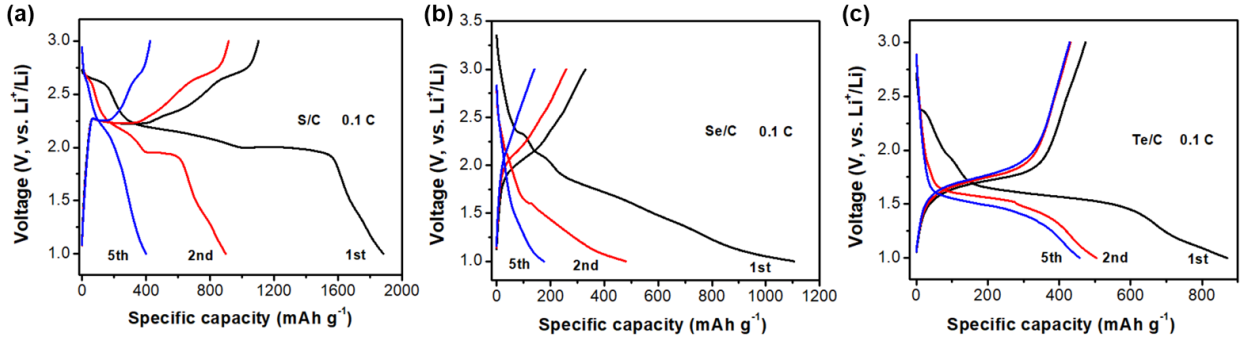

Figure 5.5.3. Galvanostatic charge-discharge profiles of (a) S/C cathode, (b) Se/C cathode, and (c) Te/C cathode in the 1st, 2nd, and 5th cycle at 0.1 C.

Table 5.5.1. Resistances of the Li/GPE/chalcogen cells.

Electrode	Before cycling			After cycling		
	R_e (Ω)	R_{SEI} (Ω)	R_{ct} (Ω)	R_e (Ω)	R_{SEI} (Ω)	R_{ct} (Ω)
S/C	31.6	-	518.8	39.5	98.8	562.8
Se/C	10.3	-	136.0	9.0	49.0	131.2
Te/C	7.0	-	131.7	2.0	8.1	91.8

5.6 Chapter Summary

In summary, the work in this chapter develops a flexible gel polymer electrolyte with high ionic conductivity of 8.0×10^{-4} S cm^{-1} at 25 °C and a broad electrochemical voltage window up to 4.82 V. This soft GPE structure ensures good interfacial contact with Li metal, leading to excellent cycling stability in Li/GPE/Li symmetric cells at room temperature. Moreover, the GPE is assembled with Te/C cathode to build a quasi-solid-state Li-Te battery, which demonstrates superior electrochemical performance than their S/C or Se/C counterparts in the same cell configuration. This work presents several facile strategies to fabricate key cathode and GPE components to develop safe and high-performance solid-state Li-Te batteries. It could be extended to manufacture other Li-based quasi-solid-state batteries. In the future, more efforts should be focused on addressing the issues of interfacial compatibility between Te and GPE and the leakage of liquid plasticizers in GPE.

Chapter 6 Composite TeS Cathodes for High-Energy-Density Batteries

6.1 Introduction

The energy density of the Li-S battery, with an average voltage of 2.15 V, can reach a maximum of 2500 W h kg^{-1} (2800 W h L^{-1}) which outperforms that of lithium-ion batteries using insertion-type cathodes (*e.g.*, $Li_{1/3}Ni_{1/3}Co_{1/3}Mn_{1/3}O_2$ and $LiFePO_4$) [86]. However, the practical application of Li-S batteries has been hindered by the low utilization of active S material, sluggish redox reaction kinetics, and the "shuttle effect" [28, 87]. The poor reaction kinetics of Li-S batteries originates from the ultralow electrical conductivity of S (5×10^{-28} S m^{-1}), which significantly decreases reversible discharge capacity, especially at high current densities [26]. The well-known "shuttle effect" results from the dissolution of polysulfide intermediates into the electrolyte and diffusion to and reaction with lithium anode, leading to rapid capacity decay and low Coulombic efficiency (CE) [158].

Extensive efforts have been devoted to developing novel sulfur cathode materials and structures to address the above challenges in Li-S batteries. For example, various porous carbon hosts (*e.g.*, activated carbon, mesoporous carbon, CMK-3 [122, 123, 125, 127]) and conducting polymers (polyacrylonitrile, *etc.* [91, 159]) have been utilized to confine S, trap polysulfides and improve the structural stability of S cathodes. Sulfiphilic metallic oxide (Ti_4O_7) [160] and sulfides (CoS_2 [161], Co_9S_8 [162]) have also been applied as polysulfide absorbents to suppress the shuttle effect and accelerate redox reactions. Refining S cathode chemistry at the molecular level is another effective strategy to manipulate the redox reactions of Li-S batteries [88]. Amine *et al.* firstly proposed the concept of Li-Se_xS_y batteries in 2012 [163]. They found that the SeS_2 cathode possessed higher energy density and faster reaction kinetics than S only cathode in lithium and sodium metal batteries. The enhanced electrochemical performance benefits from the superior electrical conductivity of selenium (1×10^{-3} S m^{-1}) and its lithium storage capability (theoretical capacity of 675 mAh g^{-1}) [17]. Lou *et al.* [164] demonstrated a long-cycle Li-SeS_2 battery by confining SeS_2 into mesoporous CMK-3 with a polydopamine (PDA) protection sheath. This cathode delivered a high capacity of more than 1,000 mAh g^{-1} at 0.2 A g^{-1}. Huang *et al.* [165]

found that the Se_5S_3 composite showed the best cycling and rate stability among a series of Se_xS_y composites with different Se/S molar ratios in a carbonate-based electrolyte composed of 1.2 M $LiPF_6$ in ethylene EC:DMC with 5 wt% fluoroethylene carbonate (FEC). The enhanced stability was attributed to the protection of a thin cathode electrolyte interphase and lowered bond-breaking and lithiation energy by S substitution in the Se_8 molecule.

Inspired by the success of Se_xS_y composites, Te_xS_y composite cathodes are gaining much attention due to the remarkably higher electrical conductivity of tellurium (Te, 2×10^2 S m^{-1}) than Se and S [69]. The highly heteropolar Te-S bond not only improved the electrical conductivity of S owing to the higher *p* orbitals of Te but also effectively anchored S in the CMK-3 scaffold to suppress the formation and dissolution of polysulfides [83]. Additionally, Qian *et al.* [80] revealed that Te doping facilitated the lithiation/delithiation reactions of the Li-S system and lowered the lithium-ion diffusion energy barrier in Li_2S based on density functional theory (DFT) simulations. Moreover, the Te-doped sulfurized polyacrylonitrile cathode (Te_xS_y@pPAN) achieved fast redox conversion from soluble S_{3-4} to Li_2S through the dissolution-deposition mechanism, thus mitigating the dissolution of polysulfides and ensuring excellent cycling performance of Te_xS_y@pPAN in the ether electrolyte (1M LiTFSI in DOL:DME with 0.2M $LiNO_3$) [85].

Previously reported Te_xS_y composite cathodes incorporated a small fraction of Te below 5 wt%. To date, there is a lack of fundamental understanding of the effect of higher Te-S alloy content. The effect of higher Te content or Te/S molar ratio on the electrochemical performance of Te_xS_y cathodes needs to be systematically explored and discussed. The optimal structure of the heteroatomic Te_xS_y molecule is worth further exploration to develop a thermodynamically and electrochemically stable cathode.

Furthermore, the reaction mechanism of Li-Te_xS_y batteries in carbonate-based electrolytes is still unclear. The selection of electrolytes in practical battery applications should take various factors into consideration, such as electrochemical window, chemical stability, ionic conductivity, and materials cost [166, 167]. Compared to ether-based electrolytes, carbonate-based electrolytes show greater promise in the commercialization of Li-S batteries due to their better safety and commercial maturity [168]. Carbonate solvents (e.g., EC, DEC, DME) usually have higher boiling points than ether solvents (DOL, DME) [168, 169]. For example, EC and DEC possess boiling points of 248

and 126 °C, respectively, much higher than DOL (78 °C) and DME (84 °C) [170]. The higher boiling point indicates the extended potential working temperature and superior safety. Moreover, some flame-redundant additives have been applied in carbonate-based electrolytes used in commercial Li-ion batteries to further enhance battery safety [171]. On the other hand, carbonate-based electrolytes have been widely used in Li-ion battery industry over 30 years [172]. Potentially, it is a good choice to employ carbonate electrolytes towards the commercialization of Li-S batteries. Most importantly, the inevitable "shuttle effect" challenge in ether electrolytes is able to be circumvented by turning the "dissolution-precipitation" reaction pathways in ether electrolytes into a solid-phase conversion mechanism without the generation of soluble lithium polysulfides in carbonate electrolytes [92, 173].

However, it is known that S/mesoporous carbon cathode is usually chemically incompatible in carbonate-based electrolytes due to the nucleophilic attack between carbonate solvents and polysulfides at either the ether or carbonyl carbon atoms on the carbonate molecules during the first discharge process [31]. To date, the study of Te_xS_y molecules confined in mesostructured carbon with carbonate electrolytes is still in its infancy, such as redox conversion, solid electrolyte interphase, and reaction kinetics. Therefore, an in-depth understanding of these fundamental issues is critical to promoting the development of high-energy-density Li-Te_xS_y batteries in carbonate-based electrolytes.

Herein, we present a wide range of Te_xS_y composites from Te_1S_7 to Te_7S_1 confined in mesoporous Ketjenblack (KB) carbon. The electrochemical performance of Te_xS_y/KB in the carbonate-based electrolyte is investigated and discussed. Theoretical simulations suggest that the lowered energy barrier for Li-ion migration in Te_1S_7 upon lithiation and substantially improved delithiation kinetics compared to S. Furtherly, kinetics analysis proves a more favorable Li-ion transport and electron transfer in Te_xS_y/KB, thus boosting the redox conversion upon lithiation/delithiation. Meanwhile, the Te_1S_7/KB cathode delivers a significantly improved capacity of 1306.7 mAh g^{-1} compared to its S/KB counterpart (483.7 mAh g^{-1}) in carbonate-based electrolytes. Excellent cycling stability and rate capability are also observed for the Te_1S_7/KB cathode, indicating enhanced utilization of active materials and reaction kinetics. Moreover, it is revealed that stable solid electrolyte interphase is generated on the surface of Te_1S_7/KB to maintain good structural stability and prevent the loss of active materials from mesopores, contributing to a highly

reversible redox conversion. This work deepens the understanding of Te-S solid solution chemistry and demonstrates a feasible strategy to achieve high-performance rechargeable Li-Te_xS_y batteries.

6.2 Synthesis and Structure Analysis of Te_xS_y Composites

Te and S powders with specific molar ratios (from 1:7 to 7:1) are firstly mixed by ball milling to prepare Te&S mixture. The color of the Te&S mixture becomes darker with increasing Te content and changes from greenish for Te_1S_7 to black for Te_7S_1 (**Figure 6.2.1**). Subsequently, the Te&S mixture is sealed in a quartz tube under vacuum and heated at 450 °C for 10 h to obtain Te_xS_y composites, as illustrated in **Figure 6.2.2a**. It was reported that Te-S covalent bonds in the molten Te_xS_y mixtures could be formed at high temperatures (**Figure 6.2.3**) [174, 175]. After heat treatment, the obtained Te_xS_y composites are analyzed by Raman and X-ray diffraction (XRD) to investigate possible Te-S interaction. Pure S and Te are also tested for comparison. **Figure 6.2.2b** shows Raman spectra of Te&S mixture and Te_xS_y composites. The ball-milled Te&S mixture with a Te/S molar ratio of 1:7 retains the characteristic peaks of Te (122 cm^{-1}) and S (154, 220, and 174 cm^{-1}), implying that ball-milling causes mainly physical mixing of Te and S. After heat treatment, the Te_1S_7 composite primarily displays the characteristic peak of Te with a peak shift to 126 cm^{-1}, suggesting the formation of Te-S bond. With more Te incorporation with S, the Te_xS_y composites (from Te_2S_6 to Te_7S_1) also show only characteristic peaks of Te. In addition, the Te_xS_y composites exhibit intense crystalline peaks of Te located at 23.0° and 27.6°, corresponding to the (100) and (011) planes of hexagonal Te (JCPDS No: 79-0736), as seen from XRD patterns in **Figure 6.2.2c**. With increasing Te content, the peaks at 23-40° originating from S gradually disappear, implying the crystal structure change of Te_xS_y composites.

Figure 6.1.1. Digital photos of Te&S mixtures after ball milling.

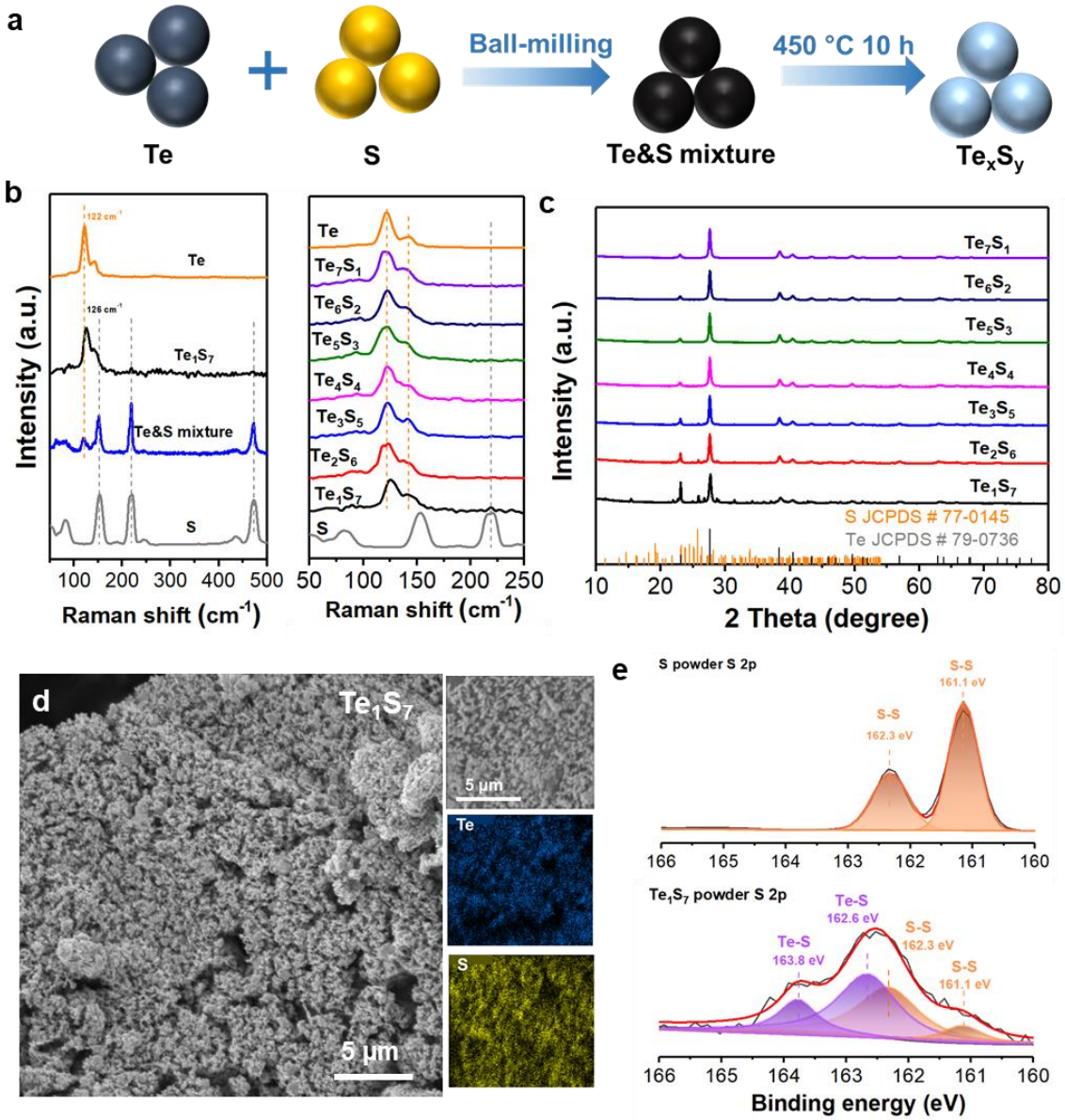

Figure 6.2.2. Preparation schematic of Te_xS_y composites and their structure and morphology. (a) Schematics of Te_xS_y composite synthesis process. (b) Raman spectra. (c) XRD patterns. (d) SEM image and EDS mapping of Te_1S_7 particles. (e) XPS S 2p spectra of S and Te_1S_7 powders.

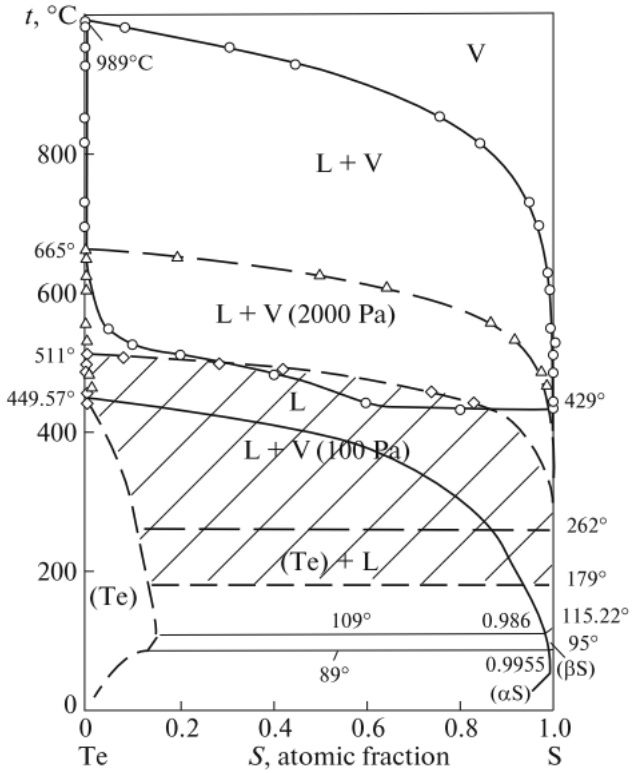

Figure 6.2.3. Te-S phase diagram. [175]

The as-prepared Te_1S_7 composite shows porous particles with uniform distribution of Te and S, as seen in SEM and EDS mapping (**Figure 6.2.2d**). The porous structure is also found in the cross-sectional Te_1S_7 particle (**Figures 6.2.4a-b**). As Te content in Te_xS_y increases, the Te_xS_y composites demonstrate a similar porous structure as seen from SEM images (**Figures 6.2.4c-h**). Moreover, the high-resolution S 2p XPS spectra are presented in **Figure 6.2.2e** to characterize the chemical state of S atoms in S and Te_1S_7. The predominant doublet located at 162.3 and 161.1 eV is assigned to S-S bonds in both S and Te_1S_7 composite. Meanwhile, a new pair of peaks at 163.8 and 162.6 eV are deconvoluted and attributed to the formation of Te-S bonds due to the strong electronegativity of S [85]. The two peaks of Te_1S_7 powder at 584.2 and 573.6 eV in Te 3d XPS spectra (**Figure 6.2.5**) further confirm Te-S bonds in Te_1S_7 composite. Therefore, the heteropolar Te-S chemical bonds are proved to form in the as-synthesized Te_xS_y composites with uniformly distributed Te.

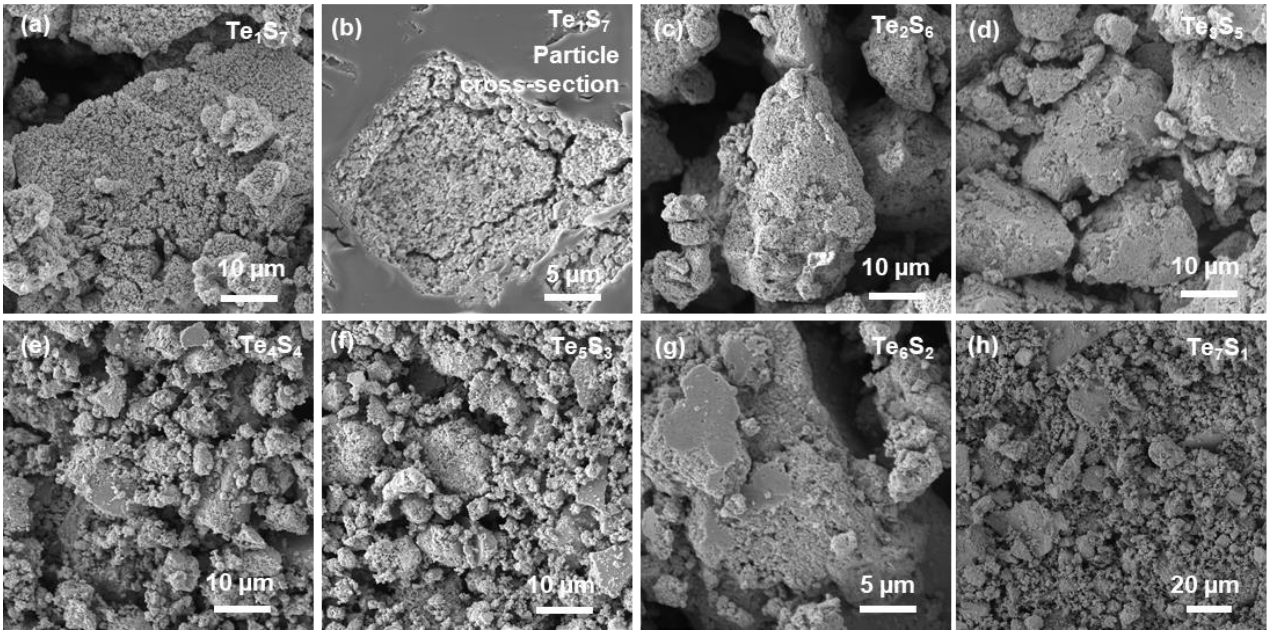

Figure 6.2.4. SEM images of (a) Te_1S_7, (b) cross-sectional Te_1S_7 particles, (c) Te_2S_6, (d) Te_3S_5, (e) Te_4S_4, (f) Te_5S_3, (g) Te_6S_2, and (h) Te_7S_1 composites.

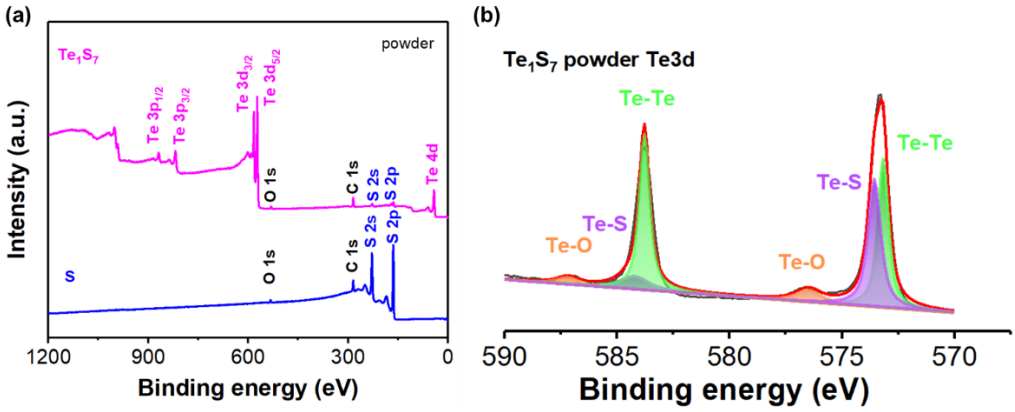

Figure 6.2.5. (a) XPS survey scans of S and Te_1S_7 powders and (b) Te 3d XPS spectra of Te_1S_7 powder.

6.3 DFT Simulations

To better understand the interplay of Te substitution into S_8 molecules, density functional theory (DFT) calculations were carried out for Te_xS_y composites. **Figure 6.3.1** illustrates the crystal structures of Li, S, Te, and Te_xS_y molecules, and the most-likely Li migration pathways in the random-solid solutions of Te and S with the atomic fractions matching the experimentally studied

stoichiometric ratios are listed in **Table 6.3.1**. In **Figure 6.3.2**, the atomic-fraction dependence of the most-likely three pathways is shown alongside those of Li_2S and Li_2Te. Among all studied atomic fractions, $Li_2Te_1S_7$ has the lowest energy barriers, indicating the easiest Li migration and eventually delithiation. Thus, we further analyze Te_1S_7 alongside S_8 to gain insight into the effects of low-concentration Te substitution in the Li redox kinetics.

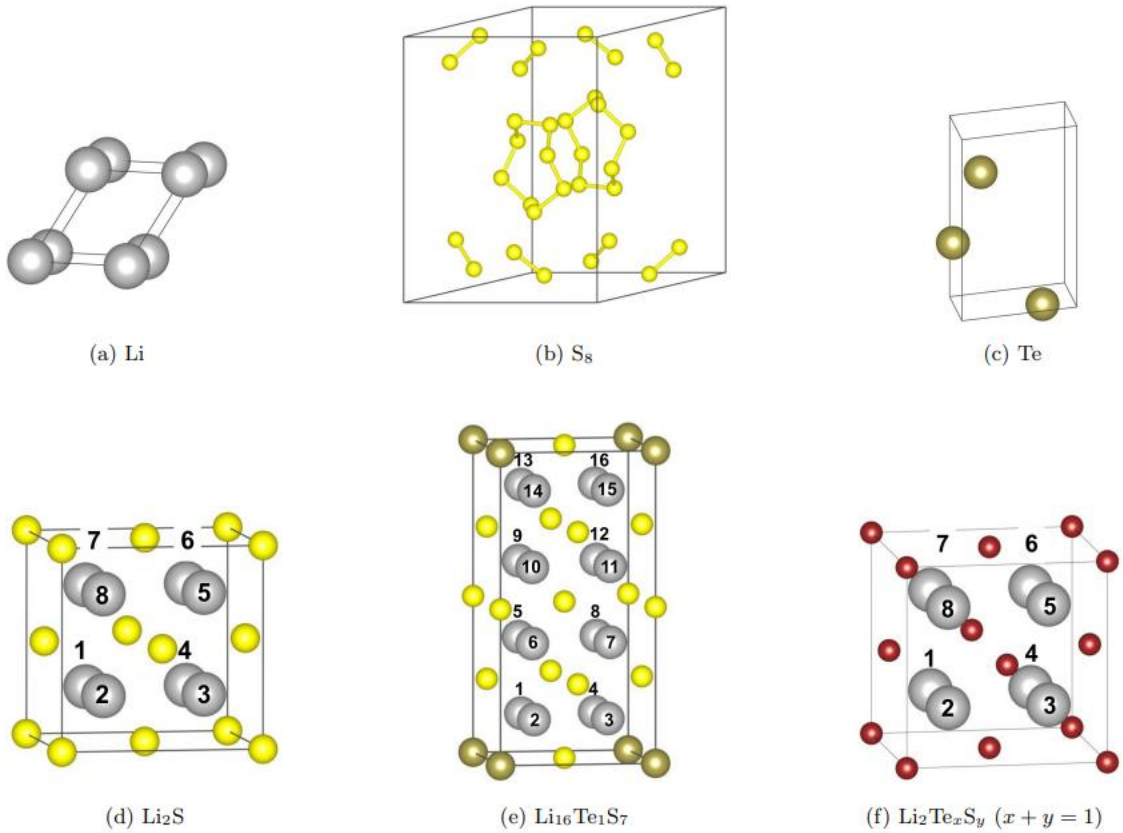

Figure 6.3.1. The representative crystal structures of (a) Li, (b) S_8, (c) Te, (d) Li_2S, (e) $Li_{16}TeS_7$, and (f) $Li_2Te_xS_y$.

Table 6.3.1. The possible migration pathways in Li_2S, $Li_{16}S_7Te$, and $Li_2Te_xS_y$. The Li atomic site numbering is shown in **Figure 6.3.1**.

Path 1: 1 → 2	Path 6: 1 → 8	Path 11: 1 → 15	Path 16: 5 → 10
Path 2: 1 → 3	Path 7: 1 → 10	Path 12: 1 → 16	Path 17: 5 → 11
Path 3: 1 → 5	Path 8: 1 → 11	Path 13: 5 → 6	Path 18: 5 → 14
Path 4: 1 → 6	Path 9: 1 → 12	Path 14: 5 → 7	Path 19: 5 → 15
Path 5: 1 → 7	Path 10: 1 → 14	Path 15: 5 → 9	

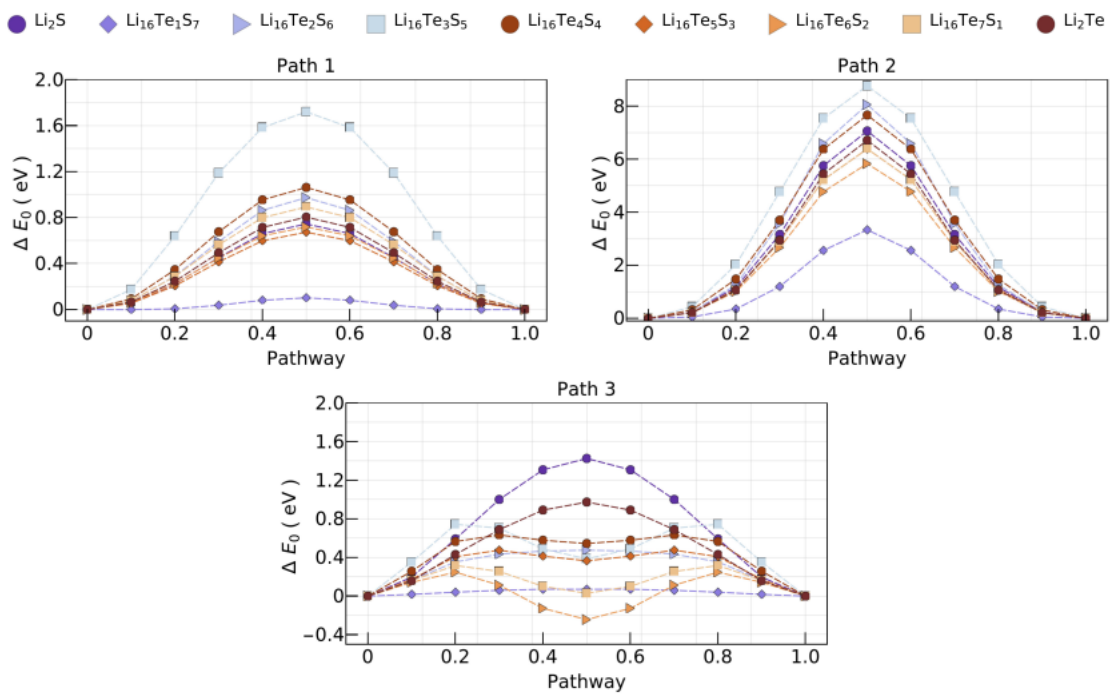

Figure 6.3.2. Composition dependence of the energy profile of possible migration pathways of the random-solid solution of $Li_2Te_xS_y$ (x + y = 1) within the conventional Kohn-Sham density-functional theory.

In **Figures 6.3.3a-d**, the optimized ring structures and the electronic density differences of S_8, Te_1S_7, Li_2S_8, and $Li_2Te_1S_7$ are shown alongside the associated Te-substitution and lithiation energies. The Te_1S_7 is energetically less favorable than S_8, albeit still stable, with a formation energy (ΔU) of −30.68 eV, as listed in **Table 6.3.2**. Comparing their respective charge density difference, the neighboring S atoms becomes more negatively charged while Te-center is overall less charged, indicating the charge transfer from Te to S atoms. When comparing Li_2S_8 and $Li_2Te_1S_7$ cases, it leads to a higher energetic lithiation by ∼0.20 eV, yet still a highly stable ring structure. In summary, the single Te substitution to S_8 does not significantly worsen or improve the stability or the lithiation process of rings. The crystallized Li_2S and $Li_{16}Te_1S_7$, shown in **Figures 6.3.3e-f**, respectively, are energetically almost equally stable as indicated by the enthalpies of mixings (ΔH) of −1.37 eV and −1.31 eV, respectively. The energy profiles of the most-likely Li-migration pathways are described in **Figure 6.3.1** and **Table 6.3.1**, using the nudged elastic band (NEB) method shown in **Figure 6.3.4**. Those with the lowest energy barriers are marked with arrows in **Figures 6.3.3e-f**, for which their energy profiles are shown in **Figure 6.3.3g**. $Li_{16}Te_1S_7$ has a significantly lower energy barrier compared to Li_2S. Moreover, $Li_{16}Te_1S_7$ has a lower delithiation energy ($\Delta E_{\mathrm{delit}}$) of 4.74 eV compared to 5.10 eV of Li_2S. Comparing the local density of states (LDOS) of the two solids (**Figures 6.3.3h-i**), the Te substitution pushes the S 2*p* states closer to the Fermi level and improves the electrical conductivity in $Li_{16}Te_1S_7$. In particular, it closes the gap between the valence-band edge, which is mostly S 2*p* and Te 5*p* states, and the conduction-band edge, which is mostly Li 2*s* states. Comparing **Figures 6.3.3j-k**, the more delocalized charge-density differences around the Te atoms in $Li_{16}Te_1S_7$ compared to site-equivalent S atoms in Li_2S indicates lower energy barriers throughout the Li migration pathway. This can be further seen when the charge-density differences are analyzed in the [001]-planes, shown in **Figure 6.3.5**, for which the positive charges are more delocalized between the Te and S atoms in $Li_{16}Te_1S_7$ rather than highly localized on the S atoms in Li_2S. Thus, it leads to a lower energy barrier and delithiation energy in $Li_{16}Te_1S_7$. In summary, $Li_{16}Te_1S_7$ has the lowest energy profile of Li migration pathways and substantially improved delithiation kinetics by the lowered energy barrier, benefiting from the delocalized charge density and improved electrical conductivity.

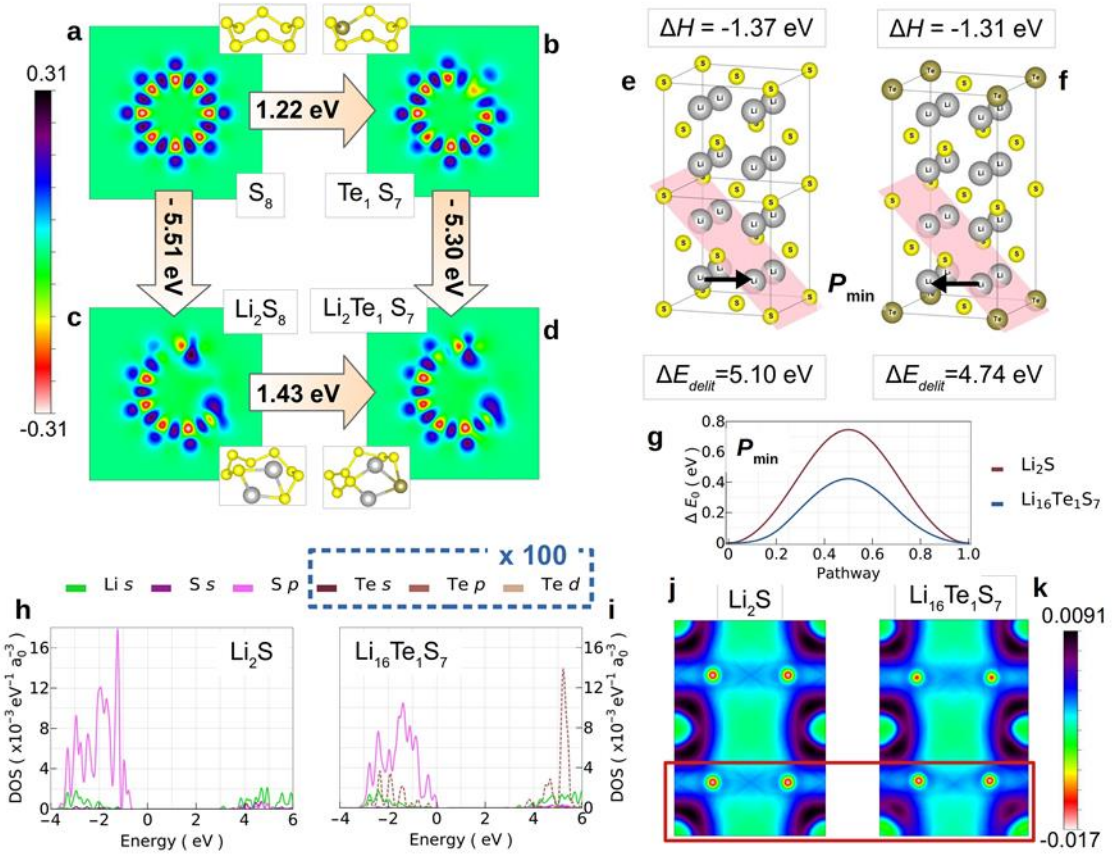

Figure 6.3.3. Density functional theory calculations. The molecular structures and electronic charge densities (minus the superposed atomic densities) of (a) S, (b) Te_1S_7, (c) Li_2S_8, and (d) $Li_2Te_1S_7$, shown alongside the relative energy differences. The crystal structures, formation energies, and the delithiation energies of (e) Li_2S and (f) $Li_{16}Te_1S_7$. The minimum migration paths are shown with black arrows. (g) The energy profiles are calculated using the nudged elastic band. The local density of states (LDOS) of (h) Li_2S and (i) $Li_{16}Te_1S_7$, for which the LDOS of the angular momentum channels of Te are scaled by 100 for a more compact illustration. The electronic charge densities (minus the superposed atomic densities) of (j) the [011] plane of Li_2S and (k) the [012] plane of $Li_{16}Te_1S_7$. The corresponding planes are illustrated in (e) and (f).

Table 6.3.2. The formation energies (ΔU) and the lithiation energies (ΔE_{lit}) of the ring structures, and the enthalpy of mixing (ΔH) and the delithiation energies (ΔE_{delit}) of the crystal structures in eV units.

	ΔU	ΔE_{lit}		ΔH	ΔE_{delit}
S_8	-31.902	-5.507	Li_2S_8	-1.366	5.099
Te_1S_7	-30.681	-5.302	$Li_{16}Te_1S_7$	-1.306	4.738
Te_8	-23.139	-5.136	Li_2Te_8	-1.054	4.192

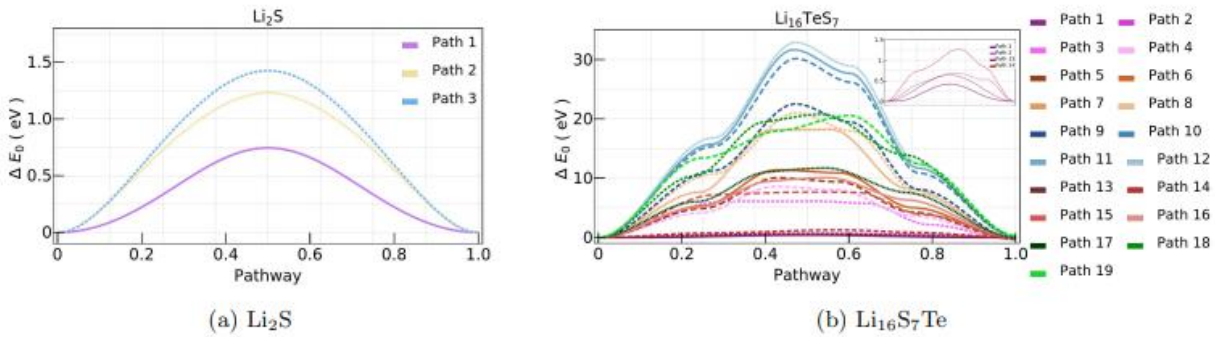

(a) Li_2S (b) $Li_{16}S_7Te$

Figure 6.3.4. The energy profiles of possible migration pathways of (a) Li_2S and (b) $Li_{16}TeS_7$ calculated within the nudged elastic band.

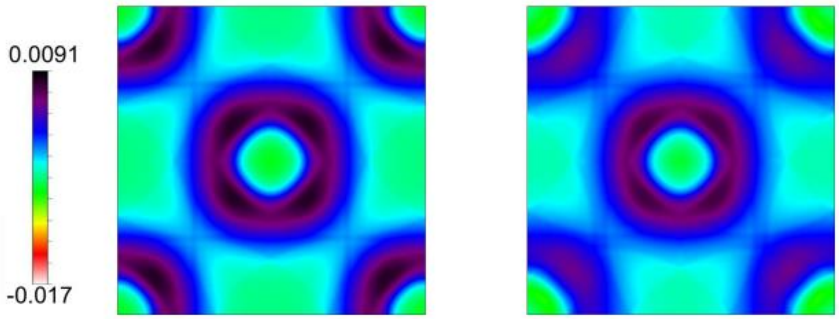

(a) Li_2S (b) $Li_{16}S_7Te$

Figure 6.3.5. The electronic charge densities (minus the superposed atomic densities) of the [001] planes for (a) Li_2S and (b) $Li_{16}TeS_7$.

6.4 Morphology and Structure of TexSy/KB Composites

The commercial KB (EC600JD) with irregular shapes (**Figure 6.4.1**) is selected as the Te_xS_y host. As seen in the BET result (**Figure 6.4.2a)**, KB possesses a type IV nitrogen adsorption/desorption isotherm, manifesting a mesopore-rich structure [120]. **Figure 6.4.2b** illustrates the narrow pore size distribution, with most pores centered at 4 nm. The pore volume and BET-specific surface area are 2.6 cm^3 g^{-1} and 1382.4 m^2 g^{-1}, respectively, providing sufficient loading sites for Te_xS_y active materials.

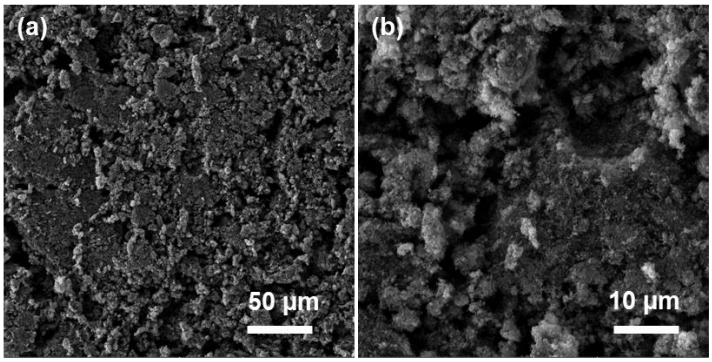

Figure 6.4.1. SEM images of Ketjenblack (KB, EC600).

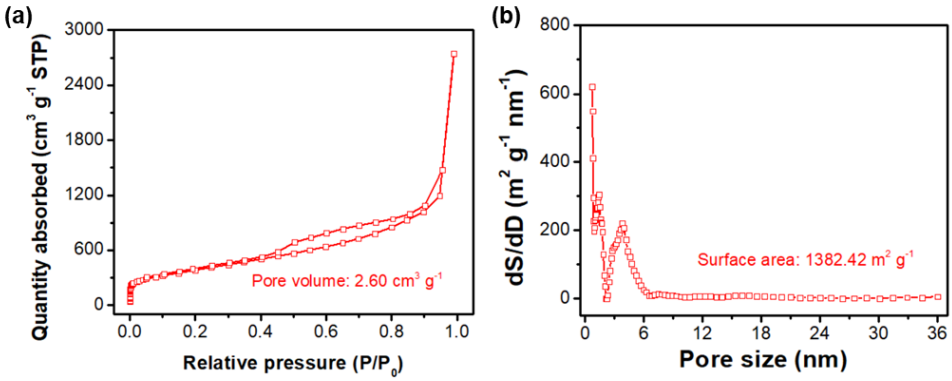

Figure 6.4.2. (a) Nitrogen adsorption/desorption isotherm curve, and (b) pore size distribution of KB.

The Te_xS_y/KB composites are prepared by a melt-diffusion method. Te_xS_y and KB powders are ball-milled for 2 h and then heated in a sealed quartz tube at 480 °C under vacuum to ensure complete infusion of Te_xS_y into KB micro/mesopores. After cooling to room temperature, the as-obtained Te_xS_y/KB shows similar morphology with particle diameters of around 2 μm as observed

in SEM images (**Figure 6.4.3a** and **Figure 6.4.4**). TEM and high-resolution TEM images in **Figures 6.4.3b-c** disclose the amorphous structure of Te_1S_7 confined in the KB skeleton. HAADF image and EDS mapping in **Figure 6.4.3d** reveal the uniform distribution of Te and S elements in the KB carbon matrix. The Te_1S_7/KB composite only shows one broad XRD diffraction peak at around 25°, which is indexed to KB carbon (**Figure 6.4.3e**) [25]. The disappearance of S and Te characteristic peaks suggests that Te_1S_7 well penetrates into the porous channels of KB [70]. With the increase of Te content in Te_xS_y composites, the crystalline peaks at 27.6° appear and become more intense and can be attributed to the (011) plane of hexagonal Te (JCPDS No. 79-0736). Similarly, the characteristic peak of Te is absent in the Te_1S_7/KB composite and present for other Te_xS_y/KB, as observed in Raman spectra (**Figure 6.4.3f**), which is consistent with corresponding XRD patterns. In particular, there is a peak shift from 129 cm^{-1} for Te_2S_6/KB to 123 cm^{-1} for Te_7S_1/KB, which is probably caused by Te-S interaction.

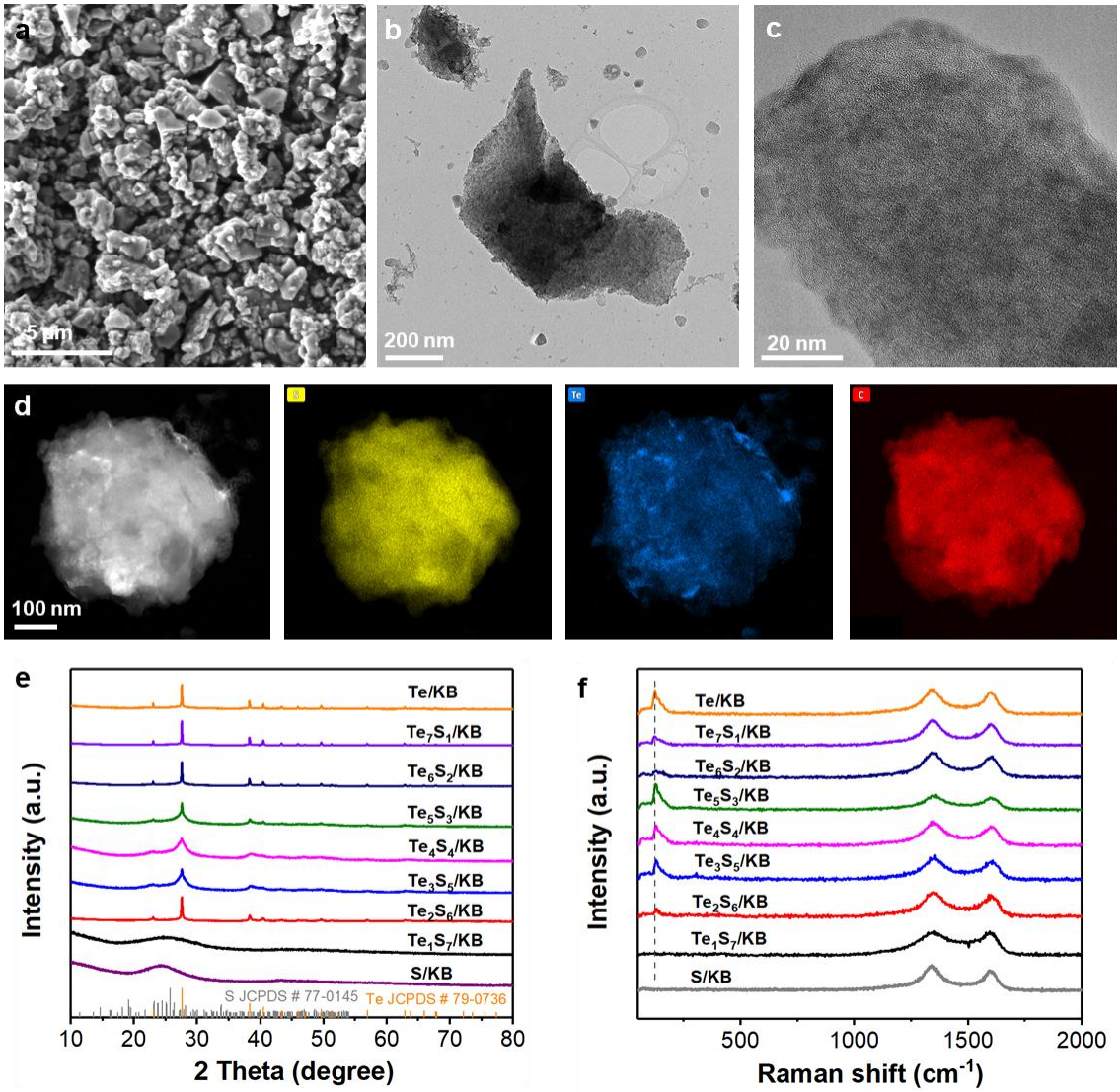

Figure 6.4.3. Morphology and structure information of Te_xS_y/KB composites. (a) SEM, (b) TEM, (c) HRTEM images of Te_1S_7/KB powder. (d) HAADF and corresponding elemental mapping of Te_1S_7/KB powder. (e) XRD patterns and (f) Raman spectra of Te_xS_y/KB composites.

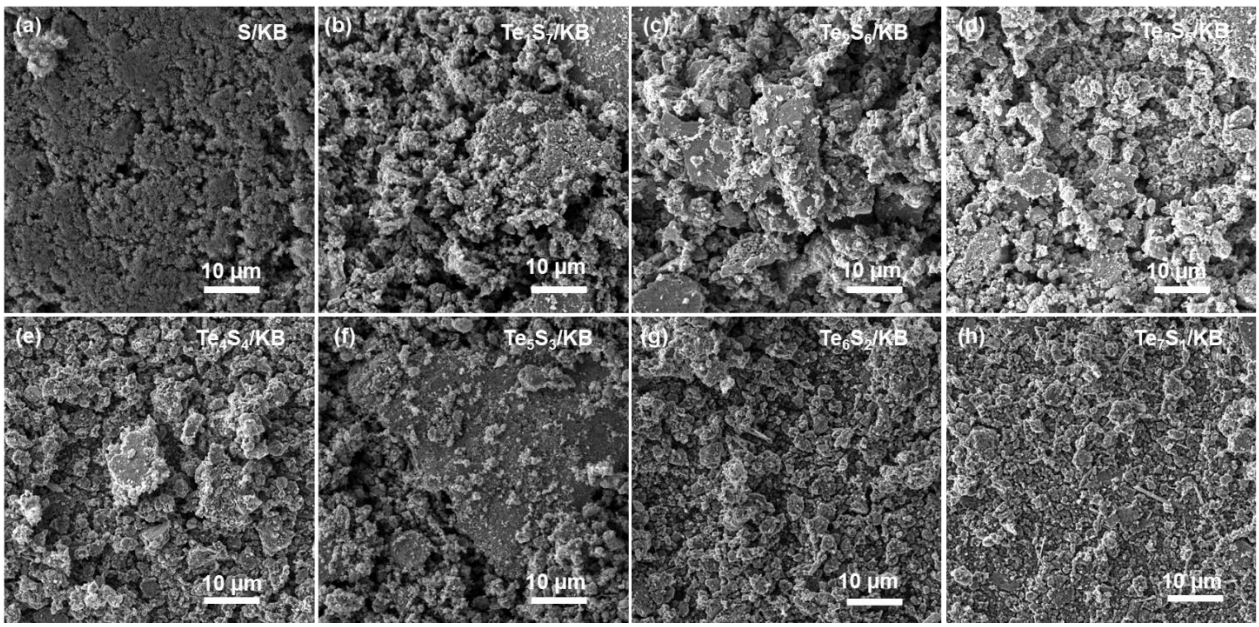

Figure 6.4.4. SEM images of (a) S/KB, (b) Te_1S_7/KB, (c) Te_2S_6/KB, (d) Te_3S_5/KB, (e) Te_4S_4/KB, (f) Te_5S_3/KB, (g) Te_6S_2/KB, (h) Te_7S_1/KB composites.

6.5 Cycling Performance of Te_xS_y/KB Cathodes

The ideal carbon as active materials host should possess sufficient micro/mesopores to accommodate the volume change of Te_xS_y upon lithiation/delithiation. Fast electron transfer across carbon matrix is also required to facilitate the redox conversion. In addition to KB, another two commercial carbons are also selected as TeS host in this work. ASAC25 is activated carbon with numerous micropores (surface area: 2345.3 m^2 g^{-1} and pore volume: 1.15 cm^3 g^{-1}), and it is proven to be an excellent Te host in our previous studies with 83.3 % capacity retention over 500 cycles at the current density of 1C (Chapter 4). However, when being chosen as Te_1S_7 host, the Te_1S_7/ASAC25 electrode delivers ultralow capacities of 122.8 and 27.3 mAh g^{-1} in the first two cycles, as shown in **Figures 6.5.1a-b**, which might be due to the poor electrical conductivity of activated carbon ASAC25 [176, 177]. Mesoporous BP2000 with a large pore volume (2.45 cm^3 g^{-1}) and surface area (1515.7 m^2 g^{-1}) is also used to confine Te_1S_7 active materials. The Te_1S_7/BP2000 exhibits better capacities of (1103.4 and 366.2 mAh g^{-1} for the initial two cycles) than Te_1S_7/ASAC25 does. By contrast, KB is the best carbon choice due to the highest reversible capacity of 546.7 mAh g^{-1} in the 2nd cycle. Furtherly, FEC additive was found to significantly elevate the discharge plateau, decrease the polarization, and contribute to higher discharge capacity

of S cathodes (**Figure 6.5.1c**), which benefit from forming a protective LiF-rich SEI layer induced by the decomposition of FEC [178, 179].

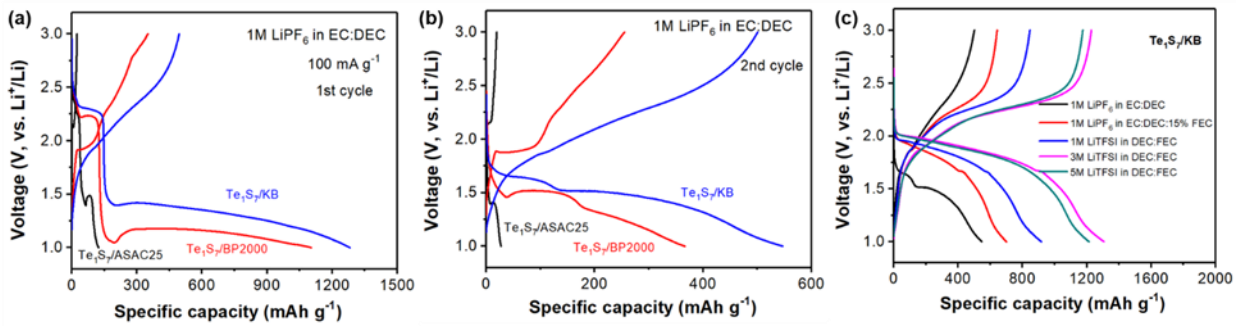

Figure 6.5.1. Charge/discharge profiles of Te_1S_7 with ASAC25, BP2000 and KB in the (a) first and (b) second cycle with the electrolyte of 1M $LiPF_6$ in EC:DEC, (c) the Te_1S_7/KB cathode using electrolytes of 1M $LiPF_6$ in EC:DEC, 1M $LiPF_6$ in EC:DEC:15%FEC, and 1M LiTFSI in DEC:FEC.

The S/KB cathode exhibits a discharge capacity of 1686.7 mAh g^{-1} in the 1st cycle and 483.7 mAh g-1 in the 2nd cycle at 0.1 A g^{-1}. The rapid decay of the S/KB cathode is mainly caused by the side reactions between polysulfides and carbonate electrolytes through nucleophilic attack during the first discharge process, indicating the poor electrochemical compatibility between S and carbonate electrolytes [27, 35, 36]. In contrast, the Te_1S_7/KB cathode delivers the highest capacity of 2183.0 mAh g^{-1} in the first cycle and maintains a stable capacity of 1306.7 mAh g^{-1} over the subsequent cycles (**Figure 6.5.2a**). With the increase of Te content, the 1st-cycle discharge capacity gradually decreases from 2183.0 mAh g^{-1} for Te_1S_7/KB to 2065.5, 1604.7, 1421.7, 1229.8, 1035.6, and 1376.3 mAh g^{-1} for Te_2S_6/KB, Te_3S_5/KB, Te_4S_4/KB, Te_5S_3/KB, Te_6S_2/KB, and Te_7S_1/KB, respectively. The decreased capacity of Te_xS_y versus the increasing Te/S molar ratio is due to the low theoretical capacity of Te (**Table 6.5.1**). Moreover, the initial CE (58.2%) of the Te_1S_7/KB cathode is remarkably higher than that of S/KB (26.7%) (**Figure 6.5.2b**), indicating superior reversibility of Li- Te_1S_7 chemistry with the incorporation of Te. More importantly, the Te_1S_7/KB cathode retains 1239.3 mAh g^{-1} after ten cycles and outperforms S/KB and other Te_xS_y /KB cathodes (**Figure 6.5.2c**).

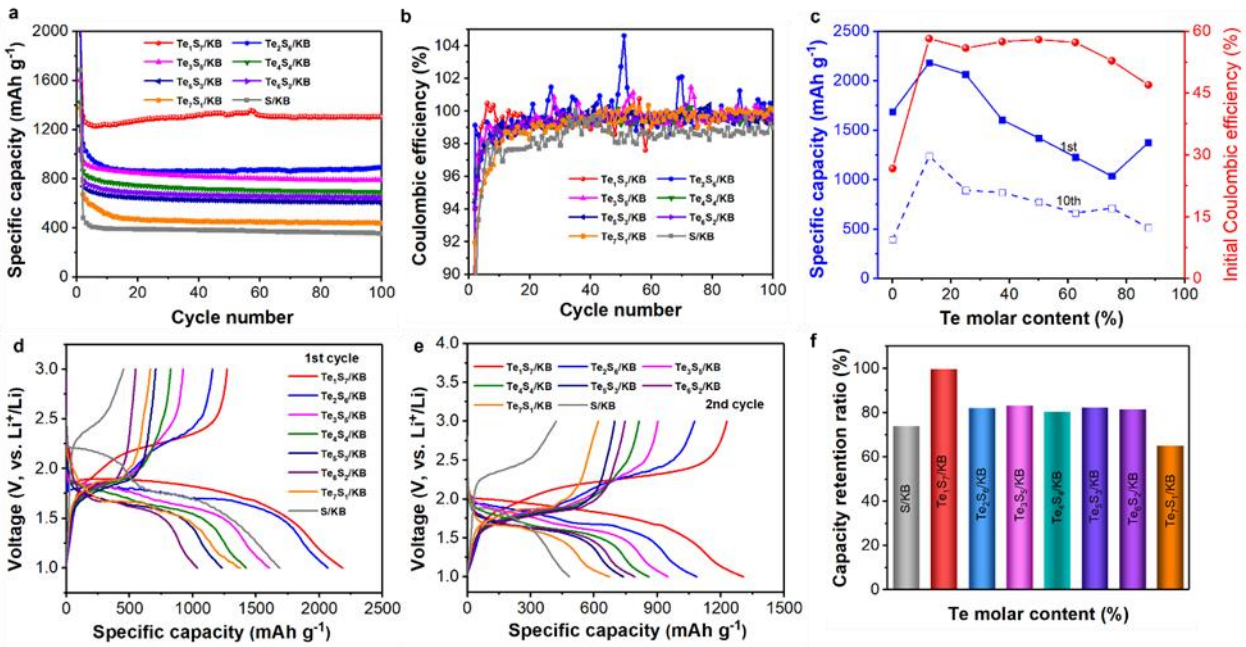

Figure 6.5.2. Cycling performance of S/KB and Te_xS_y/KB cathodes at 0.1 A g^{-1}. (a) Specific discharge capacity over cycles. (b) Coulombic efficiency. (c) Specific capacities in the 1st and 10th cycles and initial Coulombic efficiency. Galvanostatic charge/discharge curves in the (d) 1st and (e) 2nd cycle. (f) Capacity retention over 100 cycles.

Table 6.5.1. Theoretical capacities of Te_xS_y composites.

Active materials	Theoretical capacity (mAh g^{-1})
S	1675.0
Te_1S_7	1518.1
Te_2S_6	1361.3
Te_3S_5	1204.4
Te_4S_4	1047.5
Te_5S_3	890.6
Te_6S_2	733.8

Active materials	Theoretical capacity (mAh g^{-1})
Te_7S_1	576.9
Te	420.0

$$Theoretical\ Capacity\ (Te_xS_y) = \frac{1675x + 420y}{8}$$

The theoretical capacity values are calculated based on the complete reduction of Te_xS_y to Li_2S and Li_2Te.

Figures 6.5.2d-e display galvanostatic charge/discharge profiles of S/KB and Te_xS_y/KB in the first two cycles. During the first discharge process, S/KB shows two plateaus at ~ 2.2 and 1.75 V, corresponding to the formation of high-order and low-order polysulfides, respectively [31]. In the second cycle, the small plateau at 2.2 V disappears due to the irreversible loss through the "solid-liquid-solid" reaction pathway [180]. However, the Te_1S_7/KB cathode presents one extended discharge plateau at ~ 1.85 V in both cycles, implying a solid-state conversion process for the Te-incorporated S cathode [85]. With the increase of Te content, the Te_xS_y/KB cathodes illustrate shortened discharge plateaus at a lower voltage, possibly due to the thermodynamic energy barrier of Te_xS_y upon lithiation. The different electrochemical behaviors of Te_xS_y/KB cathodes are also found in CV plots (**Figure 6.5.3**). Moreover, capacities of 357.4, 1301.9, 891.2, 789.5, 691.4, 608.1, 646.1, and 438.9 mAh g^{-1} are retained for S/KB, Te_1S_7/KB, Te_2S_6/KB, Te_3S_5/KB, Te_4S_4/KB, Te_5S_3/KB, Te_6S_2/KB, and Te_7S_1/KB, respectively, corresponding to the capacity retention ratio of 73.9%, 99.6%, 82.1%, 83.1%, 80.4%, 82.3%, 81.5%, and 65.2%, respectively (**Figure 6.5.2f**). At the current density of 0.1 A g^{-1}, the Te/KB cathode delivers the high capacity of 2339.3 mAh g^{-1} with an ultralow CE of 21.1% in the first cycle, followed by a drastic decrease to 352.5 mAh g^{-1} for the 10th cycle, as shown in **Figure 6.5.4a**. Compared to S/KB and Te_1S_7/KB cathodes, the Te/KB also demonstrated the lowest discharge plateau of 1.6 V, as observed in **Figure 6.5.4b**. The fast capacity decline of the Te/KB cathode could be attributed to the ineffective confinement of active materials in KB induced by the acute volume expansion and subtraction of Te upon lithiation/delithiation [60, 61]. Therefore, the Te_1S_7/KB cathode shows the optimal reversible capacity, CE, and cycling stability than S/KB and other Te_xS_y/KB counterparts.

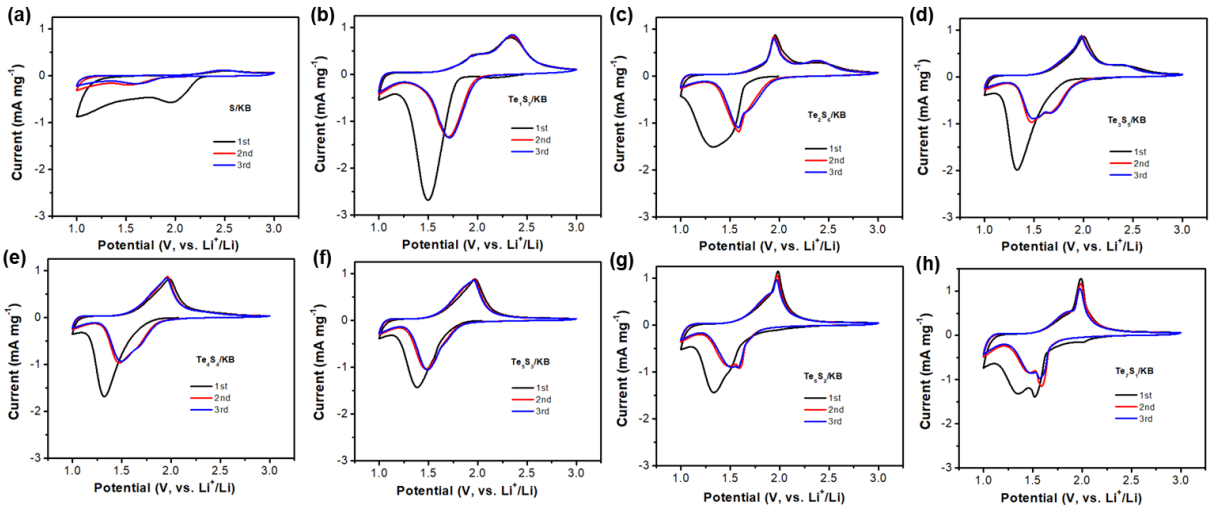

Figure 6.5.3. CV plots of (a) S/KB, (b) Te_1S_7/KB, (c) Te_2S_6/KB, (d) Te_3S_5/KB, (e) Te_4S_4/KB, (f) Te_5S_3/KB, (g) Te_6S_2/KB, (h) Te_7S_1/KB cathodes at 0.2 mV s^{-1}.

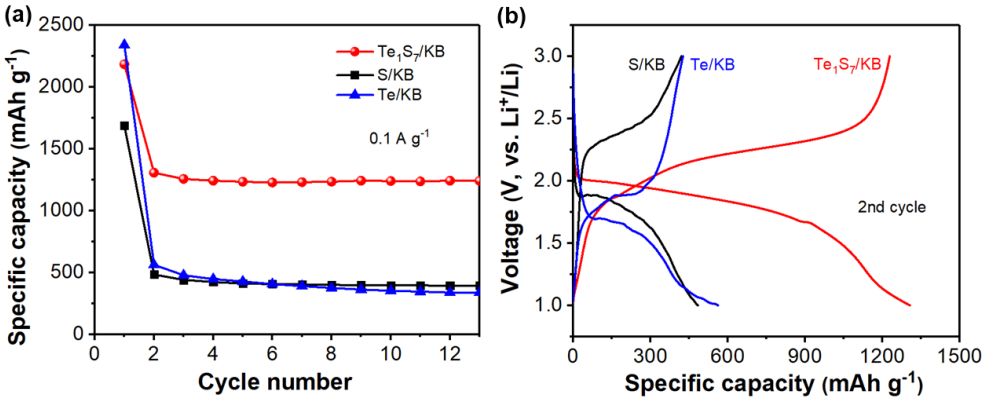

Figure 6.5.4. (a) Cycling performance and (b) Charge/discharge profiles of S/KB, Te/KB, and Te_1S_7/KB cathodes at 0.1 A g^{-1}.

6.6 Galvanostatic Charge/Discharge Profiles, Rate and Long-Cycling Performance of S/KB and Te_1S_7/KB Cathodes in Concentration-Varied Electrolytes

It is found that employing a high-concentrated electrolyte enabled a solid phase reaction for S/mesoporous cathode with carbonate electrolytes [169]. Herein, electrolyte concentrations of 1, 3, and 5 M in the mixed solvents of DEC:FEC are employed to investigate different reaction mechanisms of S/KB and Te_1S_7/KB cathodes. **Figure 6.6.1** displays the cycling performance of

S/KB and Te_1S_7/KB cathodes in 1, 3, and 5 M electrolytes and corresponding charge/discharge profiles at 0.1 A g^{-1}. The S/KB cathode delivers improved reversible capacities of 267.8, 483.7, and 1167.5 mAh g^{-1} for the 2nd cycle at 1M, 3M, and 5M electrolytes, respectively (**Figures 6.6.1a-c**). However, rapid capacity decay is observed in the 5M electrolyte, with only 674.9 mAh g^{-1} retained after 100 cycles, probably due to unfavorable Li-ion mobility in high-viscosity concentrated electrolytes [39, 40]. In contrast, the Te_1S_7/KB cathode shows excellent cycling stability and maintains a reversible capacity of 1288.2 mAh g^{-1} over 100 cycles, even in 5M electrolytes. The big Li-ion storage capacity difference versus electrolyte concentration implies different redox conversion mechanisms. For the S/KB cathode, during the first discharge process, the small plateau at 2.27 V in 1M electrolyte representing the conversion from S_8 to high-order polysulfides becomes shortened and lower (2.17 and 2.11 V for 3M and 5M, respectively) (**Figures 6.6.1d-f**). A possible reason is that the high-concentrated carbonate electrolyte has fewer free solvents to dissolve polysulfides, thus proceeding with the reaction to form a low-order sulfide species [181]. Meanwhile, the S/KB cathode has an improved initial CE of 11.3%, 26.7%, and 52.6% for 1, 3, and 5M, respectively. In comparison, the Te_1S_7/KB cathode presents a much narrower plateau at 2.27 V, which emerges with a prominent wide plateau at 1.77 V with a significantly high initial CE of 52.3% in 1M electrolyte (**Figure 6.6.1g**) during the first discharge process. A single voltage plateau is found in the subsequent cycles, indicating a one-step conversion from Te_1S_7 to Li_2S/Li_2Te [83]. With increased LiTFSI concentration from 1M to 3M and 5M, the Te_1S_7/KB cathode delivers close capacities of 1306.7and 1212.9 mAh g^{-1} and enhanced initial CE of 58.2% and 63.4% (**Figures 6.6.1h-i**). It can be concluded that Te_1S_7/KB possesses better electrochemical activity and reversibility than S/KB, thus inducing a solid-phase reaction pathway and high reversible capacity.

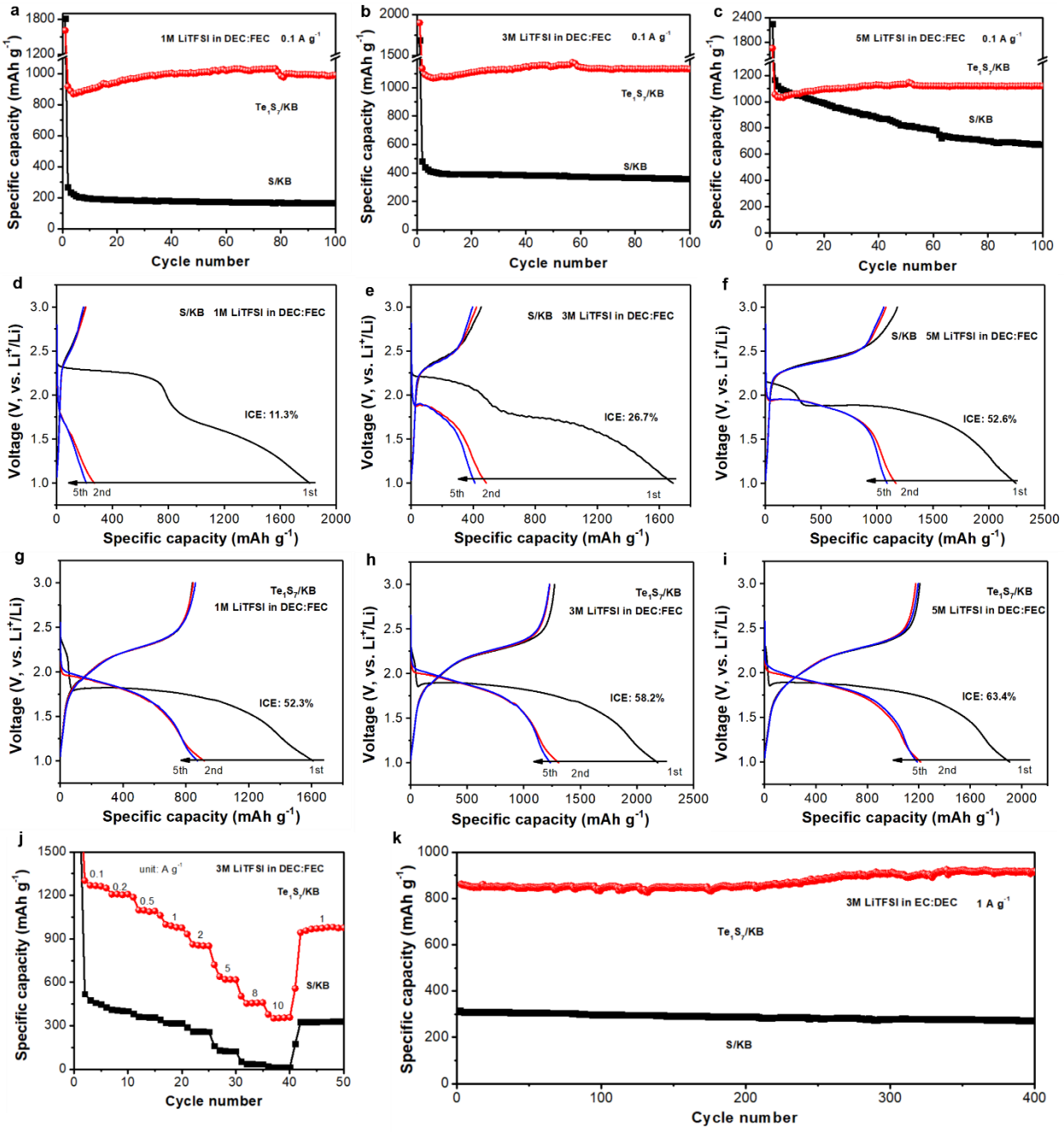

Figure 6.6.1. Cycling and rate performance of S/KB and Te_1S_7/KB cathodes. (a-c) Cycling performance and galvanostatic charge/discharge profiles of (d-f) S/KB and (g-i) Te_1S_7/KB cathodes at 0.1 A g^{-1} with 1, 3, and 5 M electrolyte. (j) Rate capabilities at 0.1-10 A g^{-1} and (k) long-term cycling at 1 A g^{-1} of S/KB and Te_1S_7/KB cathodes with 3M electrolyte.

The rate capability and long-term cycling performance of S/KB and Te_1S_7/KB cathodes are also tested and evaluated. The Te_1S_7/KB cathode outperforms S/KB at various current densities with 1, 3, and 5M electrolytes (**Figure 6.6.2** and **Figure 6.6.1j**). When working in 3M electrolyte, the Te_1S_7/KB cathode delivers reversible capacities of 1302.3, 1208.3, 1097.8, 999.4, 861.9, 639.9, 454.6, and 351.9 mAh g^{-1} at 0.1, 0.2, 0.5, 1, 2, 5, 8 and 10 A g^{-1}, respectively. When the current density is set back to 1 A g^{-1}, the cell still displays a high discharge capacity of 672.9 mAh g^{-1}. However, the S/KB cathode shows low discharge capacities of 519.9, 412.9, 363.5, 319.9, 261.9, 129.8, 37.9, and 14.2 mAh g^{-1} at 0.1, 0.2, 0.5, 1, 2, 5, 8 and 10 A g^{-1}, respectively. Moreover, the discharge capacities of 827.2 and 959.8 mAh g^{-1} for Te_1S_7/KB can be maintained at a high current density of 1 A g^{-1} after 400 cycles using 1M and 3M electrolytes, respectively (**Figure 6.6.2c** and **Figure 6.6.1k**). As a comparison, S/KB retains only 77.5 and 273.6 mAh g^{-1} with 1M and 3M electrolytes, respectively. It is seen that both S/KB and Te_1S_7/KB cathodes demonstrate fast capacity fading at 5M electrolyte, with 309.7 and 448.4 remaining after 400 cycles at 1 A g^{-1} (**Figure 6.6.2d**). The capacity decline at concentrated electrolytes is attributed to slow Li^+ transference with excess LiTFSI concentration due to high viscosity [169]. The superior rate capacity of Te_1S_7/KB than S/KB suggests boosted redox kinetics of Li-S chemistry by Te-induced molecular regulation.

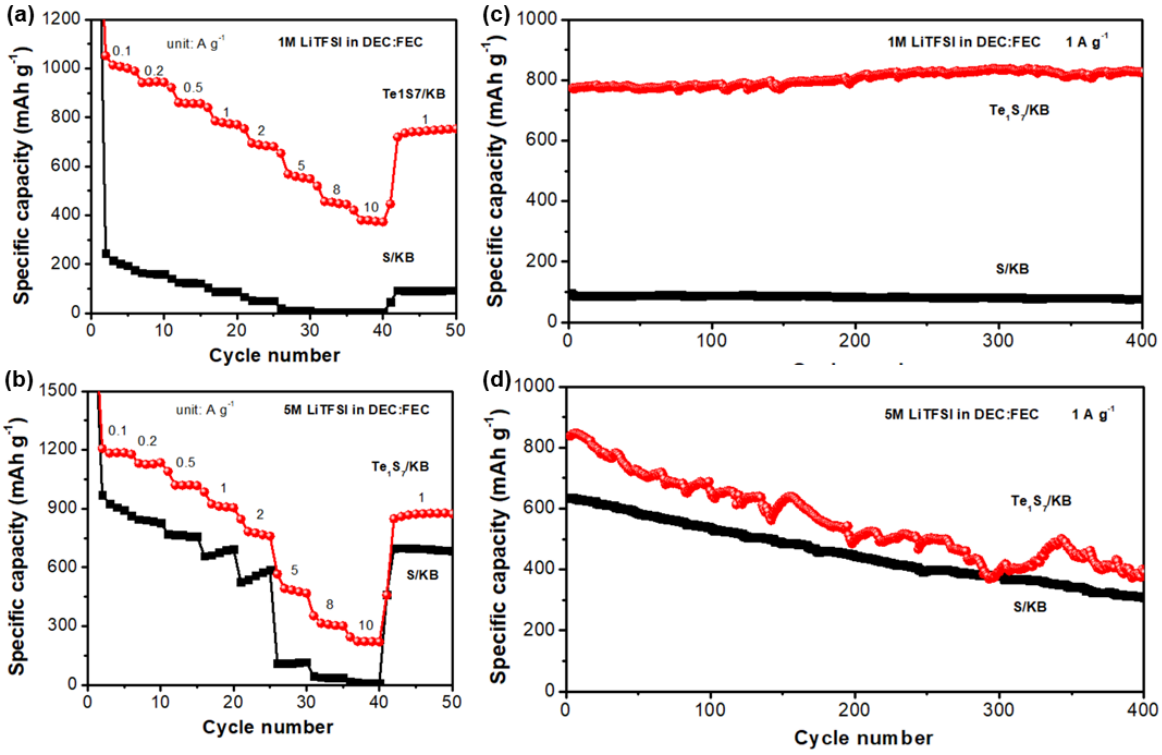

Figure 6.6.2. Rate capabilities of S/KB and Te_1S_7/KB cathodes at 0.1-10 A g^{-1} with (a) 1M and (b) 5M electrolyte, and (c-d) long-term cycling of S/KB and Te_1S_7/KB cathodes at 1 A g^{-1} with 1M and 5M electrolyte.

6.7 Redox Kinetics Analysis of S/KB and Te_1S_7/KB Cathodes upon Lithiations/Delithiation

To reveal the effect of Te incorporation in Te_1S_7 molecules on reaction kinetics, EIS and GITT characterizations are conducted to analyze electron and Li-ion transfer in S/KB and Te_1S_7/KB cathodes. The smaller semicircle of Te_1S_7/KB than the S/KB counterpart (**Figure 6.7.1a**) represents a lower charge transfer resistance of 137 Ω than 224.8 Ω for S/KB. The lower overpotential of 0.38 V for Te_1S_7/KB than that of S/KB (0.66 V) (**Figure 6.7.1b**) indicates decreased reaction overpotential by Te-induced molecular regulation. Additionally, the Te_1S_7/KB cathode shows a pair of much more intense reduction/oxidation peaks with a smaller potential difference of 0.64 V than S/KB does (**Figure 6.7.1c**), revealing superior electrochemical activity and better reversibility of Te_1S_7/KB. Based on the CV curves at various scan rates, the Li-ion coefficients of Te_1S_7/KB for oxidation and reduction process are calculated to be 1.9 and 5.3 × 10^{-}

^{8} cm^2 s^{-1}, respectively, which are two magnitude orders higher than Li-ion coefficients of S/KB (3.7 and 3.4 × 10^{-10} cm^2 s^{-1}, respectively, for oxidation and reduction process) (**Figure 6.7.1d**). **Figures 6.7.1e-f** illustrate the voltage response profiles of Te_1S_7/KB and S/KB in the second cycle using the GITT technique. The reaction resistance at the different lithiation/delithiation stages is calculated to analyze *in situ* interfacial resistance, which is obtained by dividing the overpotential by the pulse current [46, 110]. As presented in **Figures 6.7.1g-h**, the reaction resistances of Te_1S_7/KB are smaller than those of S/KB at different charge/discharge stages, suggesting a faster charge transfer rate and enhanced lithiation/delithiation kinetics of Te_1S_7/KB [80]. Based on the above results, Li-ion diffusion and electron transfer are remarkably facilitated in the heteroatomic Te_1S_7 molecules, which benefit from the improved redox chemistry manipulated effectively by Te-induced molecular regulation. The enhanced kinetics analysis is attributed to the lower energy barrier for Li-ion migration upon lithiation and superior electrical conductivity, as discussed in DFT simulations (**Figure 6.3.3**).

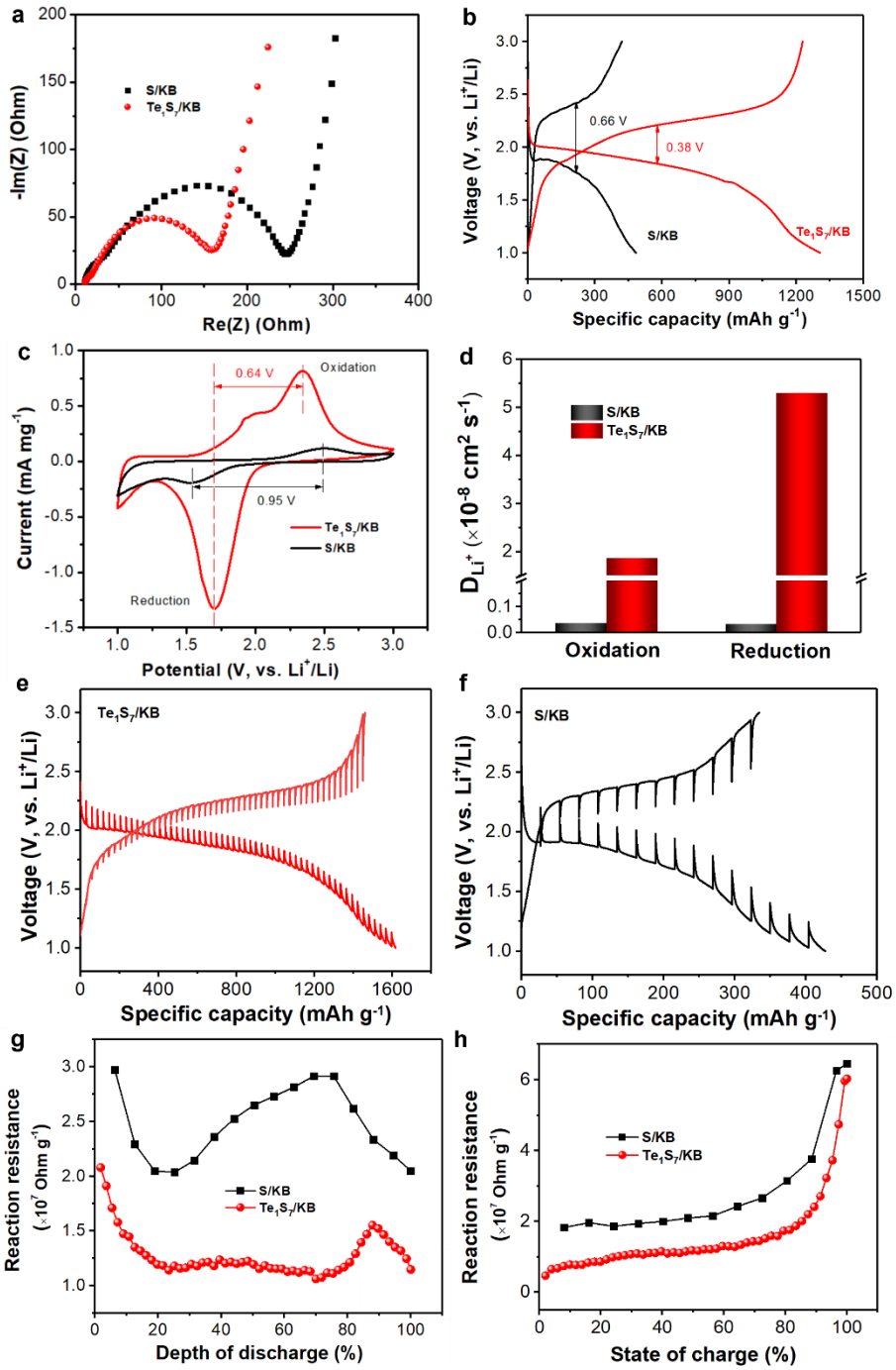

Figure 6.7.1. Reaction kinetics analysis for S/KB and Te_1S_7/KB cathodes. (a) Nyquist plots. (b) charge-discharge curves. (c) CV plots. (d) Li-ion diffusion coefficients of S/KB and Te_1S_7/KB cathodes. GITT curves of (e) Te_1S_7/KB and (f) S/KB cathodes. Reaction resistance of S/KB and Te_1S_7/KB cathodes during (g) discharge and (h) charge process.

6.8 Ex-Situ Surface Analysis and Mechanistic Study of Cycled S/KB and Te_1S_7/KB Cathodes

Ex situ analytical techniques have been performed to investigate the surface chemistry of cycled Te_1S_7/KB and S/KB electrodes. As shown in **Figure 6.8.1a**, the surface of Te_1S_7/KB keeps a relatively compact morphology. At the nanometer level, Te_1S_7 active materials are still confined into the pore structure of KB (**Figures 6.8.1b-c**) with uniform elemental distributions (**Figure 6.8.1d** and **Figure 6.8.2**), indicating the excellent structural stability of Te_1S_7/KB. In comparison, abundant bright spherical particles around 20 nm are agglomerated on the surface of S/KB (**Figure 6.8.1ee** and **Figure 6.8.3**). Due to the poor electric conductivity of S, the charging effect is observed from the TEM images of cycled S/KB electrode (**Figures 6.8.1f-g**, **Figure 6.8.4**). Interestingly, the bright particles on the S/KB electrode surface are also found in dilute (1M) and concentrated (5M) electrolytes (**Figure 6.8.5**). On the other hand, the disassembled S/KB cathodes after being discharged to 1V, 2V or charged to 3V were immersed in DME solvent to monitor the color change of solutions. However, there is no noticeable color change for the solutions after one-month immersion, and UV-vis shows no signal of long-chain polysulfides (**Figure 6.8.6**), indicating minor or no polysulfides dissolution. It is likely that short-chain Li_2S are dominantly generated upon lithiation in the S/KB cathode.

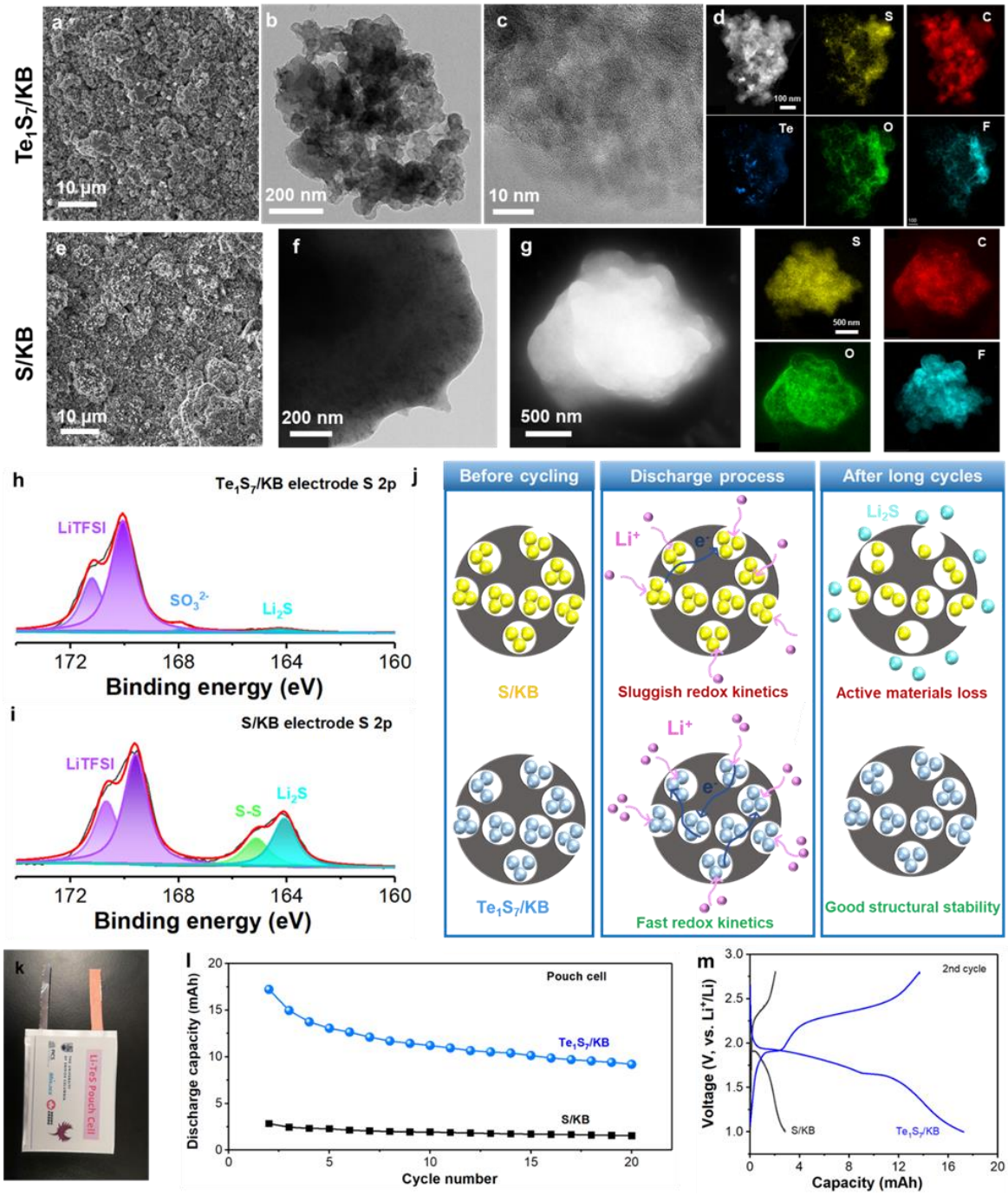

Figure 6.8.1. *Ex situ* morphology and surface analysis, working mechanism schematic and pouch cell. (a) SEM, (b) TEM, (c) HRTEM, (d) HAADF and EDS mapping of Te_1S_7/KB electrode after 100 cycles. (e) SEM, (f) TEM, (g) HAADF and EDS mapping of S/KB electrode after 100 cycles. S 2p XPS spectra of cycled (h) Te_1S_7/KB and (i) S/KB electrodes. (j) Mechanism analysis of Te_1S_7/KB and S/KB electrodes. (k) Digital photo of the Li-Te_1S_7/KB

pouch cell. (l) Cycling performance of the Li-Te_1S_7/KB and Li-S/KB pouch cells. (m) Voltage-capacity profiles of the Li-Te_1S_7/KB and Li-S/KB pouch cells in the 2nd cycle.

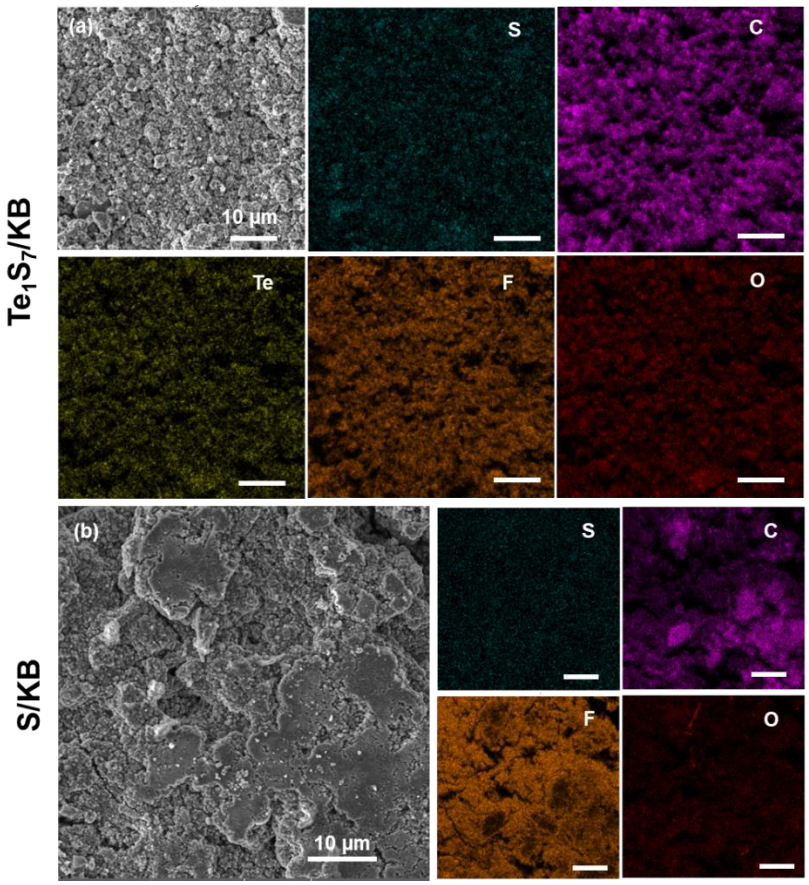

Figure 6.8.2. SEM images and EDS mapping of cycled (a) S/KB and (b) Te_1S_7/KB cathodes with the 3M electrolyte.

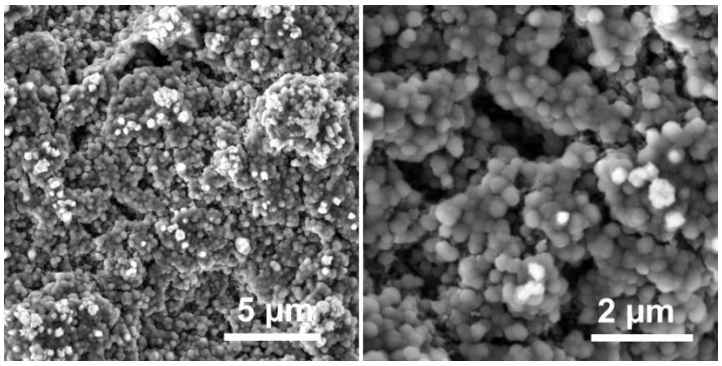

Figure 6.8.3. SEM images of cycled S/KB electrode with 3M electrolyte.

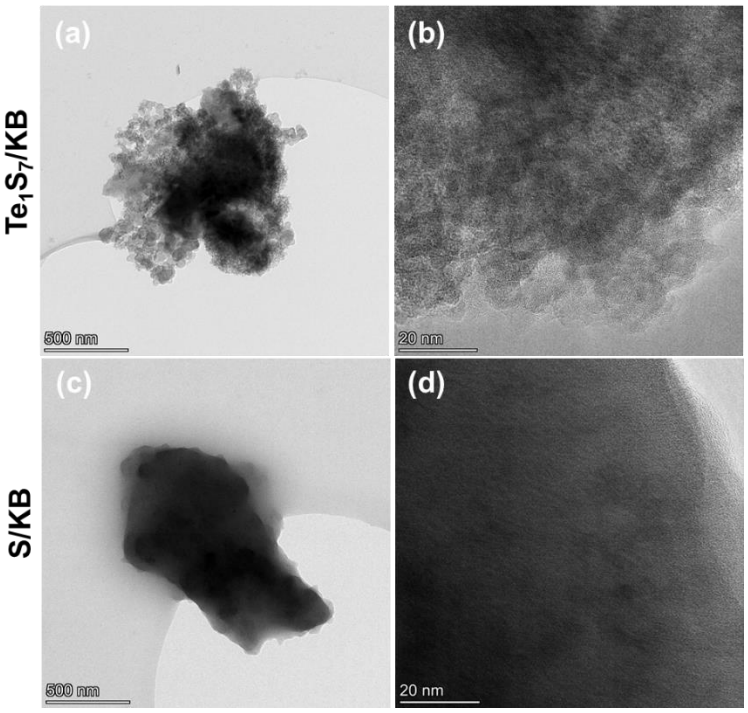

Figure 6.8.4. HRTEM images of cycled (a, b) Te_1S_7/KB and (c, d) S/KB cathodes with 3M electrolyte.

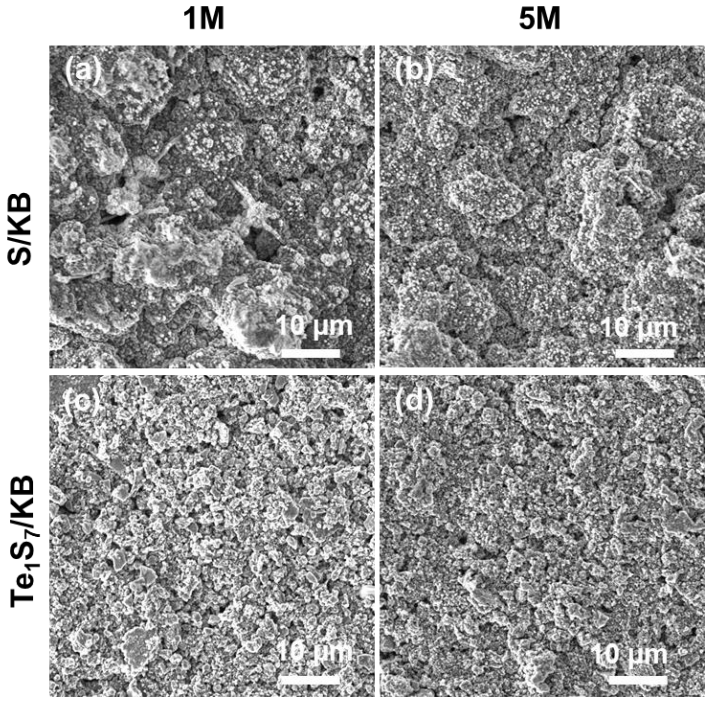

Figure 6.8.5. SEM images of cycled (a) S/KB and (b) Te_1S_7/KB cathodes with 1M and 5M electrolytes.

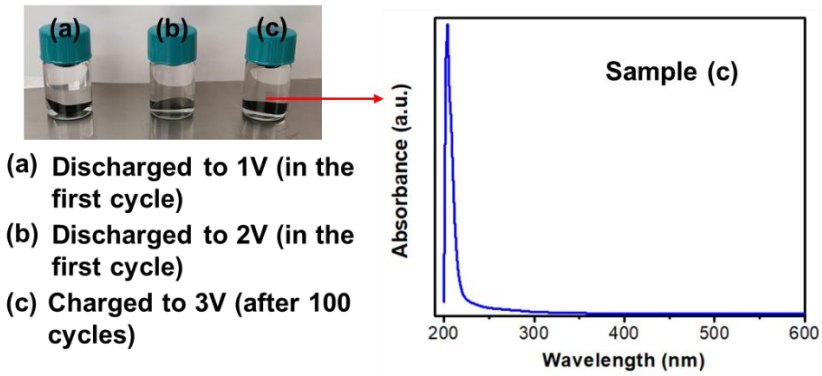

Figure 6.8.6. Digital photos of disassembled S/KB cathodes immersed in DME solvent for 1 month after being discharged to 1V (sample a), 2V (sample b), or charged to 3V (sample c) and corresponding UV-vis plot of sample c.

XPS measurement is carried out to identify the species and understand the different SEI compositions of Te_1S_7/KB and S/KB electrodes. **Figure 6.8.7** shows a similar XPS survey spectrum of Te_1S_7/KB and S/KB surface consisting of C, O, F, and S elements (**Table 6.8.1**), and Te_1S_7/KB has a weak Te 3d signal on the SEI layer. Concerning C 1s XPS spectra of the SEI film, S/KB and Te_1S_7/KB electrodes possess similar peaks at 284.8/284.8, 285.7/285.7, 287.3/287.5, 289.2/289.6, 291.5/290.8, and 293.4/293.8 eV, respectively (**Figure 6.8.8a**), which are assigned to C-C, C=C, C-O, C=O, COOLi, and C-F bonds, respectively, primarily resulting from the decomposition of liquid electrolyte [169]. The deconvoluted O 1s spectra of S/KB and Te_1S_7/KB show three characteristic peaks at 532.6/532.5, 533.5/533.4, and 534.5/534.1 eV, respectively (**Figure 6.8.8b**), corresponding to COOLi, C-C, and C=O bonds, respectively [169]. The high-resolution F 1s spectra are fitted with LiF and C-F bonds at 685.4/685.9 and 689.0/689.5 eV for S/KB and Te_1S_7/KB SEI layers, respectively (**Figure 6.8.8c**) [169]. The pair of peaks in Te 3d spectra (**Figure 6.8.8d**) implies the formation of Te-containing SEI film on the Te_1S_7/KB electrode surface. It should be noted that the S/KB and Te_1S_7/KB electrodes were disassembled after 100 discharge-charge cycles. Assuming the redox conversion between S (Te_1S_7) and Li_2S (Li_2S and Li_2Te) is complete, only S or Te_1S_7 is expected to exist as active materials. As shown in **Figure 6.8.1h**, the high-resolution S 2p spectra of the Te_1S_7/KB surface display two prominent peaks at

171.7 and 171.2 eV originating from the sulfone group of TFSI anion and low-intensity peaks at 170.0 eV representing sulfite (SO_3^{2-}) [182, 183]. There is an unnoticeable peak at 167.9 eV corresponding to the formation of Li_2S [184, 185], indicating the highly reversible electrochemical conversion from Li_2S/Li_2Te to Te_1S_7 after the charge process completes and good confinement of active materials in KB. However, the peak representing Li_2S on the surface of S/KB is much more intense (**Figure 6.8.1i**), implying the poor reversibility of S/KB from Li_2S to S upon delithiation. Additionally, S-S bond is also observed at 165.1 eV in the deconvoluted S 2p XPS spectra, suggesting the loss of partial S species from mesopores of KB host over cycles. Therefore, the Te-containing SEI layer of Te_1S_7/KB enables reversible redox conversion and outstanding structural stability over long cycles, while the S/KB electrode suffers from active materials loss and incomplete Li_2S-S conversion. **Figure 6.8.1j** illustrates the mechanism analysis of Te_1S_7/KB and S/KB electrodes according to the above redox kinetics and surface chemistry discussion. The insulating nature of S/KB cathode causes the sluggish reaction kinetics and poor reversibility of redox conversion from Li_2S to S, thus leading to the low utilization of active materials and poor discharge capacity over long cycles. In comparison, the Te_1S_7/KB possesses fast Li-ion and electron transfer upon lithiation/delithiation, contributing to the excellent cycling and structural stability in the cycling test.

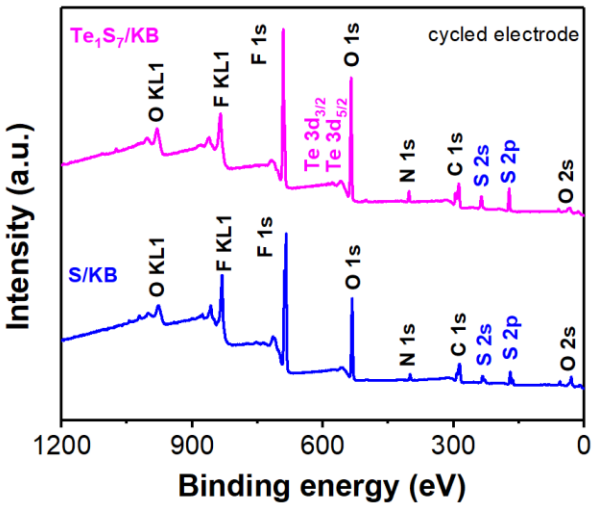

Figure 6.8.7. XPS survey scans of cycled S/KB and Te_1S_7/KB cathodes.

Table 6.8.1. Elemental composition of cycled S/KB and Te_1S_7/KB electrodes from XPS.

Electrodes	Mass concentration (wt%)						
	F	Te	O	N	C	S	Li
S/KB	33.0	0.8	23.35	2.44	20.37	13.2	6.49
Te_1S_7/KB	39.21	-	17.94	1.54	17.18	10.8	12.17

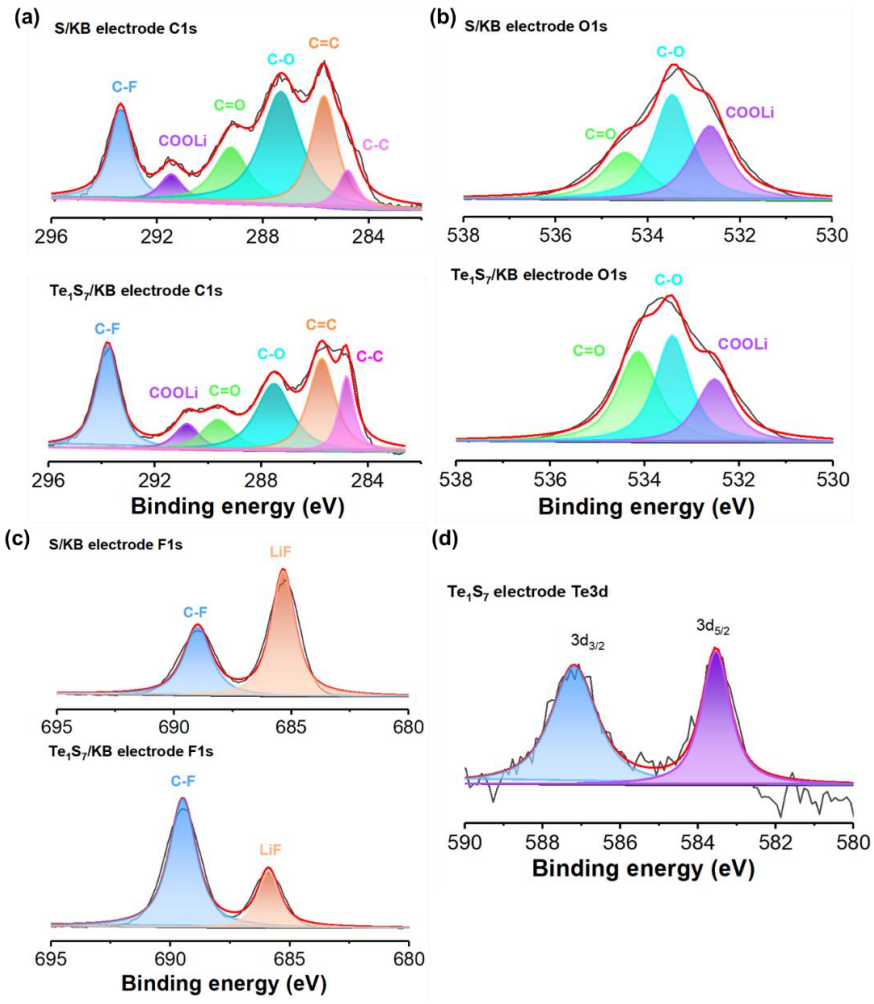

Figure 6.8.8. (a) C 1s, (b) O 1s, (c) F 1s, and (d) Te 3d XPS spectra of cycled S/KB and Te_1S_7/KB cathodes with 3M electrolytes.

The corresponding Li metals from Li-S or Li-Te_1S_7 cells are also examined by SEM to analyze the effect of Te on Li metal anodes. As illustrated in **Figure 6.8.9**, the Li metal disassembled from the Li-S cell shows loose morphology with nodule-like particles of ~ 5 μm, and the gaps between particles leave the large surface area to continuously consume electrolyte solvents and Li salt and form excessive passivation layers [186]. By contrast, the Li anode surface from the Li-Te_1S_7 cell demonstrates dense and compact morphology. The well-regulated Li growth might benefit from the generation of a stable SEI layer induced by Te. It is revealed that Te inclusion can react with polysulfides to form soluble polytellurosulfides, which migrate to the Li anode and stabilize Li deposition by generating a stable SEI containing lithium thiotellurate and lithium telluride [187]. Therefore, the Li metal of the Li-Te_1S_7 cell is protected and regulated to resist excessive dendrite growth, thus ensuring excellent cycling stability of Te_1S_7/KB.

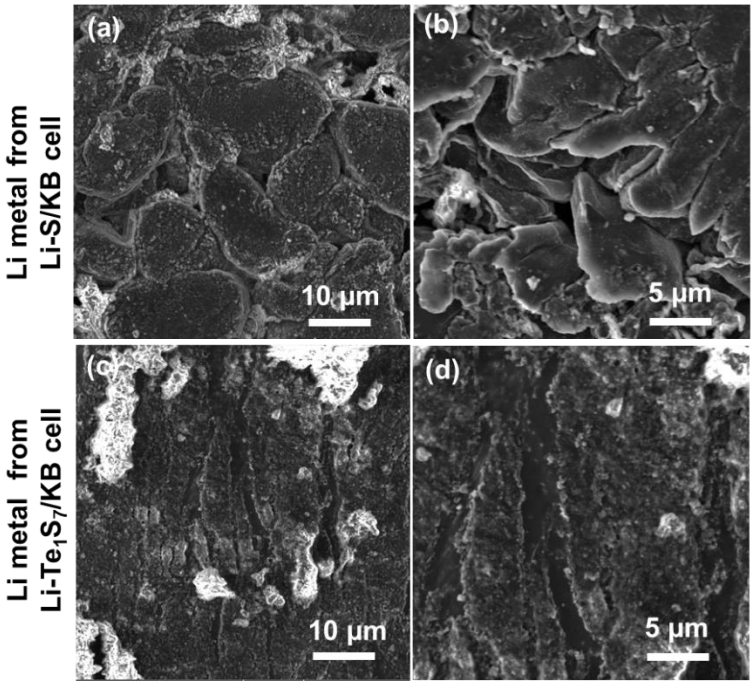

Figure 6.8.9. SEM images of cycled Li metals from (a, b) Li-S/KB and (c, d) Li-Te_1S_7/KB cells.

6.9 Li-S/KB and Li-Te_1S_7/KB Pouch Cell Performance

Furthermore, Li-Te_1S_7/KB pouch cell was assembled as shown in **Figure 6.9.1** and **Figure 6.8.1k**. For pouch cell assembly, Li foil with a size of 5.8 × 4.5 cm^2 was pressed onto a piece of copper foil as the anode. Te_1S_7/KB cathode with a mass loading of 1.5 mg cm^{-2} was cut into 5.6 × 4.3 cm^2

by a gas-driven die cutter (MSK-180SP, MTI Corporation). Subsequently, anode, Celgard 2500 separator, and cathode were stacked and placed inside the aluminum-laminated case. 800 uL optimal electrolyte of 3M LiTFSI in DEC:FEC was injected into the battery pack, which was further vacuum sealed (MSK-115A-S, MTI Corporation). Finally, the Li-TeS pouch cell was connected to BioLogic workstation for EIS and cycling testing. All pouch cell assembly and cell testing were carried out in an Ar-filled glovebox. Li-S pouch cell was assembled following the same procedure.

The Li-Te_1S_7/KB pouch cell exhibits a remarkably higher discharge capacity of 17.2 mAh over 20 cycles with highly overlapped voltage-capacity profiles (**Figures 6.8.1l-m**, **Figure 6.9.2**) and significantly lowered electron transfer resistance (**Figure 6.9.3**) than the Li-S/KB pouch cell, suggesting the superior kinetics and Li-ion storage capacity of the Te_1S_7/KB cathodes.

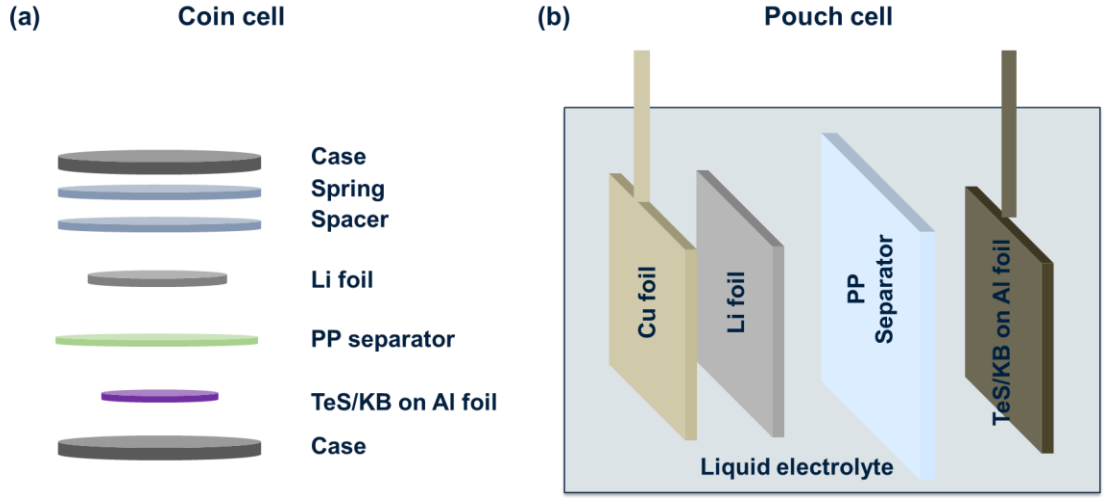

Figure 6.9.1. Components and configurations of Li-Te_1S_7/KB cells. (a) Coin cell. (b) Pouch cell.

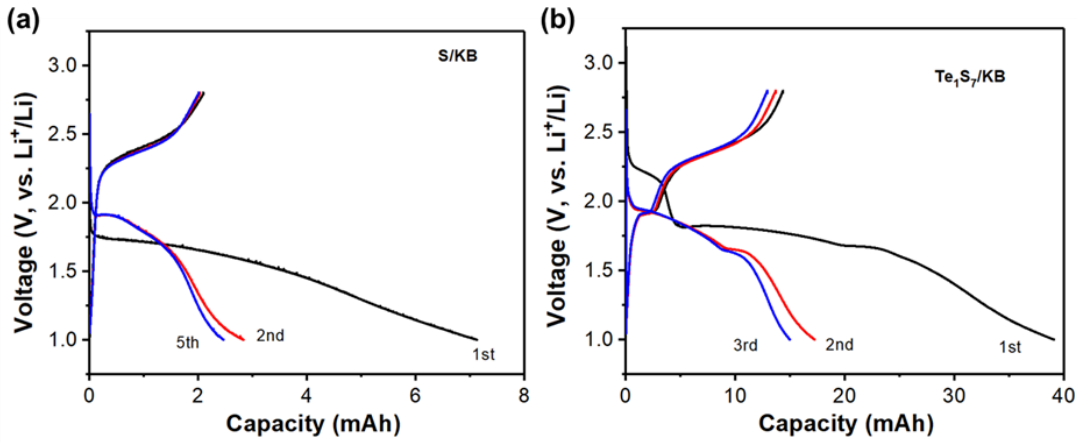

Figure 6.9.2. Charge/discharge profiles of (a) Li-S/KB and (b) Li-Te_1S_7/KB pouch cells in the first three cycles.

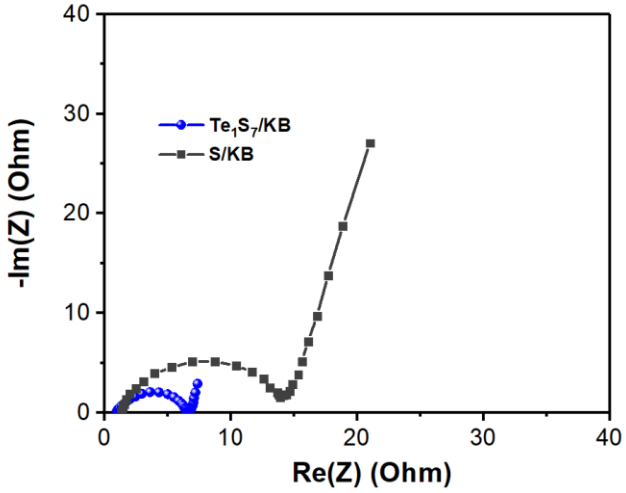

Figure 6.9.3. Nyquist plots of Li-S/KB and Li-Te_1S_7/KB pouch cells before cycling.

On the other hand, there are some interesting findings different from the study of Te_xS_y cathodes in previous studies. The Te_xS_y (1~5 wt% Te content) compounds reported by Xie *et al.* [85] illustrate intense characteristic peaks of S instead of Te in Raman spectra. In contrast, our Te_xS_y compounds from Te_1S_7 to Te_7S_1 show notable characteristic peaks of Te with a peak shift implying Te-S interaction. The diametrically opposite phenomenon might be due to various Te contents and Te distribution. Our SEM/EDS and XPS results suggest that Te element is uniformly anchored to S by the strong chemical bonds after ball-milling and annealing procedures, which causes intense signals of Te as detected by EDS, Raman, XRD and XPS.

Zhou *et al.* [83] also developed Te_xS_y encapsulated into mesoporous CMK-3 with carbonate electrolytes (1M $LiPF_6$ in EC:DMC). The optimal $Te_{0.1}S_{0.9}$/CMK-3 cathode retains 845 mAh g^{-1} after 100 cycles at 0.25 A g^{-1} and 485 mAh g^{-1} after 500 cycles at 1 A g^{-1}. In comparison, our Te_1S_7/KB cathode maintains a stable reversible capacity of 959.8 mAh g^{-1} over 400 cycles at 1 A g^{-1} with our carefully selected electrolyte (3M LiTFSI in DEC:FEC). More importantly, the failure mechanism of S/KB is well investigated and elucidated in our work. The agglomeration of poorly conductive Li_2S on S/KB cathode surface results in the loss of active materials and fast capacity fading. The incorporation of Te accelerates the redox kinetics and contributes to the enhanced utilization of active materials, thus exhibiting superior specific capacity and cycling stability with the help of a stable SEI layer.

On the whole, previous studies in Te_xS_y cathodes report low Te content to reshape Li-S kinetics. The effect of Te content on Li-S chemistry is unclear from both theoretical and experimental perspectives. Also, there has been a lack of in-depth analysis of Te/mesoporous carbon cathodes in carbonate electrolytes. Considering these limitations, our work develops a wide range of Te_xS_y composites with comprehensive characterization and analysis. The detailed simulation results reveal that the Te_1S_7 possesses the lowest energy barrier for Li-ion migration as compared to other Te_xS_y composites. This conclusion is furtherly confirmed and supported by the battery performance and kinetics analysis. In particular, the optimal Te_1S_7/KB cathode outperforms S/KB cathode at both coin cell and pouch cell levels. Furthermore, it is proven that the Te-incorporated S cathode is able to facilitate redox conversion and enhance the utilization of active materials in carbonate electrolytes, thus delivering remarkable reversible capacity and cycling stability.

6.10 GPE-Based Li-S/KB and Li-Te_1S_7/KB Cell Performance

The quasi-solid-state Li-Te_1S_7/KB and Li-S/KB cells were also constructed using the gel polymer electrolytes (GPE) fabricated in Chapter 5. As shown in **Figure 6.10.1**, the GPE-based Li-Te_1S_7/KB cell delivers the specific capacities of 1415.7, 741.5, and 584.5 mAh g^{-1} in the 1st, 2^{nd,} and 5th cycle, respectively, at the current density of 0.1 A g^{-1}. In comparison, the Li-S/KB shows inferior capacities of 1713.7, 549.1, and 243.1 mAh g^{-1} in the 1st, 2^{nd,} and 5th cycle, respectively. With a similar cell configuration, it is reasonable to conclude that the better capacity retention and initial Coulombic efficiency of Li-Te_1S_7/KB cell benefit from faster redox kinetics. Therefore, the

advantages of reaction kinetics and cell performance for the Li-Te_1S_7/KB cell are revealed with both liquid and gel polymer electrolytes.

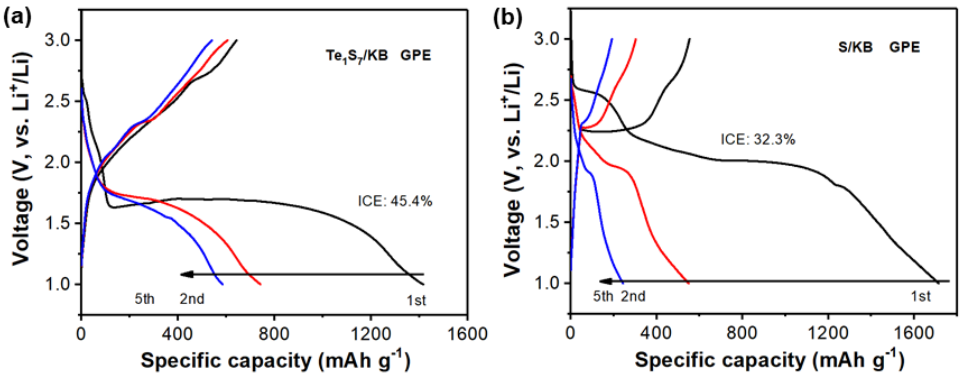

Figure 6.10.1. Charge/discharge profiles of GPE-based quasi-solid-state (a) Li-Te_1S_7 and (b) Li-S cells.

6.11 Chapter Summary

In summary, this work develops Te_xS_y solid solutions with covalent Te-S bonds and reveals the underlying mechanism of Te_xS_y/KB cathodes in carbonate-based electrolytes toward lithium metal anode. Theoretical calculations suggest the more delocalized charge-density differences around the Te atoms in $Li_{16}Te_1S_7$ compared to site-equivalent S atoms in Li_2S, and $Li_{16}Te_1S_7$ possesses lower energy barriers throughout the Li migration pathway. On the other hand, by tuning the molar ratio of Te/S, the Te_xS_y/KB cathodes demonstrate remarkably improved electrochemical performance than S/KB. The Te_1S_7/KB cathode delivers a higher capacity of 1306.7 mAh g^{-1} compared to the S/KB counterpart (483.7 mAh g^{-1}) in carbonate-based electrolytes, due to the boosted lithium-ion transport and electron transfer upon lithiation/delithiation induced by Te. Moreover, Te plays a critical role in forming a stable SEI layer on the surface of Te_xS_y/KB cathode, which helps maintain excellent structural stability, promotes fast redox conversion, and enhances the utilization of active materials. This work provides a prospective strategy to manipulate redox kinetics of Li-S chemistry by rational design of Te_xS_y cathode, opening opportunities to overcome the bottlenecks of current Li-S systems.

Chapter 7 Electrolyte Chemistry and Cathode Structure for K-Te Batteries

7.1 Introduction

Potassium batteries are an emerging energy storage technology due to the large abundance of potassium, low cost, and potentially high energy density. However, it remains challenging to find suitable electrode materials with high energy density and good cycling stability due to the structural instability and kinetics issues resulting from large-size K^+. There is a lack of fundamental understanding of the K-Te battery system. Herein, a durable and high-capacity K-Te battery was developed by rational design of Te/C electrode and electrolyte salt chemistry.

This chapter can be broadly divided into the following sections:

(1) cycling and rate performance of K-Te batteries with KFSI and KPF_6 salts

It was found that the electrolyte salts (KPF_6 and KFSI) had significant impacts on the electrochemical performance of K-Te batteries. The Te/C electrode in the KPF_6-based carbonate electrolyte exhibited higher specific capacity and better rate performance than the Te/C electrode in the KFSI-based one.

(2) redox kinetics analysis of KFSI and KPF_6 based K-Te cells

Mechanism studies revealed that the KPF_6 salt resulted in organic species-rich solid electrolyte interphase (SEI) on Te/C electrode, allowing for fast electron transfer and K-ion diffusion and enhanced K-ion storage performance in K-Te batteries.

(3) investigation of solid electrolyte interphase layer on the Te/C electrode surface

KFSI salt was found to induce the formation of a KF-rich SEI layer, which had much higher resistances for electron and K-ion transport and was less effective for the well-confined Te/C electrode.

Our work finds that the Te electrode and electrolyte chemistry need to be simultaneously optimized and tailored towards K-ion storage in K-Te batteries. It is expected that the finding reported herein might be inspirable for the future development of K- chalcogen (S/Se/Te) batteries.

7.2 Cycling and Rate Performance of K-Te Batteries with KFSI and KPF_6 Salts

The electrochemical performance of the Te/C electrode is evaluated in K-Te cells with two types of carbonate electrolytes (0.8 M KPF_6 and 1 M KFSI, both in EC:DEC) with the bulky Te electrode as the baseline sample. **Figures 7.2.1a-b** compare the cycling stability and Coulombic efficiency (CE) of Te/C and bulky Te electrodes in KPF_6 and KFSI electrolytes. Overall, the Te/C composite electrode outperforms the bulky Te electrode in specific capacity, cycling stability, and CE. The bulky Te only delivers a specific capacity of 384.9 mAh g^{-1} in the KPF_6 electrolyte and of 478.2 mAh g^{-1} in the KFSI electrolyte in the first cycle, followed by a rapid decline to 14.4 mAh g^{-1} and 13.6 mAh g^{-1} after five cycles. **Figures 7.2.1c-d** illustrate the charge-discharge curves of the bulky Te electrode in both KPF_6 and KFSI electrolytes in the first two cycles. During the first discharge process, the bulky Te electrodes exhibit two plateaus at about 1.8 and 1.0 V, respectively, in both the KPF_6 and KFSI electrolytes. The discharge plateau at 1.8 V disappears after the first cycle, which might be mainly due to the decomposition of the electrolyte and the formation of SEI layers. The discharge plateau at 1.0 V corresponds to the potassiation of the Te cathode into K_nTe ($0 < n \leq 2$) [104]. However, the bulky Te electrode shows poor reversibility, as indicated by the low charge capacity in the first cycle (~ 100 mAh g^{-1}) and low initial CE of ~ 24% in both KPF_6 and KFSI electrolytes. The poor electrochemical performance of the bulky Te might result from the acute volume change between Te and K_nTe in the first few cycles and the slow reaction kinetics in the bulky Te.

Compared with the bulky Te, the Te/C electrode shows superior cycling stability with remarkably improved capacity and CE in both KPF_6 and KFSI electrolytes. For example, in the first discharge cycle, the Te/C electrode delivers a specific capacity of 782.7 mAh g^{-1} in the KPF_6 electrolyte and 543 mAh g^{-1} in the KFSI electrolyte at 0.1 C (**Figure 7.2.1a**). The higher capacity of Te/C electrodes than the theoretical value of Te (420 mAh g^{-1} based on K_2Te) is mainly due to the decomposition of electrolytes and the formation of SEI in the first cycle. The capacity contribution from porous carbon was also tested under the same current as Te/C electrodes, and the cycling performance at 0.1C (based on the mass of Te) was shown in **Figure 7.2.2a**. Considering the mass ratio of porous carbon to Te (1:1), the carbon only contributes to 28 and 15 mAh g^{-1} in KPF_6 and

KFSI electrolytes, respectively. Therefore, the discharge capacity of Te/C cathodes primarily comes from Te active materials. The revised cycling capacity of Te/C cathodes subtracting carbon contribution is included in **Figure 7.2.2b**. After the first five cycles at 0.1 C, with the current density increasing to 0.2 C, the Te/C electrode maintains relatively stable performance in the subsequent cycling. After 105 cycles, the specific capacity of the Te/C cathode remains at 233.5 mAh g^{-1} and 166.7 mAh g^{-1} in the KPF_6 and KFSI electrolytes, respectively. Therefore, the KPF_6 electrolyte leads to a higher specific capacity of the Te/C cathode than the KFSI electrolyte. With a higher Te loading (1.2 mg cm^{-2}), Te/C electrode in the KPF_6 electrolyte outperforms the one in the KFSI electrolyte, furtherly confirming the effect of electrolyte salt on the electrochemical performance of the Te/C electrode (**Figure 7.2.3**).

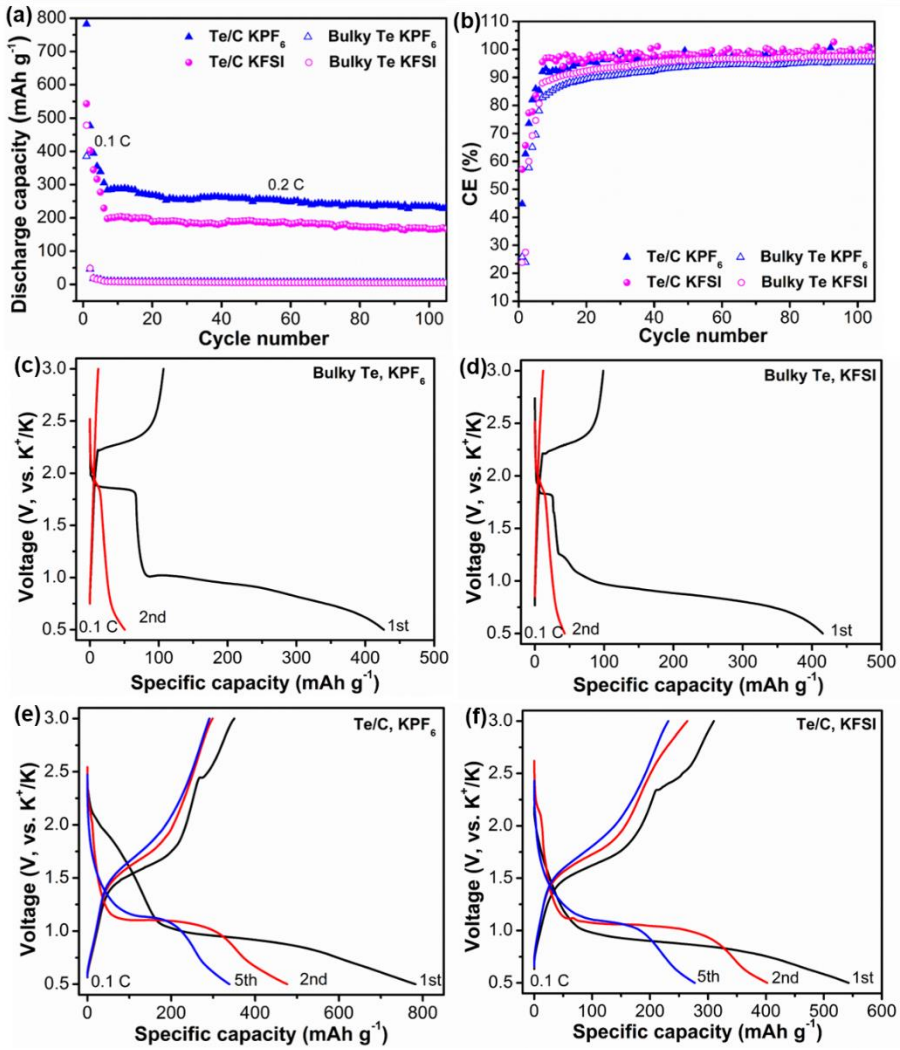

Figure 7.2.1. (a) Cycling stability and (b) CE of the Te/C and bulky Te electrodes in the KPF_6 and KFSI electrolytes, galvanostatic charge-discharge profiles of (c) bulky Te and (e) Te/C electrodes in the KPF_6 electrolyte, (d) bulky Te and (f) Te/C electrodes in the KFSI electrolyte at 0.1C (1 C = 420 mA g^{-1}).

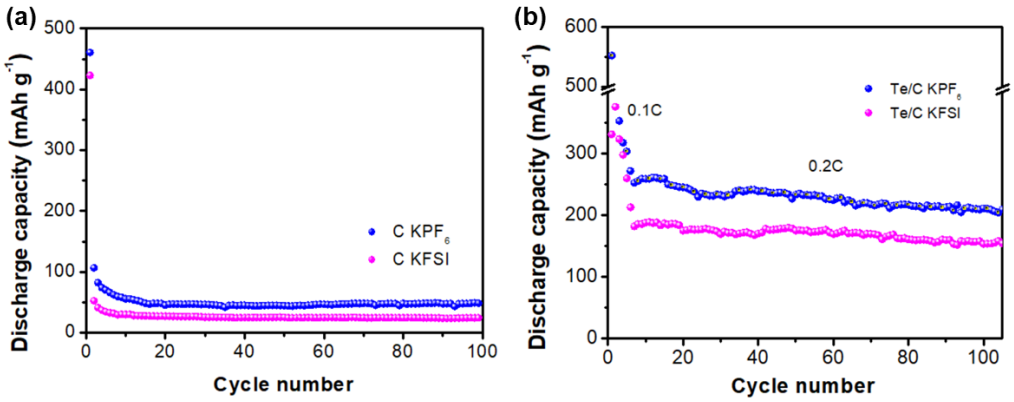

Figure 7.2.2. Specific discharge capacity of (a) carbon at the same current as Te/C cathodes (0.1C), (b) Te/C cathodes (subtracting the capacity of carbon) in the KPF_6 and KFSI electrolytes at 0.1 C and 0.2 C.

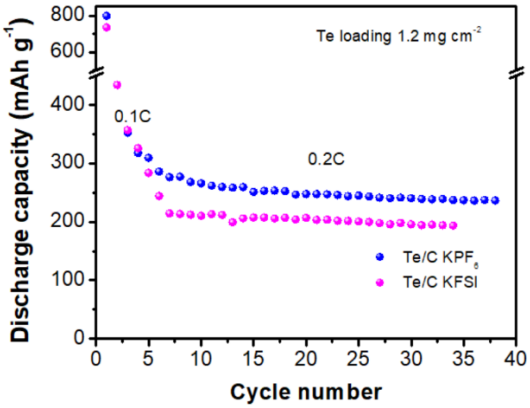

Figure 7.2.3. Cycling performance of Te/C electrodes in KPF_6 and KFSI electrolytes with the Te loading of 1.2 mg cm^{-2} at 0.2 C.

However, the Te/C electrode demonstrates a higher CE in the KFSI electrolyte than in the KPF_6 one, especially in the first 20 cycles, as shown in **Figure 7.2.1b**. The CE of Te/C cathode is 44.8% and 57.1% in the first cycle and gradually reaches 97% and 93% in the subsequent 20 cycles for the KPF_6 and KFSI electrolytes, respectively. Moreover, **Figure 7.2.1b** also shows the higher CE of bulky Te electrode in KPF_6 electrolyte than in the KFSI one over long cycles, despite their relatively low K-ion storage capacities. CE comparison suggests that the decomposition of the KPF_6 electrolyte is more severe than the KFSI one on Te/C cathode, consistent with the observation of more extended irreversible plateaus (1-2V) in the former (**Figures 7.2.1c** and **7.2.1e**)

than the latter (**Figures 7.2.1d** and **7.2.1f**). The electrolyte of 1M KFSI in DME was also employed to evaluate the cycling performance of Te/C cathode in ether electrolytes. The discharge capacities versus cycle number and charge-discharge curves are illustrated in **Figure 7.2.4**. It could be observed that when the current density increases from 0.1C to 0.2 C, the capacity of the Te/C cathode drastically drops to 200 mAh g^{-1} in the 17th cycle and then stabilizes for 50 cycles (**Figure 7.2.4a**). A significant capacity fluctuation is observed in the last 15 cycles, and probably due to that, the excessive K dendrites pierce the separator and react with Te, thus causing a short circuit in ether electrolyte [188, 189]. The galvanostatic charge-discharge curves in **Figure 7.2.4b** show two short discharge plateaus at 1.9 and 1.4 V, corresponding to the multi-step phase transformation from Te to K_2Te_3 and finally to K_5Te_3 [105]. In comparison, the Te/C cathodes possess superior cycling performance in carbonate electrolytes (KPF_6 or KFSI in EC:DEC). Therefore, carbonate electrolyte is used to develop stable K-Te batteries in this work.

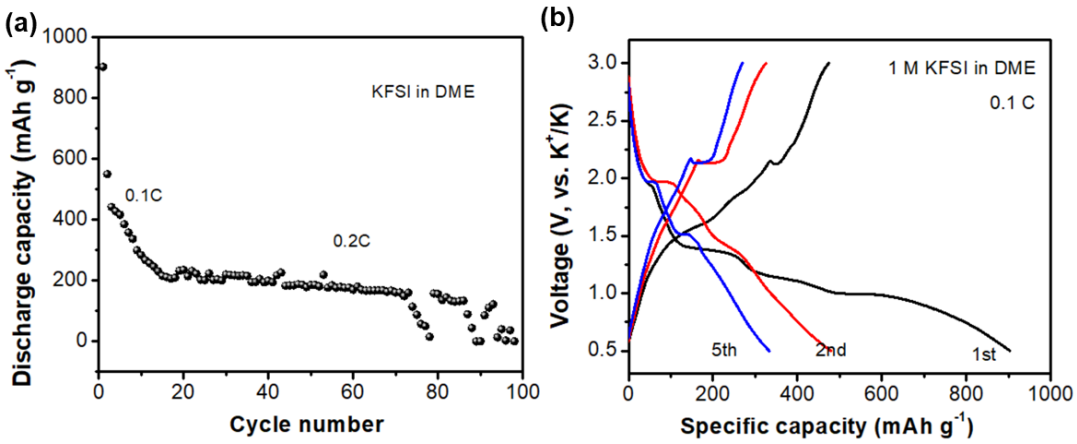

Figure 7.2.4. (a) Cycling performance and (b) charge-discharge curves of the Te/C cathode in the 1st, 2nd, and 5th cycle in 1M KFSI in DME.

Figures 7.2.1e-f also indicate that after the first cycle, the Te/C cathode displays one sloped charge and discharge plateau, corresponding to the transformation between Te and K_nTe $(0 < n \leq 2)$ [104], in both KPF_6 and KFSI electrolytes. To find out the possible reaction mechanism, we recover Te/C cathodes from K-Te cells discharged to 0.5 V for XRD analysis (**Figure 7.2.5**). The XRD patterns of the potassiated Te/C electrodes show one peak at 31.0°, attributed to the (220) plane of K_2Te (JCPDS PDF # 77-2154), and three additional peaks at 27.5°, 38.5°, and 39.3°, assignable to (330), (402), and (600) planes of K_5Te_3 (JCPDS PDF # 79-1056). In addition to K_2Te as expected, the

appearance of K_5Te_3 might result from incomplete potassiation of Te/C cathode when discharged to 0.5 V at 0.1 C [105]. This would explain the relatively lower K-ion storage capacity of the Te/C cathode than the theoretical value of Te (420 mAh g^{-1}) because K_5Te_3 could only deliver a specific capacity of 357 mAh g^{-1}). It is interesting to note that a previous work also found K_2Te_3 and K_5Te_3, instead of mere K_2Te, as discharge products of Te-based cathode discharged to 0.5 V in K-Te batteries [105]. In contrast, Guo and co-authors [104] confirmed the dominance of the K_2Te discharge product of the Te-G-CNT electrode at the cut-off voltage of 0.3 V by HRTEM, XRD, and XPS analysis. Moreover, they performed density functional theory calculation on the formation energy of K_nTe and found that K_2Te possessed the lowest formation energy (-1.028 eV, *vs.* -0.965 eV for K_5Te_3, -0.84 eV for K_2Te_2, and -0.719 eV for K_2Te_3) and was the most thermodynamically stable form. Therefore, we speculate that extending discharge cut-off voltage or using a smaller current density could achieve a complete transformation from Te to K_2Te in Te/C cathode in our work.

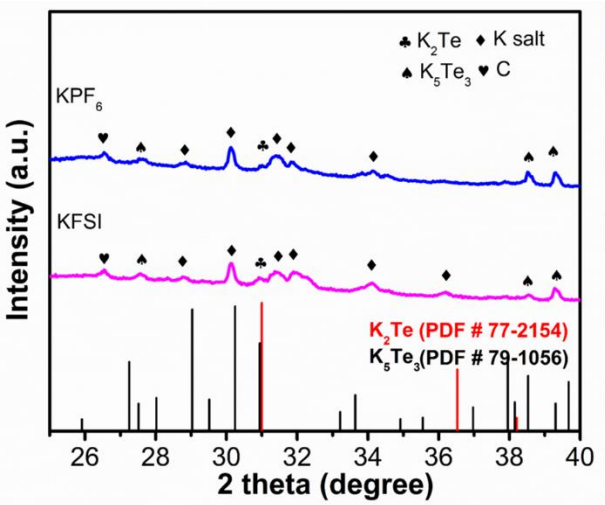

2 theta	Substance	PDF #	(hkl)
26.6	C	26-1079	0 0 3
27.5	K_5Te_3	79-1056	3 3 0
28.8	K salt	11-0658	-2 1 1
30.1	K salt	11-0658	0 1 2
31.0	K_2Te	77-2154	2 2 0
31.3	K salt	43-1020	1 1 0
31.8	K salt	47-1329	3 3 0
34.1	K salt	16-0820	1 1 2
36.1	K salt	47-1329	3 3 2
38.5	K_5Te_3	79-1056	4 0 2
39.3	K_5Te_3	79-1056	6 0 0

Figure 7.2.5. XRD patterns of the Te/C electrodes after discharge to 0.5 V in the KPF_6 and KFSI electrolytes at 0.1C.

The rate performance of the Te/C and bulky Te cathodes in the KPF_6 and KFSI electrolytes is shown in **Figure 7.2.6**. As seen in **Figure 7.2.6a**, the Te/C cathode demonstrates a considerably better rate capability than the bulky Te in both electrolytes. Moreover, Te/C cathode exhibits a higher capacity and better rate capability in the KPF_6 electrolyte than in the KFSI one. For example, the Te/C cathode delivers a specific capacity of 336.5, 260.0, 187.3, and 143.9 mAh g^{-1} in the

KPF_6 electrolyte and of 292.1, 199.9, 123.5, and 91.1 mAh g^{-1} in the KFSI one, at 0.1, 0.2, 0.5, and 1 C, respectively. Moreover, the Te/C cathode recovers a reversible capacity of 356.4 mAh g^{-1} in the KPF_6 electrolyte once the current density is reversed from 1C back to 0.1 C. **Figures 7.2.6b-d** compare charge-discharge curves of Te/C cathodes at 0.1, 0.2, and 0.5 C in the KPF_6 and KFSI electrolytes. The overpotential between charge and discharge processes of Te/C cathode is smaller in the KPF_6 electrolyte than the KFSI one, suggesting faster reaction kinetics in the former than the latter. The effect of KPF_6 and KFSI salts on the overpotential of Te/C cathodes is amplified at higher currents.

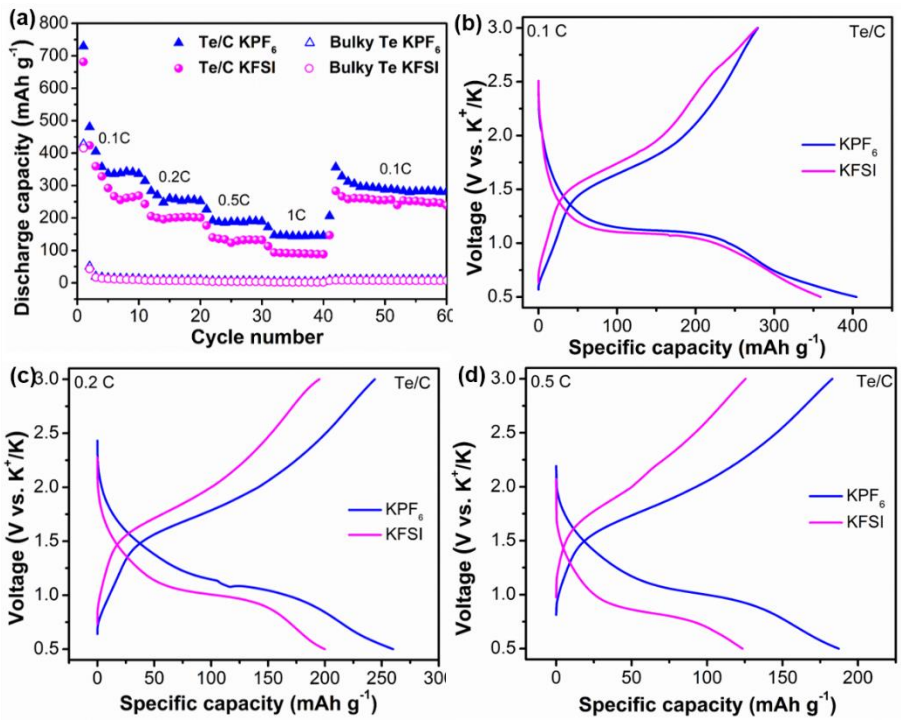

Figure 7.2.6. (a) Rate capabilities of the Te/C and bulky Te electrodes in the KPF_6 and KFSI electrolytes, charge-discharge profiles of the Te/C electrodes at (b) 0.1 C, (c) 0.2 C, and (d) 0.5 C.

7.3 Redox Kinetics Analysis of KFSI and KPF_6 Based K-Te Batteries

To find out the effect of KPF_6 and KFSI salts on the reaction kinetics, CV measurement was carried out on the Te/C cathodes at various scan rates of 0.2, 0.3, 0.4, 0.5, 0.6, and 1 mV s^{-1}, and the results are presented in **Figure 7.3.1**. As shown in **Figures 7.3.1a-b**, the CV curves of Te/C cathodes in

KPF_6 and KFSI electrolytes exhibit mainly one pair of reduction and oxidation peaks at 0.6 V and 1.8 V, respectively, at 0.2 mV s^{-1}, which agree with the one discharge and charge plateaus (**Figures 7.3.1e-f**) and correspond to conversion between Te and K_2Te/K_5Te_3. Similar phenomena have also been observed in Te/porous carbon (Te-G-CNTs) cathode in K-Te batteries with carbonate electrolytes, which underwent a one-step transformation from Te to K_2Te [28].

With the increasing scan rates from 0.2 to 1 mV s^{-1}, it is found that the peak currents (I_p) change with the scan rates (v) following the Randles-Sevcik equation [110]:

$$I_p = 2.69 \times 10^5\, n^{3/2} A D^{1/2} v^{1/2} C = B \times v^{1/2} \qquad \text{Eq. 7.1}$$

Where I_p is the peak current, n is the number of electron transfer, A is the effective reaction area, D is the K-ion diffusion coefficient, v is the scan rate, C is the K-ion concentration, and B is the slope of the fitted I_p-$v^{1/2}$ curves (**Figure 7.3.1c**). From **Figure 7.3.1c**, it is evident that the reduction and oxidation peak currents are linear to the square root of scan rate, indicating a diffusion-controlled process for potassiation and depotassiation of Te cathode [104]. By fitting the I_p-$v^{1/2}$ curves in **Figure 7.3.1c**, K-ion diffusion coefficient (D) in Te/C cathode is calculated to be 1.02×10^{-10} (reduction) and 4.87×10^{-10} cm^2 s^{-1} (oxidation) for the KPF_6 electrolyte, and 4.36×10^{-11} (reduction) and 2.82×10^{-10} cm^2 s^{-1} (oxidation) for the KFSI one (**Figure 7.3.1d**).Te/C cathode shows higher K-ion diffusion rates and faster redox kinetics in the KPF_6 electrolyte than the KFSI one, explaining the better rate capability and higher specific capacity of the Te/C cathode in the former than the latter.

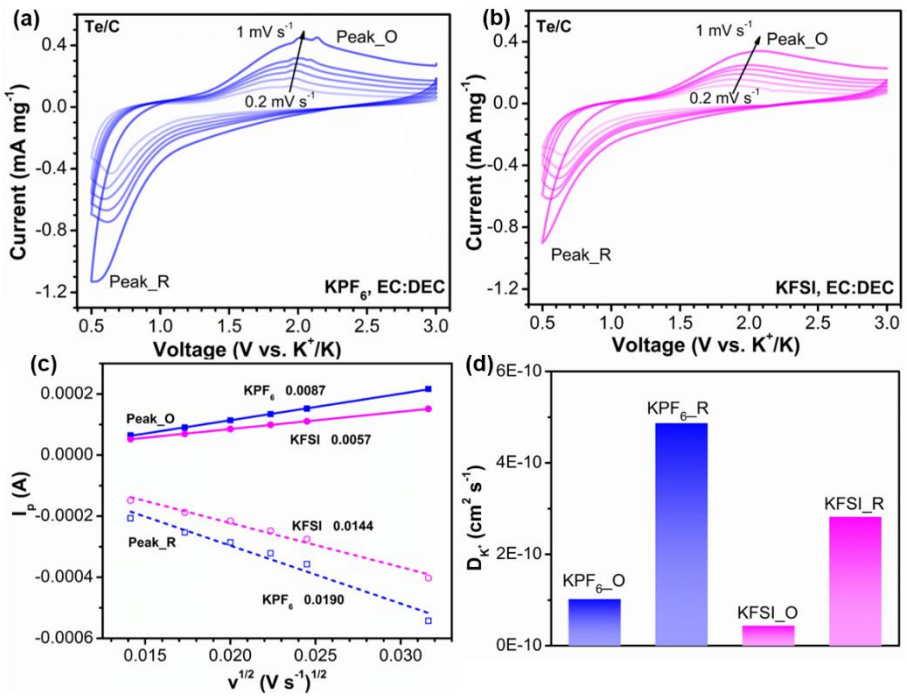

Figure 7.3.1. CV curves of the Te/C cathodes in (a) KPF_6 and (b) KFSI electrolytes at scan rates from 0.2 to 1 mV s^{-1}; (c) linear fits of the CV peak current *vs.* square root of scan rate, (d) calculated K-ion diffusion coefficients in the Te/C cathodes in the KPF_6 and KFSI electrolytes.

EIS measurement was performed in K-Te cells before and after cycling to obtain a better understanding of the salt effect on interface resistances. The Nyquist plots are presented in **Figures 7.3.2a-b**. Before cycling, the charge transfer resistance (R_{ct}) of Te/C cathode is 413.9 Ω and 1096.0 Ω in the KPF_6 electrolyte and the KFSI one. After 105 cycles, it can be seen that the semicircle originating from SEI resistance (R_{SEI}) and R_{ct} is more extensive in the KFSI electrolyte (**Figure 7.3.2b**) than the KPF_6 one (**Figure 7.3.2a**). By fitting Nyquist plots using the equivalent circuit in the inset of **Figure 7.3.2b**, the R_{SEI} and R_{ct} for both samples are quantified and compared in Table 1. It can be found that the R_{SEI} and R_{ct} for the Te/C in the KPF_6 electrolyte gradually increase from 4.5 and 540.5 Ω in the 7th cycle to 50.0 and 643.1 Ω in the 105th cycle, respectively. The elevation in both R_{SEI} and R_{ct} is likely due to the continuous decomposition of the electrolyte. Compared to the KPF_6 electrolyte, the KFSI one results in much higher R_{SEI} and R_{ct} (**Table 7.3.1**). The higher R_{SEI} and R_{ct} of Te/C cathode in the KFSI electrolyte might slow down the K-ion diffusion through the SEI layers and is believed to be responsible for its lower specific capacities and worse rate capabilities than Te/C cathode in the KPF_6 electrolyte.

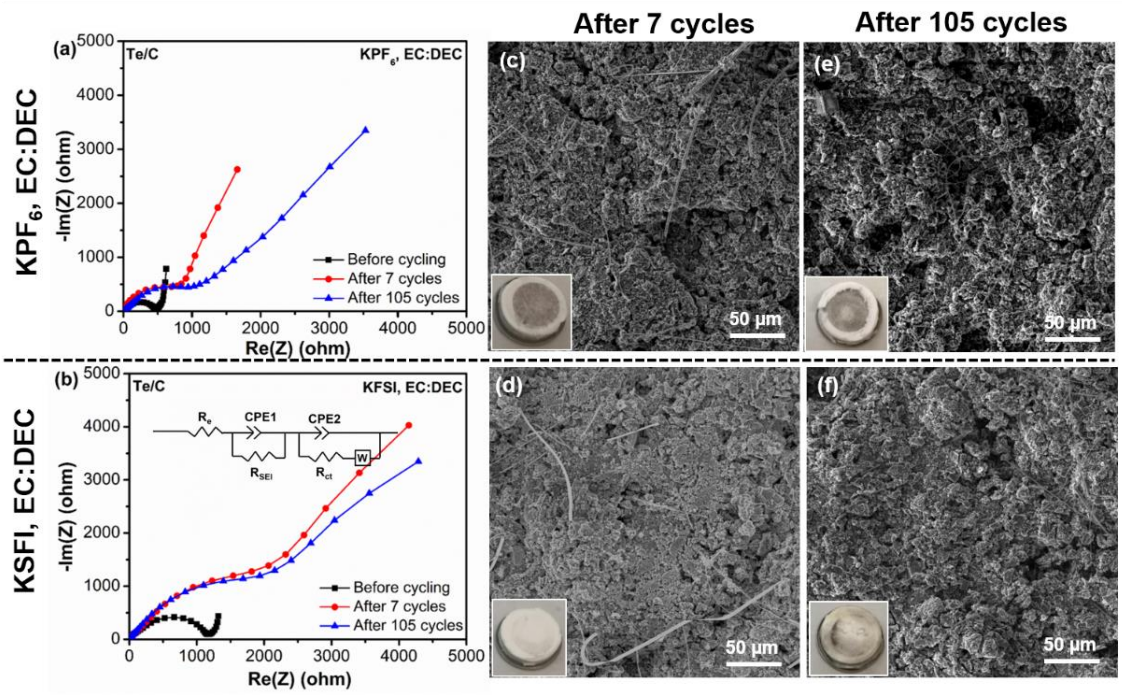

Figure 7.3.2. (a, b) Nyquist plots of the K-Te cells with KPF_6 and KFSI electrolytes and SEM images of the Te/C electrodes recovered from K-Te cells after (c, d) 7 cycles and (e, f) 105 cycles (inset in (b) is the equivalent circuit used to fit the Nyquist plots after 7 and 105 cycles).

Table 7.3.1. Calculated R_e, R_{SEI}, and R_{ct} from the Nyquist plots in Figures 5a and 5b.

Te/C electrode	In KPF_6			In KFSI		
	R_e (Ω)	R_{SEI} (Ω)	R_{ct} (Ω)	R_e (Ω)	R_{SEI} (Ω)	R_{ct} (Ω)
Before cycling	4.0	-	413.9	2.6	-	1096.0
After 7 cycles	4.7	4.5	540.5	2.8	286.4	743.6
After 105 cycles	6.4	50.0	643.1	2.8	235.8	951.2

The morphologies of Te/C cathodes obtained from the K-Te cells after the 7th and 105th cycles are displayed in **Figures 7.3.2c-f**. The cycled Te/C electrode in the KFSI electrolyte possesses a flat

and compact surface, while the one from the KPF_6 electrolyte becomes rougher with increasing cycle numbers. The glass-fiber separator from the KPF_6 electrolyte turns blackish even after seven cycles (the inset in **Figure 7.3.2c**) because Te/C active material peeled off from the Al current collector over cycling. This would explain the gradual increase in R_{SEI} and R_{ct} of the Te/C electrode in the KPF_6 electrolyte (**Figure 7.3.2a**). In contrast, there is no apparent change in the separator from the KFSI electrolyte after 7 and 105 cycles (**Figures 7.3.2d-f**). This observation suggests that, compared to KPF_6, the KFSI enables better mechanical stability of the Te/C electrode to accommodate the stress generated from volume changes, thus effectively preventing active material exfoliation and maintaining electrode integrity [190, 191]. Meanwhile, KFSI results in considerably higher interfacial resistances on the Te/C electrode than KPF_6 does in K-Te batteries. The influence of electrolyte salts is likely due to their abilities to generate SEI layers, which ultimately affect electrochemical performance, interface resistance, and mechanical properties of the Te/C electrode during potassiation and depotassiation processes.

7.4 Investigation of Solid Electrolyte Interphase Layer on the Te/C Electrode Surface

XPS analysis was performed on the Te/C cathodes discharged to 0.5 V to obtain deeper insight into the influence of electrolyte salts on the chemical compositions of SEI layers, and the spectra are illustrated in **Figure 7.4.1**. The full survey in **Figure 7.4.1a** and atomic composition in **Table 7.4.1** show that the SEI layers consist of mainly C, Te, O, F, and K elements in both KPF_6 and KFSI electrolytes. Si and Na elements are detected on the Te/C electrode in KPF_6 electrolyte, likely from the residual glass fiber separator and sodium carboxymethyl cellulose binder on the electrode. As seen in **Figure 7.4.1b**, the C 1s spectra in KPF_6 and KFSI electrolytes could be decomposed into four peaks at 284.6, 286.0, 287.5, 289.5, and 290.5 eV, corresponding to C-C, ROK, C-O-C, C=O, and ROCOOK, respectively [192]. The O 1s spectra (**Figure 7.4.1c**) are composed of three peaks located at 531.6, 532.5, and 534.0 eV, respectively, assignable to C-O, C=O, and ROOK. The C-O and C=O species appear on Te/C surface in KPF_6 and KFSI electrolytes and may originate from the decomposition of the electrolyte salts and the reduction of carbonate solvents (EC and DEC) [193, 194]. One main difference between the SEI layers from KPF_6 and KFSI electrolytes is revealed in the F1s spectra (**Figure 7.4.1d**). In the KPF_6 electrolyte,

the peak at 688.4 eV originates from the P-F species, which is further verified by its P 2p spectrum (**Figure 7.4.1e**) and probably due to incomplete decomposition of KPF_6 salt [190]. In the KFSI electrolyte, the peak at 689.5 eV results from S-F species in the electrolyte, and the other two peaks at 683.8 and 685.3 eV are a strong indication of K-F species [195]. The K-F species found in the sample in the KFSI electrolyte may be from the reduction of S-F bonds in FSI^- [190]. It is worth noting that the K-F species is not detected in the SEI generated from the KPF_6 electrolyte. Besides, the two peaks of Te 3d XPS spectra at 573.5 eV and 583.9 eV in pristine Te/C shift to 583.3 eV and 572.9 eV for the discharged Te/C electrode (**Figure 7.4.1f**), confirming the transformation from Te to K_nTe ($0 < n \leq 2$) in both KPF_6 and KFSI electrolytes [104]. XPS analysis reveals that the SEI layer in both electrolytes is very different due to the use of different salts. A KF-rich and stable SEI layer is formed on Te/C cathode in the KFSI-containing electrolyte, while an organic species-rich, KF-deficient, and less stable SEI layer is generated in the KPF_6-containing electrolyte.

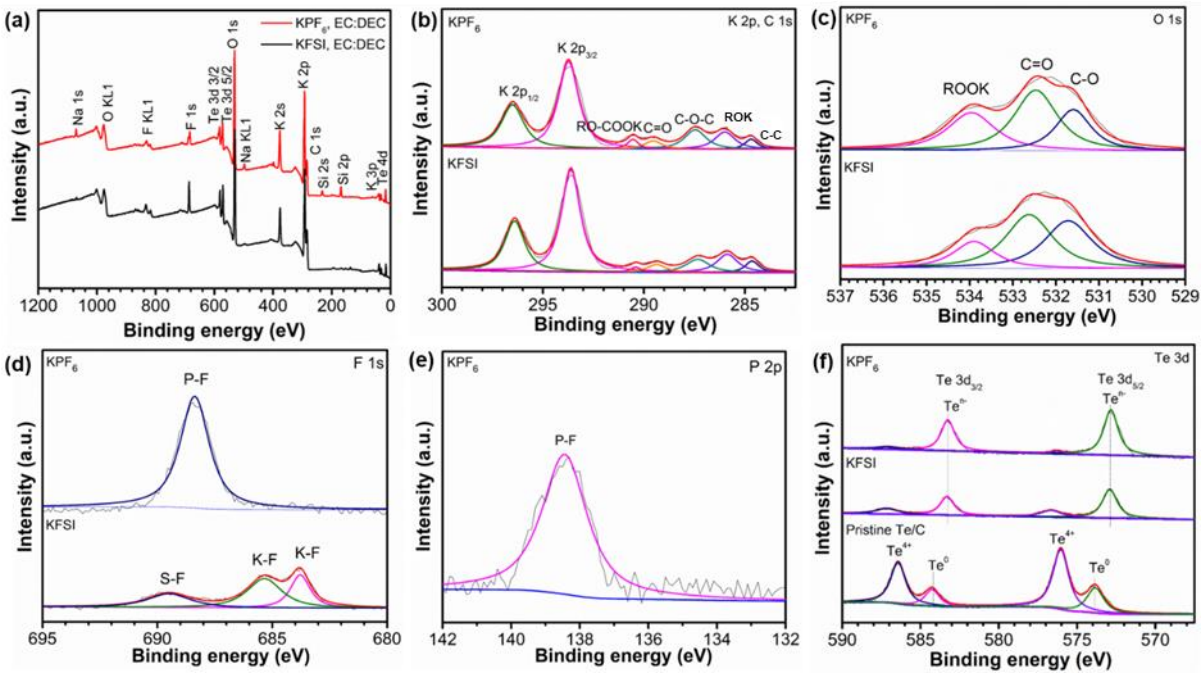

Figure 7.4.1. (a) XPS full survey, (b) K 2p and C 1s, (c) O 1s, (d) F 1s, (e) P 2p, and (f) Te 3d spectra of the Te/C cathodes discharged to 0.5 V in K-Te cells with KPF_6 and KFSI electrolytes.

Table 7.4.1. Atomic compositions of the Te/C electrodes discharged to 0.5 V.

Electrolyte	C	O	F	Te	K	S	P	Si	Na
KPF_6, EC:DEC	33.97	33.67	6.13	1.65	22.95	0	0.72	0.73	0.19
KFSI, EC:DEC	30.01	33.39	4.30	1.25	23.86	3.91	0.12	0.42	0.80

From the results above, we can find that the electrolyte salt plays a critical role in determining the electrochemical performance of Te/C cathodes in K-Te batteries by affecting the SEI layers formed. KPF_6 electrolyte induces an organic species-rich and less-stable SEI layer, which, however, offers less SEI and charge transfer resistances and higher K-ion diffusion coefficients in the Te/C cathode. On the other hand, KFSI electrolyte causes the formation of a KF-rich and stable SEI layer, which leads to higher CE of the Te/C cathode but much elevated internal resistances and reduced K-ion diffusion coefficients. Although the KF-rich SEI layer enables better mechanical stability, higher CE, and less side reaction on the Te/C electrode, it also results in significantly reduced reaction kinetics, which outperforms the benefits accompanied. In the KPF_6 electrolyte, the Te/C cathode exhibits much improved K-ion storage performance, high rate capability, and fast reaction kinetics owing to the lower interface resistances and better K-ion diffusion coefficients, despite the less stable SEI layer. It should be noted that the influence of KPF_6 and KFSI electrolytes has been reported in the anode (MoS_2, Sn_4P_3, Bi, and GeP_5) in PIBs [190-192, 196-201]. The general trend was KFSI-containing electrolytes enabled the better electrochemical performance of these anode materials than KPF_6-containing ones did due to a more stable SEI layer, suppressed excessive side reactions, and enhanced potassium storage stability by the former than the latter. The finding in our work is opposite to the previous observations in the anode. One possible reason could be due to the Te/C composite, in which Te is wholly impregnated into numerous micropores of activated carbon and exists as amorphous nanoparticles with sizes of less than 3 nm. The majority of Te is embedded into the carbon micropores and has much less physical contact with the electrolyte than these nanostructured anodes reported previously. As such, the stable SEI layer induced by KFSI is less significant in the Te/C electrode than in these anodes. Instead, the negative effect of the KF-rich SEI layer by KFSI becomes the dominant limiting factor in the electrochemical performance

of Te/C cathode. From the above results, it can be found that the electrolyte salt is a double-edged sword and needs to be tailored and optimized towards different electrode materials for PIBs.

On the other hand, this Te/C electrode could also be used as a conversion-type anode in KIBs, considering its relatively low voltage (around 1 V). To assess the suitability of Te/C as an anode, we evaluated its performance in an extended voltage window of 0.1 - 3 V, and the results are shown in **Figure 7.4.2**. The Te/C electrode delivered capacities of 443 and 374 mAh g^{-1} in the KPF_6 and KFSI electrolyte, respectively, at 0.2C. The superior potassium-ion storage capacity makes Te/C electrodes a potential anode to couple with a high-voltage cathode in KIBs.

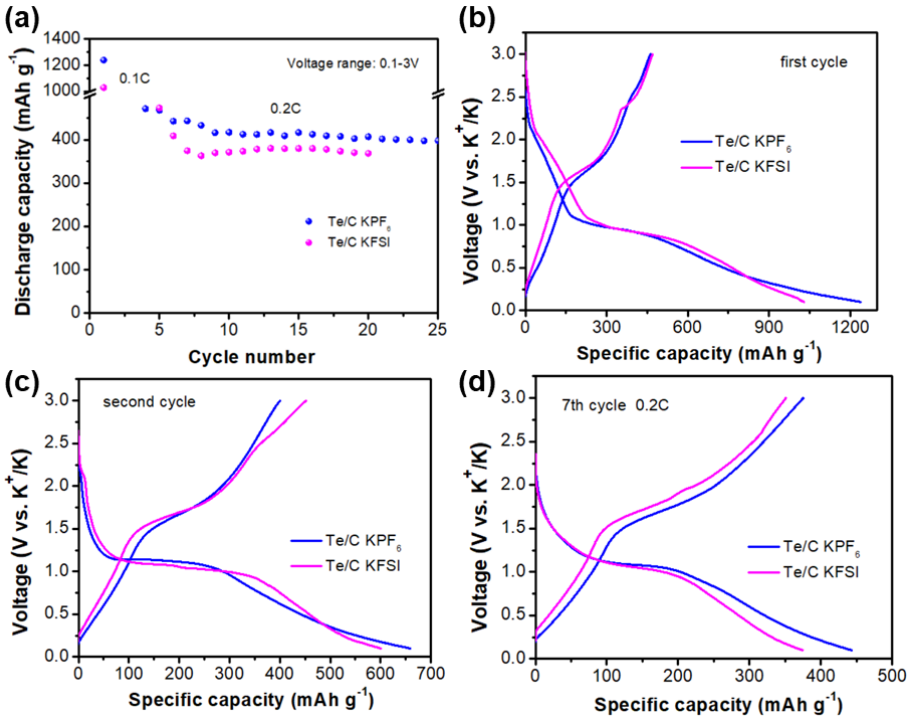

Figure 7.4.2. (a) Cycling performance and (b-d) charge-discharge curves at the 1st, 2nd, and 7th cycle of the Te/C electrode in KPF_6 and KFSI electrolytes in an extended voltage range of 0.1-3 V.

7.5 Chapter Summary

In summary, a durable K-Te battery with carbonate electrolytes is developed by confining Te into numerous micropores of activated carbon. Compared to the bulky Te, the Te/C cathode shows remarkably boosted potassium storage performance and cycling stability due to the alleviated

volume change accompanied by the potassiation and depotassiation processes. Moreover, it is revealed that the two electrolyte salts (KPF_6 and KFSI) induce similar phase transformation from Te to K_nTe ($0 < n \leq 2$) but different specific capacities, reaction kinetics, and SEI compositions on the Te/C cathode. KPF_6 is proven to possess lower interfacial resistance and higher K-ion diffusion coefficient, thus contributing to faster redox kinetics and superior potassium storage capacity. However, the organic species-rich SEI layer induced by KPF_6 is less stable. In contrast, a KF-rich and stable SEI layer is generated on the Te/C cathode when using KFSI as the electrolyte salt, which suppresses the side reactions and results in improved CE and structural integrity, despite slower reaction kinetics. This work provides a feasible strategy for cathode and electrolyte design for K-Te batteries, paving the way for the development of low-cost energy storage systems.

Chapter 8 Improving Cathode Structure Stability by Atomic Layer Deposition Technique

8.1 Introduction

The emerging potassium-tellurium (K-Te) battery system is expected to realize fast reaction kinetics and excellent rate performance due to the exceptional electrical conductivity of Te. To date, there has been a lack of fundamental knowledge about this new K-Te system, including the reaction mechanism and cathode structure design. Chapter 7 presents our new findings of the effect of K salts on K-Te battery performance involving capacity, CE, kinetics, and SEI composition. However, the Te/C cathode delivers a relatively low specific capacity (below 300 mAh g^{-1} at 0.2C) in comparison with its theoretical value (420 mAh g^{-1}). Employing a more electrically conductive carbon as Te host might facilitate electron transfer and enable faster redox conversion, thus enhancing K-ion storage performance.

Herein, a well-confined cathode structure is designed with Te encapsulated into BP2000 porous carbon. A two-step reaction pathway from Te to K_2Te_3 and ultimately to K_5Te_3 is investigated in carbonate electrolyte-based K-Te batteries by X-ray diffraction, high-resolution transmission electron microscopy, and selected area electron diffraction characterizations. Additionally, the atomic layer deposition technique is adopted to deposit an ultrathin aluminum oxide (Al_2O_3) film on the electrode surface, which induces the generation of a stable solid electrolyte interphase layer and reduces the loss of active materials effectively. Consequently, the rationally fabricated Te/porous carbon cathode with functional Al_2O_3 coating delivers remarkable long-term cycling stability over 500 cycles at 1 C with an ultralow capacity decay of only 0.01% per cycle. This interface engineering strategy is validated to stabilize the electrode surface, enhance the structural integrity and ensure reliable electron transfer and K-ion conduction over repeated potassiation/depotassiation cycles. These findings are expected to promote the development of high-energy-density K-S/Se/Te batteries.

8.2 Te/C Cathode Design

Previous studies showed that the phase transformation from Te to K_2Te during the discharge process accompanied massive volume expansion (398%) [104]. The undesirable volume change causes pulverization of Te active materials and irreversible capacity loss [46, 50]. Herein, porous carbon BP2000 is utilized as the Te host *via* the melt diffusion method to effectively confine Te during the potassiation/depotassiation process. SEM images in **Figure 8.2.1a** shows irregular shapes of BP2000 powders. BP2000 consists of a majority of micropores below 2 nm and a small portion of mesopores with a pore size of 3 nm, as indicated by the hysteresis at high relative pressure above 0.9 in the pore size distribution (**Figure 8.2.1b**). **Figure 8.2.1c** demonstrates the characteristics of both type II and type IV isotherms of BP2000, confirming that BP2000 possesses mixed micropores and mesopores. The large surface area of 1515.7 m^2 g^{-1} and pore volume of 2.45 cm^3 g^{-1} can offer sufficient Te loading sites to confine Te and accommodate its volume change. After incorporating Te, Te/BP2000 shows no significant difference in the SEM images (**Figure 8.2.1d**) compared to BP2000. By characterizing Te/BP2000 composite at the nanometer level, abundant dark particles are observed (**Figure 8.2.1e**), implying a successful infusion of Te into micro/mesopores. HRTEM images in **Figures 8.2.1f-g** illustrate amorphous structure in most areas and a small proportion of ordered planes. The interplanar distance of 0.32 nm is assigned to the (011) plane of crystalline Te. The SAED inset in **Figure 8.2.1g** also proves the existence of crystalline Te. High-angle annular dark field (HAADF) and EDS mapping in **Figure 8.2.1h** suggest the uniform distribution of Te in the BP2000 matrix. XRD pattern of Te/BP2000 composite in **Figure 8.2.1i** demonstrates only one broad characteristic peak of Te at 27.6° agreeing with the (011) plane of Te (JCPDS PDF # 79-0736). Based on these results, Te is wholly impregnated into porous carbon BP2000 in the existence of dominant amorphous Te and minor crystalline Te.

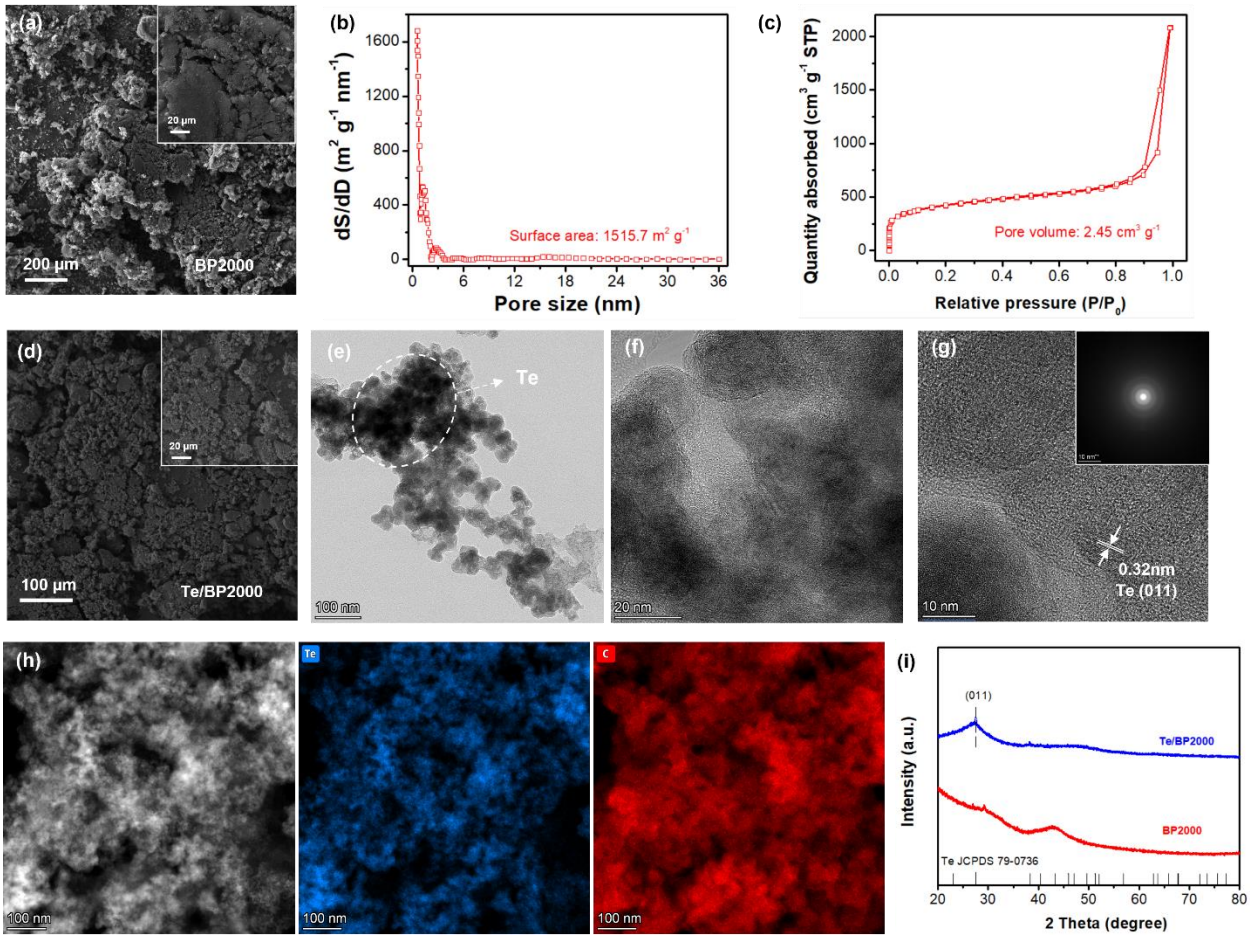

Figure 8.2.1. (a) SEM image, (b) pore size distribution, (c) nitrogen adsorption-desorption isotherm of BP2000 porous carbon; (d) SEM, (e) TEM, (f, g) HRTEM images of Te/BP2000 (the inset in (g) is its corresponding SAED pattern), (h) HAADF and elemental mapping of Te/BP2000, and (i) XRD patterns of BP2000 and Te/BP2000.

8.3 Electrochemical Performance of K-Te/BP2000 Batteries

The electrochemical performance of Te/BP2000 is evaluated in a K-Te cell at various current densities from 0.1 to 10 A g^{-1}. S/BP2000 and Se/BP2000 cathodes are also prepared by the same melt diffusion method and slurry casting process and tested at the same current density and voltage range (0.5-3 V) for a fair comparison. The broad XRD patterns of S/BP2000 and Se/BP2000 in **Figure 8.3.1** imply the impregnation of S and Se into carbon pores. **Figure 8.3.2** confirms active materials contents in the cathodes, *i.e.*, 54 wt% S in S/BP2000, 52 wt% Se in Se/BP2000, and 46 wt% Te in Te/BP2000.

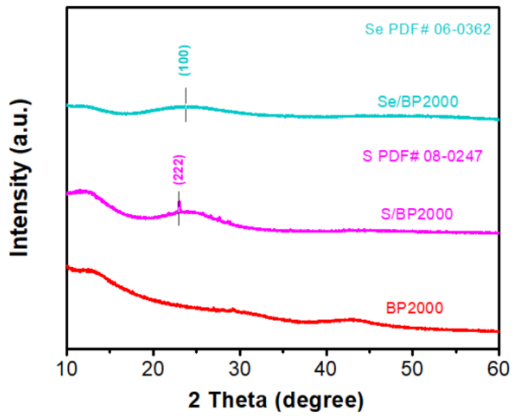

Figure 8.3.1. XRD patterns of S/BP2000 and Se/BP2000.

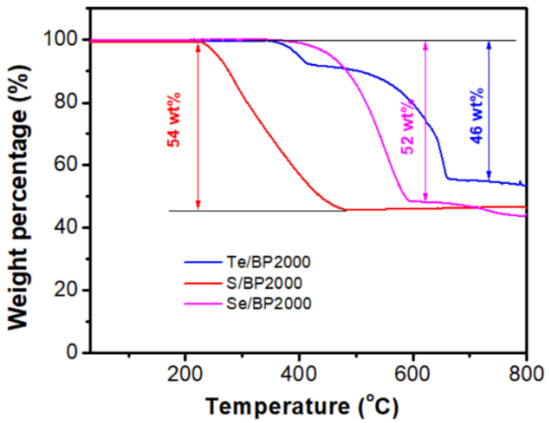

Figure 8.3.2. TGA curves of S/BP2000, Se/BP2000, and Te/BP2000 composites measured at nitrogen atmosphere.

Figures 8.3.3a-c shows galvanostatic charge/discharge profiles of S/BP2000, Se/BP2000, and Te/BP2000 cathodes, respectively. The specific capacity is calculated based on the mass of active materials (S, Se, or Te). In the first potassiation process at 0.1 A g^{-1}, S/BP2000, Se/BP2000, and Te/BP2000 cathodes deliver a specific capacity of 1442.5, 1026.7, and 1180.5 mAh g^{-1}, respectively. The multiple discharge platforms for S/BP2000 and Se/BP2000 could be attributed to the formation of polysulfides and polyselenides [202, 203], which are also observed from several oxidation/reduction peaks in the 1st cyclic voltammetry (CV) scan (**Figure 8.3.4**). The irreversible capacity between the 1st and 2nd cycles is due to the decomposition of electrolytes, the formation of solid electrolyte interphase (SEI), and the irreversible capacity contribution from the carbon host [204-206]. The capacity contribution of BP2000 carbon is presented in **Figure 8.3.5**.

BP2000 delivered a high initial capacity of 637 mAh g^{-1} followed by a fast decline to 100 mAh g^{-1}, suggesting high irreversible capacity from the BP2000 carbon host. Moreover, it should be noted that, due to the mass ratio of Te/BP2000 (54:46), BP2000 only contributed to 46 mAh g^{-1} for the K-Te/BP2000 cell. The majority of the reversible capacity is attributed to active materials Te via K-Te electrochemistry. The discharge capacities for the 2nd and 5th cycle drastically drop to 189.6 and 112.8 mAh g^{-1}, respectively, for S/BP2000 cathode, and 478.4 and 344.8 mAh g^{-1}, respectively, for Se/BP2000 cathode. The rapid capacity decline for S/BP2000 and Se/BP2000 cathodes could be ascribed to the shuttle effect [207, 208]. By contrast, Te/BP2000 cathode demonstrates superior capacities of 459.7 and 440 mAh g^{-1} for the 2nd and 5th cycle, respectively.

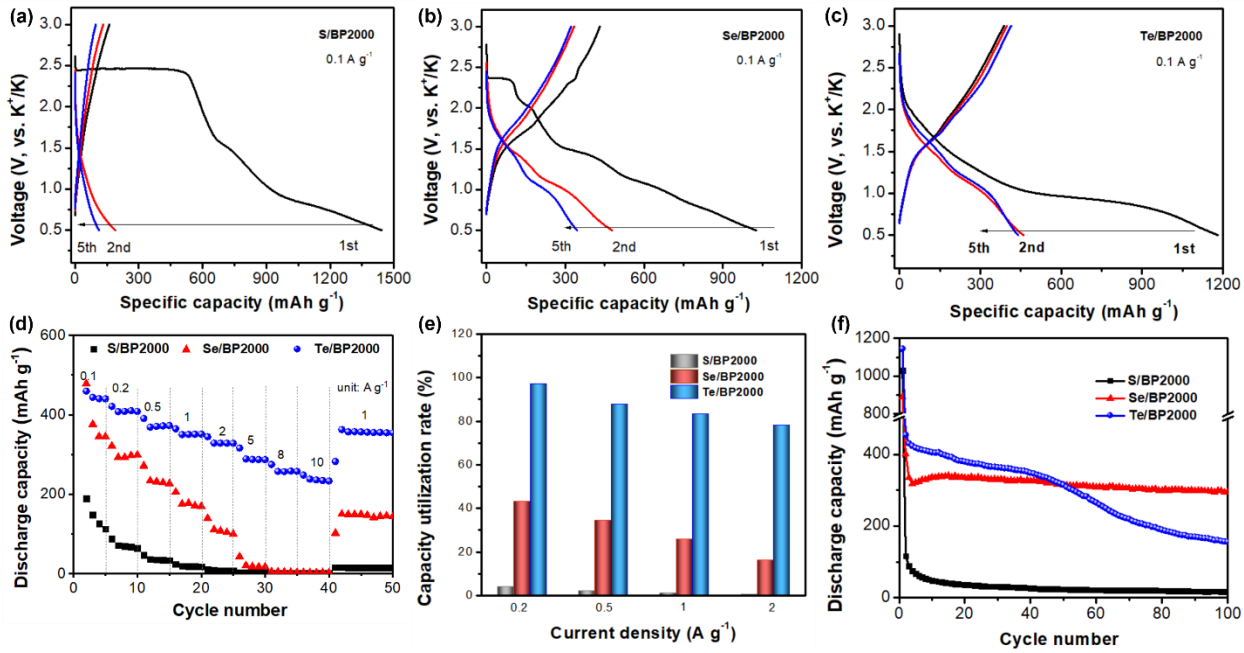

Figure 8.3.3. Charge-discharge profiles at initial cycles at 0.1 A g^{-1} for (a) S/BP2000, (b) Se/BP2000, and (c) Te/BP2000, (d) rate capabilities, (e) capacity utilization at 0.1-1 A g^{-1}, and (f) cycling performance of S/BP2000, Se/BP2000, and Te/BP2000 at 0.1 C (based on their own theoretical capacities).

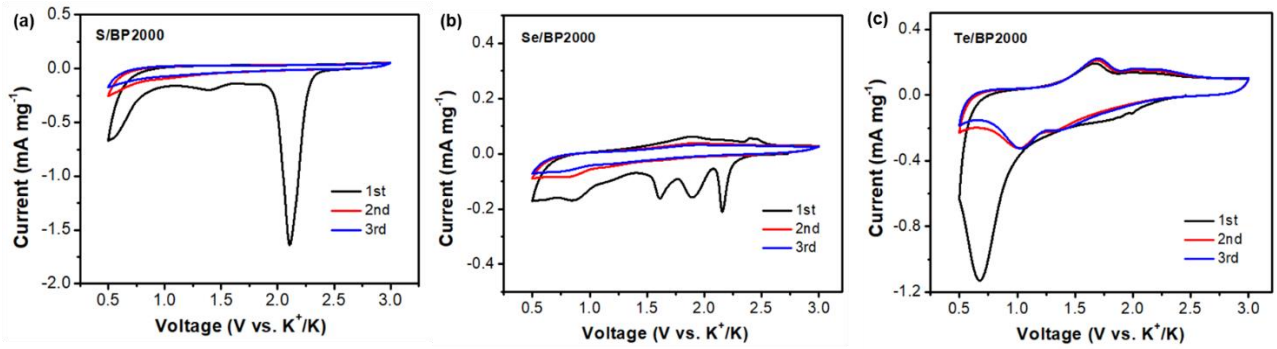

Figure 8.3.4. CV curves of (a) S/BP2000, (b) Se/BP2000, and (c) Te/BP2000 cathodes at 0.2 mV s^{-1}.

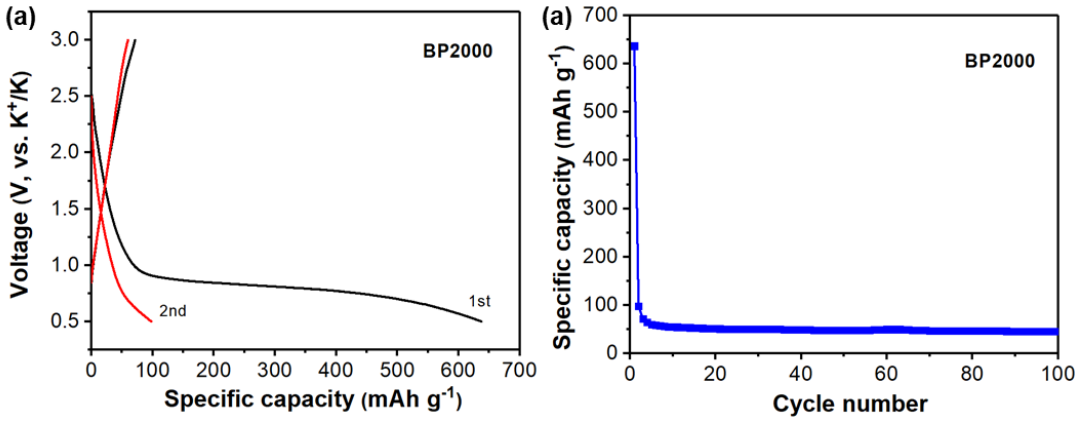

Figure 8.3.5. (a) Initial charge/discharge curves and (b) cycling performance of a K-BP2000 cell.

As shown in **Figures 8.3.3d-e**, the Te/BP2000 cathode delivers remarkable rate capacities of 459.7, 408.1, 368.8, 350.2, 328.7, 289.0, 257.5, and 238.0 mAh g^{-1}, as the current density increases from 0.1 to 10 A g^{-1}, respectively. When the current density is set back to 1 A g^{-1}, the capacity of Te/BP2000 cathode is restored to 357.1 mAh g^{-1}. However, S/BP2000 and Se/BP2000 exhibit poor rate capacities of 189.6, 71.4, 36.4, 19.1, 8.6, 2.2, 1.7 mAh g^{-1}, and 478.4, 292.9, 233.8, 175.4, 111.0, 20.9, 4.6, 2.7 mAh g^{-1}, respectively, under the same condition. Additionally, capacity utilization is defined by dividing the reversible capacity by the corresponding theoretical value (1,675 mAh g^{-1} for S, 675 mAh g^{-1} for Se, and 420 mAh g^{-1} for Te). It could be observed that Te/BP2000 has the highest capacity utilization of 97%, 88%, 83%, and 78% at 0.2, 0.5, 1, and 2 C, whereas S/BP2000 and Se/BP2000 display poor utilization of 4%-0.5% and 43%-16%,

respectively. As the K-S/Se/Te batteries have the same cell configuration and undergo identical testing currents and voltages, the superior rate performance and reversibility of Te/BP2000 could be attributed to the fast electron transfer due to Te's electrical conductivity. It should be noted that the S/BP2000 and Se/BP2000 cathode in this work could be further optimized by structural or electrolyte design [209, 210]. The main point is that, with the help of fast electron transfer of Te, the redox kinetics in the K-Te system is boosted, thus illustrating better rate performance and higher capacity utilization, especially at high current densities. This K-Te battery can deliver a high capacity (420 mAh g_{Te}^{-1} or 2621 mAh cm_{Te}^{-3}) and an average potential of 1.3 V. Accordingly, the energy density of the K-Te battery can reach up to 546 Wh kg_{Te}^{-1} or 3407 Wh L_{Te}^{-1}. The low crustal abundance (0.001 mg kg^{-1}) of Te is a big challenge for the commercialization of Te-based batteries. Nevertheless, the recent U.S. Geological Survey indicates that the current tellurium reserve is sufficient and can satisfy the demand for Te for several decades [3]. The increasing demand for Te-based batteries could increase production and recycling technologies around Te and eventually reduce the material cost [1, 108].

8.4 Reaction Mechanism of K-Te Electrochemistry in Carbonate Electrolytes

To uncover the K-ion storage mechanism of Te, *ex-situ* XRD and TEM tests are conducted to identify the phase compositions of Te/BP2000 cathodes at different discharge/charge states. As shown in **Figure 8.4.1a**, the charge/discharge profile possesses two voltage plateaus. Herein, XRD patterns of Te/BP2000 cathodes are collected when discharged to 1.3 V and 0.5 V and charged to 1.9 V and 3 V. Upon discharge to 1.3 V (point A), the diffraction peaks located at 33.6°, 38.8°, 44.8°, 53.3°, 54.5° are assigned to the (222), (102), (402), (042), and (060) planes of K_2Te_3 (JCPDS #71-0490). The noticeable diffraction rings in SAED (**Figure 8.4.1b**) can also be well indexed to (630), (301), and (803) crystal planes, and the lattice fringes of 0.32 and 0.29 nm in the HRTEM image (**Figure 8.4.1e**) correspond to the (221) and (411) planes of K_2Te_3. Upon further discharge to 0.5V, the peaks at 23.9°, 30.2°, 39.3°, 41.5°, 44.5°, 53.3°, and 54.6° agree with the (301), (411), (600), (620), (541), (800), and (343) planes of K_5Te_3 (JCPDS #79-1056). **Figures 8.4.1c** and **8.4.1f** also confirm the formation of K_2Te_3 by the diffraction rings originating from (305), (611), and (002) planes and lattice fringes of 0.68, 0.55, and 0.32 nm corresponding to (200), (001), (002) planes of K_2Te_3. Therefore, when the K-Te/BP2000 cell is discharged from 3 V to 0.5 V, the Te

phase is firstly converted to K_2Te_3 and finally discharged to K_5Te_3. For the charging process, K_2Te_3 is detected again as the cell is charged to 1.9 V. The newly appeared peaks at 27.5° and 38.3° when fully charged to 3 V are attributed to the (011) and (102) planes of Te (JCPDS #79-0736), indicating the final charge product of Te. The SAED pattern and HRTEM image in **Figures 8.4.1d** and **8.4.1g** further support the generation of Te as the final charge product. **Figure 8.4.2** demonstrates the uniform distribution of Te in the carbon host during the potassiation and depotassiation process. These observations reveal that the K-Te battery system experiences a reversible two-step phase transformation from Te to K_2Te_3 and finally to K_5Te_3, as schematically illustrated in **Figure 8.4.1h**.

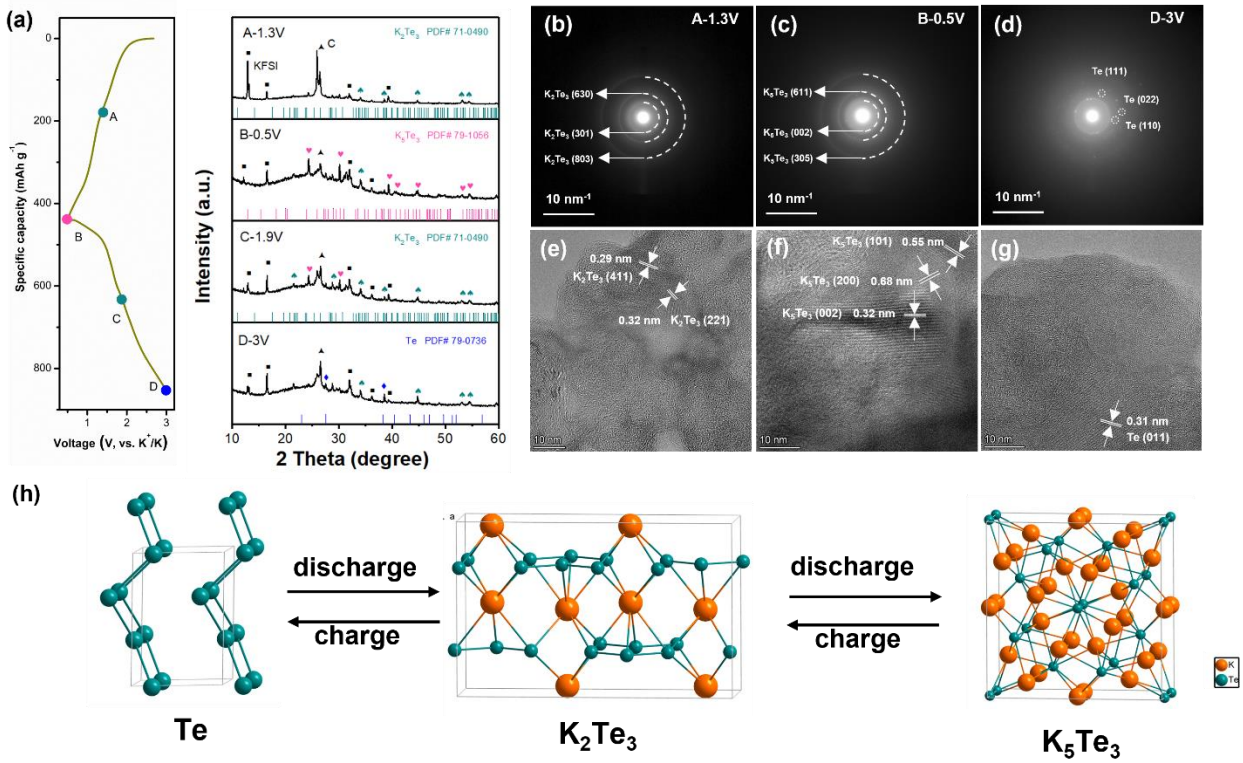

Figure 8.4.1. (a) Galvanostatic charge-discharge profile of a K-Te battery and XRD patterns of Te/C electrodes at different charge/discharge states, (b-d) SAED and (e-g) HRTEM images for Te/C electrodes at different charge/discharge states, (b, e) for 1.3 V, (c, f) for 0.5 V, (d, g) for 3 V, and (h) phase transformation from Te to K_5Te_3.

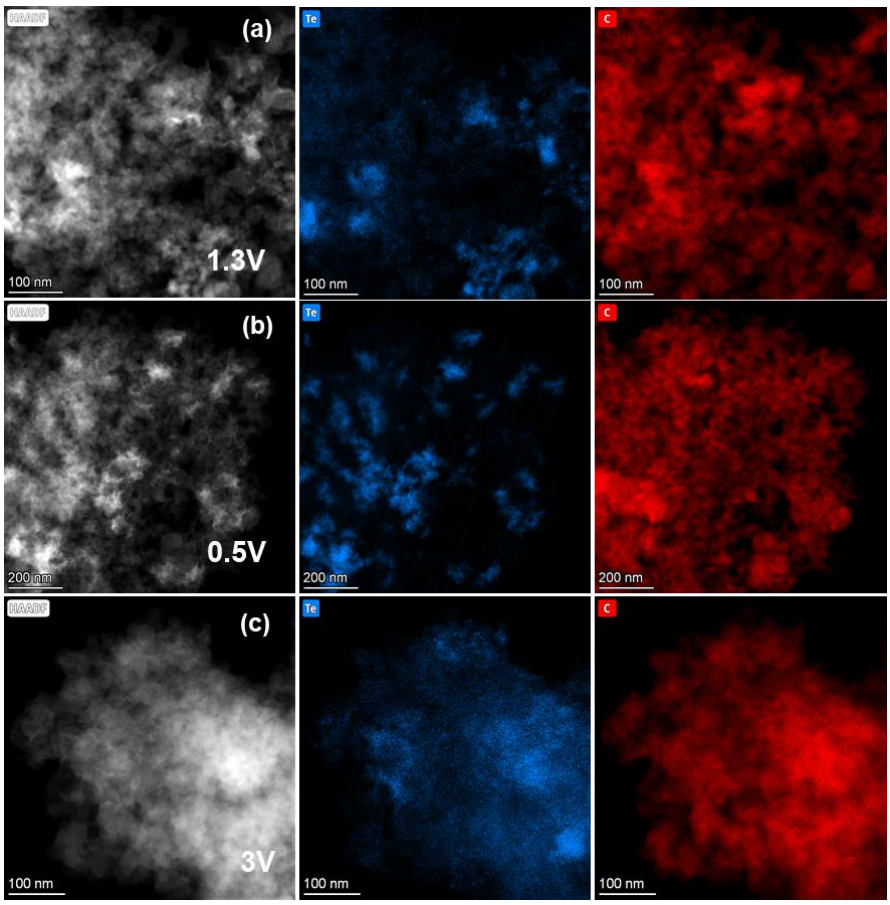

Figure 8.4.2. HAADF and EDS mapping of Te/C cathodes at (a) 1.3 V, (b) 0.5 V, and (c) 3 V.

Our findings of the stepwise electrochemical conversion of Te are consistent with the ether-based K-Te battery at 0.5-3 V [105]. It should be noted that Guo *et al.* [104] claimed K_2Te as the most thermodynamically stable discharge product due to its lowest formation energy of -1.028 eV) *vs.* -0.965 eV for K_5Te_3) when the K-Te cell is operated at 0.3-2.8 V. The reaction pathway in our work, from Te to K_2Te_3 and finally to K_5Te_3, is likely due to the wider cut-off voltage of 0.5-3 V.

A higher discharge voltage limit is also favorable since Te is used as cathode material in the K-Te battery system. Moreover, the pore structure is critical in affecting K-ion storage capacity and reaction pathways for K-Te batteries. Chapter 7 reported a Te/C cathode with activated carbon (ASAC25) as the Te host, and this Te/ASAC25 cathode possessed only one pair of anodic/cathodic peaks in the same voltage range of 0.5-3 V, suggesting a one-step electrochemical conversion from

Te to K_2Te or K_5Te_3. This Te/ASAC25 showed stable cycling performance without significant capacity fading after 100 cycles at 0.2 C because of the effective Te confinement by highly microporous carbon. Unfortunately, this Te/ASAC25 electrode delivered poor rate capabilities with only about 150 mAh g^{-1} at 1 C, probably due to the low electrical conductivity of activated carbon. In contrast, BP2000 is more electrically conductive and presents superior rate performance. The rapid capacity decline possibly results from less effectiveness of mesopores than micropores in Te confinement, which was discussed in the Li-Te batteries (Chapter 4). Therefore, it is necessary to introduce other strategies to stabilize the Te/BP2000 electrode and improve its structural integrity.

8.5 Surface Coating on Te/BP2000 Electrode Surface

As discussed above, Te/BP2000 cathode delivers superior rate performance than S/BP2000 and Se/BP2000 due to its excellent electrical conductivity, despite a drastic capacity decline after 40 cycles. This capacity fading could be mainly ascribed to the significant volume expansion of Te when reacted with K-ion upon discharging [104]. To address this potential structural instability, one ultrathin aluminum oxide (Al_2O_3) layer is fabricated by atomic layer deposition (ALD). The thickness of the Al_2O_3 layer is precisely controlled to about 1 nm by using 10 ALD cycles (TMA pulse/TMA purge/H_2O pulse/H_2O purge) [211]. SEM images in **Figures 8.5.1a-b** show similar particle sizes of Te/BP2000 and Te/BP2000@$Al_2O_3$10. The brighter image of Te/BP2000@$Al_2O_3$10 is due to the SEM charging effect, suggesting the inferior electrical conductivity of the electrode surface due to the non-conductive Al_2O_3 layer. The strong signal of the Al element in the EDS spectra (**Figure 8.5.2**) confirms the successful coating layer of Al_2O_3. Furtherly, Al 2s and 2p spectra are detected in the XPS survey and high-resolution spectra, as illustrated in **Figures 8.5.1c-d** and **Table 8.5.1**. The high-resolution Al 2p is decomposed into one prominent peak at 74.7 eV, corresponding to the formation of Al-O bond [212], which is verified by the peak located at 531.3 eV in O 1s spectra (**Figure 8.5.1f**). The Al peak is absent in Te/BP2000 (**Figure 8.5.1e**). XPS C1s and Te 3d spectra are demonstrated in **Figure 8.5.3**.

Furthermore, the Te/BP2000@$Al_2O_3$10 cathode exhibits a shoulder at 0.8 V on the first cathodic scan (**Figure 8.5.1g**) and a lower discharge plateau in the first cycle (**Figure 8.5.1h**) compared to Te/BP2000. The slightly increased overpotential of Te/BP2000@$Al_2O_3$10 might be due to the

elevated charge transfer resistance across the Al_2O_3-induced SEI layer [213]. The decreased initial discharge capacity possibly comes from suppressed side reactions by the unique SEI layer induced by Al_2O_3. Based on these results, it can be concluded that the thin Al_2O_3 layer is successfully deposited on the Te/BP2000 electrode surface and is expected to confine active materials effectively and enhance the electrode's long-term structural stability.

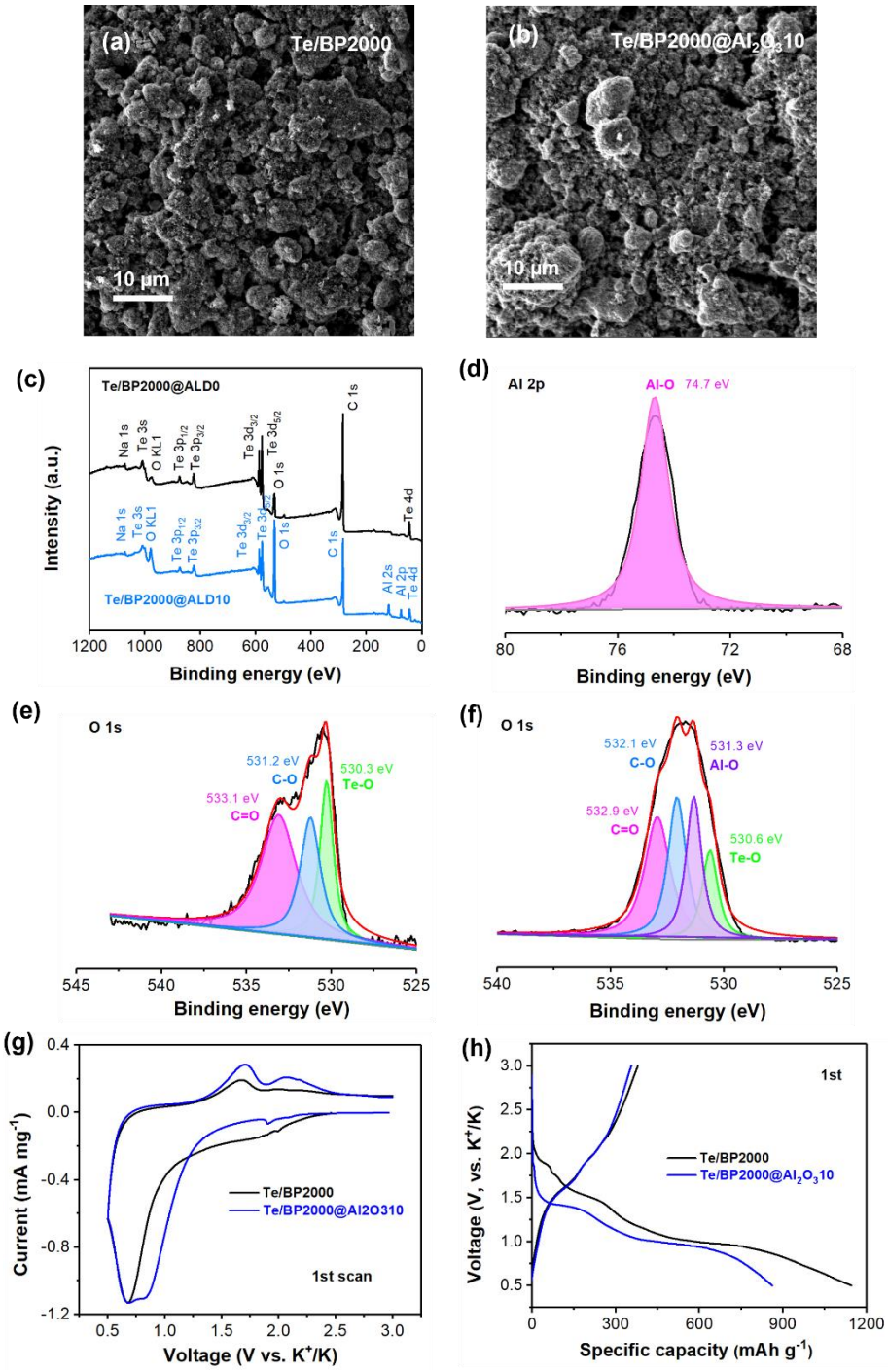

Figure 8.5.1. SEM images of (a) Te/BP2000, (b) Te/BP2000@$Al_2O_3$10, (c) XPS survey, (d) Al 2p spectra of Te/BP2000@$Al_2O_3$10, (e, f) O 1s spectra of Te/BP2000 and Te/BP2000@$Al_2O_3$10, (g) the first CV scan, (h) the first charge/discharge profiles of Te/BP2000 and Te/BP2000@$Al_2O_3$10.

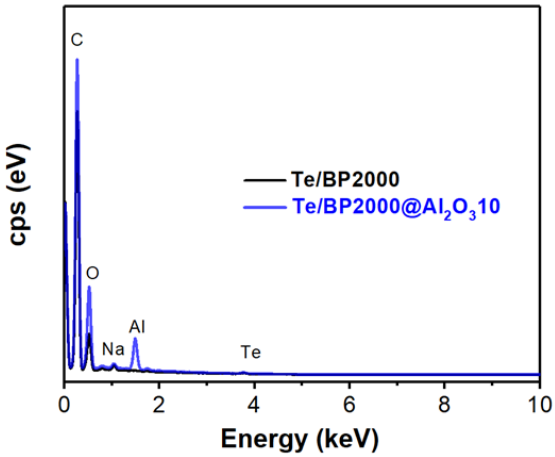

Figure 8.5.2. EDS spectra of Te/BP2000 and Te/BP2000@$Al_2O_3$10 electrodes.

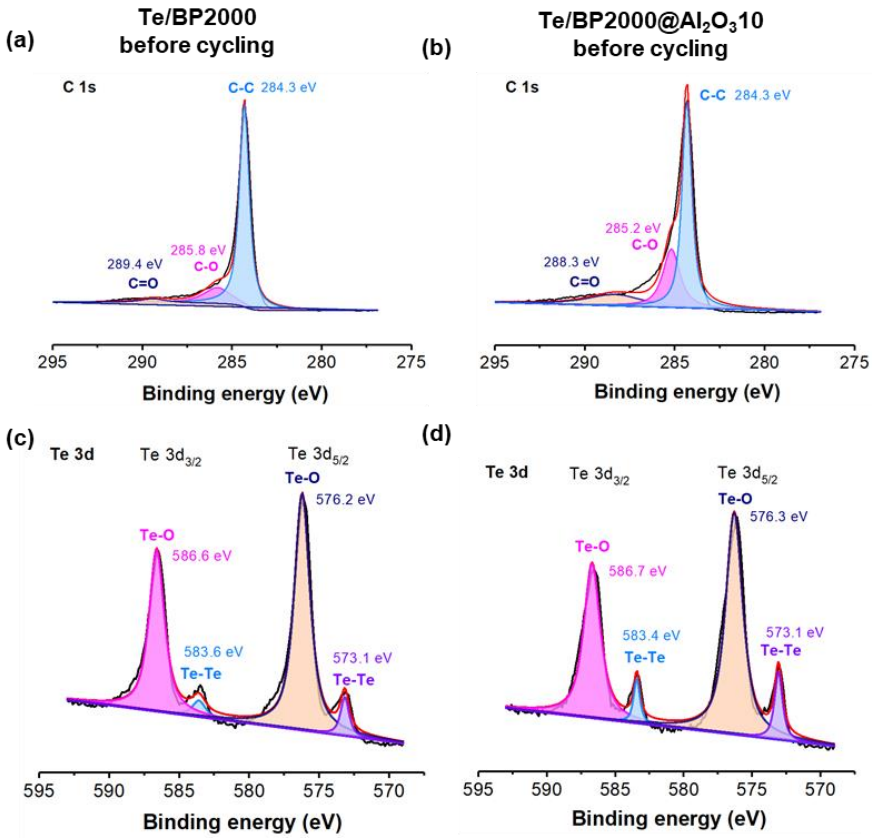

Figure 8.5.3. (a, b) XPS C 1s and (c, d) Te 3d spectra of Te/BP2000 and Te/BP2000@$Al_2O_3$10 electrodes before cycling.

Table 8.5.1. Elemental composition of Te/BP2000 and Te/BP2000@$Al_2O_3$10 electrodes from XPS before battery tests.

	Te (wt%)	O (wt%)	C (wt%)	Al (wt%)	Na (wt%)
Te/BP2000	19.66	8.32	70.47	0.77	0.68
Te/BP2000@$Al_2O_3$10	14.68	22.62	49.16	13.08	0.45

8.6 Effect of Ultrathin Al_2O_3 Film on Electrochemical Performance and Structural Stability of the K-Te/BP2000 Batteries

The electrochemical performance of Te/BP2000 and Te/BP2000@$Al_2O_3$10 are evaluated and compared in K-Te cells with the cut-off voltage of 0.5-3 V. As shown in **Figure 8.6.1a**, the Te/BP2000 delivers a high initial capacity of 1145.8 mAh g^{-1} at 0.1 C, followed by a gradual decrease to 348.3 mAh g^{-1} in the 40th cycle. Afterward, the capacity drops dramatically and only retains 156.4 mAh g^{-1} after 100 cycles. In comparison, the Al_2O_3-coated Te/BP2000 cathode shows a slightly smaller capacity of 861.4 mAh g^{-1} in the first cycle. It maintains superior cycling stability with 300.9 mAh g^{-1} remaining after 100 cycles, twice the Te/BP2000 cathode. **Figure 8.6.1b** depicts Coulombic efficiency (CE) of Te/BP2000 and Te/BP2000@$Al_2O_3$10 cathodes over cycles. The Te/BP2000 cathode has a lower initial CE of 33.1% than Te/BP2000@$Al_2O_3$10 (41.3%), and the latter always displays a higher CE than the former in the next 99 cycles. It could be speculated that Al_2O_3 induces the *in-situ* generation of a more stable SEI layer to confine the active materials, accommodate the volume change of Te and passivate the electrode surface, thus enhancing the cycling stability of Te/BP2000 cathode. Moreover, an ether electrolyte-based K-Te battery was reported [105] to provide initial CEs of 40 % and 60 %, respectively, for 1M and 5M KTFSI-in-DEGDME electrolytes. Our K-Te battery system with 1M electrolyte showed comparable CE with this work. The as-mentioned improved CE in 5M electrolyte can be explained by the fact that concentrated electrolyte effectively mitigates the dissolution of polytellurides and shuttle reactions.

The rate capabilities of the two cathodes are also compared and shown in **Figure 8.6.1c**. As the current density increases from 0.1 to 5 C, Te/BP2000 and Te/BP2000@$Al_2O_3$10 cathodes deliver

capacities of 454.2/437.8, 388.6/392.3, 359.6/362.5, 343.5/341.3, 320.9/314.9, and 291.1/286.5 mAh g^{-1}, respectively. The long-term cycling test at 1 C is also performed and illustrated in **Figure 8.6.1d**. The Al_2O_3-coated Te/BP2000 cathode demonstrates exceptional stability over 500 cycles and remains even 330.5 mAh g^{-1} with an ultralow capacity decay of only 0.01% per cycle. By contrast, the capacity of bare Te/BP2000 cathode steadily decreases versus repeated potassiation/depotassiation cycles, and its corresponding capacity decay is 0.04% per cycle. The excellent cyclability of Te/BP2000@$Al_2O_3$10 cathode could be attributed to the strengthened structural stability of the in-situ generated SEI layer resulting from the Al_2O_3 film.

Figures 8.6.1e-f present galvanostatic charge/discharge profiles of Te/BP2000 and Te/BP2000@$Al_2O_3$10 cathodes in the 2^{nd}, 40^{th}, and 80^{th} cycles. It could be seen that, with the cycle number increasing to 80, the discharge plateau of Te/BP2000 at around 1 V becomes narrower, implying the incomplete conversion from K_2Te_3 to K_5Te_3 or the loss of active materials. In comparison, the Al_2O_3-coated cathode delivers a wider discharge plateau at 1 V, ensuring that K_2Te_3 is completely converted to K_5Te_3. **Figure 8.6.1g** compares the Nyquist plots of Te/BP2000 and Te/BP2000@$Al_2O_3$10 cathodes before and after 100 cycles operated at 0.1 C. On the other hand, by electrochemical impedance spectroscopy (EIS) simulation using the equivalent model in **Figure 8.6.2**, the Te/BP2000@$Al_2O_3$10 cathode possesses a slightly higher charge transfer resistance R_{ct} than the bare Te/BP2000 cathode because it is difficult for electrons to pass through the insulating Al_2O_3 layer. After 100 cycles, the R_{SEI} and R_{ct} of Te/BP2000@$Al_2O_3$10 cathode are 133.3 and 801.8 Ω, respectively, whereas the Te/BP2000 cathode has significantly enlarged R_{SEI} and R_{ct} of 801.8 and 4.2E4 Ω. Two reasons could explain the markedly increased R_{SEI} and R_{ct} of Te/BP2000. Firstly, Te active materials are gradually lost from the micro/mesopores of BP2000 due to large volume change, causing structural instability, pulverization, and isolation of active materials from the current collector. Secondly, the SEI layer on the surface of the Te/BP2000 electrode is repeatedly destroyed and rebuilt, resulting in drastically increased interfacial resistance. In contrast, the ultrathin Al_2O_3 film enables the *in-situ* generated SEI layer to enhance structural integrity, confine Te effectively, and prevent active material loss over long-term cycles, extending the lifetime of Te/BP2000 with ultrahigh capacity retention as shown in **Figure 8.6.1d**.

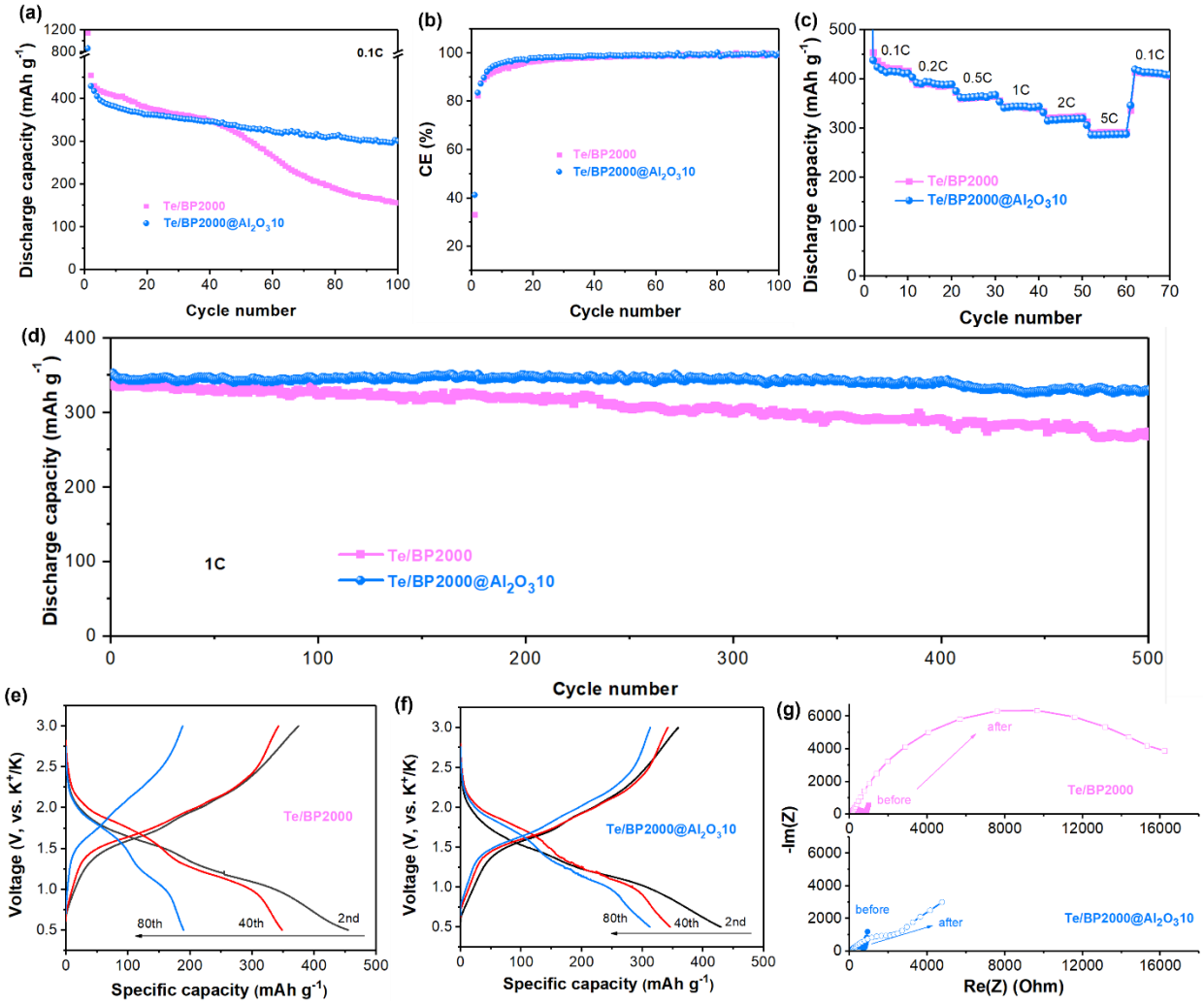

Figure 8.6.1. Electrochemical performance of Te/BP2000 and Te/BP2000@$Al_2O_3$10. (a) Discharge capacity, (b) Coulombic efficiency over 100 cycles at 0.1 C, (c) rate performance, (d) long-term cycling performance at 1 C, galvanostatic charge/discharge profiles of (e) Te/BP2000 and (f) Te/BP2000@$Al_2O_3$10 at 2nd, 40th, and 80th, and (g) Nyquist plots of Te/BP2000 and Te/BP2000@$Al_2O_3$10 before and after 100 cycles at 0.1 C.

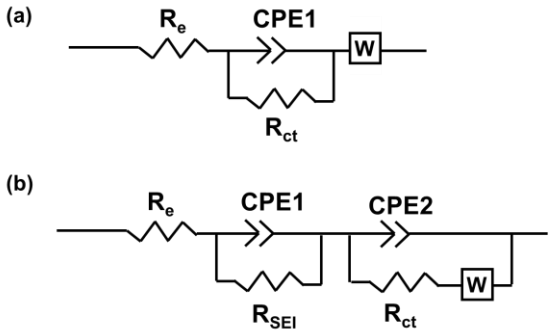

Figure 8.6.2. EIS equivalent circuit models of K-Te cells. (a) Before cycling, (b) After cycling.

Table 8.6.1. Calculated resistance values of Te/BP2000 and Te/BP2000@$Al_2O_3$10 electrodes.

Cathodes	Before cycling		After 50 cycles		
	R_e (Ω)	R_{ct} (Ω)	R_e (Ω)	R_{ct} (Ω)	R_{SEI} (Ω)
Te/BP2000	2.7	682.4	3.5	4.2E4	801.8
Te/BP2000@$Al_2O_3$10	2.7	708.4	4.5	1598	133.3

To reveal the surface chemistry on the Te/BP2000 cathode, the cycled K-Te/BP2000 and K-Te/BP2000@$Al_2O_3$10 cells are disassembled for post-characterizations. **Figures 8.6.3a-b** and **Figure 8.6.4** show top-view and cross-sectional SEM images of K-Te/BP2000 and K-Te/BP2000@$Al_2O_3$10 electrodes after 100 cycles at 0.1 C. Some particles are separated from the surface of Te/BP2000, and a majority of active materials are peeled off from the Al current collector. The delamination causes the electrical isolation from Al foil, which explains the drastic capacity decline and enlarged interfacial resistance in **Figure 8.6.1**. Meanwhile, the Te/BP2000@$Al_2O_3$10 active materials are firmly attached to the Al foil, ensuring efficient charge transfer and K-ion conduction. The XPS survey spectra in **Figure 8.6.3c** and the prominent Al-O peak in **Figure 8.6.3d** confirm the existence of Al in the SEI layer on the Te/BP2000@$Al_2O_3$10 surface. K 2p, C 1s, and O 1s spectra are illustrated in **Figure 8.6.5**. The two peaks at 687.8 and 684.4 eV in F 1s (**Figure 8.6.3e**) are assigned to the S-F and K-F bonds for Te/BP2000 [190], which shift to 685.4 and 683.5 eV for cycled Te/BP2000@$Al_2O_3$10 (**Figure 8.6.3f**), respectively.

The binding energy shift indicates different charge states of F, which might be caused by the interaction with Al. On the other hand, the intensities of Te-Te bonds are much more intense, and Te-O bonds become far weaker for Te/BP2000@$Al_2O_3$10 (**Figure 8.6.3g**) in Te 3d spectra than Te/BP2000 (**Figure 8.6.3h**), implying higher electrochemical activity of Te for the Al_2O_3-coated electrode. Based on the above results, it could be inferred that the Al_2O_3 film induces the formation of the KAl_xO_y-rich SEI layer, which effectively passivates the Te/BP2000 electrode and enhances its structural stability after long-term potassiation/depotassiation behaviors [212, 214].

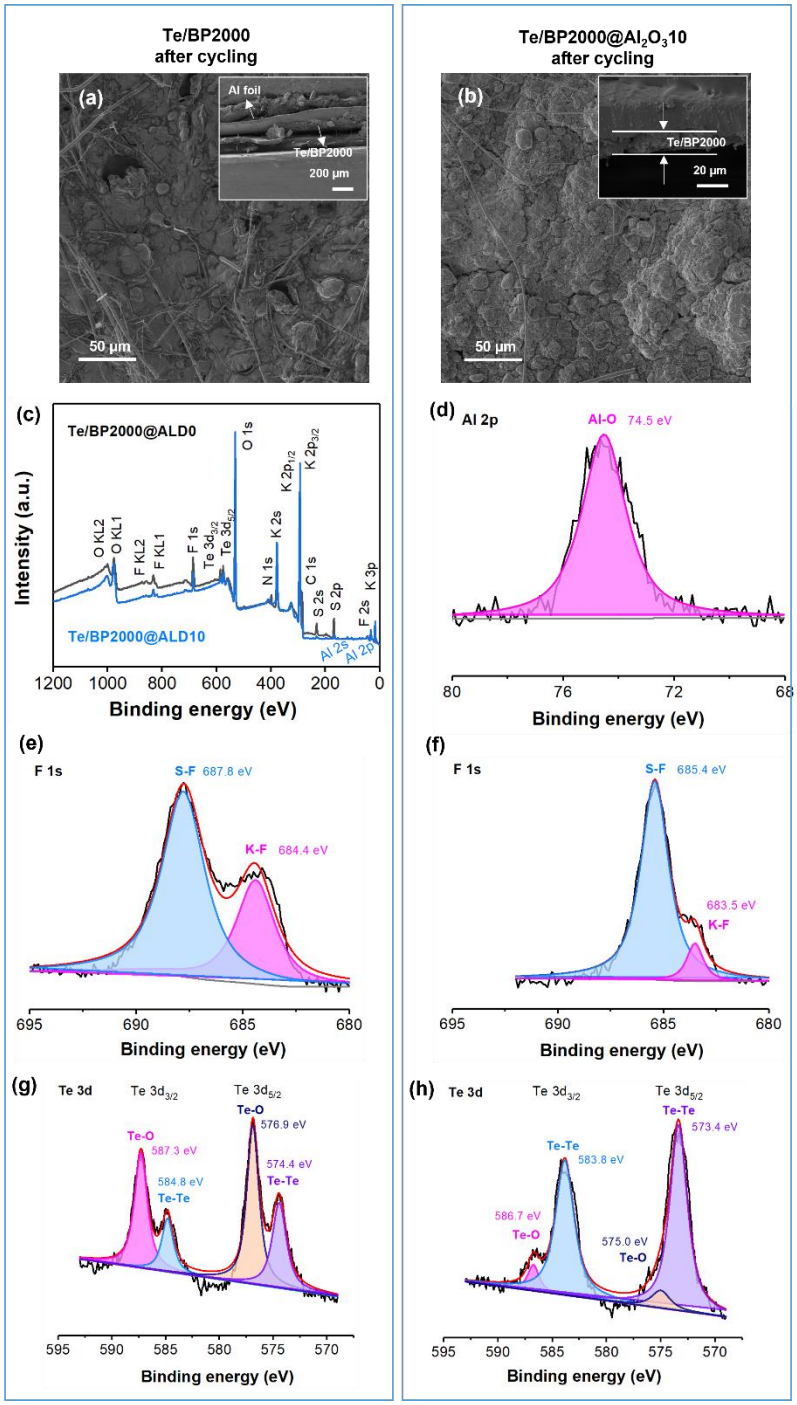

Figure 8.6.3. Top-view and cross-section SEM images of (a) Te/BP2000 and (b) Te/BP2000@$Al_2O_3$10 after 100 cycles, (c) XPS survey spectra, (d) Al 2p of Te/BP2000@$Al_2O_3$10, (e, f) F 1s and (g, h) Te 3d spectra of Te/BP2000 and Te/BP2000@$Al_2O_3$10 after cycling.

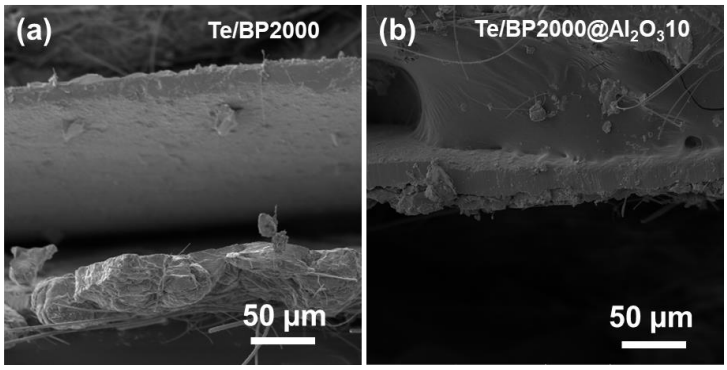

Figure 8.6.4. Cross-section SEM images of (a) Te/BP2000 and (b) Te/BP2000@$Al_2O_3$10 after 100 cycles.

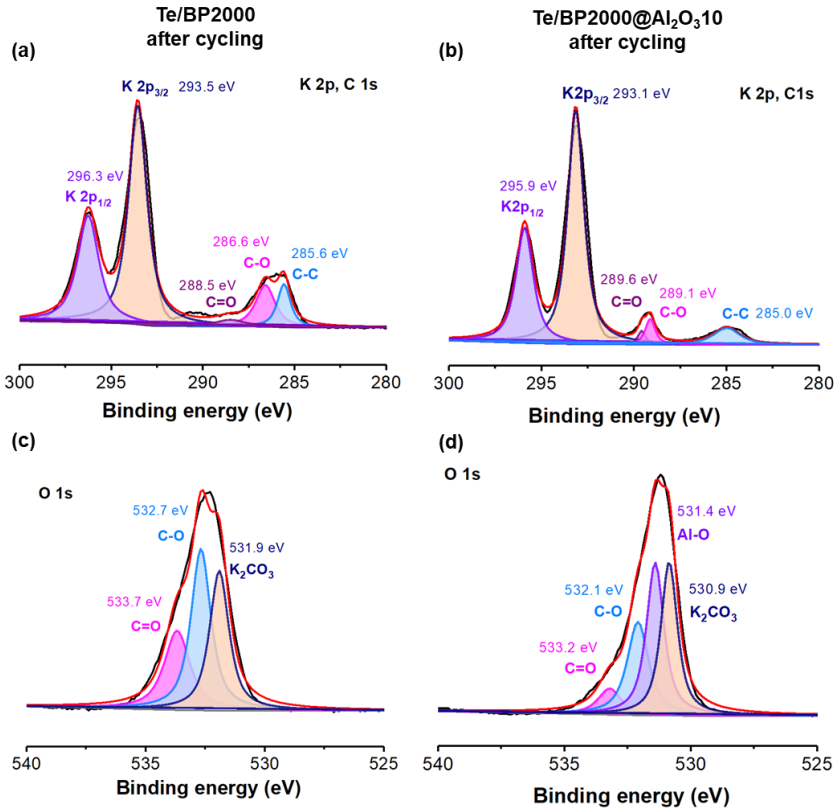

Figure 8.6.5. (a, b) XPS K 2p, C 1s and (c, d) O 1s spectra of Te/BP2000 and Te/BP2000@$Al_2O_3$10 electrodes after 100 cycles.

Table 8.6.2. Elemental composition of Te/BP2000 and Te/BP2000@$Al_2O_3$10 electrodes from XPS after 100 cycles.

Cathodes	Weight percentage (wt%)										
	F	Te	O	K	C	S	Cl	Al	Na	Si	N
Te/BP2000	6.5	2.84	25.12	40.6	10.63	10.65	0.54	0	0.2	0.69	2.25
Te/BP2000@$Al_2O_3$10	3.27	1.4	33.84	47.96	4.01	4.39	0.96	2.05	0.26	1.09	0.75
Te/BP2000@$Al_2O_3$10 (960s etching)	2.95	2.38	26.56	61.21	1.98	1.98	0.36	1.6	0.26	-	-

8.7 Working Mechanism Analysis of Surface-Coated Te/BP2000 Electrodes

Figure 8.7.1 illustrates the structural change of Te/BP2000 and Te/BP2000@$Al_2O_3$10 after long-term cycles based on the electrochemical performance and ex-situ morphology or structural characterization results. For the bare Te/BP2000 cathode, the mesopores in the carbon host are pretty large and could not confine Te species effectively, resulting in pulverization and loss of active materials after long cycling. The delamination isolates Te species from the current collector, leading to drastically increased interfacial resistance and rapid capacity decline. In comparison, the deposited ultrathin Al_2O_3 film induces the generation of a stable SEI, which protects active materials from loss and enables fast electron transfer for complete electrochemical conversion from Te to K_5Te_3. It is speculated that 10-cycle ALD is likely to leave some small gaps on the surface of micropores, and the ALD layer is effective in blocking the loss of large-size Te active materials inside micro/mesoporous carbon. Benefiting from the functional interface layer, the Te/BP2000@$Al_2O_3$10 delivers superior cling stability with 95% capacity retention at 1 C.

On the other hand, the Al_2O_3 layer was also deposited on the surface of S/BP2000 and Se/BP2000 cathodes to investigate the effect of the interface layer on S or Te potassiation/depotassiation behaviors. As shown in **Figure 8.7.2**, both S/BP2000@$Al_2O_3$10 and Se/BP2000@$Al_2O_3$10 delivered higher capacities after the deposition of 1-nm Al_2O_3, which furtherly confirms the effectiveness of the Al_2O_3 layer in stabilizing the cathode interface and preventing the loss of active

materials. Therefore, ALD is an effective strategy to stabilize S/Se/Te cathode and electrolyte interface to enable durable and high-capacity K-chalcogen batteries.

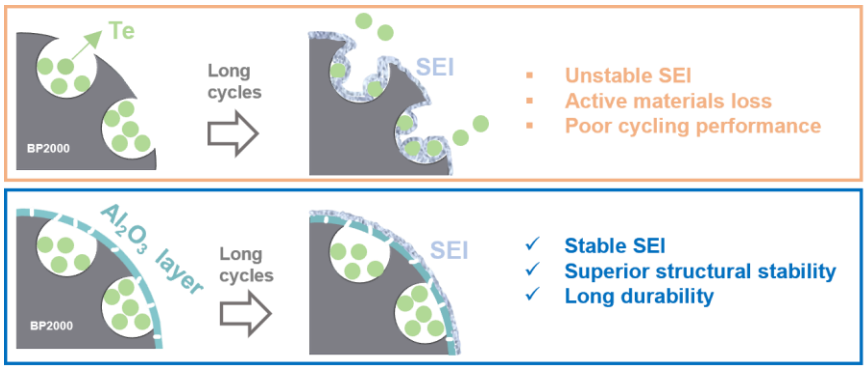

Figure 8.7.1. Schematic illustration of the structural change of Te/BP2000 and Te/BP2000@$Al_2O_3$10 after long-term cycles.

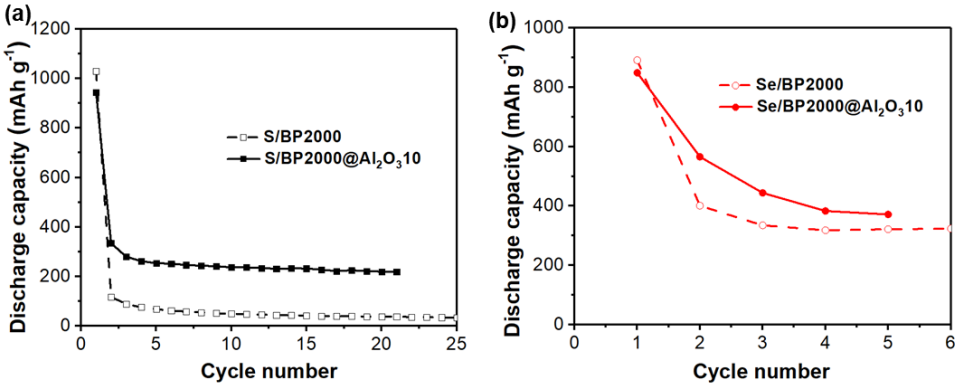

Figure 8.7.2. Cycling performance of (a) S/BP2000 and S/BP2000@$Al_2O_3$10 and (b) Se/BP2000 and Se/BP2000@$Al_2O_3$10.

8.8 Chapter Summary

In summary, Te/BP2000 has been demonstrated to deliver superior specific capacity and rate performance than its counterparts S/BP2000 and Se/BP2000 due to the significantly higher electrical conductivity of Te than S and Se. The K-ion storage mechanism of Te/BP2000 cathode in carbonate electrolytes was revealed with a stepwise phase transformation from Te to K_2Te_3 and ultimately to K_5Te_3 by XRD, HRTEM, and SAED analysis. Moreover, ultrathin Al_2O_3 film with 1nm thickness was deposited on Te/BP2000 surface to induce a stable SEI layer and protect active

materials from loss after long-term cycles. The Te/BP2000@$Al_2O_3$10 delivered highly reversible capacity over 500 cycles at 1 C with an ultralow capacity decay of only 0.01% per cycle, corresponding to 95% capacity retention. In contrast, the uncoated Te/BP2000 only maintains 80% of its initial capacity after long-term cycling. The notably improved cycling stability and enhanced structural integrity can be attributed to the passivation of the Al_2O_3-induced SEI layer, which could effectively confine Te species, accommodate their volume change, and prevent the loss of active materials. These findings provide feasible strategies for developing durable and high-rate K-Te batteries.

Chapter 9 Composite Gel Polymer Electrolytes for K Anode

9.1 Introduction

Potassium-ion battery is an emerging energy storage technology due to its potential low cost and reasonably high energy density. However, PIB suffers from severe potassium (K) dendrites growth and even short circuit caused by the high reactivity of K metal. There are still significant limitations in K metal anodes for K metal batteries. For example, most K metal batteries used glass fiber separators, which consumed a large amount of liquid electrolytes (100-200 μL per coin cell) for complete wetting. The large pore sizes of the glass fibers might induce random K metal plating and cause rapid internal short circuits. The issues associated with glass fibers have been overlooked so far. Moreover, the use of flammable organic solvents poses a potential safety hazard to K metal batteries.

In this regard, replacing liquid electrolytes with solid electrolytes is a feasible approach to mitigate safety issues. Gel or solid polymer electrolytes have been developed to construct safe quasi-solid-state or all-solid-state K metal batteries [215]. For example, Goodenough's group [216] developed a cross-linked polymer-gel electrolyte architecture to generate a stable solid electrolyte interphase (SEI) at the electrolyte-electrode interface, extending the lifetime of K metal and enabling excellent compatibility with a polyaniline cathode. Feng *et al.* [217] fabricated a polyethylene oxide (PEO)-KFSI solid polymer electrolyte with an ionic conductivity of 2.7×10^{-4} S cm^{-1} at 60 °C. This K/PEO-KFSI/Ni_3S_2@Ni battery delivered an initial capacity of 312 mAh g^{-1} at 25 mA g^{-1}. Nevertheless, the ionic conductivity of the PEO-KFSI and cumulative K plating capacities in previous works are considerably low. More efforts are needed to develop novel gel polymer electrolytes with suitable ionic conductivity, high cumulative K plating capacity without failure, and deepen the fundamental understanding of K metal/solid electrolyte interface for K metal batteries.

In this chapter, we developed a composite gel polymer electrolyte (CGPE) based on poly(vinylidene fluoride-hexafluoropropylene) (PVDF-HFP), potassium bis(fluorosulfonyl)imide (KFSI), and electronspun polyacrylonitrile (PAN) nanofibers (PVDF-HFP-KFSI@PAN). It is found that the introduction of PAN nanofibers not only improves the mechanical properties but

also widens electrochemical stability window of the CGPE. As a result, the CGPE is much more effective in regulating K stripping/plating and enabling stable K metal anode. K metal symmetrical cells with CGPE exhibit a lifetime of over 1,200 h at the current density of 0.5 mA cm^{-2}, in contrast to 22 h for PVDF-HFP-KFSI and 185 h for conventional glass fiber separators. The main reasons for the excellent performance of K metal cells with CGPE are attributed to the suppressed K dendrite growth, good structural integrity, and electrochemical stability of the CGPE, and stable KF-rich solid electrolyte interphase (SEI) layer at the electrode-CGPE interface. It is expected that this facile strategy to stabilize K metal will pave the way for safer and more durable K metal batteries.

9.2 Preparation Process of PVDF-HFP-KFSI@PAN Composite Gel Polymer Electrolytes

Figure 9.2.1 illustrates the synthesis process of PVDF-HFP-KFSI and PAN-reinforced composite gel polymer electrolyte (PVDF-HFP-KFSI@PAN) for K metal batteries, as described in Section 3.1.5. Firstly, PVDF-HFP is dissolved into NMP solvent to prepare a transparent polymer solution, and then KFSI salt is added to obtain PVDF-HFP-KFSI solution. PVDF-HFP-KFSI membrane is prepared by a facile solution casting of the PVDF-HFP-KFSI solution followed by vacuum drying. To prepare the PVDF-HFP-KFSI@PAN composite gel polymer electrolyte (CGPE), PAN nanofibers, produced by an electrospinning method [218], are immersed in the above PVDF-HFP-KFSI solution and dried under vacuum overnight. The diameter of electrospun PAN fibers is a function of electric field voltage, polymer concentration, and solution flow rate [219, 220]. The PAN nanofibers are expected to enhance structural stability and suppress K dendrite growth.

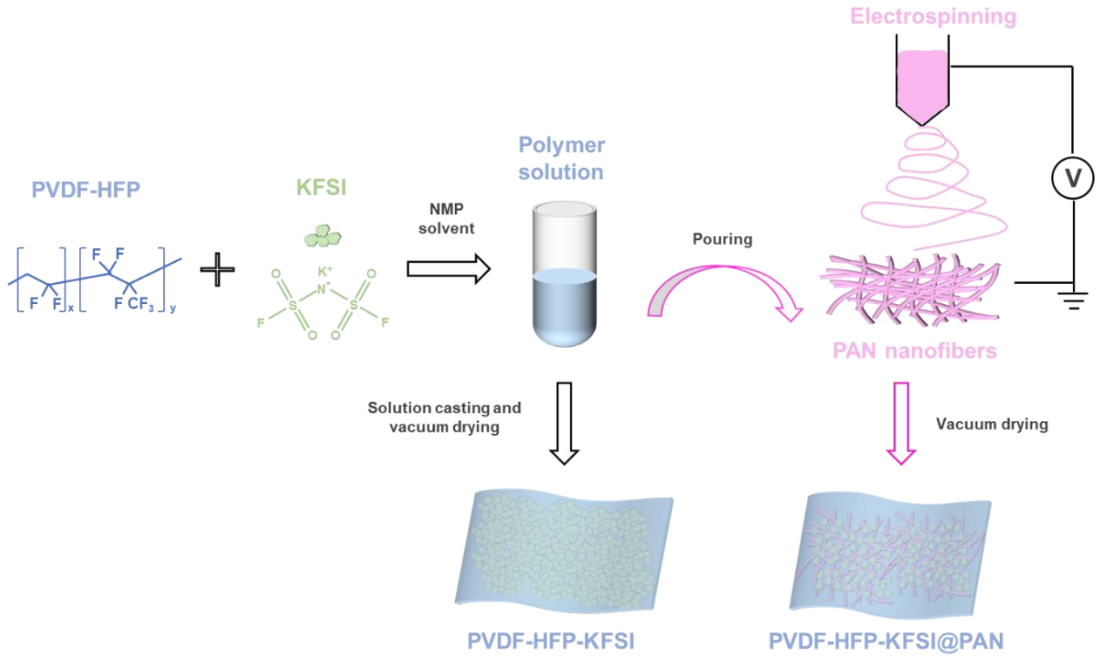

Figure 9.2.1. Schematics of the preparation process for PVDF-HFP-KFSI and PVDF-HFP-KFSI@PAN.

9.3 Morphology and Structural Stability of PVDF-HFP-KFSI@PAN CGPE

Morphologies of PAN nanofibers, PVDF-HFP-KFSI, and PVDF-HFP-KFSI@PAN CGPE are presented in **Figure 9.3.1**. The PAN nanofibers possess a uniform fiber diameter less than 0.5 µm and smooth fibrous surface. There is no bead or droplet formation under the electrospinning conditions (**Figures 9.3.1a-b**). The PVDF-HFP-KFSI membrane consists of packed irregular polymer particles with an average diameter of ~ 20 µm (**Figures 9.3.1c-d**). In contrast, for PVDF-HFP-KFSI@PAN, the gel polymer immerses the PAN nanofibers to fill the pores, forming a well-connected 3D network to facilitate K-ion transfer and improve the structural rigidity. Moreover, the polymer particles less than 10 µm are attached to PAN nanofiber surface (**Figures 9.3.1e-f**) and serve as the interlayer between CGPE and K metal in K/K symmetrical cells. Micro X-ray computed tomography (MicroXCT) is employed to reveal the 3D structure of PVDF-HFP-KFSI@PAN, and the results are shown in **Figures 9.3.1g-h**. As seen, PVDF-HFP-KFSI@PAN is composed of a tri-layer structure with dense PAN nanofibers sandwiched between porous PVDF-HFP-KFSI layers (**Figure 9.3.2**). The immersion of the polymer in the PAN nanofibers fills the pores, leading to the relatively denser structure of the central PVDF-HFP-KFSI@PAN layer than

PVDF-HFP-KFSI layers at the top and bottom. The formation of porous PVDF-HFP-KFSI layers is due to the voids resulting from the shrinkage of polymer solution during vacuum drying (**Figure 9.3.1f**).

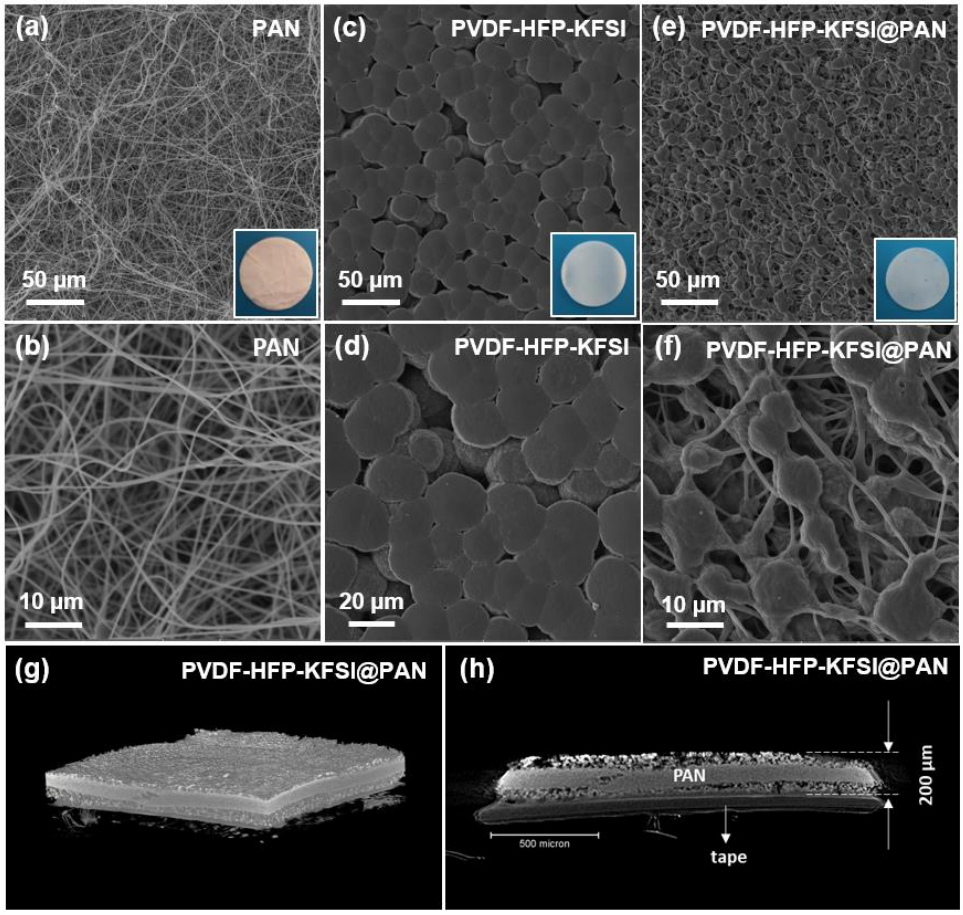

Figure 9.3.1. SEM images of (a, b) PAN nanofibers, (c, d) PVDF-HFP-KFSI, (e, f) PVDF-HFP-KFSI@PAN membranes. Micro X-ray computed tomography (MicroXCT) images of PVDF-HFP-KFSI@PAN from (g) 3D view and (h) cross-section view.

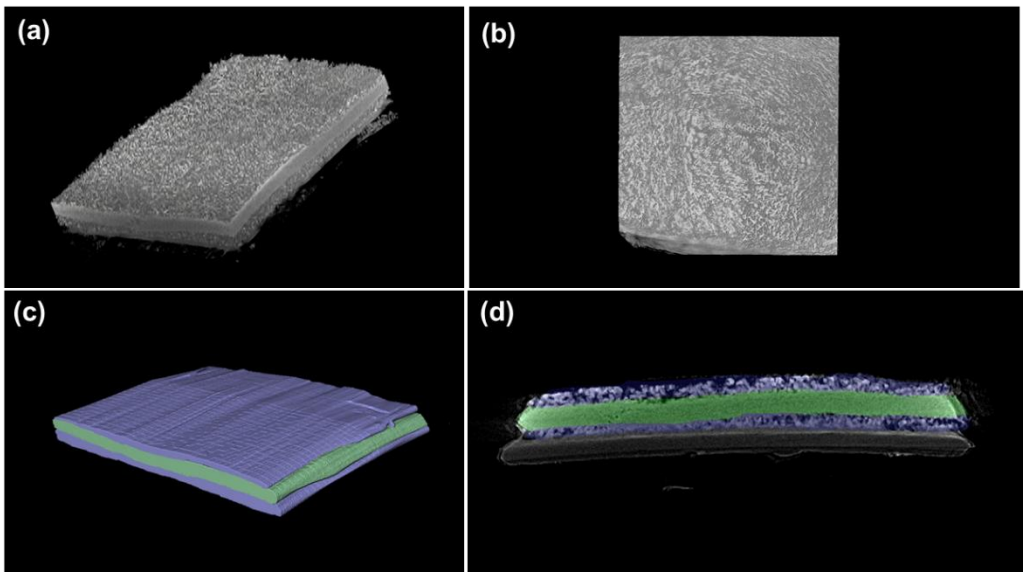

Figure 9.3.2. Micro-XCT images of the PVDF-HFP-KFSI@PAN membrane. (a) 3D view, (b) top view, (c) 3D view in color, (d) cross-section in color.

Figure 9.3.3 demonstrates random fiber distribution and high porosity of a glass fiber (GF) separator commonly used in K metal batteries. For each preparation of PVDF-HFP-KFSI@PAN, 4 g solution was poured onto 6 cm × 6 cm PAN fibers on a glass plate and dried overnight. Subsequently, the 6 cm × 6 cm area was peeled off and denoted as PVDF-HFP-KFSI@PAN. The content of PAN nanofibers could be calculated by dividing the mass of pure PAN fibers by the mass of PVDF-HFP-KFSI@PAN. The mass fraction of PAN nanofibers in PVDF-HFP-KFSI@PAN was 5 wt%. It should be noted that this recipe can enable PVDF-HFP polymer and KFSI salt to completely fill into the PAN backbone to create a dense structure, as confirmed by SEM and MicroXCT. If the polymer solution is added too little (2.5 g), PAN would be partly immersed as shown in **Figure 9.3.4**, which may allow K dendrite piercing and cause an unexpected short circuit. To evaluate the structural stability of PVDF-HFP-KFSI and PVDF-HFP-KFSI@PAN, the two membranes are heated at 150 °C for 10 min and their size changes are recorded and shown in **Figure 9.3.5**. The diameter of PVDF-HFP-KFSI pallet shrank from 20 mm to 16.5 mm after thermal treatment, whereas PVDF-HFP-KFSI@PAN had a larger diameter of 19 mm, suggesting superior structural stability reinforced by PAN.

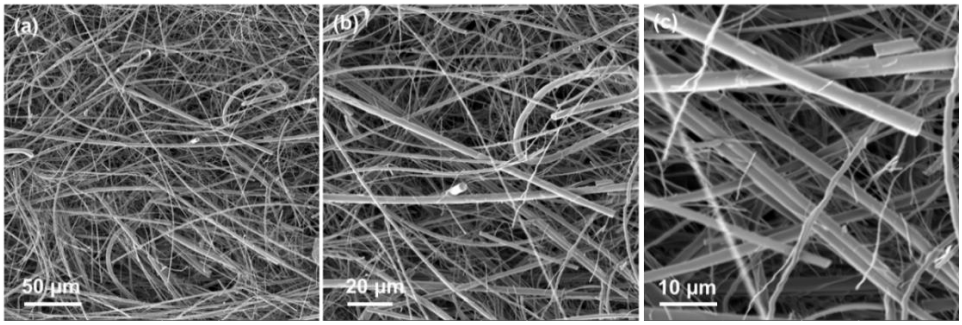

Figure 9.3.3. SEM images of glass fibers (GF) (Whatman glass fiber (GF/D), thickness 0.67 mm, pore size: 2.7 μm).

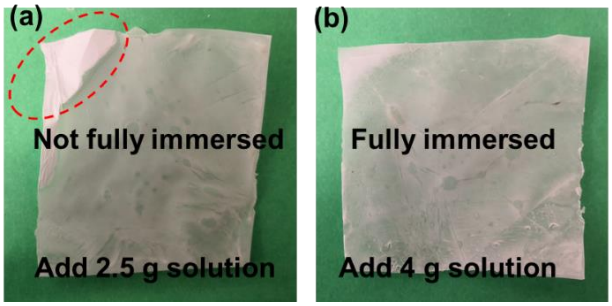

Figure 9.3.4. Digital photos of PVDF-HFP-KFSI@PAN with (a) 2.5 g and (b) 4 g polymer solution addition.

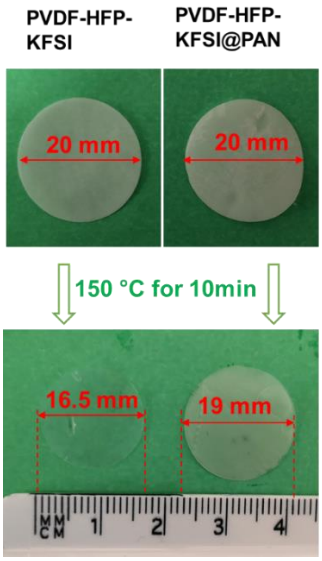

Figure 9.3.5. Size changes of PVDF-HFP-KFSI and PVDF-HFP-KFSI@PAN after heating treatment.

9.4 Mechanical Strength, Crystal Structure, and Chemical Composition of PVDF-HFP-KFSI@PAN CGPE

Figure 9.4.1 shows the mechanical property, structure, and composition of PVDF-HFP-KFSI@PAN. The tensile test is carried out to evaluate the mechanical property of PVDF-HFP-KFSI@PAN and PVDF-HFP-KFSI membranes, and the stress-strain curves are compared in **Figure 9.4.1a.** The PVDF-HFP-KFSI@PAN exhibits typical yielding behavior for ductile materials. The tensile strength at fracture increases significantly from 0.6 MPa for PVDF-HFP-KFSI to 3.5 MPa for PVDF-HFP-KFSI@PAN, and the elongation at break from 32.5% for PVDF-HFP-KFSI to 161.2% for PVDF-HFP-KFSI@PAN with reinforcement of PAN nanofibers. Therefore, electrospun PAN nanofibers serve as a rigid skeleton and strengthen the mechanical properties of PVDF-HFP-KFSI [221, 222].

The XRD patterns of PVDF-HFP-KFSI@PAN membrane are compared with those of PVDF-HFP and PAN nanofibers in **Figure 9.4.1b**. For PVDF-HFP, three intense peaks are identified at 18.4°, 20.8°, and 26.6°, assignable to (110), (020), and (110) planes, respectively [143]. The electrospun PAN nanofibers exhibit two broad peaks at 16.8° and 26.0°, corresponding to the (100) and (002) planes of PAN, respectively.[14] In comparison, PVDF-HFP-KFSI@PAN shows broadened diffraction features, and the two peaks at around 17° and 20° likely originate from PVDF-HFP and PAN, respectively.

Figures 9.4.1c-f illustrate the XPS survey and high-resolution spectra of PVDF-HFP-KFSI@PAN CGPE. The two peaks at 295.0 and 292.1 eV are ascribed to K $2p_{1/2}$ and K $2p_{3/2}$, respectively. C 1s spectra could be decomposed into three peaks at 289.5, 285.0, and 283.6 eV, attributed to O-C=O, C-O-C, and C-C, respectively [190]. The existence of C-O and C=O bonds is confirmed by the peaks at 532.0 and 531.1 eV in O 1s spectra (**Figure 9.4.1e**). The intense peak at 686.7 eV and the weak peak at 682.0 eV is assigned to S-F and K-F bonds, respectively, originating from the KFSI salt [190]. In summary, the PVDF-HFP-KFSI@PAN CGPE possesses decreased crystallinity and improved tensile strength.

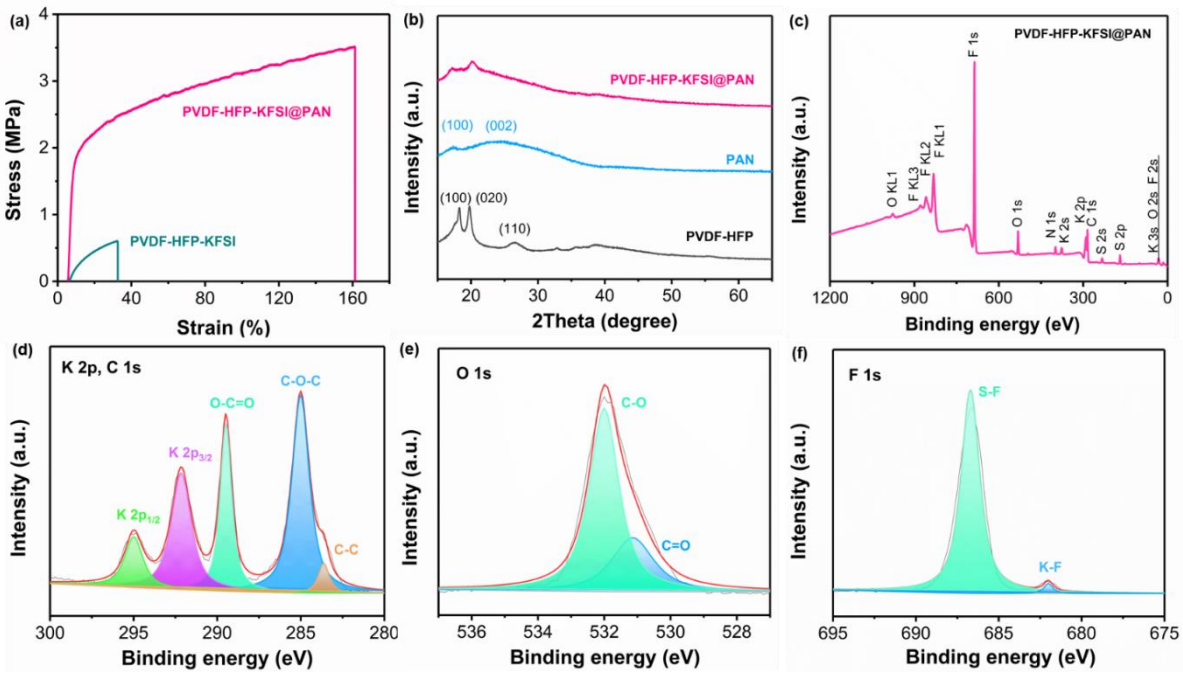

Figure 9.4.1. (a) Stress-strain curves of PVDF-HFP-KFSI and PVDF-HFP-KFSI@PAN, (b) XRD patterns of PAN, PVDF-HFP, and PVDF-HFP-KFSI@PAN, (c) XPS full survey and deconvolution of (d) K 2p and C 1s, (e) O 1s, and (f) F 1s spectra of the PVDF-HFP-KFSI@PAN.

9.5 Electrochemical Properties of PVDF-HFP-KFSI@PAN CGPE

CV and LSV tests are performed to assess the electrochemical properties of PVDF-HFP-KFSI@PAN and PVDF-HFP-KFSI with stainless steel (SS) as the working electrode and K metal as the reference electrode, and the results are shown in **Figure 9.5.1**. In the CV curve (**Figure 9.5.1a**), a pair of unstable reduction/oxidation peaks are present for PVDF-HFP-KFSI, indicating poor reversibility of K plating and striping. By contrast, the steady peaks located at -0.49/0.26 V (*vs.* K^+/K) for PVDF-HFP-KFSI@PAN suggest the stable K plating/striping to/from the working electrode [223]. In **Figure 9.5.1b**, the strong current occurring at 3.2V for PVDF-HFP-KFSI implies the decomposition of the polymer electrolyte. At the same time, PVDF-HFP-KFSI@PAN is stable up to 4.1 V (*vs.* K^+/K), indicating its wide electrochemical stability window.

The ionic conductivities of PVDF-HFP-KFSI and PVDF-HFP-KFSI@PAN in a temperature range of 20-60 °C are compared in **Figure 9.5.1c**. PVDF-HFP-KFSI and PVDF-HFP-KFSI@PAN

exhibit ionic conductivities of 2.2 × 10^{-4} and 3.6 × 10^{-4} S cm^{-1} at 25 °C, respectively, much higher than those (10^{-7}-10^{-5} S cm^{-1}) for PEO/PVA/PVC-based polymer electrolytes reported [224-230] (**Table 9.5.1**). With the temperature going up to 60 °C, ionic conductivities of 5.5 × 10^{-3} and 5.7 × 10^{-3} S cm^{-1} are achieved for PVDF-HFP-KFSI and PVDF-HFP-KFSI@PAN, respectively. Although the PMMA/KPF_6/EC: DEC: FEC electrolyte has reported superior conductivity and electrochemical stability window [216], the critical K/K symmetrical cell performance is not provided, similar to some other publications [223, 231]. K/K symmetrical cells are assembled and tested in the following section to comprehensively evaluate the PVDF-HFP-KFSI@PAN CGPE.

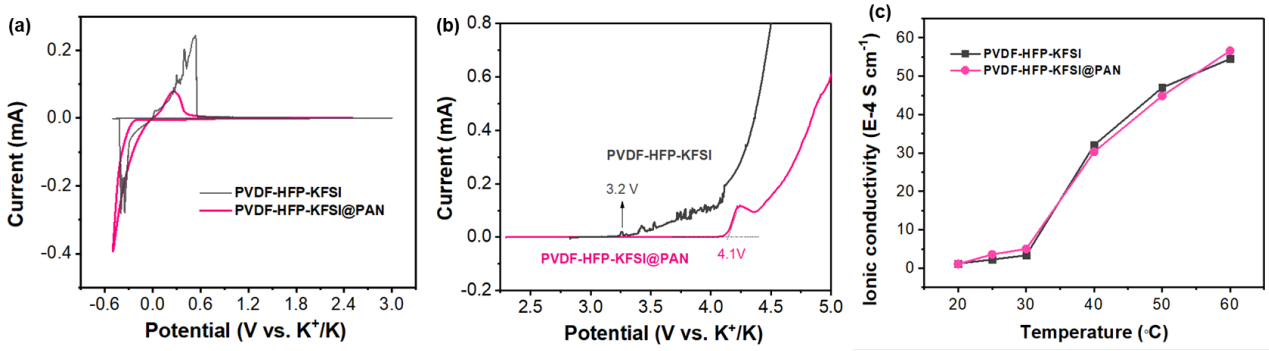

Figure 9.5.1. Electrochemical properties of the PVDF-HFP-KFSI and PVDF-HFP-KFSI@PAN composite gel polymer electrolyte. (a) CV curve, (b) LSV plot of K‖ PVDF-HFP-KFSI@PAN ‖SS at 0.2 mV s^{-1}, and (c) ionic conductivity measured between 20 and 60 °C.

Table 9.5.1. Ionic conductivity and electrochemical stability window of polymer-based electrolytes for K metal batteries in literature and this work.

Electrolyte composition	Ionic conductivity at RT (S cm^{-1})	Electrochemical stability window (V)	Ref.
P.E.O./$KBrO_3$	4.36 × 10^{-7}	-	[226]
P.E.O./KBr	5.01 × 10^{-7}	-	[232]
PEO/CH_3COOK	2.74 × 10^{-7}	-	[233]
PEO/KFSI	1.16 × 10^{-6}	-	[217]
PEO/PVA/KIO_3	4.77 × 10^{-6}	-	[225]

Electrolyte composition	Ionic conductivity at RT (S cm^{-1})	Electrochemical stability window (V)	Ref.
PEO/PVC/KBr	2.56×10^{-5}	-	[234]
PEO/PVC/KCl	8.29×10^{-6}	-	[235]
PEO/KI/CeO_2	2.15×10^{-3}	-	[236]
PEO/KBr/SiO_2	2.5×10^{-5}	-	[237]
PEO/KNO_3/KI	6.15×10^{-6}	-	[229]
PVP/KIO_3	1×10^{-9}	-	[224]
P.V.A./KCl	9.68×10^{-7}	-	[227]
P.V.A./KBr	1.23×10^{-5}	-	[230]
PUA/KI	1.59×10^{-4}	2	[238]
PPCB/KFSI	1.36×10^{-5}	4	[231]
P(AHG)/KI	3.41×10^{-4}	-	[239]
PFSA-K	9.31×10^{-5}	4.25	[223]
PAN/KI/EC:DMF	2.089×10^{-5}	-	[228]
PMMA/KPF_6/EC:DEC:FEC	4.3×10^{-3}	4.9	[216]
PVDF-HFP-KFSI	2.2×10^{-4}	3.2	This work
PVDF-HFP-KFSI@PAN	3.6×10^{-4}	4.1	This work

9.6 Interfacial Stability of PVDF-HFP-KFSI@PAN CGPE Against K Metal Anode

Symmetrical K/K cells are used (**Figure 9.6.1a**) to investigate the cycling stability of K metal with PVDF-HFP-KFSI@PAN as the separator in comparison with conventional GF separator. 40-μL

liquid electrolyte (1M KFSI in EC: DEC) is added in K|| PVDF-HFP-KFSI ||K and K|| PVDF-HFP-KFSI@PAN ||K cells to enable a good interfacial contact between K metal and CGPE. For the K||GF||K cells, 240-μL liquid electrolyte is required for fully wetting the GF separator. **Figure 9.6.1b** presents voltage-time profiles of K/K cells with PVDF-HFP-KFSI@PAN and GF at different rates of 0.1-1 mA cm^{-2}. The negative and positive voltage values correspond to the K plating and stripping processes, respectively. The K‖ PVDF-HFP-KFSI ‖K cell shows the smallest overpotential in the initial 30 h with a low current density of 0.1 mA cm^{-2}, followed by fluctuated voltage oscillation until a short circuit at 0.2 mA cm^{-2}. The K‖ PVDF-HFP-KFSI@PAN ‖K cell delivers a higher voltage hysteresis than the K‖GF‖K one during the initial cycles, which could be attributed to larger K^+ transfer resistance due to the smaller volume of liquid electrolyte used in the former than the latter. However, the K‖ PVDF-HFP-KFSI@PAN ‖K cell presents flattened voltages in the subsequent cycles (**Figures 9.6.1c-e**), suggesting the formation of a stable SEI layer at the surface of K metal [240]. When the current density increases from 0.1 to 1 mA cm^{-2}, the K‖ PVDF-HFP@PAN ‖K cell experiences a sudden voltage rise, followed by a rapid drop and then stabilization. It can be seen that the voltage hysteresis of the K‖ PVDF-HFP-KFSI@PAN ‖K cell is always flatter than that of the K‖ GF ‖K cell. When the current density is reversed back to 0.1 mA cm^{-2}, the voltage hysteresis of the K‖ GF ‖K cell becomes larger, and a short-circuit occurs at 550 h, which might be mainly induced by nonuniform K deposition and excessive dendrite growth [241]. In contrast, the K‖ PVDF-HFP-KFSI@PAN ‖K cell delivers an ultra-stable voltage hysteresis over 700 h without apparent oscillation, suggesting the superior reversibility of K plating/striping with PVDF-HFP-KFSI@PAN CGPE. Therefore, the CGPE is able to enable fast K-ion conduction (3.6×10^{-4} S cm^{-1} at 25 °C), reduce local current density, and regulate uniform K deposition, especially at high current densities. Besides, the PAN-reinforced CGPE is most likely to resist K dendrite piercing and prevent the cells from a short circuit.

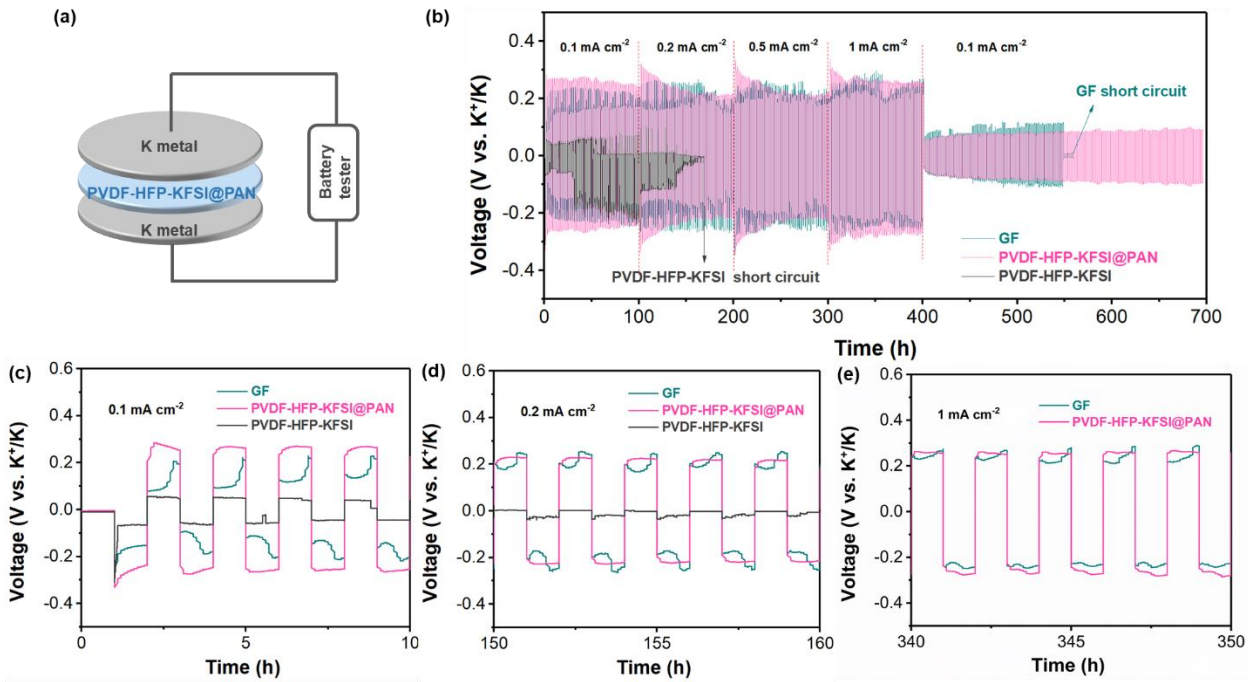

Figure 9.6.1. The rate capability of K/K symmetrical cells with PVDF-HFP-KFSI@PAN CGPE comparison with PVDF-HFP-KFSI and GF separators. (a) Cell configuration of K‖PVDF-HFP-KFSI@PAN‖K, and voltage profiles of K/K symmetrical cells at (b) 0.1-1 mA cm^{-2}, (c) 0.1, (d) 0.2, and (e) 1 mA cm^{-2}.

A long-term cycling test of K/K symmetrical cells is performed at 0.5 mA cm^{-2} to investigate K plating/stripping behavior further. The K‖ GF ‖K cell delivers unstable voltage profiles in the first five cycles but only maintains for 185 h (or 92 cycles) before the short circuit (**Figure 9.6.2a**). The K‖ PVDF-HFP-KFSI ‖K cell shows acute voltage oscillation in the first 10 hours and fast short-circuit after only 11 cycles, indicating the poor reversibility of K plating/stripping and interfacial incompatibility of PVDF-HFP-KFSI with K metal. In contrast, the K‖ PVDF-HFP-KFSI@PAN ‖K cell demonstrates exceptional stability over 1,200 h (600 cycles) without any voltage fluctuation (**Figure 9.6.2b**). In particular, the voltage response remains flat, and the hysteresis is almost stabilized at 0.74 V even during 1,190-1,200 h (**Figures 9.6.2c-e**). **Table 9.6.1** summarizes the cycling performance of K/K cells with liquid electrolytes at various current densities in published work and this work. Most symmetrical K metal batteries have been reported to show 100-500 h lifespan at 0.1-1 mA cm^{-2} with more than 100-µL electrolyte and GF separators. This work reports a K metal anode with the most extended cycles and time (>1,200 h) with the least liquid electrolyte,

to the best of our knowledge. Additionally, the K metal/electrolyte interface resistance can be further decreased by absorbing liquid Na-K alloy into a carbon nanotube membrane [242]. Regardless, our PVDF-HFP-KFSI@PAN CGPE presents the highest cumulative K plating capacity of 300 mAh cm^{-2}, which is far greater than other reported K/K cells (**Table 9.6.1** and **Figure 9.6.2f**). This smooth electrode-electrolyte (liquid-liquid) interface contributed to a long lifespan of 1,600 h, even at 1 mA cm^{-2}. That would be a promising direction to realize a more stable K metal anode in the future.

Moreover, the EIS plot gives the opposite trend of battery resistance after repeated cycles (**Figures 9.6.2g-h**). Before K plating/stripping, the charge transfer resistance (R_{ct}) for the K/K cell with PVDF-HFP-KFSI@PAN (3,019 Ω) is bigger than that of K‖ GF ‖K cell (2,232 Ω), possibly due to less liquid electrolyte in the former than the latter (**Table 9.6.2**). After 50 cycles, the K‖ PVDF-HFP-KFSI@PAN ‖K cell possesses a smaller SEI resistance (R_{SEI}) (2,119 Ω) than K‖ GF ‖K (3,544 Ω). In summary, PVDF-HFP-KFSI@PAN CGPE induces the generation of a stable SEI layer to regulate K dendrites growth, thus prolonging the electrochemical stability and lifetime of K/K symmetrical cells.

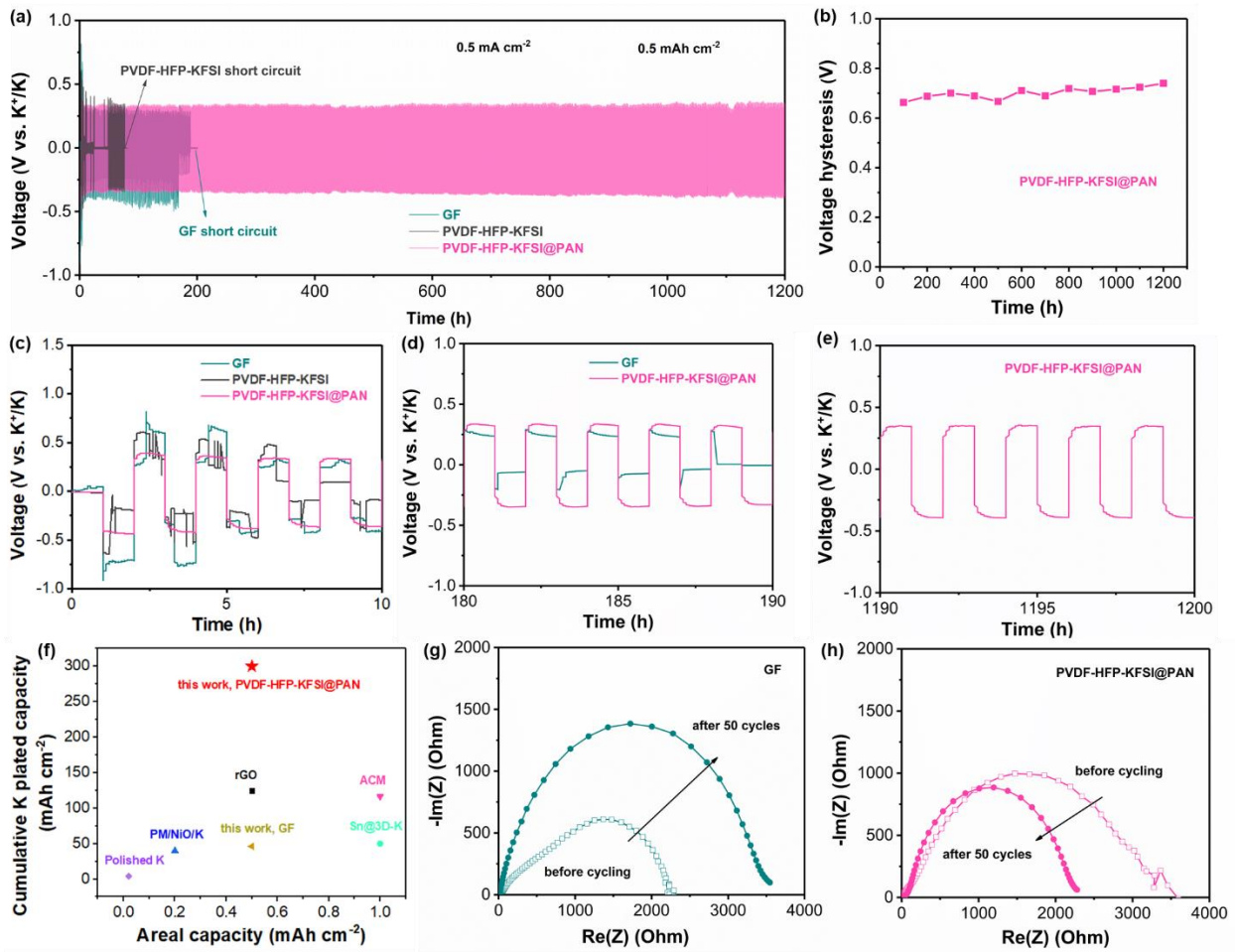

Figure 9.6.2. Electrochemical performance of K/K symmetrical cells with PVDF-HFP-KFSI@PAN compared to PVDF-HFP-KFSI and GF separator. (a) Long-cycling stability at 0.5 mA cm^{-2}, (b)voltage hysteresis of K‖ PVDF-HFP-KFSI@PAN ‖K cell, voltage-time profiles during (c) 0-10 h, (d) 180-190 h, and (e) 1190-1200 h, (f) comparison of cumulative K plated capacity in previous studies and this work, and Nyquist plots of (g) K‖ GF ‖K and (h) K‖ PVDF-HFP-KFSI@PAN ‖K cells before and after 50 cycles.

Table 9.6.1. Cycling performance of K/K symmetrical cells in literature and this work.

K metal	Separator	Electrolyte	Electrolyte volume (μL)	Current density (mA cm^{-2})/areal capacity (mAh cm^{-2})	Lifetime	Cumulative plated K capacity (mAh cm^{-2})	Ref.
K-rGO@3D-Cu	GF	0.8M KPF_6 in EC/DEC/PC	120	0.5/0.5	500 h	125	[243]
Sn@3D-K	GF	0.5M KFSI in DME	NA	1/1	100 h	50	[244]
PM/NiO/K	GF	1M KPF_6 in EC/DEC	NA	0.4/0.2	200 cycles	40	[240]
K-ACM	Two pieces of GF	0.8M KPF_6 in EC/DEC	NA	1/1	233 h	116.5	[245]
Polished K	GF	1M KTFSI in DME	NA	0.1/0.02	200 cycles	4	[246]
K foil	GF	1M KFSI in EC/DEC	240	0.5/0.5	185 h	46.25	This work
K foil	PVDF-HFP-KFSI@PAN	1M KFSI in EC/DEC	40	0.5/0.5	1200 h	300	This work

NA: not available; GF: Glass fiber

Table 9.6.2. EIS impedance values for K|| PVDF-HFP-KFSI@PAN || K and K|| GF ||K cells.

Cell configuration	Before cycling		After 50 cycles		
	R_e (Ω)	R_{ct} (Ω)	R_e (Ω)	R_{ct} (Ω)	R_{SEI} (Ω)
K|| PVDF-HFP-KFSI@PAN || K	12.9	3019.0	12.2	100.9	2119.0
K|| GF ||K	26.8	2232.0	5.7	3.8	3544.0

9.7 Post-Cycling Observations of GF, PVDF-HFP-KFSI and PVDF-HFP-KFSI@PAN

SEM observation is performed after repeated K stripping/plating cycles to characterize the surface of the separator. The cycled PVDF-HFP-KFSI is completely broken, as depicted in the inset photo of **Figure 9.7.1a**. Larger pores or gaps between KFSI particles are observed in top-view and cross-sectional SEM images in **Figures 9.7.1a-c** and explain a fast short circuit mainly caused by poor structural rigidity. **Figures 9.7.1d-e** present EDS mapping and spectra of the selected area from **Figure 9.7.1c**. In contrast, PVDF-HFP-KFSI@PAN maintains a good structure after 100 cycles, as shown in the inset photo in **Figure 9.7.1f**. The SEM images in **Figures 9.7.1f-h** illustrate a uniform surface and compact cross-section area. This great structural stability might benefit from the passivation of the KF-rich SEI layer [214], which is confirmed by the EDS mapping (**Figure 9.7.1i**) and the intense KF peak in the XPS spectrum (**Figure 9.7.1j**). It should be noted that the thickness and interface in **Figure 9.7.1h** are different from **Figure 9.3.1h**, which could be due to pressure and SEI layer formation. The 200 µm thickness of PVDF-HFP-KFSI@PAN in **Figure 9.3.1h** was scanned by MicroXCT before cell testing. An average thickness of 150 µm is selected for cell assembly. When assembling and disassembling the K/CGPE/K cell, a pressure of 1100 psi was applied, which was likely to decrease the thickness of CGPE. Glass fiber also had a significant thickness reduction from the original 600 µm to 360 µm. On the other hand, **Figure 9.7.1h** illustrates the interface of PVDF-HFP-KFSI@PAN after 50 repeated K plating/stripping cycles, and an SEI layer was supposed to form on the surface of PVDF-HFP-KFSI@PAN. Moreover, K metal was plated/stripped in a coin cell where CGPE underwent considerable pressure. Therefore, pressure and SEI are possible reasons for causing different interfaces and thicknesses of CGPE.

XPS C1s and O 1s spectra are presented in **Figure 9.7.2**. Note that the K‖ GF ‖K cell is short-circuited after 100 cycles at 0.5 mA cm^{-2} according to **Figure 9.7.2a**, which is explained by a couple of large K chucks piercing the porous GF separator (**Figures 9.7.1k-m**). The limited F element percentage and its disordered distribution (**Figures 9.7.1n-o**, **Table 9.7.1**) also indicate the nonuniform SEI layer on K metal. Numerous K dendrites spread irregularly and grow excessively across the gap between glass fibers and, therefore, induce a rapid short-circuit failure. It could be concluded that the electrospun PAN nanofibers are robust to restrain the piercing behavior from K dendrites due to the reinforced mechanical strength of CGPE. On the other hand, the KF-rich SEI layer enables the regulation of K dendrites, thus contributing to a long-durability symmetrical K/K cell over 1,200 h.

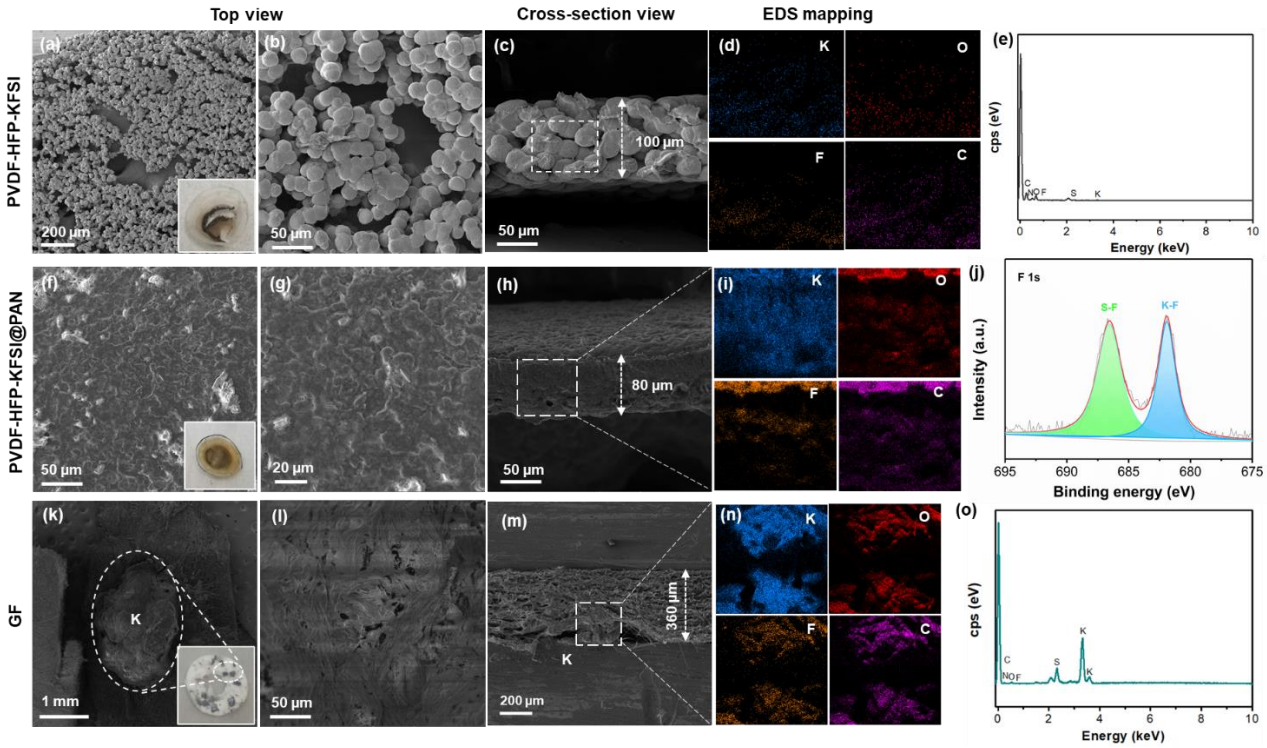

Figure 9.7.1. Morphology of PVDF-HFP-KFSI, PVDF-HFP-KFSI@PAN, and GF separators recovered from K|K symmetric cells after 100 cycles or failure. (a, b, f, g, k, l) Top view, (c, h, m) cross-section view and (d, i, n) EDS mapping of (a-c) PVDF-HFP-KFSI (f-h) PVDF-HFP-KFSI@PAN and (k-m) GF (insets in (a), (f) and (k) are corresponding digital photos of the separators). (j) XPS F 1s spectra of cycled PVDF-HFP-KFSI@PAN surface, (e, o) EDS spectrum of cycled PVDF-HFP-KFSI and GF.

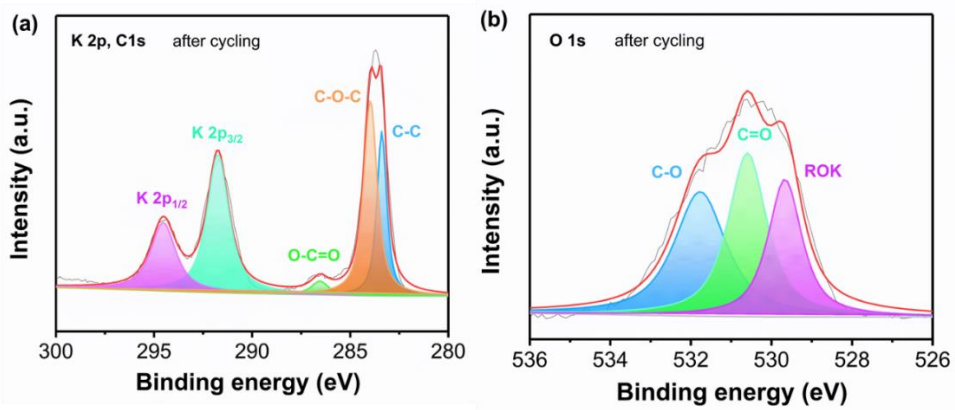

Figure 9.7.2. (a) XPS K 2p and C 1s and (b) O 1s of cycled PVDF-HFP-KFSI@PAN.

Table 9.7.1. Elemental composition of cycled PVDF-HFP-KFSI@PAN and GF from EDS.

Separator	Weight percentage (wt%)								
	K	O	C	F	S	N	Al	Si	Na
PVDF-HFP-KFSI@PAN	44.3	22.4	10.1	10.8	6.5	2.8	3.1	-	-
PVDF-HFP-KFSI	10.9	21.5	57.8	5.1	3.6	1.1	-	-	-
GF	81.4	2.4	0.9	0.1	12.7	1.3	0.7	0.3	0.1

Based on the discussions above, the addition of PAN 3D fibers reinforced the mechanical strength of PVDF-HFP-KFSI. The higher tensile strength (3.5 MPa) of PVDF-HFP-KFSI@PAN than that of PVDF-HFP-KFSI is evidence to support the mechanical property improvement. Moreover, the cycled PVDF-HFP-KFSI@PAN CGPE maintained a uniform and dense surface after experiencing repeated K plating/stripping from the digital photo and SEM images shown in **Figures 9.7.1f-h**. In contrast, the PVDF-HFP-KFSI only had a 0.6 MPa tensile strength, which is likely to cause K dendrites to pierce the membrane and lead to a short circuit. The broken membrane piece and large pores or gaps from **Figures 9.7.1a-c** indicated its poor mechanical strength. Therefore, it's reasonable to conclude that the PAN nanofibers enhance the mechanical strength of polymer electrolyte and make it robust to resist K dendrites growth. On the other hand, the steady oxidation/reduction peaks in CV, wide electrochemical stability window up to 4.1 V (**Figure**

9.5.1b), and an extra-long lifetime of 1,200 h together indicate superior electrochemical stability of CGPE. Some research groups have found that polymer could fully fill into the PAN network, thereby enhancing the electrochemical stability of the electrolyte [222, 247]. Previous studies found that PAN-based electrolytes had a strong oxidation resistance [248], and the fiber network improved the electrochemical stability window [247]. The wider electrochemical stability window up to 4.1 V in **Figure 9.5.1b,** steady K plating/stripping profile, and superior cycling stability in **Figure 9.6.2a** together suggest that CGPE is more electrochemically stable against K metal due to the introduction of PAN fibers. Accordingly, the PAN nanofibers are confirmed to significantly enhance the structural and electrochemical stability of polymer electrolytes and ensure a highly stable K metal anode.

9.8 Different Electrochemical Deposition Behaviors of K Metal with GF, PVDF-HFP-KFSI, and PVDF-HFP-KFSI@PAN

Figure 9.8.1 illustrates different electrochemical deposition behaviors of K metal with GF separator, PVDF-HFP-KFSI, and PVDF-HFP-KFSI@PAN CGPE. As discussed above, the commercially available GFs possess plenty of gaps or pores, making them easy to absorb liquid electrolytes and facilitating K^+ diffusion. However, these porous sites are also easily attacked by continuously generated irregular K dendrites, resulting in shortened battery life. The large consumption of liquid electrolytes containing flammable organic solvents poses another potential safety hazard. The PVDF-HFP-KFSI has poor mechanical strength and structural stability, and it turns out to be broken and pierced by K dendrites, resulting in a fast short circuit. By contrast, our PVDF-HFP-KFSI@PAN CGPE is reinforced by electrospun PAN nanofibers to resist the attack by K dendrites. Besides, the *in-situ* formed KF-rich SEI layer regulates K dendrite growth and enhances the electrochemical stability of K metal. The pre-added KFSI salt in the CGPE is substantial K-ion conducting units to facilitate the conduction of K-ions. With the help of KFSI salt and an interconnected PAN network, only 40 μL liquid electrolyte is required to ensure an efficient K plating/stripping process, thus achieving a long-life K metal anode above 1,200 h.

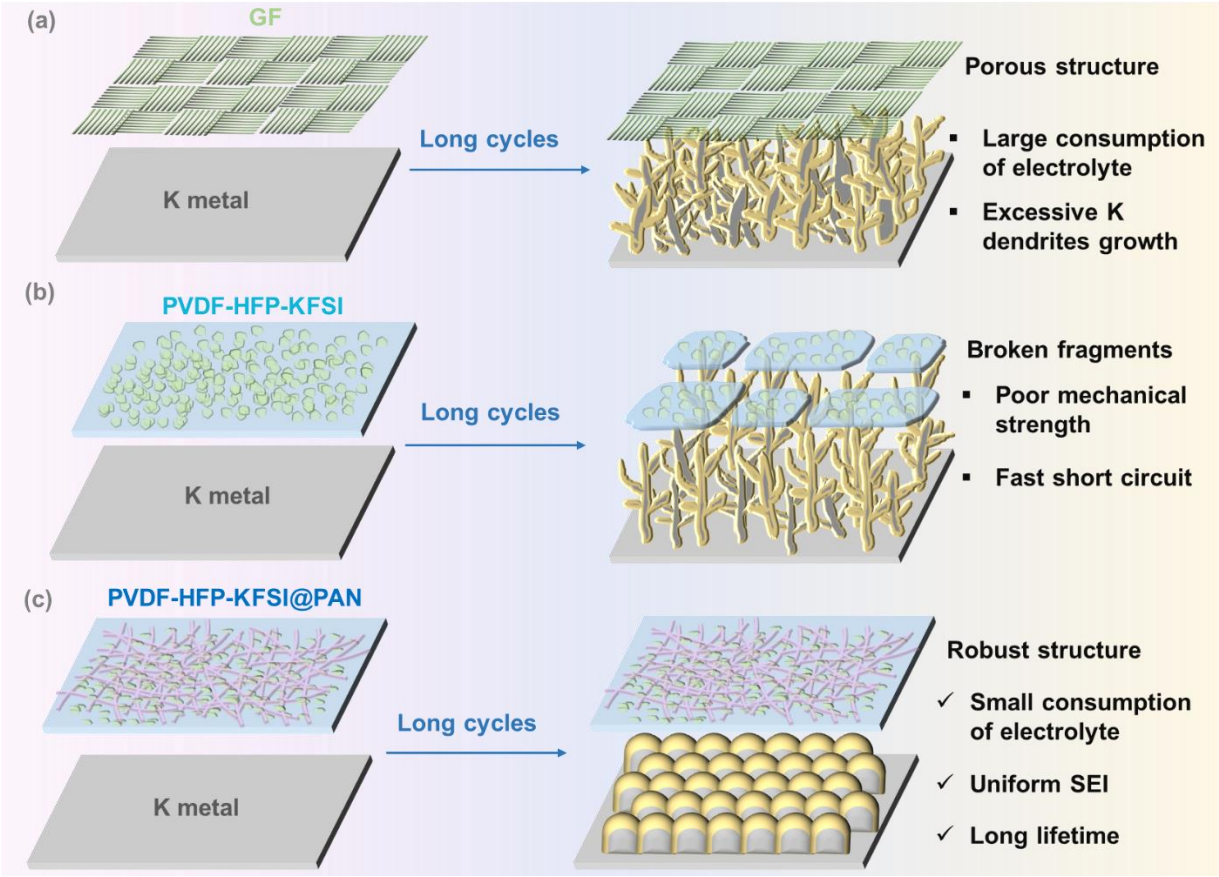

Figure 9.8.1. Schematic illustration of the electrochemical deposition behaviors of K metal using (a) GF separator, (b) PVDF-HFP-KFSI, and (c) PVDF-HFP-KFSI@PAN.

Moreover, K-Te cells are constructed with the Te/BP2000 cathode (developed in Chapter 8) and PVDF-HFP-KFSI and PVDF-HFP-KFSI@PAN polymer electrolytes. Te is selected due to its significantly higher electrical conductivity (2×10^{2} S m^{-1}) than sulfur (5×10^{-16} S m^{-1}) or selenium (1×10^{-4} S m^{-1}) [47]. This excellent feature is expected to boost reaction kinetics upon potassiation/depotassiation processes. **Figure 9.8.2** presents galvanostatic charge/discharge profiles in the first 5 cycles at 0.1C. Theoretically, Te electrode is able to deliver a specific capacity of 420 mAh g^{-1} if Te is fully discharged to K_2Te [104]. It is observed that the K-Te cell with CGPE delivered initial capacities of 1172.4, 423.3, and 398.8 mAh g^{-1} in the 1st, 2nd, and 5th cycle, respectively. The large specific capacity difference between 1st and 2nd might be due to the formation of solid electrolyte interphase [105]. Regardless, **Figure 9.8.2** validates the applicability of our CGPE in K-Te battery system.

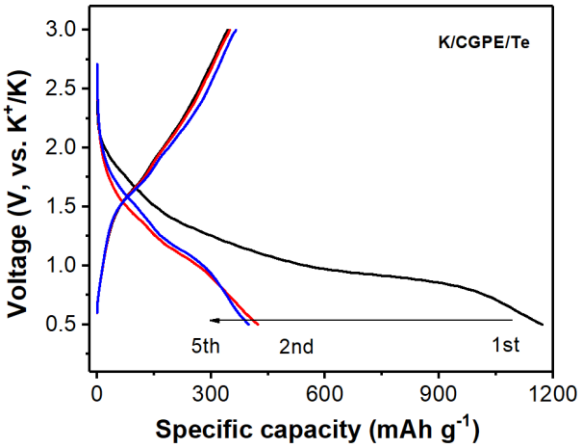

Figure 9.8.2. Charge-discharge profiles of K-Te cells with PVDF-HFP-KFSI@PAN electrolyte and Te/BP2000 cathode in the 1st, 2nd, and 5th cycle.

9.9 Chapter Summary

In summary, a long-durability K metal anode was realized by manipulating the generation of the SEI layer and using a PAN-reinforced composite gel polymer electrolyte (CGPE). The CPGE possessed a layer-by-layer structure, as revealed by SEM and MicroXCT analysis. This typical structure and composition design of CGPE ensured a high ionic conductivity of 3.6 $\times 10^{-4}$ S cm^{-1} at 25 °C and an electrochemical stability of up to 4.1 V. In addition, only 40 µL liquid electrolyte was required to achieve a super stable symmetrical K metal anode (> 1,200 h) at the current density of 0.5 mA cm^{-2}. It should be noted that the K/K symmetrical cell with PVDF-HFP-KFSI@PAN CGPE has delivered the highest cumulative K plating capacity reported so far (300 mAh cm^{-2}). The flat voltage response, intense KF peak signal, and small interfacial resistance suggested that this CGPE induced the formation of a stable SEI layer to regulate the growth of K dendrites over repeated K plating/stripping cycles. This work is expected to shed light on the design of composite gel polymer electrolytes for safe and long-lifetime K metal batteries.

Chapter 10 Conclusions, Contributions, and Perspectives

10.1 Conclusions

This dissertation was conducted to develop next-generation Te-based rechargeable batteries with the well-designed cathodes, electrolytes, and compatible electrode/electrolyte interface, aiming at resolving the critical issues of cathode durability, electrolyte compatibility, and interface stability for Li-Te or K-Te batteries. Rational materials design, comprehensive characterizations, and in-depth analysis for metal-Te battery systems accomplished the goals. Morphology, structure, electrochemical performance, and battery cyclability were characterized and evaluated systematically. The main conclusions from this dissertation are as follows:

In Chapter 4, the effect of carbon pore structure on the electrochemical performance of Te/C electrodes is elucidated. The ideal carbon should possess large pore volume, surface area, and sufficient micro-/mesopores as Te loading sites. Micropores are found to be more effective in Te confinement than mesopores due to the stronger Te-C interaction. Moreover, lignin is a sustainable precursor to customize pore structure through carbonization and activation procedures. The optimal Te/AC700 cathode delivers a reversible capacity of 418 mAh g^{-1}, high capacity retention of 90% after 100 cycles, and exceptional cyclability over 1000 cycles at 2 C.

With the well-confined Te/C structure in Chapter 4, a quasi-solid-state Li-Te battery is constructed with flexible gel polymer electrolytes, as depicted in Chapter 5. The ionic conductivity of GPE is dependent on the NMP uptake and can reach up to 8.0×10^{-4} S cm^{-1} at 25 °C. The Te/C cathodes outperform their S/C or Se/C counterparts in terms of cycling stability and rate capability due to the faster charge transfer in Te/C cathodes.

Furtherly, the high-electrical-conductivity advantage of Te is integrated with low-cost S to develop a wide range of Te_xS_y composite cathodes in Chapter 6. The Te_1S_7 is found to have the lowest energy barrier for Li-ion migration than other Te_xS_y composites, which is confirmed by the cycling test, redox kinetics analysis, and electrochemical impedance analysis. Moreover, the correlation between the Te/S molar ratio and electrolytes with the electrochemical properties of the Te_xS_y cathode is comprehensively investigated. The optimized Li-TeS battery consisting of 3M LiTFSI in DEC:FEC electrolyte and Te_1S_7/KB cathode) shows a reversible capacity of ~ 1,300 mAh g^{-1} at

0.1 A g^{-1} for 100 cycles and ~ 960 mAh g^{-1} at 1 A g^{-1} for 400 cycles. The advantages of Te_1S_7/KB versus S/KB are also illustrated by cycling performance and electrochemical impedance spectroscopy at the pouch cell level.

On the other hand, the electrochemistry fundamental of the promising K-Te energy storage technology is deepened in this dissertation due to the abundance and low cost of K resources. In Chapter 7, two K salts, KPF_6 and KFSI, induce the same phase transformation between Te and K_2Te during potassiation/depotassiation. At the same time, they significantly influence the specific capacity, reaction kinetics, and rate capability of the Te/C cathode by affecting the SEI layers. KPF_6 salt induces the formation of SEI layers with faster K-ion diffusion and electron transfer rates than KFSI, thus enabling higher K-ion storage capacity and better rate capability in the Te/C cathode. KFSI causes more stable KF-rich SEI layers on the Te/C cathode than KPF_6, leading to enhanced Coulombic efficiency (CE) and electrode structural stability in K-Te batteries.

To enhance the K-ion storage capability of Te electrodes, a well-confined Te/C cathode is developed. A surface coating layer is precisely deposited in Chapter 8 by our lab's advanced atomic layer deposition technique to improve Te/electrolyte stability. Mechanistic studies reveal a two-step reaction pathway from Te to K_2Te_3 and ultimately to K_5Te_3 in carbonate electrolyte-based K-Te batteries. The introduction of 1-nm Al_2O_3 film induces the generation of a stable solid electrolyte interphase layer and reduces the loss of active materials effectively. The rationally fabricated Te/C cathode with functional Al_2O_3 coating delivers remarkable long-term cycling stability over 500 cycles at 1 C with an ultralow capacity decay of only 0.01% per cycle.

Meanwhile, the K dendrites growth is suppressed by the as-prepared robust composite gel polymer electrolyte in Chapter 9 to replace commercial thick glass fiber separators and reduce the amount of liquid electrolyte to only 40 µL (vs. 200 µL consumption for glass fiber). The CGPE has a high ionic conductivity of 3.6×10^{-4} S cm^{-1} at 25 °C and electrochemical stability up to 4.1 V. Besides, the reinforced CGPE induces the generation of *in-situ* formed KF-rich SEI layer, which regulates K dendrite growth. Consequently, the CGPE ensures a long-life K metal anode above 1,200 h at the current density of 0.5 mA $cm^{-2,}$ with the highest cumulative K plating capacity reported so far (300 mAh cm^{-2}). The Te/C electrode discussed in Chapter 8 well matches the PAN-reinforced CGPE.

10.2 Contributions

The main contributions originating from this dissertation are summarized in the following aspects:

(1) Fundamental investigation of Li-Te electrochemistry

This study reveals critical pore structure properties for porous carbon employed as Te host in Li-Te batteries. High pore volume, large surface area, and proper pore size distribution are indispensable parameters to accommodate the volume change of Te accompanied by lithiation/delithiation. The interplay between Te and C is also unraveled by comprehensive morphology/structure characterizations and electrochemical/kinetics/surface chemistry analysis. Additionally, quasi-solid-state Li-Te batteries are fabricated for the first time to the best of our knowledge, outperforming the Li-S and Li-Se batteries with the same configuration. These findings are inspirable for the future development of Li-Te batteries.

(2) Development of emerging Li-Te_xS_y battery systems

This work pioneers the theoretical calculation and experimental analysis of Li-Te_xS_y battery systems. The Te_1S_7 is found to maximumly take the advantages of Te (high electrical conductivity) and S (low-cost, high theoretical capacity). The correlation between Te/S ratio and Li-ion storage performance is disclosed, together with the effect of electrolyte chemistry on the lithiation behavior of Te_xS_y cathodes. More importantly, the superior cycling performance and kinetics of Te_xS_y/KB than S/KB are also demonstrated at the pouch cell level.

(3) Electrolyte investigation and interface control of K-Te batteries

This research reveals the internal reaction mechanism of K-Te batteries in carbonate electrolytes and identifies the role of two electrolyte roles in K-ion storage capability, kinetics, and SEI composition. Moreover, nanometer-level surface coating is proven effective in enhancing the cycling stability and structural integrity of Te/C electrodes. Our self-made CGPE shows high ionic conductivity, wide electrochemical window, and tensile strength and induces the formation of a stable SEI layer to regulate K dendrite growth. This encouraging CGPE outperforms commercial glass fiber separators in terms of structural stability and the lifetime of K symmetrical cells. The amount of liquid electrolyte is significantly reduced to only one-fifth of the consumption with

commercial separators, while the K metal anode obtains an extended lifetime over 1,200 h with a K cumulative capacity of 300 mAh cm^{-2}.

These contributions in this dissertation are expected to stimulate more research in developing safe, durable, and high-energy-density Te-based batteries.

10.3 Limitations

This dissertation deepens the fundamental understanding of Li-Te or K-Te batteries through rational materials design and interface engineering strategies. Despite these great progresses, there are still limitations that have not been addressed in this project.

(1) The dynamic morphology and structure changes of the Te cathode or Te/electrolyte interface have not been visualized. In-situ structural or morphological characterizations, *e.g.*, XRD, Raman, HRTEM, *etc.*, are helpful in monitoring the phase change and determining the volume change of Te upon lithiation/delithiation behavior.

(2) The theoretical simulation about the Te-C interaction at the atomic level has not been realized. Overcoming this problem would facilitate an in-depth understanding of the carbon pore structure effect on Li-Te electrochemistry.

(3) The temperature variation during long-term cycling tests has not been studied. The possible effect of temperature on interface stability, cathode structure integrity, and SEI layer formation deserves more attention and discussion.

(4) The Te or TeS content in Te/C or TeS/C composites is about less than 60 wt% with the average mass loading of 1-2 mg cm^{-2}. Increasing Te (or TeS) content and their mass loadings is necessary to enable a higher overall energy density of Li-Te or K-Te batteries.

10.4 Perspectives

The desirable advantages of Te have inspired multiple strategies to address the problems associated with the electrochemical behaviors in Te-based cathodes, such as Te-impregnated carbon, nanostructured Te, electrolyte optimization, and carbon interlayers. Moreover, Te has been successfully used as a doping element in S to fabricate Te_xS_y cathodes to accelerate the reaction kinetics and electrochemical reversibility. Despite these promising findings, extensive research is

required to explore the underlying mechanism and make use of the unique Te and Li/K interaction. In the future, research and studies could focus on the following aspects:

(1) Cathodes

Future work is required to obtain a deep understanding of the carbon pore size effect on the performance of Li-Te batteries, such as atomic-level interaction between porous carbon and Te through theoretical simulation, the interplay between micropore carbon/Te (or mesopores carbon/Te) and carbonate-based electrolytes, and *in-situ* analysis on Te phase change during battery cycling to track Te dissolution.

(2) Anodes

The state-of-the-art *in-situ* characterization techniques, such as synchrotron radiation, x-ray diffraction, high-resolution transmission electron microscopy, *etc.*, play an essential role in unraveling the unclear SEI formation and Li/K dendrite regulation mechanism in Te-based electrochemistry.

(3) Interface Studies

More investigations and quantitative analysis are required to evaluate the mechanical properties and electrochemical stability between Te-based cathodes and solid/liquid electrolytes. It is essential to employ suitable *operando* techniques to observe the instant interfacial change and find the critical point where the cathode structure failure (pulverization or delamination) occurs over cycling. *In-situ* temperature and pressure monitor would be helpful in analyzing the interplay between cathodes and electrolytes.

(4) Practical Criteria

Another required future work is to establish a standard protocol to assess the volumetric energy density of Li-Te-based batteries compared to other Li-chalcogen and Li-ion batteries. One of the motivations for using Te cathodes is based on its high volumetric energy density (2621 mAh cm^{-3}) comparable to S and Se and much higher than $LiCoO_2$ (700 mAh cm^{-3}). However, there are several challenges to obtaining meaningful and comparable values for the volumetric energy density of rechargeable Te-based batteries. Although several research findings provide volumetric

specific capacities of Te cathodes, these values were based on Te cathode volume only, without considering the other components (current collectors, separator, and Li metal anode) and factors (electrode porosity and electrolyte). Further work may be performed to fabricate more Te-based cathodes for pouch cell evaluation to reveal the actual values in close-to-application scenarios.

(5) Commercialization

For commercial applications of Te-based batteries, it is essential to maximize Te's strengths by increasing Te loading and reducing the fraction of host materials to raise the overall energy density of battery systems. Te loading on cathodes must be increased to a level that can deliver an areal capacity of ~ 4 mAh cm^{-2} for practical applications. Unfortunately, current Te cathodes have only areal capacities of ~ 1-1.5 mAh cm^{-2} or less, and together with the excessive Li metal, they do not necessarily reflect the holistic performance of Li-Te batteries. Simultaneously, the cost of materials and devices should be minimized for scalable energy storage applications. The recycling technology of Te materials could be furtherly promoted to satisfy the increasing demand for Te and decrease the cost of Te-based batteries.

Bibliography

[1] O. Arslan, Technoeconomic analysis of electricity generation from wind energy in Kutahya, Turkey, Energy, 35 (2010) 120-131.

[2] Z. Yang, J. Zhang, M.C. Kintner-Meyer, X. Lu, D. Choi, J.P. Lemmon, et al., Electrochemical energy storage for green grid, Chem. Rev., 111 (2011) 3577-3613.

[3] P.J. Meier, P.P. Wilson, G.L. Kulcinski, P.L. Denholm, US electric industry response to carbon constraint: a life-cycle assessment of supply side alternatives, Energy Policy, 33 (2005) 1099-1108.

[4] F.J. de Sisternes, J.D. Jenkins, A. Botterud, The value of energy storage in decarbonizing the electricity sector, Appl. Energy, 175 (2016) 368-379.

[5] D. Gielen, F. Boshell, D. Saygin, M.D. Bazilian, N. Wagner, R. Gorini, The role of renewable energy in the global energy transformation, Energy Strategy Rev., 24 (2019) 38-50.

[6] C.A. Powell, B.D. Morreale, Materials challenges in advanced coal conversion technologies, MRS Bull., 33 (2008) 309-315.

[7] A. Shahsavari, M. Akbari, Potential of solar energy in developing countries for reducing energy-related emissions, Renew. Sust. Energ. Rev., 90 (2018) 275-291.

[8] B.K. Sahu, Wind energy developments and policies in China: A short review, Renew. Sust. Energ. Rev., 81 (2018) 1393-1405.

[9] E. Asmelash, G. Prakash, R. Gorini, D. Gielen, Role of IRENA for Global Transition to 100% Renewable Energy, in: Accelerating the Transition to a 100% Renewable Energy Era, Springer, 2020, pp. 51-71.

[10] R. Adib, H. Murdock, F. Appavou, A. Brown, B. Epp, A. Leidreiter, et al., Renewables 2015 global status report, REN21 Secretariat, Paris, France, 162 (2015).

[11] J. Gong, C. Li, M.R. Wasielewski, Advances in solar energy conversion, Chem. Soc. Rev., 48 (2019) 1862-1864.

[12] V. Khare, S. Nema, P. Baredar, Solar–wind hybrid renewable energy system: A review, Renew. Sust. Energ. Rev., 58 (2016) 23-33.

[13] B. Scrosati, J. Garche, Lithium batteries: Status, prospects and future, J. Power Sources, 195 (2010) 2419-2430.

[14] T.M. Gür, Review of electrical energy storage technologies, materials and systems: challenges and prospects for large-scale grid storage, Energy Environ. Sci., 11 (2018) 2696-2767.

[15] L. Yao, B. Yang, H. Cui, J. Zhuang, J. Ye, J. Xue, Challenges and progresses of energy storage technology and its application in power systems, J. Mod. Power Syst. Clean Energy, 4 (2016) 519-528.

[16] J.B. Goodenough, Y. Kim, Challenges for Rechargeable Li Batteries†, Chem. Mater., 22 (2010) 587-603.

[17] A. Manthiram, An Outlook on Lithium Ion Battery Technology, ACS Cen. Sci., 3 (2017) 1063-1069.

[18] K. Mizushima, P. Jones, P. Wiseman, J.B. Goodenough, LixCoO2 (0< x<-1): A new cathode material for batteries of high energy density, Mater. Res. Bull., 15 (1980) 783-789.

[19] A. Padhi, K. Nanjundaswamy, C. Masquelier, S. Okada, J.B. Goodenough, Effect of structure on the Fe3+/Fe2+ redox couple in iron phosphates, J. Electrochem. Soc., 144 (1997) 1609.

[20] M. Thackeray, W. David, P. Bruce, J.B. Goodenough, Lithium insertion into manganese spinels, Mater. Res. Bull., 18 (1983) 461-472.

[21] N. Nitta, F. Wu, J.T. Lee, G. Yushin, Li-ion battery materials: present and future, Mater. Today, 18 (2015) 252-264.

[22] R. Chebiam, F. Prado, A. Manthiram, Structural Instability of Delithiated Li1− x Ni1− y Co y O2 Cathodes, J. Electrochem. Soc., 148 (2001) A49-A53.

[23] A. Eftekhari, The rise of lithium–selenium batteries, Sustain. Energy Fuels, 1 (2017) 14-29.

[24] J. Kim, D.-J. Lee, H.-G. Jung, Y.-K. Sun, J. Hassoun, B. Scrosati, An Advanced Lithium-Sulfur Battery, Adv. Funct. Mater., 23 (2013) 1076-1080.

[25] L. Ma, K.E. Hendrickson, S. Wei, L.A. Archer, Nanomaterials: Science and applications in the lithium–sulfur battery, Nano Today, 10 (2015) 315-338.

[26] Q. Pang, X. Liang, C.Y. Kwok, L.F. Nazar, Advances in lithium–sulfur batteries based on multifunctional cathodes and electrolytes, Nat. Energy, 1 (2016) 1-11.

[27] J.W. Fergus, Recent developments in cathode materials for lithium ion batteries, J. Power Sources, 195 (2010) 939-954.

[28] X. Ji, L.F. Nazar, Advances in Li–S batteries, J. Mater. Chem., 20 (2010) 9821.

[29] M.H. Aboonasr Shiraz, H. Zhu, Y. Liu, X. Sun, J. Liu, Activation-free synthesis of microporous carbon from polyvinylidene fluoride as host materials for lithium-selenium batteries, J. Power Sources, 438 (2019) 227059.

[30] V. Kolosnitsyn, E. Karaseva, Lithium-sulfur batteries: Problems and solutions, Russ. J. Electrochem., 44 (2008) 506-509.

[31] J. Wang, Y.S. He, J. Yang, Sulfur-based composite cathode materials for high-energy rechargeable lithium batteries, Adv. Mater., 27 (2015) 569-575.

[32] S.S. Zhang, Liquid electrolyte lithium/sulfur battery: Fundamental chemistry, problems, and solutions, J. Power Sources, 231 (2013) 153-162.

[33] S. Xin, L. Gu, N.H. Zhao, Y.X. Yin, L.J. Zhou, Y.G. Guo, et al., Smaller sulfur molecules promise better lithium-sulfur batteries, J. Am. Chem. Soc., 134 (2012) 18510-18513.

[34] Z. Li, L. Yuan, Z. Yi, Y. Liu, Y. Huang, Confined selenium within porous carbon nanospheres as cathode for advanced Li–Se batteries, Nano Energy, 9 (2014) 229-236.

[35] D.B. Babu, K. Ramesha, Constraining polyselenide formation in ether based electrolytes through confinement of Se in microporous carbon matrix for Li-Se batteries, Electrochim. Acta, 219 (2016) 295-304.

[36] Y. Cui, A. Abouimrane, J. Lu, T. Bolin, Y. Ren, W. Weng, et al., (De) Lithiation mechanism of Li/SeS x (x= 0–7) batteries determined by in situ synchrotron X-ray diffraction and X-ray absorption spectroscopy, J. Am. Chem. Soc., 135 (2013) 8047-8056.

[37] Y. Cui, A. Abouimrane, C.-J. Sun, Y. Ren, K. Amine, Li–Se battery: absence of lithium polyselenides in carbonate based electrolyte, Chem. Commun., 50 (2014) 5576-5579.

[38] C. Luo, Y. Xu, Y. Zhu, Y. Liu, S. Zheng, Y. Liu, et al., Selenium@mesoporous carbon composite with superior lithium and sodium storage capacity, ACS Nano, 7 (2013) 8003-8010.

[39] C.P. Yang, S. Xin, Y.X. Yin, H. Ye, J. Zhang, Y.G. Guo, An advanced selenium–carbon cathode for rechargeable lithium–selenium batteries, Angew. Chem. Int. Ed., 52 (2013) 8363-8367.

[40] J. Jin, X. Tian, N. Srikanth, L.B. Kong, K. Zhou, Advances and challenges of nanostructured electrodes for Li–Se batteries, J. Mater. Chem. A, 5 (2017) 10110-10126.

[41] P. Zhao, M.H.A. Shiraz, H. Zhu, Y. Liu, L. Tao, J. Liu, Hierarchically porous carbon from waste coffee grounds for high-performance Li–Se batteries, Electrochim. Acta, 325 (2019) 134931.

[42] X. Wu, L. Yuan, S. Zhou, S. Lou, Y. Wang, T. Gao, et al., Controlled synthesis of multi-morphology Te crystals by a convenient Lewis acid/base-assisted solvothermal method, J. Nanopart. Res., 14 (2012) 1009.

[43] Q. Lu, F. Gao, S. Komarneni, Biomolecule-Assisted Reduction in the Synthesis of Single-Crystalline Tellurium Nanowires, Adv. Mater., 16 (2004) 1629-1632.

[44] A. Zhao, C. Ye, G. Meng, L. Zhang, P. Ajayan, Tellurium nanowire arrays synthesized by electrochemical and electrophoretic deposition, J. Mater. Res., 18 (2003) 2318-2322.

[45] Z. Wang, L. Wang, J. Huang, H. Wang, L. Pan, X. Wei, Formation of single-crystal tellurium nanowires and nanotubes via hydrothermal recrystallization and their gas sensing properties at room temperature, J. Mater. Chem., 20 (2010) 2457-2463.

[46] Y. Liu, J. Wang, Y. Xu, Y. Zhu, D. Bigio, C. Wang, Lithium–tellurium batteries based on tellurium/porous carbon composite, J. Mater. Chem. A, 2 (2014) 12201-12207.

[47] J. He, Y. Chen, W. Lv, K. Wen, Z. Wang, W. Zhang, et al., Three-Dimensional Hierarchical Reduced Graphene Oxide/Tellurium Nanowires: A High-Performance Freestanding Cathode for Li-Te Batteries, ACS Nano, 10 (2016) 8837-8842.

[48] B. Mayers, Y. Xia, One-dimensional nanostructures of trigonal tellurium with various morphologies can be synthesized using a solution-phase approach, J. Mater. Chem., 12 (2002) 1875-1881.

[49] N. Furuta, Y. Ohasi, H. Itinose, Y. Igarashi, Kinetics of vapor-grown tellurium whiskers, Jpn. J. Appl. Phys., 14 (1975) 929.

[50] J.U. Seo, G.K. Seong, C.M. Park, Te/C nanocomposites for Li-Te Secondary Batteries, Sci. Rep., 5 (2015) 7969.

[51] J. Xu, J. Ma, Q. Fan, S. Guo, S. Dou, Recent Progress in the Design of Advanced Cathode Materials and Battery Models for High-Performance Lithium-X (X = O_2, S, Se, Te, I_2, Br_2) Batteries, Adv. Mater., 29 (2017).

[52] Z. Chen, Y. Zhao, F. Mo, Z. Huang, X. Li, D. Wang, et al., Metal-Tellurium Batteries: A Rising Energy Storage System, Small Struct., 2000005.

[53] J. He, W. Lv, Y. Chen, K. Wen, C. Xu, W. Zhang, et al., Tellurium-Impregnated Porous Cobalt-Doped Carbon Polyhedra as Superior Cathodes for Lithium-Tellurium Batteries, ACS Nano, 11 (2017) 8144-8152.

[54] Z. Gao, H. Sun, L. Fu, F. Ye, Y. Zhang, W. Luo, et al., Promises, Challenges, and Recent Progress of Inorganic Solid-State Electrolytes for All-Solid-State Lithium Batteries, Adv. Mater., 30 (2018) e1705702.

[55] A. Manthiram, X. Yu, S. Wang, Lithium battery chemistries enabled by solid-state electrolytes, Nat. Rev. Mater., 2 (2017).

[56] C. Sun, J. Liu, Y. Gong, D.P. Wilkinson, J. Zhang, Recent advances in all-solid-state rechargeable lithium batteries, Nano Energy, 33 (2017) 363-386.

[57] F. Zheng, M. Kotobuki, S. Song, M.O. Lai, L. Lu, Review on solid electrolytes for all-solid-state lithium-ion batteries, J. Power Sources, 389 (2018) 198-213.

[58] D. Larcher, J.M. Tarascon, Towards greener and more sustainable batteries for electrical energy storage, Nat. Chem., 7 (2015) 19-29.

[59] Y. Li, Y. Lu, C. Zhao, Y.-S. Hu, M.-M. Titirici, H. Li, et al., Recent advances of electrode materials for low-cost sodium-ion batteries towards practical application for grid energy storage, Energy Storage Mater., 7 (2017) 130-151.

[60] H. Kim, J.C. Kim, M. Bianchini, D.-H. Seo, J. Rodriguez-Garcia, G. Ceder, Recent Progress and Perspective in Electrode Materials for K-Ion Batteries, Adv. Energy Mater., 8 (2018) 1702384.

[61] A. Eftekhari, Z. Jian, X. Ji, Potassium secondary batteries, ACS Appl. Mater. Interfaces, 9 (2017) 4404-4419.

[62] C. Vaalma, G.A. Giffin, D. Buchholz, S. Passerini, Non-Aqueous K-Ion Battery Based on Layered K0.3MnO2and Hard Carbon/Carbon Black, J. Electrochem. Soc., 163 (2016) A1295-A1299.

[63] K. Lei, C. Wang, L. Liu, Y. Luo, C. Mu, F. Li, et al., A porous network of bismuth used as the anode material for high-energy-density potassium-ion batteries, Angew. Chem., 130 (2018) 4777-4781.

[64] Z. Jian, W. Luo, X. Ji, Carbon electrodes for K-ion batteries, J. Am. Chem. Soc., 137 (2015) 11566-11569.

[65] M. Okoshi, Y. Yamada, S. Komaba, A. Yamada, H. Nakai, Theoretical Analysis of Interactions between Potassium Ions and Organic Electrolyte Solvents: A Comparison with Lithium, Sodium, and Magnesium Ions, J. Electrochem. Soc., 164 (2016) A54-A60.

[66] I. Sultana, M.M. Rahman, Y. Chen, A.M. Glushenkov, Potassium-Ion Battery Anode Materials Operating through the Alloying-Dealloying Reaction Mechanism, Adv. Funct. Mater., 28 (2018) 1703857.

[67] X. Wu, D.P. Leonard, X. Ji, Emerging Non-Aqueous Potassium-Ion Batteries: Challenges and Opportunities, Chem. Mater., 29 (2017) 5031-5042.

[68] D. Munoz-Torrero, J. Palma, R. Marcilla, E. Ventosa, A critical perspective on rechargeable Al-ion battery technology, Dalton transactions, 48 (2019) 9906-9911.

[69] T. Koketsu, B. Paul, C. Wu, R. Kraehnert, Y. Huang, P. Strasser, A lithium–tellurium rechargeable battery with exceptional cycling stability, J. Appl. Electrochem., 46 (2016) 627-633.

[70] J. Zhang, Y.-X. Yin, Y. You, Y. Yan, Y.-G. Guo, A High-Capacity Tellurium@Carbon Anode Material for Lithium-Ion Batteries, Energy Technol., 2 (2014) 757-762.

[71] N. Ding, S.-F. Chen, D.-S. Geng, S.-W. Chien, T. An, T.S.A. Hor, et al., Tellurium@Ordered Macroporous Carbon Composite and Free-Standing Tellurium Nanowire Mat as Cathode Materials for Rechargeable Lithium-Tellurium Batteries, Adv. Energy Mater., 5 (2015) 1401999.

[72] Y. Li, L. Hu, B. Shen, C. Dai, Q. Xu, D. Liu, et al., Rib-like hierarchical porous carbon as reservoir for long-life and high-rate Li-Te batteries, Electrochim. Acta, 250 (2017) 10-15.

[73] Y. Li, M.-Q. Wang, Y. Chen, L. Hu, T. Liu, S. Bao, et al., Muscle-like electrode design for Li-Te batteries, Energy Storage Mater., 10 (2018) 10-15.

[74] X. Ji, K.T. Lee, L.F. Nazar, A highly ordered nanostructured carbon–sulphur cathode for lithium–sulphur batteries, Nat. Mater., 8 (2009) 500-506.

[75] Y. Li, Y. Zhang, Q. Xu, L. Hu, B. Shen, H. Liu, et al., Nitrogen-Doped Carbon as a Host for Tellurium for High-Rate Li–Te and Na–Te Batteries, ChemSusChem, 12 (2019) 1196-1202.

[76] J. Liu, J. Liang, C. Wang, J. Ma, Electrospun CoSe@ N-doped carbon nanofibers with highly capacitive Li storage, J. Energy Chem., 33 (2019) 160-166.

[77] J. Xu, S. Xin, J.-W. Liu, J.-L. Wang, Y. Lei, S.-H. Yu, Elastic Carbon Nanotube Aerogel Meets Tellurium Nanowires: A Binder- and Collector-Free Electrode for Li-Te Batteries, Adv. Funct. Mater., 26 (2016) 3580-3588.

[78] D. Huang, S. Li, X. Xiao, M. Cao, L. Gao, Y.-G. Xiang, et al., Ultrafast synthesis of Te nanorods as cathode materials for lithium-tellurium batteries, J. Power Sources, 371 (2017) 48-54.

[79] H. Yin, X.-X. Yu, Y.-W. Yu, M.-L. Cao, H. Zhao, C. Li, et al., Tellurium nanotubes grown on carbon fiber cloth as cathode for flexible all-solid-state lithium-tellurium batteries, Electrochim. Acta, 282 (2018) 870-876.

[80] K. Xu, X. Liu, J. Liang, J. Cai, K. Zhang, Y. Lu, et al., Manipulating the Redox Kinetics of Li–S Chemistry by Tellurium Doping for Improved Li–S Batteries, ACS Energy Lett., 3 (2018) 420-427.

[81] S. Lee, H. Choi, K. Eom, Enhancing the electrochemical performances of a tellurium-based cathode for a high-volumetric capacity Li battery via a high-energy ball mill with sulfur edge-functionalized carbon, J. Power Sources, 430 (2019) 112-119.

[82] S. Li, J. Ma, Z. Zeng, W. Hu, W. Zhang, S. Cheng, et al., Enhancing the kinetics of lithium–sulfur batteries under solid-state conversion by using tellurium as a eutectic accelerator, J. Mater. Chem. A, 8 (2020) 3405-3412.

[83] F. Sun, B. Zhang, H. Tang, Z. Yue, X. Li, C. Yin, et al., Heteroatomic Te_xS_{1-x} molecule/C nanocomposites as stable cathode materials in carbonate-based electrolytes for lithium–chalcogen batteries, J. Mater. Chem. A, 6 (2018) 10104-10110.

[84] J. Li, Y. Yuan, H. Jin, H. Lu, A. Liu, D. Yin, et al., One-step nonlinear electrochemical synthesis of Te_xS_y@PANI nanorod materials for Li-Te_xS_y battery, Energy Storage Mater., 16 (2019) 31-36.

[85] S. Li, Z. Han, W. Hu, L. Peng, J. Yang, L. Wang, et al., Manipulating kinetics of sulfurized polyacrylonitrile with tellurium as eutectic accelerator to prevent polysulfide dissolution in lithium-sulfur battery under dissolution-deposition mechanism, Nano Energy, 60 (2019) 153-161.

[86] Y.X. Yin, S. Xin, Y.G. Guo, L.J. Wan, Lithium-sulfur batteries: electrochemistry, materials, and prospects, Angew. Chem. Int. Ed. Engl., 52 (2013) 13186-13200.

[87] M. Wild, L. O'Neill, T. Zhang, R. Purkayastha, G. Minton, M. Marinescu, et al., Lithium sulfur batteries, a mechanistic review, Energy Environ. Sci., 8 (2015) 3477-3494.

[88] S. Li, W. Zhang, Z. Zeng, S. Cheng, J. Xie, Selenium or Tellurium as Eutectic Accelerators for High-Performance Lithium/Sodium–Sulfur Batteries, Electrochem. Energy Rev., (2020).

[89] R.S. Laitinen, P. Pekonen, R.J. Suontamo, Homo-and heteroatomic chalcogen rings, Coord. Chem. Rev., 130 (1994) 1-62.

[90] J. Taavitsainen, R.S. Laitinen, Tellurium-containing chalcogen rings, Main Group Chem., 3 (1999) 59-67.

[91] X. Wang, Y. Qian, L. Wang, H. Yang, H. Li, Y. Zhao, et al., Sulfurized Polyacrylonitrile Cathodes with High Compatibility in Both Ether and Carbonate Electrolytes for Ultrastable Lithium–Sulfur Batteries, Adv. Funct. Mater., 29 (2019) 1902929.

[92] S. Zhang, K. Ueno, K. Dokko, M. Watanabe, Recent Advances in Electrolytes for Lithium-Sulfur Batteries, Adv. Energy Mater., 5 (2015) 1500117.

[93] S. Wei, L. Ma, K.E. Hendrickson, Z. Tu, L.A. Archer, Metal-Sulfur Battery Cathodes Based on PAN-Sulfur Composites, J. Am. Chem. Soc., 137 (2015) 12143-12152.

[94] T. Li, X. Bai, U. Gulzar, Y.J. Bai, C. Capiglia, W. Deng, et al., A Comprehensive Understanding of Lithium–Sulfur Battery Technology, Adv. Funct. Mater., 29 (2019) 1901730.

[95] S. Zhang, Understanding of Sulfurized Polyacrylonitrile for Superior Performance Lithium/Sulfur Battery, Energies, 7 (2014) 4588-4600.

[96] S. Li, Z. Zeng, J. Yang, Z. Han, W. Hu, L. Wang, et al., High Performance Room Temperature Sodium–Sulfur Battery by Eutectic Acceleration in Tellurium-Doped Sulfurized Polyacrylonitrile, ACS Appl. Energy Mater., 2 (2019) 2956-2964.

[97] Y. Jung, S. Kim, B.-S. Kim, D.-H. Han, S.-M. Park, J. Kwak, Effect of organic solvents and electrode materials on electrochemical reduction of sulfur, Int. J. Electrochem. Sci, 3 (2008) 566-577.

[98] D. Lei, K. Shi, H. Ye, Z. Wan, Y. Wang, L. Shen, et al., Progress and Perspective of Solid-State Lithium-Sulfur Batteries, Adv. Funct. Mater., 28 (2018) 1707570.

[99] Y. Liu, P. He, H. Zhou, Rechargeable Solid-State Li-Air and Li-S Batteries: Materials, Construction, and Challenges, Adv. Energy Mater., 8 (2018) 1701602.

[100] X. Yang, J. Luo, X. Sun, Towards high-performance solid-state Li-S batteries: from fundamental understanding to engineering design, Chem. Soc. Rev., 49 (2020) 2140-2195.

[101] V. Palomares, P. Serras, I. Villaluenga, K.B. Hueso, J. Carretero-González, T. Rojo, Na-ion batteries, recent advances and present challenges to become low cost energy storage systems, Energy Environ. Sci., 5 (2012) 5884.

[102] D. Aurbach, Y. Gofer, Z. Lu, A. Schechter, O. Chusid, H. Gizbar, et al., A short review on the comparison between Li battery systems and rechargeable magnesium battery technology, J. Power Sources, 97 (2001) 28-32.

[103] M. Song, H. Tan, D. Chao, H.J. Fan, Recent Advances in Zn-Ion Batteries, Adv. Funct. Mater., 28 (2018) 1802564.

[104] S. Dong, D. Yu, J. Yang, L. Jiang, J. Wang, L. Cheng, et al., Tellurium: A High-Volumetric-Capacity Potassium-Ion Battery Electrode Material, Adv. Mater., (2020) e1908027.

[105] Q. Liu, W. Deng, C.-F. Sun, A potassium–tellurium battery, Energy Storage Mater., 28 (2020) 10-16.

[106] S. Chen, C. Niu, H. Lee, Q. Li, L. Yu, W. Xu, et al., Critical Parameters for Evaluating Coin Cells and Pouch Cells of Rechargeable Li-Metal Batteries, Joule, 3 (2019) 1094-1105.

[107] C. Niu, H. Lee, S. Chen, Q. Li, J. Du, W. Xu, et al., High-energy lithium metal pouch cells with limited anode swelling and long stable cycles, Nat. Energy, 4 (2019) 551-559.

[108] C.P. Yang, Y.X. Yin, Y.G. Guo, Elemental Selenium for Electrochemical Energy Storage, J. Phys. Chem., 6 (2015) 256-266.

[109] N.T. Nassar, T.E. Graedel, E. Harper, By-product metals are technologically essential but have problematic supply, Sci. Adv., 1 (2015) e1400180.

[110] Y. Zhu, C. Wang, Galvanostatic intermittent titration technique for phase-transformation electrodes, J. Phys. Chem. C, 114 (2010) 2830-2841.

[111] P. Hohenberg, W. Kohn, Inhomogeneous electron gas, Phys. Rev., 136 (1964) B864.

[112] W. Kohn, L.J. Sham, Self-consistent equations including exchange and correlation effects, Phys. Rev., 140 (1965) A1133.

[113] D.C. Langreth, J.P. Perdew, Theory of nonuniform electronic systems. I. Analysis of the gradient approximation and a generalization that works, Phys. Rev. B, 21 (1980) 5469.

[114] J.P. Perdew, Density-functional approximation for the correlation energy of the inhomogeneous electron gas, Phys. Rev. B, 33 (1986) 8822.

[115] J.P. Perdew, J. Chevary, S. Vosko, K.A. Jackson, M.R. Pederson, D. Singh, et al., Erratum: Atoms, molecules, solids, and surfaces: Applications of the generalized gradient approximation for exchange and correlation, Phys. Rev. B, 48 (1993) 4978.

[116] P. Giannozzi, S. Baroni, N. Bonini, M. Calandra, R. Car, C. Cavazzoni, et al., QUANTUM ESPRESSO: a modular and open-source software project for quantum simulations of materials, J. Phys.: Condens. Matter, 21 (2009) 395502.

[117] P. Giannozzi, O. Andreussi, T. Brumme, O. Bunau, M.B. Nardelli, M. Calandra, et al., Advanced capabilities for materials modelling with Quantum ESPRESSO, J. Phys.: Condens. Matter, 29 (2017) 465901.

[118] T. Chivers, R.S. Laitinen, Tellurium: a maverick among the chalcogens, Chem. Soc. Rev., 44 (2015) 1725-1739.

[119] X. Wu, H. Zhang, Z.-B. Zhai, J. Xu, K.-J. Huang, Tellurium-impregnated P-doped porous carbon nanosheets as both cathode and anode for an ultrastable hybrid aqueous energy storage, J. Mater. Chem. A, 8 (2020) 17185-17192.

[120] P. Schneider, Adsorption isotherms of microporous-mesoporous solids revisited, Applied Catalysis A: General, 129 (1995) 157-165.

[121] M. Al Bahri, L. Calvo, M.A. Gilarranz, J.J. Rodriguez, Activated carbon from grape seeds upon chemical activation with phosphoric acid: Application to the adsorption of diuron from water, Chem. Eng. J., 203 (2012) 348-356.

[122] X. Ji, K.T. Lee, L.F. Nazar, A highly ordered nanostructured carbon-sulphur cathode for lithium-sulphur batteries, Nat. Mater., 8 (2009) 500-506.

[123] J.T. Lee, Y. Zhao, H. Kim, W.I. Cho, G. Yushin, Sulfur infiltrated activated carbon cathodes for lithium sulfur cells: The combined effects of pore size distribution and electrolyte molarity, J. Power Sources, 248 (2014) 752-761.

[124] X. Zhuang, Y. Liu, J. Chen, H. Chen, B. Yi, Sulfur/carbon composites prepared with ordered porous carbon for Li-S battery cathode, J. Energy Chem., 23 (2014) 391-396.

[125] C. Liang, N.J. Dudney, J.Y. Howe, Hierarchically Structured Sulfur/Carbon Nanocomposite Material for High-Energy Lithium Battery, Chem. Mater., 21 (2009) 4724-4730.

[126] P. Wu, L.-H. Chen, S.-S. Xiao, S. Yu, Z. Wang, Y. Li, et al., Insight into the positive effect of porous hierarchy in S/C cathodes on the electrochemical performance of Li–S batteries, Nanoscale, 10 (2018) 11861-11868.

[127] Y. Qu, Z. Zhang, X. Zhang, G. Ren, Y. Lai, Y. Liu, et al., Highly ordered nitrogen-rich mesoporous carbon derived from biomass waste for high-performance lithium–sulfur batteries, Carbon, 84 (2015) 399-408.

[128] H. Li, D. Yuan, C. Tang, S. Wang, J. Sun, Z. Li, et al., Lignin-derived interconnected hierarchical porous carbon monolith with large areal/volumetric capacitances for supercapacitor, Carbon, 100 (2016) 151-157.

[129] W.E. Tenhaeff, O. Rios, K. More, M.A. McGuire, Highly Robust Lithium Ion Battery Anodes from Lignin: An Abundant, Renewable, and Low-Cost Material, Adv. Funct. Mater., 24 (2014) 86-94.

[130] H. Zhang, F. Yu, W. Kang, Q. Shen, Encapsulating selenium into macro-/micro-porous biochar-based framework for high-performance lithium-selenium batteries, Carbon, 95 (2015) 354-363.

[131] I. Okman, S. Karagöz, T. Tay, M. Erdem, Activated Carbons From Grape Seeds By Chemical Activation With Potassium Carbonate And Potassium Hydroxide, Appl. Surf. Sci., 293 (2014) 138-142.

[132] K.C. Kemp, S.B. Baek, W.G. Lee, M. Meyyappan, K.S. Kim, Activated carbon derived from waste coffee grounds for stable methane storage, Nanotechnol., 26 (2015) 385602.

[133] J.K. Kim, Y.C. Kang, Encapsulation of Se into Hierarchically Porous Carbon Microspheres with Optimized Pore Structure for Advanced Na-Se and K-Se Batteries, ACS Nano, 14 (2020) 13203-13216.

[134] Z. Lei, Y. Lei, X. Liang, L. Yang, J. Feng, High stable rate cycling performances of microporous carbon spheres/selenium composite (MPCS/Se) cathode as lithium–selenium battery, J. Power Sources, 473 (2020) 228611.

[135] L. Fan, S. Wei, S. Li, Q. Li, Y. Lu, Recent Progress of the Solid-State Electrolytes for High-Energy Metal-Based Batteries, Adv. Energy Mater., 8 (2018) 1702657.

[136] E. Umeshbabu, B. Zheng, Y. Yang, Recent Progress in All-Solid-State Lithium−Sulfur Batteries Using High Li-Ion Conductive Solid Electrolytes, Electrochem. Energy Rev., 2 (2019) 199-230.

[137] J. Yue, M. Yan, Y.-X. Yin, Y.-G. Guo, Progress of the Interface Design in All-Solid-State Li-S Batteries, Adv. Funct. Mater., 28 (2018) 1707533.

[138] J.P.T. Guisao, A.J.F. Romero, Interaction between Zn^{2+} cations and n-methyl-2-pyrrolidone in ionic liquid-based Gel Polymer Electrolytes for Zn batteries, Electrochim. Acta, 176 (2015) 1447-1453.

[139] X. Zhang, T. Liu, S. Zhang, X. Huang, B. Xu, Y. Lin, et al., Synergistic coupling between $Li_{6.75}La_3Zr_{1.75}Ta_{0.25}O_{12}$ and poly (vinylidene fluoride) induces high ionic conductivity, mechanical

strength, and thermal stability of solid composite electrolytes, J. Am. Chem. Soc., 139 (2017) 13779-13785.

[140] X. Shen, X. Cheng, P. Shi, J. Huang, X. Zhang, C. Yan, et al., Lithium–matrix composite anode protected by a solid electrolyte layer for stable lithium metal batteries, J. Energy Chem., 37 (2019) 29-34.

[141] H. Wang, K. Xie, L. Wang, Y. Han, N-methyl-2-pyrrolidone as a solvent for the non-aqueous electrolyte of rechargeable Li-air batteries, J. Power Sources, 219 (2012) 263-271.

[142] H. Jia, H. Onishi, N. von Aspern, U. Rodehorst, K. Rudolf, B. Billmann, et al., A propylene carbonate based gel polymer electrolyte for extended cycle life and improved safety performance of lithium ion batteries, J. Power Sources, 397 (2018) 343-351.

[143] J. Jie, Y. Liu, L. Cong, B. Zhang, W. Lu, X. Zhang, et al., High-performance PVDF-HFP based gel polymer electrolyte with a safe solvent in Li metal polymer battery, J. Energy Chem., 49 (2020) 80-88.

[144] Y. Feng, W. Li, Y. Hou, Y. Yu, W. Cao, T. Zhang, et al., Enhanced dielectric properties of PVDF-HFP/BaTiO3-nanowire composites induced by interfacial polarization and wire-shape, J. Mater. Chem. C, 3 (2015) 1250-1260.

[145] S. Ferrari, E. Quartarone, P. Mustarelli, A. Magistris, M. Fagnoni, S. Protti, et al., Lithium ion conducting PVdF-HFP composite gel electrolytes based on N-methoxyethyl-N-methylpyrrolidinium bis(trifluoromethanesulfonyl)-imide ionic liquid, J. Power Sources, 195 (2010) 559-566.

[146] M.R. Busche, T. Drossel, T. Leichtweiss, D.A. Weber, M. Falk, M. Schneider, et al., Dynamic formation of a solid-liquid electrolyte interphase and its consequences for hybrid-battery concepts, Nat. Chem., 8 (2016) 426-434.

[147] J. Qian, B. Jin, Y. Li, X. Zhan, Y. Hou, Q. Zhang, Research progress on gel polymer electrolytes for lithium-sulfur batteries, J. Energy Chem., 56 (2021) 420-437.

[148] P.-L. Kuo, C.-H. Tsao, C.-H. Hsu, S.-T. Chen, H.-M. Hsu, A new strategy for preparing oligomeric ionic liquid gel polymer electrolytes for high-performance and nonflammable lithium ion batteries, J. Membr. Sci., 499 (2016) 462-469.

[149] X. Zhan, J. Zhang, M. Liu, J. Lu, Q. Zhang, F. Chen, Advanced Polymer Electrolyte with Enhanced Electrochemical Performance for Lithium-Ion Batteries: Effect of Nitrile-Functionalized Ionic Liquid, ACS Appl. Energy Mater., 2 (2019) 1685-1694.

[150] L. Chen, Y. Li, S.-P. Li, L.-Z. Fan, C.-W. Nan, J.B. Goodenough, PEO/garnet composite electrolytes for solid-state lithium batteries: From “ceramic-in-polymer” to “polymer-in-ceramic”, Nano Energy, 46 (2018) 176-184.

[151] X. Judez, M. Martinez-Ibañez, A. Santiago, M. Armand, H. Zhang, C. Li, Quasi-solid-state electrolytes for lithium sulfur batteries: Advances and perspectives, J. Power Sources, 438 (2019) 226985.

[152] N. Wang, Y. NuLi, S. Su, J. Yang, J. Wang, Effects of binders on the electrochemical performance of rechargeable magnesium batteries, J. Power Sources, 341 (2017) 219-229.

[153] J. He, H. Zhong, J. Wang, L. Zhang, Investigation on xanthan gum as novel water soluble binder for LiFePO 4 cathode in lithium-ion batteries, J. Alloys Compd., 714 (2017) 409-418.

[154] J. Hu, Y. Wang, D. Li, Y.-T. Cheng, Effects of adhesion and cohesion on the electrochemical performance and durability of silicon composite electrodes, J. Power Sources, 397 (2018) 223-230.

[155] W. Bao, Z. Zhang, Y. Gan, X. Wang, J. Lia, Enhanced cyclability of sulfur cathodes in lithium-sulfur batteries with Na-alginate as a binder, J. Energy Chem., 22 (2013) 790-794.

[156] G. Li, M. Ling, Y. Ye, Z. Li, J. Guo, Y. Yao, et al., Acacia Senegal-Inspired Bifunctional Binder for Longevity of Lithium-Sulfur Batteries, Adv. Energy Mater., 5 (2015) 1500878.

[157] Q. Qi, X. Lv, W. Lv, Q.-H. Yang, Multifunctional binder designs for lithium-sulfur batteries, J. Energy Chem., 39 (2019) 88-100.

[158] S.-Y. Li, W.-P. Wang, H. Duan, Y.-G. Guo, Recent progress on confinement of polysulfides through physical and chemical methods, J. Energy Chem., 27 (2018) 1555-1565.

[159] Z.-Q. Jin, Y.-G. Liu, W.-K. Wang, A.-B. Wang, B.-W. Hu, M. Shen, et al., A new insight into the lithium storage mechanism of sulfurized polyacrylonitrile with no soluble intermediates, Energy Storage Mater., 14 (2018) 272-278.

[160] Q. Pang, D. Kundu, M. Cuisinier, L.F. Nazar, Surface-enhanced redox chemistry of polysulphides on a metallic and polar host for lithium-sulphur batteries, Nat. Commun., 5 (2014) 4759.

[161] Z. Yuan, H.J. Peng, T.Z. Hou, J.Q. Huang, C.M. Chen, D.W. Wang, et al., Powering Lithium-Sulfur Battery Performance by Propelling Polysulfide Redox at Sulfiphilic Hosts, Nano Lett., 16 (2016) 519-527.

[162] T. Chen, L. Ma, B. Cheng, R. Chen, Y. Hu, G. Zhu, et al., Metallic and polar Co_9S_8 inlaid carbon hollow nanopolyhedra as efficient polysulfide mediator for lithium−sulfur batteries, Nano Energy, 38 (2017) 239-248.

[163] A. Abouimrane, D. Dambournet, K.W. Chapman, P.J. Chupas, W. Weng, K. Amine, A new class of lithium and sodium rechargeable batteries based on selenium and selenium-sulfur as a positive electrode, J. Am. Chem. Soc., 134 (2012) 4505-4508.

[164] Z. Li, J. Zhang, H.B. Wu, X.W.D. Lou, An Improved Li-SeS_2 Battery with High Energy Density and Long Cycle Life, Adv. Energy Mater., 7 (2017) 1700281.

[165] B. He, D. Liu, Z. Cheng, Z. Miao, Z. Rao, H. Zhang, et al., Enabling Selenium-Rich Se_xS_y

Cathodes to Work in Carbonate-Based Electrolytes, Adv. Energy Mater., 12 (2021) 2102832.

[166] K. Xu, Nonaqueous liquid electrolytes for lithium-based rechargeable batteries, Chem. Rev., 104 (2004) 4303-4418.

[167] X. Li, M. Banis, A. Lushington, X. Yang, Q. Sun, Y. Zhao, et al., A high-energy sulfur cathode in carbonate electrolyte by eliminating polysulfides via solid-phase lithium-sulfur transformation, Nat. Commun., 9 (2018) 4509.

[168] A. Rafie, J.W. Kim, K.K. Sarode, V. Kalra, A review on the use of carbonate-based electrolytes in Li-S batteries: A comprehensive approach enabling solid-solid direct conversion reaction, Energy Storage Mater., 50 (2022) 197-224.

[169] M. He, X. Li, X. Yang, C. Wang, M.L. Zheng, R. Li, et al., Realizing Solid-Phase Reaction in Li–S Batteries via Localized High-Concentration Carbonate Electrolyte, Adv. Energy Mater., 11 (2021) 2101004.

[170] E.P. Roth, C.J. Orendorff, How electrolytes influence battery safety, Electrochem. Soc. Interface, 21 (2012) 45.

[171] D.H. Doughty, E.P. Roth, C.C. Crafts, G. Nagasubramanian, G. Henriksen, K. Amine, Effects of additives on thermal stability of Li ion cells, J. Power Sources, 146 (2005) 116-120.

[172] D. Aurbach, Y. Talyosef, B. Markovsky, E. Markevich, E. Zinigrad, L. Asraf, et al., Design of electrolyte solutions for Li and Li-ion batteries: a review, Electrochim. Acta, 50 (2004) 247-254.

[173] B. He, Z. Rao, Z. Cheng, D. Liu, D. He, J. Chen, et al., Rationally Design a Sulfur Cathode with Solid-Phase Conversion Mechanism for High Cycle-Stable Li–S Batteries, Adv. Energy Mater., 11 (2021) 2003690.

[174] C. Jones, M. Mauguin, A 125Te and 129I Mössbauer study of tellurium–selenium and tellurium–sulfur phases, J. Chem. Phys., 67 (1977) 1587-1593.

[175] V.N. Volodin, S.A. Trebukhov, B.K. Kenzhaliyev, A.V. Nitsenko, N.M. Burabaeva, Melt–Vapor Phase Diagram of the Te–S System, Russ. J. Phys. Chem. , 92 (2018) 407-410.

[176] A.M. Abioye, F.N. Ani, Recent development in the production of activated carbon electrodes from agricultural waste biomass for supercapacitors: A review, Renew. Sust. Energ. Rev., 52 (2015) 1282-1293.

[177] A. Barroso Bogeat, Understanding and Tuning the Electrical Conductivity of Activated Carbon: A State-of-the-Art Review, Crit. Rev. Solid State Mater. Sci., 46 (2019) 1-37.

[178] J.-H. Song, J.-T. Yeon, J.-Y. Jang, J.-G. Han, S.-M. Lee, N.-S. Choi, Effect of Fluoroethylene Carbonate on Electrochemical Performances of Lithium Electrodes and Lithium-Sulfur Batteries, J. Electrochem. Soc., 160 (2013) A873-A881.

[179] W.J. Chen, B.Q. Li, C.X. Zhao, M. Zhao, T.Q. Yuan, R.C. Sun, et al., Electrolyte regulation towards stable lithium-metal anodes in lithium–sulfur batteries with sulfurized polyacrylonitrile cathodes, Angew. Chem. Int. Ed., 59 (2020) 10732-10745.

[180] J. Zhou, Y. Guo, C. Liang, J. Yang, J. Wang, Y. Nuli, Confining small sulfur molecules in peanut shell-derived microporous graphitic carbon for advanced lithium sulfur battery, Electrochim. Acta, 273 (2018) 127-135.

[181] F. Huang, L. Gao, Y. Zou, G. Ma, J. Zhang, S. Xu, et al., Akin solid–solid biphasic conversion of a Li–S battery achieved by coordinated carbonate electrolytes, J. Mater. Chem. A, 7 (2019) 12498-12506.

[182] X. Liang, C. Hart, Q. Pang, A. Garsuch, T. Weiss, L.F. Nazar, A highly efficient polysulfide mediator for lithium-sulfur batteries, Nat. Commun., 6 (2015) 5682.

[183] M.I. Nandasiri, L.E. Camacho-Forero, A.M. Schwarz, V. Shutthanandan, S. Thevuthasan, P.B. Balbuena, et al., In Situ Chemical Imaging of Solid-Electrolyte Interphase Layer Evolution in Li–S Batteries, Chem. Mater., 29 (2017) 4728-4737.

[184] J.H. Ahn, G.K. Veerasubramani, S.-M. Lee, T.-S. You, D.-W. Kim, Improvement of Li-Sulfur Cell Cycling Performance by Use of Fe1-xS@NC as a Functional Additive for Chemical Confinement of Lithium Polysulfides, J. Electrochem. Soc., 166 (2018) A5201-A5209.

[185] Y.-X. Song, Y. Shi, J. Wan, S.-Y. Lang, X.-C. Hu, H.-J. Yan, et al., Direct tracking of the polysulfide shuttling and interfacial evolution in all-solid-state lithium–sulfur batteries: a degradation mechanism study, Energy Environ. Sci., 12 (2019) 2496-2506.

[186] G. Wan, F. Guo, H. Li, Y. Cao, X. Ai, J. Qian, et al., Suppression of Dendritic Lithium Growth by in Situ Formation of a Chemically Stable and Mechanically Strong Solid Electrolyte Interphase, ACS Appl. Mater. Interfaces, 10 (2018) 593-601.

[187] S. Nanda, A. Bhargav, A. Manthiram, Anode-free, Lean-Electrolyte Lithium-Sulfur Batteries Enabled by Tellurium-Stabilized Lithium Deposition, Joule, 4 (2020) 1121-1135.

[188] X. Zhao, Y. Lu, Z. Qian, R. Wang, Z. Guo, Potassium-sulfur batteries: Status and perspectives, EcoMat, 2 (2020).

[189] X.L. Huang, Z. Guo, S.X. Dou, Z.M. Wang, Rechargeable Potassium–Selenium Batteries, Adv. Funct. Mater., 31 (2021) 2102326.

[190] Q. Zhang, J. Mao, W.K. Pang, T. Zheng, V. Sencadas, Y. Chen, et al., Boosting the Potassium Storage Performance of Alloy-Based Anode Materials via Electrolyte Salt Chemistry, Adv. Energy Mater., 8 (2018) 1703288.

[191] W. Zhang, Z. Wu, J. Zhang, G. Liu, N.-H. Yang, R.-S. Liu, et al., Unraveling the effect of salt chemistry on long-durability high-phosphorus-concentration anode for potassium ion batteries, Nano Energy, 53 (2018) 967-974.

[192] L. Deng, Y. Zhang, R. Wang, M. Feng, X. Niu, L. Tan, et al., Influence of KPF6 and KFSI on the Performance of Anode Materials for Potassium-Ion Batteries: A Case Study of MoS2, ACS Appl. Mater. Interfaces, 11 (2019) 22449-22456.

[193] L. Madec, V. Gabaudan, G. Gachot, L. Stievano, L. Monconduit, H. Martinez, Paving the Way for K-Ion Batteries: Role of Electrolyte Reactivity through the Example of Sb-Based Electrodes, ACS Appl. Mater. Interfaces, 10 (2018) 34116-34122.

[194] H. Wang, D. Yu, X. Wang, Z. Niu, M. Chen, L. Cheng, et al., Electrolyte Chemistry Enables Simultaneous Stabilization of Potassium Metal and Alloying Anode for Potassium-Ion Batteries, Angew. Chem. Int. Ed. Engl., 58 (2019) 16451-16455.

[195] S. Liu, J. Mao, L. Zhang, W.K. Pang, A. Du, Z. Guo, Manipulating the Solvation Structure of Nonflammable Electrolyte and Interface to Enable Unprecedented Stability of Graphite Anodes beyond 2 Years for Safe Potassium-Ion Batteries, Adv. Mater., 33 (2021) e2006313.

[196] I. Sultana, T. Ramireddy, M.M. Rahman, Y. Chen, A.M. Glushenkov, Tin-based composite anodes for potassium-ion batteries, Chem. Commun. (Camb), 52 (2016) 9279-9282.

[197] N. Xiao, W.D. McCulloch, Y. Wu, Reversible Dendrite-Free Potassium Plating and Stripping Electrochemistry for Potassium Secondary Batteries, J. Am. Chem. Soc., 139 (2017) 9475-9478.

[198] L. Fan, S. Chen, R. Ma, J. Wang, L. Wang, Q. Zhang, et al., Ultrastable Potassium Storage Performance Realized by Highly Effective Solid Electrolyte Interphase Layer, Small, 14 (2018) e1801806.

[199] V. Gabaudan, R. Berthelot, L. Stievano, L. Monconduit, Inside the Alloy Mechanism of Sb and Bi Electrodes for K-Ion Batteries, J. Phys. Chem. C, 122 (2018) 18266-18273.

[200] W. Zhang, W.K. Pang, V. Sencadas, Z. Guo, Understanding High-Energy-Density Sn4P3 Anodes for Potassium-Ion Batteries, Joule, 2 (2018) 1534-1547.

[201] Z. Wang, K. Dong, D. Wang, S. Luo, Y. Liu, Q. Wang, et al., A nanosized SnSb alloy confined in N-doped 3D porous carbon coupled with ether-based electrolytes toward high-performance potassium-ion batteries, J. Mater. Chem. A, 7 (2019) 14309-14318.

[202] X. Yu, A. Manthiram, A reversible nonaqueous room-temperature potassium-sulfur chemistry for electrochemical energy storage, Energy Storage Mater., 15 (2018) 368-373.

[203] X. Huang, Q. Xu, W. Gao, T. Yang, R. Zhan, J. Deng, et al., Rechargeable K-Se batteries based on metal-organic-frameworks-derived porous carbon matrix confined selenium as cathode materials, J. Colloid Interface Sci., 539 (2019) 326-331.

[204] C. Lin, L. Ouyang, C. Zhou, R. Hu, L. Yang, X. Yang, et al., A novel selenium-phosphorous amorphous composite by plasma assisted ball milling for high-performance rechargeable potassium-ion battery anode, J. Power Sources, 443 (2019) 227276.

[205] S. Ma, P. Zuo, H. Zhang, Z. Yu, C. Cui, M. He, et al., Iodine-doped sulfurized polyacrylonitrile with enhanced electrochemical performance for room-temperature sodium/potassium sulfur batteries, Chem. Commun. (Camb), 55 (2019) 5267-5270.

[206] J. Zhou, D. Shen, X. Yu, B. Lu, Building ultra-stable K–Te battery by molecular regulation, J. Energy Chem., 69 (2022) 100-107.

[207] X. Ge, H. Di, P. Wang, X. Miao, P. Zhang, H. Wang, et al., Metal-Organic Framework-Derived Nitrogen-Doped Cobalt Nanocluster Inlaid Porous Carbon as High-Efficiency Catalyst for Advanced Potassium-Sulfur Batteries, ACS Nano, 14 (2020) 16022-16035.

[208] R. Xu, Y. Yao, H. Wang, Y. Yuan, J. Wang, H. Yang, et al., Unraveling the Nature of Excellent Potassium Storage in Small-Molecule Se@Peapod-Like N-Doped Carbon Nanofibers, Adv. Mater., 32 (2020) e2003879.

[209] X. Yuan, B. Zhu, J. Feng, C. Wang, X. Cai, K. Qiao, et al., Electrochemical Insights, Developing Strategies, and Perspectives toward Advanced Potassium-Sulfur Batteries, Small, 16 (2020) e2003386.

[210] X. Huang, J. Sun, L. Wang, X. Tong, S.X. Dou, Z.M. Wang, Advanced High-Performance Potassium-Chalcogen (S, Se, Te) Batteries, Small, 17 (2021) e2004369.

[211] K. Kaliyappan, J. Liu, B. Xiao, A. Lushington, R. Li, T.-K. Sham, et al., Enhanced Performance of P2-$Na_{0.66}(Mn_{0.54}Co_{0.13}Ni_{0.13})O_2$ Cathode for Sodium-Ion Batteries by Ultrathin Metal Oxide Coatings via Atomic Layer Deposition, Adv. Funct. Mater., 27 (2017) 1701870.

[212] X. Zhang, I. Belharouak, L. Li, Y. Lei, J.W. Elam, A. Nie, et al., Structural and Electrochemical Study of Al2O3and TiO2Coated Li1.2Ni0.13Mn0.54Co0.13O2Cathode Material Using ALD, Adv. Energy Mater., 3 (2013) 1299-1307.

[213] C. Luo, H. Zhu, W. Luo, F. Shen, X. Fan, J. Dai, et al., Atomic-Layer-Deposition Functionalized Carbonized Mesoporous Wood Fiber for High Sulfur Loading Lithium Sulfur Batteries, ACS Appl. Mater. Interfaces, 9 (2017) 14801-14807.

[214] W. Liu, P. Liu, D. Mitlin, Review of Emerging Concepts in SEI Analysis and Artificial SEI Membranes for Lithium, Sodium, and Potassium Metal Battery Anodes, Adv. Energy Mater., 10 (2020) 2002297.

[215] H. Yin, C. Han, Q. Liu, F. Wu, F. Zhang, Y. Tang, Recent Advances and Perspectives on the Polymer Electrolytes for Sodium/Potassium-Ion Batteries, Small, 17 (2021) e2006627.

[216] H. Gao, L. Xue, S. Xin, J.B. Goodenough, A high-energy-density potassium battery with a polymer-gel electrolyte and a polyaniline cathode, Angew. Chem., 130 (2018) 5547-5551.

[217] H. Fei, Y. Liu, Y. An, X. Xu, J. Zhang, B. Xi, et al., Safe all-solid-state potassium batteries with three dimentional, flexible and binder-free metal sulfide array electrode, J. Power Sources, 433 (2019) 226697.

[218] A. Bahi, J. Shao, M. Mohseni, F.K. Ko, Membranes based on electrospun lignin-zeolite composite nanofibers, Sep. Purif. Technol., 187 (2017) 207-213.

[219] S.S.S. Bakar, K.C. Fong, A. Eleyas, M.F.M. Nazeri, Effect of Voltage and Flow Rate Electrospinning Parameters on Polyacrylonitrile Electrospun Fibers, IOP Conference Series: Materials Science and Engineering, 318 (2018) 012076.

[220] T. Wang, S. Kumar, Electrospinning of polyacrylonitrile nanofibers, J. Appl. Polym. Sci., 102 (2006) 1023-1029.

[221] Z. Zhang, YingHuang, G. Zhang, L. Chao, Three–dimensional fiber network reinforced polymer electrolyte for dendrite–free all–solid–state lithium metal batteries, Energy Storage Mater., 41 (2021) 631-641.

[222] L. Gao, J. Li, B. Sarmad, B. Cheng, W. Kang, N. Deng, A 3D polyacrylonitrile nanofiber and flexible polydimethylsiloxane macromolecule combined all-solid-state composite electrolyte for efficient lithium metal batteries, Nanoscale, 12 (2020) 14279-14289.

[223] G. Du, M. Tao, D. Liu, M.K. Aslam, Y. Qi, J. Jiang, et al., Low-operating temperature quasi-solid-state potassium-ion battery based on commercial materials, J. Colloid Interface Sci., 582 (2021) 932-939.

[224] J. Siva Kumar, M. Jaipal Reddy, U.V. Subba Rao, Ion transport and battery studies of a new (PVP + KIO_3) polymer electrolyte system, J. Mater. Sci., 41 (2006) 6171-6173.

[225] B. Sarada, P.B. Bhargav, A. Sharma, V. Rao, Studies on (PEO+ PVA+ KIO3) polymer blend electrolyte films for electrochemical cell applications, Mater. Res. Innovations, 15 (2011) 394-400.

[226] A. CHANDRA, A. CHANDRA, S. THAKUR, SYNTHESIS AND CHARACTERIZATION OF HOT-PRESSED SOLID POLYMER ELECTROLYTES:(1-x) PEO: x KBrO3, International Journal of Chemistry Research, (2012) 81-85.

[227] Y. Pavani, M. Ravi, S. Bhavani, A.K. Sharma, V.V.R. Narasimha Rao, Characterization of poly(vinyl alcohol)/potassium chloride polymer electrolytes for electrochemical cell applications, Polym. Eng. Sci., 52 (2012) 1685-1692.

[228] N.K. Jyothi, K.K. Venkataratnam, P.N. Murty, K.V. Kumar, Preparation and characterization of PAN–KI complexed gel polymer electrolytes for solid-state battery applications, Bull. Mater. Sci., 39 (2016) 1047-1055.

[229] P. Kesharwani, D.K. Sahu, Y.K. Mahipal, R.C. Agrawal, Conductivity enhancement in K+-ion conducting dry Solid Polymer Electrolyte (SPE): [PEO: KNO3]: A consequence of KI dispersal and nano-ionic effect, Mater. Chem. Phys., 193 (2017) 524-531.

[230] Y. Pavani, M. Ravi, S. Bhavani, R.S. Karthikeya, V.V.R.N. Rao, Physical investigations on pure and KBr doped poly(vinyl alcohol) (PVA) polymer electrolyte films for solid state battery applications, J. Mater. Sci. Mater. Electron., 29 (2018) 5518-5524.

[231] H. Fei, Y. Liu, Y. An, X. Xu, G. Zeng, Y. Tian, et al., Stable all-solid-state potassium battery operating at room temperature with a composite polymer electrolyte and a sustainable organic cathode, J. Power Sources, 399 (2018) 294-298.

[232] A. Chandra, Hot pressed K+ ion conducting solid polymer electrolytes: synthesis, ion conduction and polymeric battery fabrication, Indian J. Phys., 90 (2015) 759-765.

[233] P. Kesharwani, D.K. Sahu, M. Sahu, T.b. Sahu, R.C. Agrawal, Study of ion transport and materials properties of K+-ion conducting solid polymer electrolyte (SPE): [(1-x) PEO: xCH_3COOK], Ionics, 23 (2016) 2823-2827.

[234] R. Nadimicherla, A.K. Sharma, V.V.R.N. Rao, W. Chen, Electrical and solid-state battery performance of a new PVC/PEO + KBr blend-based polymer electrolyte system, Ionics, 21 (2014) 1587-1594.

[235] N. Reddeppa, A.K. Sharma, V.V.R. Narasimha Rao, W. Chen, AC conduction mechanism and battery discharge characteristics of (PVC/PEO) polyblend films complexed with potassium chloride, Measurement, 47 (2014) 33-41.

[236] A. Dey, S. Karan, A. Dey, S.K. De, Structure, morphology and ionic conductivity of solid polymer electrolyte, Mater. Res. Bull., 46 (2011) 2009-2015.

[237] A. Chandra, Temperature dependent ionic conductivity and cell performance studies of hot-pressed nanocomposite polymer electrolytes, Comp. Comm., 4 (2017) 33-36.

[238] M. Rayung, M.M. Aung, A. Ahmad, M.S. Su'ait, L.C. Abdullah, S.N. Ain Md Jamil, Characteristics of ionically conducting jatropha oil-based polyurethane acrylate gel electrolyte doped with potassium iodide, Mater. Chem. Phys., 222 (2019) 110-117.

[239] R. Singh, J. Baghel, S. Shukla, B. Bhattacharya, H.-W. Rhee, P.K. Singh, Detailed electrical measurements on sago starch biopolymer solid electrolyte, Phase Transit., 87 (2014) 1237-1245.

[240] Y. Li, L. Zhang, S. Liu, X. Wang, D. Xie, X. Xia, et al., Original growth mechanism for ultra-stable dendrite-free potassium metal electrode, Nano Energy, 62 (2019) 367-375.

[241] X. Tang, D. Zhou, P. Li, X. Guo, B. Sun, H. Liu, et al., MXene-Based Dendrite-Free Potassium Metal Batteries, Adv. Mater., 32 (2020) e1906739.

[242] L. Zhang, X. Xia, Y. Zhong, D. Xie, S. Liu, X. Wang, et al., Exploring Self-Healing Liquid Na-K Alloy for Dendrite-Free Electrochemical Energy Storage, Adv. Mater., 30 (2018) e1804011.

[243] P. Liu, Y. Wang, Q. Gu, J. Nanda, J. Watt, D. Mitlin, Dendrite-Free Potassium Metal Anodes in a Carbonate Electrolyte, Adv. Mater., 32 (2020) e1906735.

[244] M. Ye, J.Y. Hwang, Y.K. Sun, A 4 V Class Potassium Metal Battery with Extremely Low Overpotential, ACS Nano, 13 (2019) 9306-9314.

[245] L. Qin, Y. Lei, H. Wang, J. Dong, Y. Wu, D. Zhai, et al., Capillary Encapsulation of Metallic Potassium in Aligned Carbon Nanotubes for Use as Stable Potassium Metal Anodes, Adv. Energy Mater., 9 (2019) 1901427.

[246] Y. Gu, W.W. Wang, Y.J. Li, Q.H. Wu, S. Tang, J.W. Yan, et al., Designable ultra-smooth ultra-thin solid-electrolyte interphases of three alkali metal anodes, Nat. Commun., 9 (2018) 1339.

[247] L. Gao, J. Li, J. Ju, B. Cheng, W. Kang, N. Deng, High-performance all-solid-state polymer electrolyte with fast conductivity pathway formed by hierarchical structure polyamide 6 nanofiber for lithium metal battery, J. Energy Chem., 54 (2021) 644-654.

[248] J.Y. Liang, X.X. Zeng, X.D. Zhang, T.T. Zuo, M. Yan, Y.X. Yin, et al., Engineering Janus Interfaces of Ceramic Electrolyte via Distinct Functional Polymers for Stable High-Voltage Li-Metal Batteries, J. Am. Chem. Soc., 141 (2019) 9165-9169.

Appendix

The following copyrighted materials were used in this dissertation:

Permissions from publishers to reuse figures/tables in thesis/dissertation

1. **Figure 4.1.1.** Comparison of (a) intercalation-type cathodes, (b) conversion-type cathode, [21]

License Number	5444411087012
License date	Dec 08, 2022

Printable Details

Licensed Content

Licensed Content Publisher	Elsevier
Licensed Content Publication	Materials Today
Licensed Content Title	Li-ion battery materials: present and future
Licensed Content Author	Naoki Nitta,Feixiang Wu,Jung Tae Lee,Gleb Yushin
Licensed Content Date	Jun 1, 2015
Licensed Content Volume	18
Licensed Content Issue	5
Licensed Content Pages	13

Order Details

Type of Use	reuse in a thesis/dissertation
Portion	figures/tables/illustrations
Number of figures/tables/illustrations	1
Format	electronic
Are you the author of this Elsevier article?	No
Will you be translating?	No

2. **Figure 1.2.1.** (c) phase transformation of Li-Te batteries in carbonate electrolyte [50]

SPRINGER NATURE

Te/C nanocomposites for Li-Te Secondary Batteries

Author: Jeong-Uk Seo et al
Publication: Scientific Reports
Publisher: Springer Nature
Date: Jan 22, 2015

Copyright © 2015, The Author(s)

Creative Commons

The request you have made is considered to be non-commercial/educational. As the article you have requested has been distributed under a Creative Commons license (Attribution-Noncommercial), you may reuse this material for non-commercial/educational purposes without obtaining additional permission from Springer Nature, providing that the author and the original source of publication are fully acknowledged (please see the article itself for the license version number). You may reuse this material without obtaining permission from Springer Nature, providing that the author and the original source of publication are fully acknowledged, as per the terms of the license. For license terms, please see http://creativecommons.org/

3. **Figure 1.5.1**. Comparisons of capacity, redox potential, and abundance of metals for anode materials. [68]

1. Dalton transactions 0.00 CAD

Article: A critical perspective on rechargeable Al-ion battery technology.

Order License ID	Pending	Publisher	ROYAL SOCIETY OF CHEMISTRY
ISSN	1477-9234		
Type of Use	Republish in a thesis/dissertation	Portion	Image/photo/illustration

Hide Details

LICENSED CONTENT

Publication Title	Dalton transactions	Rightsholder	Royal Society of Chemistry
Article Title	A critical perspective on rechargeable Al-ion battery technology.	Publication Type	e-Journal
Author/Editor	Royal Society of Chemistry (Great Britain)	Start Page	9906
Date	01/01/2003	End Page	9911
Language	English	Issue	27
Country	United Kingdom of Great Britain and Northern Ireland	Volume	48

4. **Figure 2.1.1.** Te/C cathodes prepared by the melt-diffusion method for Li-Te batteries. (a) Synthesis approach, (b) BET, (c) charge/discharge curves, and (d) rate performance of CMK-3/Te cathodes. [69]

License Number	5444420992099
License date	Dec 08, 2022

Printable Details

Licensed Content

Licensed Content Publisher	Springer Nature
Licensed Content Publication	Journal of Applied Electrochemistry
Licensed Content Title	A lithium–tellurium rechargeable battery with exceptional cycling stability
Licensed Content Author	Toshinari Koketsu et al
Licensed Content Date	Apr 9, 2016

Order Details

Type of Use	Thesis/Dissertation
Requestor type	academic/university or research institute
Format	electronic
Portion	figures/tables/illustrations
Number of figures/tables/illustrations	2
Will you be translating?	no
Circulation/distribution	1 - 29
Author of this Springer Nature content	no

5. **Figure 2.1.2.** (a)TEM image and elemental distribution of Te@ordered microporous carbon (OMC), (b) adsorption-desorption isotherms of OMC and Te@OMC, (c) GITT plot, (d) Nyquist plot, (e) cycling performance and (f) rate capability of S@OMC, Se@OMC, and Te@OMC. [71]

License Number	5444421379881
License date	Dec 08, 2022

Printable Details

Licensed Content

Licensed Content Publisher	John Wiley and Sons
Licensed Content Publication	Advanced Energy Materials
Licensed Content Title	Tellurium@Ordered Macroporous Carbon Composite and Free-Standing Tellurium Nanowire Mat as Cathode Materials for Rechargeable Lithium–Tellurium Batteries
Licensed Content Author	Yun Zong, Shu-Hong Yu, Zhao-Lin Liu, et al
Licensed Content Date	Jan 21, 2015
Licensed Content Volume	5
Licensed Content Issue	8
Licensed Content Pages	7

Order Details

Type of use	Dissertation/Thesis
Requestor type	University/Academic
Format	Electronic
Portion	Figure/table
Number of figures/tables	3
Will you be translating?	No

6. **Figure 2.1.3.** (a) synthesis process and morphology, (b) CV plots, (c) charge/discharge profiles, (d) cycling, (e) rate performance of Te/C-Co-N cathodes, (f) molecular structure of lithium polytellurides, and (g) DFT simulations of the adsorption energy of lithium polytellurides with C-Co-N derived from ZIF-67. [53]

ACS Publications
Most Trusted. Most Cited. Most Read.

Tellurium-Impregnated Porous Cobalt-Doped Carbon Polyhedra as Superior Cathodes for Lithium–Tellurium Batteries

Author: Jiarui He, Weiqiang Lv, Yuanfu Chen, et al
Publication: ACS Nano
Publisher: American Chemical Society
Date: Aug 1, 2017

Copyright © 2017, American Chemical Society

PERMISSION/LICENSE IS GRANTED FOR YOUR ORDER AT NO CHARGE

This type of permission/license, instead of the standard Terms and Conditions, is sent to you because no fee is being charged for your order. Please note the following:

- Permission is granted for your request in both print and electronic formats, and translations.
- If figures and/or tables were requested, they may be adapted or used in part.
- Please print this page for your records and send a copy of it to your publisher/graduate school.
- Appropriate credit for the requested material should be given as follows: "Reprinted (adapted) with permission from {COMPLETE REFERENCE CITATION}. Copyright {YEAR} American Chemical Society." Insert appropriate information in place of the capitalized words.
- One-time permission is granted only for the use specified in your RightsLink request. No additional uses are granted (such as derivative works or other editions). For any uses, please submit a new request.

If credit is given to another source for the material you requested from RightsLink, permission must be obtained from that source.

7. **Figure 2.1.4.** Nanostructured Te cathodes for Li-Te batteries. (a) Synthesis process and morphology and (b) electrochemical performance of three-dimensional rGO/Te nanowire aerogel (3DGT)**.** [47]

ACS Publications
Most Trusted. Most Cited. Most Read.

Three-Dimensional Hierarchical Reduced Graphene Oxide/Tellurium Nanowires: A High-Performance Freestanding Cathode for Li–Te Batteries

Author: Jiarui He, Yuanfu Chen, Weiqiang Lv, et al
Publication: ACS Nano
Publisher: American Chemical Society
Date: Sep 1, 2016

Copyright © 2016, American Chemical Society

PERMISSION/LICENSE IS GRANTED FOR YOUR ORDER AT NO CHARGE

This type of permission/license, instead of the standard Terms and Conditions, is sent to you because no fee is being charged for your order. Please note the following:

- Permission is granted for your request in both print and electronic formats, and translations.
- If figures and/or tables were requested, they may be adapted or used in part.
- Please print this page for your records and send a copy of it to your publisher/graduate school.
- Appropriate credit for the requested material should be given as follows: "Reprinted (adapted) with permission from {COMPLETE REFERENCE CITATION}. Copyright {YEAR} American Chemical Society." Insert appropriate information in place of the capitalized words.
- One-time permission is granted only for the use specified in your RightsLink request. No additional uses are granted (such as derivative works or other editions). For any uses, please submit a new request.

If credit is given to another source for the material you requested from RightsLink, permission must be obtained from that source.

8. **Figure 2.1.5.** (a) synthesis and cathode architectures of Te nanowires/elastic carbon nanotube (Te@CNT and Te/CNTs) aerogel, (b) morphology of TeNWs and CNTs, and electrochemical performance of (c-d) Te@CNT and (e-f) Te/CNTs. [77]

License Number	5444430421906
License date	Dec 08, 2022

Printable Details

Licensed Content

Licensed Content Publisher	John Wiley and Sons
Licensed Content Publication	Advanced Functional Materials
Licensed Content Title	Elastic Carbon Nanotube Aerogel Meets Tellurium Nanowires: A Binder- and Collector-Free Electrode for Li-Te Batteries
Licensed Content Author	Jie Xu, Sen Xin, Jian-Wei Liu, et al
Licensed Content Date	May 11, 2016
Licensed Content Volume	26
Licensed Content Issue	21
Licensed Content Pages	9

Order Details

Type of use	Dissertation/Thesis
Requestor type	University/Academic
Format	Electronic
Portion	Figure/table
Number of figures/tables	4
Will you be translating?	No

9. **Figure 2.1.6.** Te_xS_y composite cathodes. Charge-discharge profiles of (a) $Te_{0.1}S_{0.9}$/CMK-3 and (b) S/CMK-3, (c) cycling performance of Te_xS_{1-x}/CMK-3 (x=0.05, 0.1, 0.2), (d) capacity stability of $Te_{0.1}S_{0.9}$/CMK-3 at 1 A g^{-1} and 3 A g^{-1}, (e) schematic diagram of the formation of Te-induced SEI layer on Te_xS_{1-x}/CMK-3 cathode surface. [83]

1. Journal of materials chemistry. A, Materials for energy and sustainability — 0.00 CAD

Article: Heteroatomic TexS1−x molecule/C nanocomposites as stable cathode materials in carbonate-based electrolytes for lithium–chalcogen batteries

Order License ID	Pending	Publisher	Royal Society of Chemistry
ISSN	2050-7496	Portion	Image/photo/illustration
Type of Use	Republish in a thesis/dissertation		

Hide Details

LICENSED CONTENT

Publication Title	Journal of materials chemistry. A, Materials for energy and sustainability	Publication Type	e-Journal
Article Title	Heteroatomic TexS1−x molecule/C nanocomposites as stable cathode materials in carbonate-based electrolytes for lithium–chalcogen batteries	Start Page	10104
		End Page	10110
		Issue	21
		Volume	6
		URL	http://pubs.rsc.org/en/journals/journ...
Author/Editor	Royal Society of Chemistry (Great Britain)		
Date	01/01/2013		
Language	English		
Country	United Kingdom of Great Britain and Northern Ireland		
Rightsholder	Royal Society of Chemistry		

10. **Figure 2.1.7.** (a) electron density differences for S, Li_2S, Te-S, Te-Li_2S, (b) formation energies of lithium insertion and extraction for the initial lithiation and delithiation process, (c) possible Li migration pathways in Te-Li_2S, (d) energy profiles for Li migration pathway 1 in Li_2S and Te-Li_2S, (e) rate performance of Te-3-S/KB and S/KB, (f) discharge capacities and corresponding capacity retention *versus* dopant ratio at the 1st and 50th cycle, long-term cycling performance of (g) Te-3-S/KB and S/KB, (h) Te-3-S/rGO at 5 A g^{-1}. [85]

Manipulating the Redox Kinetics of Li–S Chemistry by Tellurium Doping for Improved Li–S Batteries

Author: Kangli Xu, Xiaojing Liu, Jianwen Liang, et al
Publication: ACS Energy Letters
Publisher: American Chemical Society
Date: Feb 1, 2018

Copyright © 2018, American Chemical Society

PERMISSION/LICENSE IS GRANTED FOR YOUR ORDER AT NO CHARGE

This type of permission/license, instead of the standard Terms and Conditions, is sent to you because no fee is being charged for your order. Please note the following:

- Permission is granted for your request in both print and electronic formats, and translations.
- If figures and/or tables were requested, they may be adapted or used in part.
- Please print this page for your records and send a copy of it to your publisher/graduate school.
- Appropriate credit for the requested material should be given as follows: "Reprinted (adapted) with permission from {COMPLETE REFERENCE CITATION}. Copyright {YEAR} American Chemical Society." Insert appropriate information in place of the capitalized words.
- One-time permission is granted only for the use specified in your RightsLink request. No additional uses are granted (such as derivative works or other editions). For any uses, please submit a new request.

If credit is given to another source for the material you requested from RightsLink, permission must be obtained from that source.

11. **Figure 2.1.8.** (a) Synthetic route of Te_xS_{1-x}@pPAN, cycling performance of $Te_{0.04}S_{0.96}$@pPAN in (b) carbonate electrolyte and (c) ether electrolyte, (d) CV plots, (e) charge-discharge profiles, (f) UV-vis spectra, (g) Li^+ diffusion coefficients, (h, i) reaction resistance during discharge and charge process of S@pPAN and $Te_{0.04}S_{0.96}$@pPAN. [85]

License Number	5444431147264
License date	Dec 08, 2022

Printable Details

Licensed Content

Licensed Content Publisher	Elsevier
Licensed Content Publication	Nano Energy
Licensed Content Title	Manipulating kinetics of sulfurized polyacrylonitrile with tellurium as eutectic accelerator to prevent polysulfide dissolution in lithium-sulfur battery under dissolution-deposition mechanism
Licensed Content Author	Shuping Li,Zhilong Han,Wei Hu,Linfeng Peng,Jiaqiang Yang,Lihui Wang,Yunyang Zhang,Bin Shan,Jia Xie
Licensed Content Date	Jun 1, 2019
Licensed Content Volume	60
Licensed Content Issue	n/a
Licensed Content Pages	9

Order Details

Type of Use	reuse in a thesis/dissertation
Portion	figures/tables/illustrations
Number of figures/tables/illustrations	3
Format	electronic
Are you the author of this Elsevier article?	No
Will you be translating?	No

12. **Figure 2.1.9.** Galvanostatic charge-discharge curves of Te/C cathodes in different electrolytes of (b) 1M LiTFSI in DOL:DME (1:1) [53]**,** (c) 1M $LiClO_4$ in DMSO [71]**,** and (d) solid electrolyte (LiTFSI-PEO) [79]**.**

ACS Publications
Most Trusted. Most Cited. Most Read.

Tellurium-Impregnated Porous Cobalt-Doped Carbon Polyhedra as Superior Cathodes for Lithium–Tellurium Batteries

Author: Jiarui He, Weiqiang Lv, Yuanfu Chen, et al
Publication: ACS Nano
Publisher: American Chemical Society
Date: Aug 1, 2017

Copyright © 2017, American Chemical Society

PERMISSION/LICENSE IS GRANTED FOR YOUR ORDER AT NO CHARGE

This type of permission/license, instead of the standard Terms and Conditions, is sent to you because no fee is being charged for your order. Please note the following:

- Permission is granted for your request in both print and electronic formats, and translations.
- If figures and/or tables were requested, they may be adapted or used in part.
- Please print this page for your records and send a copy of it to your publisher/graduate school.
- Appropriate credit for the requested material should be given as follows: "Reprinted (adapted) with permission from {COMPLETE REFERENCE CITATION}. Copyright {YEAR} American Chemical Society." Insert appropriate information in place of the capitalized words.
- One-time permission is granted only for the use specified in your RightsLink request. No additional uses are granted (such as derivative works or other editions). For any uses, please submit a new request.

If credit is given to another source for the material you requested from RightsLink, permission must be obtained from that source.

License Number	5444421379881
License date	Dec 08, 2022

Printable Details

Licensed Content

Licensed Content Publisher	John Wiley and Sons
Licensed Content Publication	Advanced Energy Materials
Licensed Content Title	Tellurium@Ordered Macroporous Carbon Composite and Free-Standing Tellurium Nanowire Mat as Cathode Materials for Rechargeable Lithium–Tellurium Batteries
Licensed Content Author	Yun Zong, Shu-Hong Yu, Zhao-Lin Liu, et al
Licensed Content Date	Jan 21, 2015
Licensed Content Volume	5
Licensed Content Issue	8
Licensed Content Pages	7

Order Details

Type of use	Dissertation/Thesis
Requestor type	University/Academic
Format	Electronic
Portion	Figure/table
Number of figures/tables	3
Will you be translating?	No

License Number	5444431439009
License date	Dec 08, 2022

Printable Details

Licensed Content

Licensed Content Publisher	Elsevier
Licensed Content Publication	Electrochimica Acta
Licensed Content Title	Tellurium nanotubes grown on carbon fiber cloth as cathode for flexible all-solid-state lithium-tellurium batteries
Licensed Content Author	Hong Yin,Xiang-Xiang Yu,Yi-Wei Yu,Ming-Lei Cao,Han Zhao,Chong Li,Ming-Qiang Zhu
Licensed Content Date	Aug 20, 2018
Licensed Content Volume	282
Licensed Content Issue	n/a
Licensed Content Pages	7

Order Details

Type of Use	reuse in a thesis/dissertation
Portion	figures/tables/illustrations
Number of figures/tables/illustrations	2
Format	electronic
Are you the author of this Elsevier article?	No
Will you be translating?	No

13. **Figure 2.1.10.** K-Te batteries. (a) HRTEM image, (b) SAED pattern, (c) HADDF and EDS mapping of Te-G-CNT electrode after discharged to 0.3V, (d) *ex situ* XRD and (e) Te 3d XPS spectra of as-prepared, discharged, and charged Te-G-CNT electrodes, (f) formation energy of K_nTe, (g) CV, (h) cycling performance, (i) charge-discharge profiles, (j) rate performance of Te-G-CNT electrode, (1M KFSI in EC:DEC). [104]

License Number	5444440389801
License date	Dec 08, 2022

Printable Details

Licensed Content

Licensed Content Publisher	John Wiley and Sons
Licensed Content Publication	Advanced Materials
Licensed Content Title	Tellurium: A High-Volumetric-Capacity Potassium-Ion Battery Electrode Material
Licensed Content Author	Shuai Dong, Dandan Yu, Jie Yang, et al
Licensed Content Date	Apr 30, 2020
Licensed Content Volume	32
Licensed Content Issue	23
Licensed Content Pages	8

Order Details

Type of use	Dissertation/Thesis
Requestor type	University/Academic
Format	Electronic
Portion	Figure/table
Number of figures/tables	2
Will you be translating?	No

14. **Figure 2.1.11.** (a) synthesis process of TeNWs/CNTs/rGO, (b) K-Te cell structure and reaction pathways, (c) CV plots of TeNWs/CNTs/rGO, (d) charge-discharge profiles, (e) cathode materials

comparison in potassium-ion batteries, and (f) cycling performance of TeNWs/CNTs/rGO using 1M and 5M KTFSI in DEGDME. [105]

License Number	5444440168492
License date	Dec 08, 2022

Printable Details

Licensed Content

Licensed Content Publisher	Elsevier
Licensed Content Publication	Energy Storage Materials
Licensed Content Title	A potassium–tellurium battery
Licensed Content Author	Qin Liu,Wenzhuo Deng,Chuan-Fu Sun
Licensed Content Date	Jun 1, 2020
Licensed Content Volume	28
Licensed Content Issue	n/a
Licensed Content Pages	7

Order Details

Type of Use	reuse in a thesis/dissertation
Portion	figures/tables/illustrations
Number of figures/tables/illustrations	4
Format	electronic
Are you the author of this Elsevier article?	No
Will you be translating?	No

15. **Figure 6.2.3**. Te-S phase diagram. [174]

License Number	5444440606463
License date	Dec 08, 2022

Printable Details

Licensed Content

Licensed Content Publisher	Springer Nature
Licensed Content Publication	Russian Journal of Physical Chemistry A
Licensed Content Title	Melt–Vapor Phase Diagram of the Te–S System
Licensed Content Author	V. N. Volodin et al
Licensed Content Date	Mar 9, 2018

Order Details

Type of Use	Thesis/Dissertation
Requestor type	academic/university or research institute
Format	electronic
Portion	figures/tables/illustrations
Number of figures/tables/illustrations	1
Will you be translating?	no
Circulation/distribution	1 - 29
Author of this Springer Nature content	no

Permissions for published articles in thesis/dissertation

A durable lithium–tellurium battery: Effects of carbon pore structure and tellurium content

Author: Yue Zhang,Wei Lu,Peter Zhao,Mohammad Hossein Aboonasr Shiraz,Dan Manaig,Donald J. Freschi,Yulong Liu,Jian Liu

Publication: Carbon

Publisher: Elsevier

Date: March 2021

© 2020 Elsevier Ltd. All rights reserved.

Journal Author Rights

Please note that, as the author of this Elsevier article, you retain the right to include it in a thesis or dissertation, provided it is not published commercially. Permission is not required, but please ensure that you reference the journal as the original source. For more information on this and on your other retained rights, please visit: https://www.elsevier.com/about/our-business/policies/copyright#Author-rights

The role of carbon pore structure in tellurium/carbon cathodes for lithium-tellurium batteries

Author: Yue Zhang,Wei Lu,Peter Zhao,Li Tao,Yulong Liu,Dan Manaig,Donald J. Freschi,Jian Liu

Publication: Electrochimica Acta

Publisher: Elsevier

Date: 20 August 2021

© 2021 Elsevier Ltd. All rights reserved.

Journal Author Rights

Please note that, as the author of this Elsevier article, you retain the right to include it in a thesis or dissertation, provided it is not published commercially. Permission is not required, but please ensure that you reference the journal as the original source. For more information on this and on your other retained rights, please visit: https://www.elsevier.com/about/our-business/policies/copyright#Author-rights

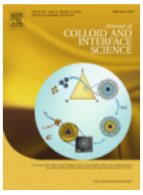

Quasi-solid-state lithium-tellurium batteries based on flexible gel polymer electrolytes

Author: Yue Zhang,Wei Lu,Dan Manaig,Donald J. Freschi,Yulong Liu,Haiming Xie,Jian Liu

Publication: Journal of Colloid and Interface Science

Publisher: Elsevier

Date: January 2022

© 2021 Elsevier Inc. All rights reserved.

Journal Author Rights

Please note that, as the author of this Elsevier article, you retain the right to include it in a thesis or dissertation, provided it is not published commercially. Permission is not required, but please ensure that you reference the journal as the original source. For more information on this and on your other retained rights, please visit: https://www.elsevier.com/about/our-business/policies/copyright#Author-rights

Enhanced Potassium Storage Performance for K-Te Batteries via Electrode Design and Electrolyte Salt Chemistry

Author: Yue Zhang, Chang Liu, Zhenrui Wu, et al
Publication: Applied Materials
Publisher: American Chemical Society
Date: Apr 1, 2021

Copyright © 2021, American Chemical Society

PERMISSION/LICENSE IS GRANTED FOR YOUR ORDER AT NO CHARGE

This type of permission/license, instead of the standard Terms and Conditions, is sent to you because no fee is being charged for your order. Please note the following:

- Permission is granted for your request in both print and electronic formats, and translations.
- If figures and/or tables were requested, they may be adapted or used in part.
- Please print this page for your records and send a copy of it to your publisher/graduate school.
- Appropriate credit for the requested material should be given as follows: "Reprinted (adapted) with permission from {COMPLETE REFERENCE CITATION}. Copyright {YEAR} American Chemical Society." Insert appropriate information in place of the capitalized words.
- One-time permission is granted only for the use specified in your RightsLink request. No additional uses are granted (such as derivative works or other editions). For any uses, please submit a new request.

If credit is given to another source for the material you requested from RightsLink, permission must be obtained from that source.

License Number	5444450272229
License date	Dec 08, 2022

Printable Details

Licensed Content

Licensed Content Publisher	John Wiley and Sons
Licensed Content Publication	Small
Licensed Content Title	High-Performance Potassium-Tellurium Batteries Stabilized by Interface Engineering
Licensed Content Author	Yue Zhang, Hongzheng Zhu, Donald J. Freschi, et al
Licensed Content Date	Feb 27, 2022
Licensed Content Volume	18
Licensed Content Issue	15
Licensed Content Pages	11

Order Details

Type of use	Dissertation/Thesis
Requestor type	Author of this Wiley article
Format	Electronic
Portion	Full article
Will you be translating?	No

License Number	5444450390405
License date	Dec 08, 2022

Printable Details

Licensed Content

Licensed Content Publisher	John Wiley and Sons
Licensed Content Publication	Small
Licensed Content Title	Polyacrylonitrile-Reinforced Composite Gel Polymer Electrolytes for Stable Potassium Metal Anodes
Licensed Content Author	Yue Zhang, Addie Bahi, Frank Ko, et al
Licensed Content Date	Jan 29, 2022
Licensed Content Volume	18
Licensed Content Issue	8
Licensed Content Pages	11

Order Details

Type of use	Dissertation/Thesis
Requestor type	Author of this Wiley article
Format	Electronic
Portion	Full article
Will you be translating?	No

ELSEVIER

Materials design and fundamental understanding of tellurium-based electrochemistry for rechargeable batteries

Author: Yue Zhang,Dan Manaig,Donald J. Freschi,Jian Liu

Publication: Energy Storage Materials

Publisher: Elsevier

Date: September 2021

© 2021 Elsevier B.V. All rights reserved.

Journal Author Rights

Please note that, as the author of this Elsevier article, you retain the right to include it in a thesis or dissertation, provided it is not published commercially. Permission is not required, but please ensure that you reference the journal as the original source. For more information on this and on your other retained rights, please visit: https://www.elsevier.com/about/our-business/policies/copyright#Author-rights